UNIVERSITY
OF TRENTO - Italy
DEPARTMENT OF INDUSTRIAL ENGINEERING

XXXI cycle

Doctoral School in Materials, Mechatronics
and Systems Engineering

Experimental and Numerical Investigation of the Micromechanical Behavior of Selective Laser Melted Ti-6Al-4V Cellular Lattices for Biomedical Applications

Michele Dallago

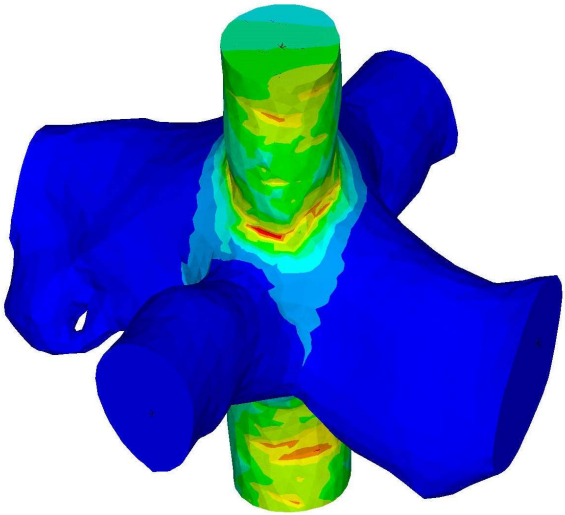

April 2019

EXPERIMENTAL AND NUMERICAL INVESTIGATION OF THE MICROMECHANICAL BEHAVIOR OF SELECTIVE LASER MELTED TI-6AL-4V CELLULAR LATTICES FOR BIOMEDICAL APPLICATIONS

Michele Dallago

E-mail: michele.dallago@unitn.it

Approved by:

Prof. Matteo Benedetti, Advisor
Department of Industrial Engineering
University of Trento, Italy.

Prof. Vigilio Fontanari,
Department of Industrial Engineering
University of Trento, Italy.

Ph.D. Commission:

Prof. Alberto Molinari,
Department of Industrial Engineering
University of Trento, Italy.

Prof. Mario Guagliano,
Department of Mechanical Engineering
Politecnico di Milano, Italy.

Prof. Filippo Berto,
Department of Mechanical and
Industrial Engineering
Norwegian University of Science and Technology, Norway.

University of Trento,

Department of Industrial Engineering

April 2018

University of Trento - Department of Industrial Engineering

Doctoral Thesis

Michele Dallago - 2019
Published in Trento (Italy) – by University of Trento

Abstract

Cellular materials are characterized by a complex interconnected structure of struts or plates and shells which make up the cells edges and faces. Their structure can be advantageously engineered in order to tailor their properties according to the specific application. This aspect makes them particularly attractive for the manufacturing of bone prosthetics since, compared to traditional fully dense implants, although more complex to produce and with less predictable properties, implants with a highly porous structure can be manufactured to match the bone stiffness and at the same time favor bone ingrowth and regeneration. The development of Selective Laser Melting (SLM) made possible to obtain metallic cellular materials with highly complex structures characterized by a wide range of cell morphologies that allow to finely tune the mechanical properties of the implant to the patient needs. Titanium alloys such as Ti-6Al-4V have shown excellent biocompatibility combined with good mechanical properties and have also been successfully used in the manufacturing of lattice structures with minute details via SLM. Nevertheless, there are still several issues to consider. For instance, despite the static mechanical properties of such lattices being addressed by many studies, the fatigue behavior still remains little investigated, even though it is a critical aspect in load-bearing biomedical implants (consider, for example, the periodic nature of human gait in the case of hip implants). In this regard, increasing the fatigue resistance of cellular lattices by finely adjusting the geometry, for instance by adding fillets at the cell-wall joints, is a new interesting opportunity made possible by additive manufacturing technologies. On the other hand, a discrepancy between the as-designed and the as-built geometry in SLM parts is an issue that can be critically important for lattices with pore size and strut thicknesses of a few hundred microns, such as biomedical lattices. Indeed, any geometrical imperfection introduces a degree of uncertainty that can alter the mechanical properties of the as-built lattice.

This work represents an attempt in the direction of building a deeper understanding of the effect of the fine geometrical details, such as the fillet radius at the joints and the thickness of the struts, on the elastic constants and on the fatigue resistance of Ti-6Al-4V SLM lattices, with the aim to develop analytical predictive models of the mechanical properties. Moreover, this work also aims at investigating the as-built/as-designed morphological discrepancy in lattices in relation to the their as-designed geometry and its effects on the elastic modulus and the fatigue resistance. In this regard, the purpose is to develop quantitative relationships between the as-designed and the as-built geometry in order to obtain design tools to predict the final morphology of the lattice by taking into account the manufacturing errors.

This thesis covers a wide range of topics, therefore, in the interest of a better presentation, the results of the research have been devided into three independent Chapters. Each of them has been provided of an abstract and an Introduction and

divided into a Materials and Methods (or Modelling) section, a Results and Discussion section and finally Conclusions and References. Naturally, the chapters are logically connected and coherent with the frame defined by the title of the thesis. Therefore, this thesis is organized into five chapters. In the first Chapter the backrground to the topics discussed in the subsequent chapters is provided and the relevant literature is reviewed, while in the fifth and last Chapter some conclusions are drawn, and future perspectives are discussed. The core of the work is contained in the three central chapters.

In Chapter II, analytical models developed to predict the elastic constants and the stress concentration factors (SCF) of 2D lattices with variously arranged square cells and filleted junctions are presented. The effect of stretching and bending actions on the elastic constants of a single cell is identified by devising an analytical model based on classical beam theory and and periodic boundary conditions. Specifically, two spatial arrangements are considered: a honeycomb with regular square cells and a honeycomb with square cells staggered by a prescribed offset of half of the cell wall length. The theoretical beam model is fitted to the results of a 2D Finite Elements (FE) model based on plane elements via an extensive parametric analysis. In this way, semi-analytical formulas are proposed to calculate the stiffness in large domains of the geometric parameters (strut thickness t_0 and fillet radius R). A numerical method is also proposed to estimate the SCFs at the cell wall junctions of a 2D regular square cellular lattice. The aim is to obtain a model capable of calculating the values of the SCF as a function of the unit cell geometrical parameters and consequently assess the stress state in the lattice, which is one of the main factors determining fatigue resistance. This was achieved by applying the FE method to the unit cell for wide intervals of t_0 and R to calculate the SCF for each couple of the parameters. The values of the SCFs were then fitted with functions. The models developed in this Chapter are then used in the subsequent chapters as a support in the design of 3D regular square lattices and in the interpretation of the mechanical characterization.

In Chapter III, the results of the mechanical and morphological characterization of different regular cubic open-cell cellular structures produced via SLM of Ti-6Al-4V alloy, all with the same nominal elastic modulus of 3 GPa that matches that of human trabecular bone, are presented. The fully reversed fatigue strength at 10^6 cycles and the elastic modulus were measured and an attempt was made to link them to the manufacturing defects (porosity and geometrical inaccuracies). Half of the specimens was subjected to a stress relief thermal treatment while the other half to Hot Isostatic Pressing (HIP), and the effect of the treatments on porosity and on the mechanical properties was assessed. The results of fatigue and quasi-static tests on regular cubic lattices were compared with FE calculations based on the as-designed geometry and on the as-built geometry reconstructed from micro X-ray computed tomography (μCT) scans. It was observed that the fatigue strength and, to a lesser extent, the elastic modulus are correlated with the number and severity of defects and that predictions on the mechanical properties based on the as-designed geometry are not accurate. The fatigue strength seems to be highly dependent on the surface irregularities and on the notches introduced during the manufacturing

process. In fully reversed fatigue tests, the high performances of stretching dominated structures compared to bending dominated structures are not found. In fact, with thicker struts, such structures proved to be more resistant, even if bending actions were present. Given the small size of the unit cells (the unit cell size is 1.5 mm and the strut thickness is 0.26 mm) and the limitations in accuracy of the printer, the fillet radii at the junctions were highly irregular and somewhat hard to recognize. In order to investigate the real benefit of filleted junctions on the stress concentration effects at the junctions and to assess the manufacturability of such minute geometrical detail, a new experimental campaign was set up. In Chapter IV, a set of cubic lattice specimens with filleted junctions was designed and produced via SLM. The size of the unit cell is considerably larger than that of the previous specimens, being 8 mm, 6 mm and 4 mm with the rest of the geometrical parameters scaled accordingly. Thus, nine combinations of the geometrical parameters of the unit cell and three orientations with respect to the printing direction are considered. The aim is to investigate the relationship between the as-designed and the as-built geometry and to find the smallest radius which can be accurately reproduced by the printer. Moreover, a compensation strategy of the morphological defects is devised using the mathematical relationships obtained between the as-designed and the as-built strut thickness. This strategy consists in modifying the input CAD to compensate for the deviations introduced by the SLM process.

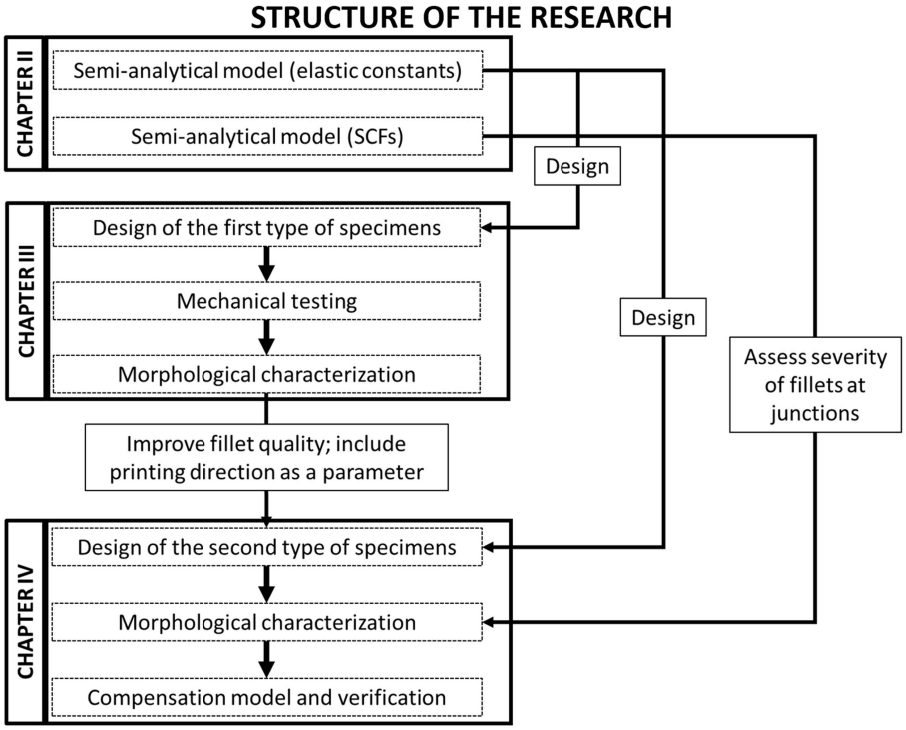
STRUCTURE OF THE RESEARCH
CHAPTER II
Semi-analytical model (elastic constants)
Semi-analytical model (SCFs)
Design
CHAPTER III
Design of the first type of specimens
Mechanical testing
Morphological characterization
Design
Assess severity of fillets at junctions
Improve fillet quality; include printing direction as a parameter
CHAPTER IV
Design of the second type of specimens
Morphological characterization
Compensation model and verification

Table of contents

Chapter I

Introduction

1.1 The human bone and the implant

1.1.1 Structure and mechanical properties of human bone

Bone is a natural composite material made of a mineral part (60-70%wt) embedded in an organic matrix (10-20%wt); the rest is water [1,2]. The peculiar mechanical properties of bone are conferred by its hierarchical structure, that goes form a sub-nanostructure to a macrostructure, as shown in Figure I - 1.

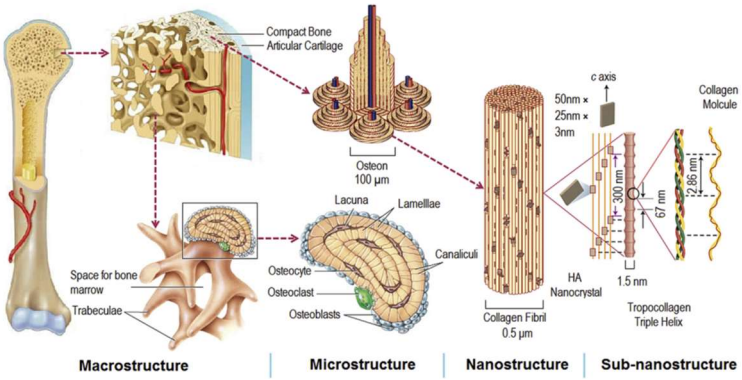

Figure I - 1. The structure of bone [1].

At the sub-nanoscale, the constituents of the organic matrix can be observed: 90% collagen (mainly type-I collagen) and 10% of non-collagenous proteins, whose role is likely related to bone remodeling. At the nanoscale, collagen is organized in fibrils, which consists of parallel arrays of tropocollagen (a triple helical molecule of roughly 300 nm in length and 1.5 nm in diameter) arranged in a regular stagger and stabilized by crosslinking. This assembly creates the characteristic bands roughly every 67 nm in the fibrils, due to the overlapping of tropocollagen molecules. The mineral (inorganic) part is largely hydroxyapatite (HA), $Ca_{10}(PO_4)_6(OH)_2$, in the form of nanometric plate-like crystals (50nm x 25 nm x 3nm). HA in the bone is not pure, but it also contains ions such as strontium, zinc, carbonates, magnesium, fluoride [3,4]. The HA crystals (platelets) nucleate in the binding sites of the tropocollagen molecules with their *c*-axis parallel to the fibril [3]. The mineral phase provides the

strength and the stiffness of the bone and is also responsible for the anisotropy of the mechanical properties due to its orientation [3,4]. On the other hand, collagen increases the toughness of the bone and controls mainly the post-yield behavior [3,4]. Even after the removal of collagen, bone retains most of its stiffness and strength because HA crystals form a continuous network [2].

Jumping to the macroscale, we can distinguish between cortical (compact) bone and cancellous (trabecular) bone (Figure I - 2). Compact bone is a dense tissue (90-95% relative density) with only microscopic channels for blood vessels and the flow of nutrients. Up to 80% of the bone mass in the human body is of the compact type and it constitutes the surface of the bones [5]. The thickness of this layer, which provides the supportive and protective function of the skeleton, increases in the areas where the mechanical loads are higher, like the shafts of long bones [6]. The building blocks of compact bone on the microscopic scale are the osteons, which are cylinders of diameter between 10 μm and 500 μm generally arranged in parallel arrays that in long bones (e.g., femur and tibia) are aligned with the longitudinal axis. The osteons are made of thin lamellae (3-7 μm in thickness) of mineralized collagen fibrils, densely packed into fibers, wrapped around a central channel in which blood vessels and nerves run (Harvesian system). Between the osteons, a complex system of lacunae (small voids that contain the osteocytes), canaliculi (small channels) and Volksmann's canals form an intercommunicating system that takes care of the transport of nutrients and the removal of waste substances [3–5].

Cancellous bone, on the other hand, is very porous (10-50% relative density) and is made of an interconnected network of plates and rods (known as trabeculae) 200 μm thick and it is found in the interior of bones protected by compact bone, such as the ends of long bones (e.g. femoral head), in the vertebrae and in the core of flat bones (e.g. pelvis, skull) [7]. In the trabeculae, the collagen fibers are arranged in thin concentric lamellae and, like the compact bone, there are lacunae with osteocytes (the cells responsible for the daily metabolic activity in the bone) and caniculi, but the Harvesian system is missing, i.e. there are no osteons and blood vessels. The voids of this trabecular structure are filled with red bone marrow [5]. The advantage of a trabecular structure is to reduce the weight of the bone without reducing its volume, thus providing a large load bearing area for joints (like in the femoral head) or a light sandwich structure (like in the bones of the skull) [7]. Moreover, the open space can be used to "store" the vital red bone marrow for the production of blood cells [5].

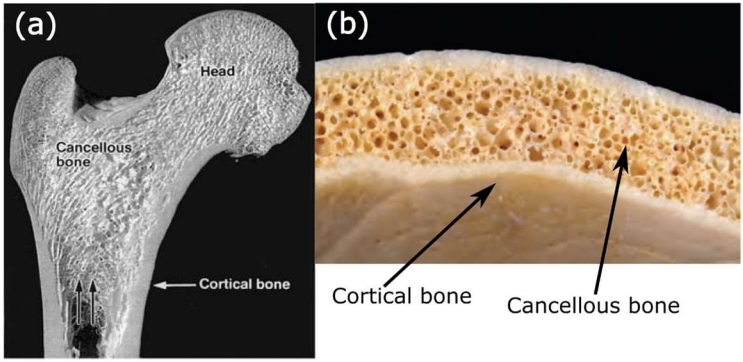

Figure I - 2. Cortical and cancellous bone: (a) head of a human femur [4], (b) part of a human skull [8].

Bone is a living tissue that undergoes a continuous remodeling process in which old bone is replaced by new tissue. Compact bone remodels through resorption of old osteons (by cells called osteoclasts) which are then replaced (by cells called osteoblasts) by new bone growing in concentric lamellae. On the other hand, cancellous bone remodels starting from the surface where old bone is directly removed and substituted by new trabecular packets. Given its greater surface, cancellous bone remodels faster than compact bone (20%wt per year vs 4%wt per year). In this way, bone has the capability of repairing small damages and of adapting to the external mechanical stimuli. Indeed, if the mechanical loads increase in a region, the newly deposited bone will be thicker. On the other hand, if the bone is under-loaded, less new tissue will be deposited [4,5]. It has been observed that bone is piezoelectric (Cowin, 2001) and thus a mechanical stimulus is translated to an electric stimulus which then directs remodeling [8]. But more on this subject in the Paragraph dedicated to stress shielding.

The mechanical properties of bone tissue are strongly correlated with degree of mineralization, age and anatomic site [1,3]. Mineral content increases the stiffness of both cortical and cancellous bone [2,4], indeed with ageing bone tissue loses stiffness and strength most likely due to a loss in bone mineral density (BMD) [2,3]. Regarding the anatomic site, for example it has been observed that tibial bone is stiffer than femoral bone [3]. It is very difficult to carry out a general discussion on the mechanical properties of bone and to provide accurate values due the variability described above. In addition, the mode of loading and the size of the specimen have a strong effect on the measured values [3]. Finally, the moisture content is also important [3,7].
Compact bone is transversely isotropic (five elastic constants are necessary to define its elastic behavior), particularly in long bones where the osteons run

prevalently parallel to the long axis of the bone [3]. Moreover, it has been observed that cortical bone is stronger in compression than in tension [3]. Some mechanical properties for compact bone are listed in Table I - 1. At low strain rates compact bone is tougher, while at higher speeds it behaves as a brittle solid, likely due to the fact that at slow rates energy absorbing microcracks can form [2,3], as shown in Figure I - 3. The density of human compact bone is 1800-2000 kg/m^3 [7].

Table I - 1. Mechanical properties of human compact (cortical) bone.

Mechanical property	Longitudinal direction	Transverse direction
Elastic modulus [GPa]	17-25 [6]; 17.4 [4]	12 [6]; 9.6 [4]
Poisson's ratio	0.58 [3]	0.46 [3]
Yield strength (tension) [MPa]	148 [9]	49 [9]
Tensile strength [MPa]	133-150 [6]	50 [6]
Compressive strength [MPa]	193 [6]	133 [6]

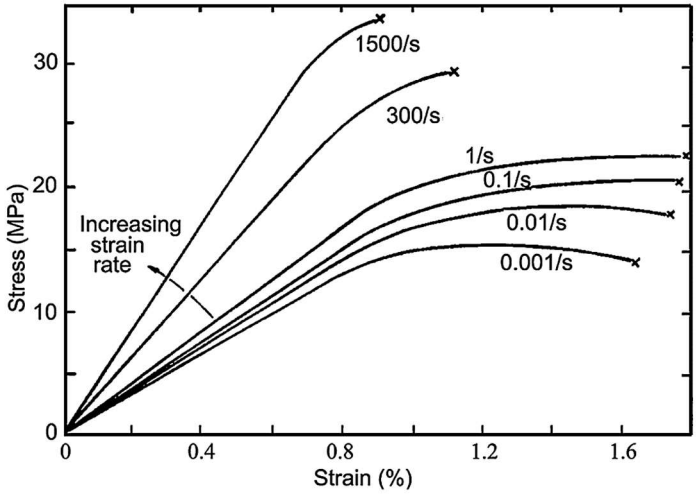

Figure I - 3. Stress-strain curves of compact bone at different strain rates [2].

Trabecular bone has a highly porous structure and it can be classified as a cellular material or more precisely as a foam, i.e. a material "made up of an interconnected network of solid struts or plates which form the edges and faces of cells" [9]. It has been observed that the trabeculae tend to develop parallel to the direction of principal stresses to increase the mechanical efficiency of the structure [7,9], in other words a functional adaptation occurs to improve the spatial arrangement of the bone tissue to better answer to the local mechanical stimuli [4,10]. As an example, in Figure I - 4 the trabecular structure of the proximal part of a femur is compared with the directions of the principal stresses: the trabeculae tend to form an orthogonal architecture (Figure I - 4a) that on average follows the directions of the principal stresses (Figure I - 4b) that guides the loads from the head and the greater trochanter to the compact bone of the shaft. Moreover, the structure has a higher relative density in the most stressed regions [7].

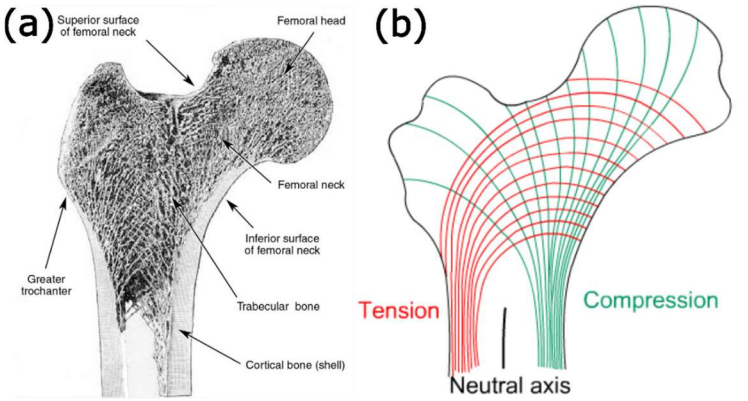

Figure I - 4. Comparison between the (a) trabecular structure of a human femur head and (b) the direction of principal stresses in a human femur head [11].

Given its cellular nature, the mechanical behavior of trabecular bone depends, among other factors such as degree of mineralization, orientation, etc., also on the relative density [7,9], as shown in Figure I - 5. As the relative density increases, so does the stiffness and the strength of trabecular bone. The stress strain curve can be divided into three regions: linear elastic response (elastic bending of the trabeculae), a horizontal plateau that corresponds to the failure by plastic buckling of the trabeculae and a final region where the trabeculae touch each other and the stresses rise steeply (densification) [7]. In tension on the other hand, plastic hinges form at the junctions between trabeculae leading to failure [7].

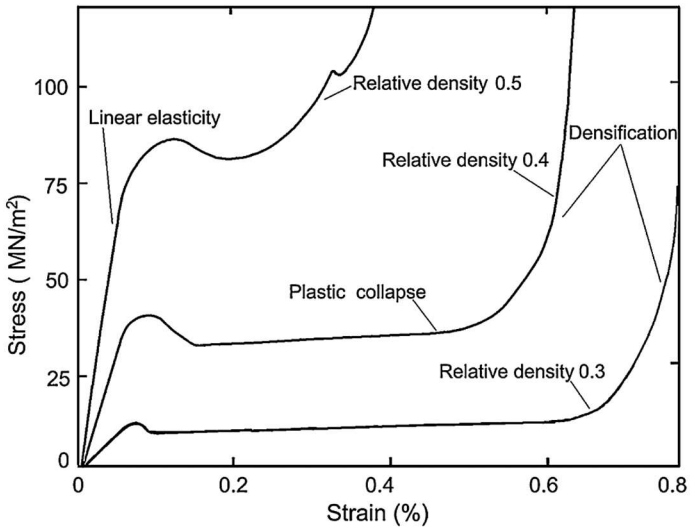

Figure I - 5. Compression stress-strain curves of cancellous bone for different relative densities [2].

As a consequence of functional adaptation to loading, trabecular bone is anisotropic: depending on the location, it can be orthotropic (proximal femur) or transversely isotropic (vertebrae) [3]. Given the anisotropy and the strong influence of porosity, it is hard to indicate a precise value for the mechanical properties for trabecular bone. In general, trabecular bone is stronger and stiffer in compression than in tension [7]. Table I - 2 reports some values for the mechanical properties of trabecular bone.

Table I - 2. Mechanical properties of human cancellous (trabecular) bone.

Mechanical property	Longitudinal direction	Transverse direction
Elastic modulus [GPa]	0.26-0.96 [6]; 5 [2]	0.1-0.4 [6]; 0.1 [2]
Compressive strength [MPa]	3.6-9.3 [6]; 12 [2]	0.6-4.9 [6]; 2 [2]

The elastic modulus of human bone and its constituents as a function of its density is plotted in Figure I - 6.

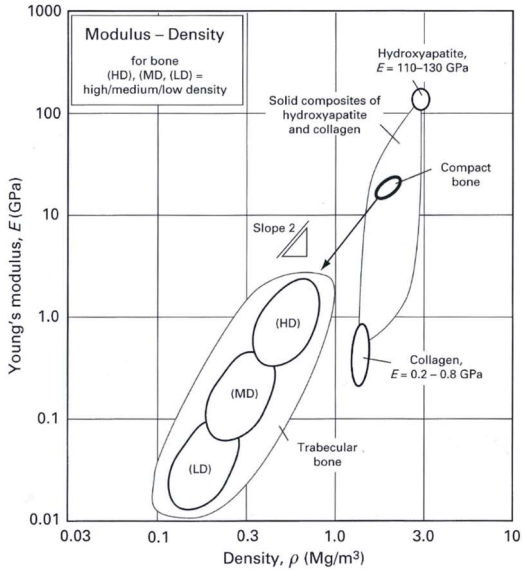

Figure I - 6. Elastic modulus of human bone and its constituents as a function of their density [7].

A thorough review of the mechanical properties of human and non-human bone with data for different anatomical locations, age and method of measurement can be found in [3], while a detailed survey of the mechanical properties of human trabecular bone can be found in [7].

1.1.2 Bone tissue repair and orthopaedic implants

Despite their ability to adjust to external loads and to continuously repair small injuries, bones (and sometimes the adjacent joint) can suffer from traumas that are beyond the capability of natural repair processes. In other cases, serious diseases or simply the effect of daily loads cause a progressive damage that considerably reduced the functionality of the anatomic part. In these cases, an external support is necessary in order to completely or at least partially restore functionality and improve the quality of life of the patient. The damaged tissue can be helped to regenerate by providing temporary mechanical support, by replacing the damaged tissue with a material that is progressively substituted by new tissue or completely replacing the part with a permanent device. The first approach is represented by temporary bone fixation devices such as plates, screws, intramedullary nails and external fixators (designed to be removed surgically), the second is represented by tissue

engineering, and the third by permanent implants. For the sake of simplicity, we will mainly discuss here permanent implants because they are the main application of SLM metallic lattices. Given the cellular nature of tissue engineering scaffolds, we will briefly review them, but we will completely avoid temporary bone fixation devices. A more complete review of bone repair devices can be found in [4].

The chirurgical procedure that replaces missing bone with some material is called bone grafting. Such grafts should not only replace missing bone, but should induce osseointegration, i.e. the process through which bone grows and binds with the graft [6]. The best option is to use bone tissue collected from another location of the skeleton of the patient (autograft), but the amount of bone that can be harvested is limited and, this procedure poses additional health risks on the patient because of its invasive nature. As an alternative, bone could be harvested from the body of another person (allograft), but also in this case the availability is limited and there are major health risks related to transmissible diseases and immunogenic and inflammatory responses. Given these limitations, engineers, scientist and medical doctors have been continuously researching materials that could be safely implanted in place of natural bone. *Tissue engineering* is "the creation of new tissue for the therapeutic reconstruction of the human body, by the deliberate and controlled stimulation of selected target cells through a systematic combination of molecular and mechanical signals" [12]. In this field, biomaterials are used to fabricate temporary scaffolds that can be implanted into the human body and constitute the extracellular matrix where cells can attach, proliferate and grow to generate the new tissue. Tissue engineering scaffolds are designed to actively promote the growth and differentiation of cells to generate a new tissue and they should provide all or part of the substances needed by the cells to correctly build the desired tissue. Ideally, over time such scaffolds should degrade at the same rate as the new tissue grows and thus preserve the overall mechanical integrity of the anatomic part until the implant is completely substituted. Indeed, the difference between biocompatibility of long-term implants and that of tissue engineering scaffolds is that while the former should only carry out their mechanical function without inducing any unusual response form the organism, the latter are designed to induce a response [3,12,13]. The degradation process obviously shouldn't leave behind any harmful substance [7]. Tissue engineering scaffolds normally have a highly porous structure and try to mimic as much as possible the composition and the structure of the extracellular matrix of the tissue to be repaired. The materials of choice are degradable polymers (natural or synthetic), or, in the case of bone, polymer composites or glasses with a high content of calcium phosphate [2,7,14]. Tissue engineering scaffolds would be the ideal solution to repair damaged bone tissue (other than natural healing, but it is not always possible as we have discussed) because they restore the functionality of the tissue and dissolve without leaving any foreign material inside the body, but they still present too many

challenges, particularly in load bearing applications [3]. Tissue engineering scaffolds are more deeply discussed in several books and reviews such as [2,3].
Permanent metallic implants are the best choice in cases where a total replacement of the bone and the joint is necessary, such as in the case of a damaged hip or knee [2–4,6,15]. Such implants have to provide the mechanical function that the damaged tissue is not able to guarantee, a task that polymeric or ceramic tissue engineering scaffolds cannot reliably carry out. For a bone implant to be effective, it should be able to withstand the cyclic loading induced by daily activities for the required amount of time (possibly, tens of years) without failing or loosening and it should also provide the kinematic stability of the movements with an adequate range of motion (ideally, restore pre-damage functional range). Moreover, the implant should be compatible with the environment of the human body, i.e. it should minimize material degradation (ion release due to corrosion and small particle due to wear) while at the same time achieving a stable integration in the surrounding tissue [4]. In other words, for these devices the main biocompatibility requirement is to not release any harmful substance in the living tissue and to maximize bonding between the bone and the implant. A biologically inert material is perfectly adequate for such applications and there is no clear evidence in the literature of the benefits of an increased bioactivity other than maybe calcium phosphate rich coatings to improve the kinetics of bone integration [12].

1.1.3 Biomaterials and biocompatibility in orthopaedic implants

All the classes of engineering materials (metals, ceramics, polymers) can be used in biomedical applications, but obviously not all materials are safe to use in the human body. Biomaterials are those materials that can exist in close contact with a living tissues without inducing adverse reactions [16]. This definition, although it applies well to implants that would be effective even if they behaved completely inertly (such as temporary metallic plates or screws for bone fracture repair), is quite simplistic. In fact, it is known that no material is completely inert in the tissue environment because even very stable materials such as passivating metallic alloys (titanium and CoCr alloys, for example) or ceramics (alumina, zirconia) can release ions or impurities. Moreover, as will be discussed in the following, as soon as the implant is inserted, there is a reaction of the surrounding tissue in the form of protein adsorption. This is to say that it is important to recognize that there is always some sort of interaction between the implant and the body: the real issue is to engineer the implant so that the interaction does not harm, or, even better, promotes healing. Indeed, in some applications, a more “active” biomaterial can be beneficial: this is the case of resorbable implants that slowly degrade while restoring the full functionality of the damaged tissue or load bearing bone implants that promote bone

growth and bonding with the implant surface [17]. Given the previous discussion, a better definition for biomaterial could be ‘‘a substance that has been engineered to take a form which, alone or as part of a complex system, is used to direct, by control of interactions with components of living systems, the course of any therapeutic or diagnostic procedure, in human or veterinary medicine’’ [16]. In fact, this definition includes also nanoparticles, hydrogels, self-assembled biological systems, and engineered cells and viruses as well as entities that fit a more traditional concept of material, such as metals, ceramics, and polymers [16]. Importantly, what makes a biomaterial is the fact that it has been *engineered* to interact with the body and to carry out a specific function so, for instance, a transplanted organ cannot be classified as a biomaterial. The way a biomaterial interacts with a living tissue is related to its *biocompatibility*, which is “the ability of a material to perform with an appropriate host response in a specific situation” [12]. In other words, biocompatibility does not depend only on the material itself, but also on the specific application: the material has not only to safely sit in the tissue, but it has to adequately perform a task in a specific situation. It is important to note that a material that qualifies as biocompatible for a certain application may not be adequate for another. Moreover, for the task to be successfully completed, factors such as the way in which the biomaterial was implanted and the condition of the patient are also important [12].

The biomaterials used in bone implants will be now briefly reviewed.

1.1.3.1 Polymers

Collagen, the main structural protein of the body, is a natural polymer: it is thus natural to think that polymers, among engineering materials, have the greatest chance to positively interact with living tissues and in the appropriate conditions even achieve direct chemical bonding [13]. The greatest advantage of polymeric materials is the high tunability of their mechanical and chemical properties: indeed, a great variety of monomers exist that can be translated into an almost infinite number of different macromolecules. From the mechanical point of view, their behavior can vary from that of a rigid solid (ultra-high molecular weight polyethylene, UHMWPE) to that of a highly deformable elastomer (silicone), while from the chemical point of view they can be highly stable (or even inert, such as polytetrafluoroethylene, PTFE) or completely biodegradable (such as polylactic acid, PLA). Thus, the number of applications of polymers in the biomedical sector is huge and include contact lenses, implants for plastic surgery, sutures, cardiac valves, drug delivery systems, implant fixation cements, scaffolds for tissue engineering, and so on [18,19]. Polymers used as biomaterials can be synthetic or natural: among the former we find collagen, gelatin, elastin, actin, keratin, chitosan, chitin, cellulose, silk and hyaluronic acid. Among the latter, the list includes polyethylene, polypropylene, polyvinylchloride,

polyurethanes, silicone, rubbers, hydrogels and polytetrafluoroethylene (PTFE). The main drawback of polymers is that they have weaker mechanical properties and lower chemical stability compared to ceramics and metals, so they cannot be used as the main load bearing component in implants, although polymer/ceramic structural composites for bone regenerating scaffolds do exist [2,20].

Non-resorbable polymers in orthopedic applications are used for load-bearing applications, such as bearing material in joint replacement implants (UHMWPE) fusion cages for spinal surgery and permanent screws (polyetheretherketone, PEEK) [21]. Despite its good wear resistance and low friction coefficient, UHMWPE wear debris is one of the main reasons for tissue adverse reaction and subsequent implant loosening [17,22]. Another use of great importance is as cement for implant fixation: polymethylmethacrylate (PMMA) is used in cemented implants. A mixture of PMMA powder and liquid monomer is injected in the cavity where the implant is placed and polymerization takes place in-situ [4,13]. Resorbable polymers are used in orthopedic applications for temporary fixation devices such as pins and screws [4], and tissue engineering scaffolds [2]. Resorbable polymers have weaker mechanical properties than non-resorbable polymers, so they are limited to non-load bearing applications [20].

1.1.3.2 Ceramics

Ceramics are rigid solids, so, differently from polymers, their use as biomaterials is practically limited to orthopaedic and dental applications [23]. Three types of ceramics are used inside the human body: structural ceramics (mainly alumina, Al_2O_3, and zirconia, ZrO_2), calcium phosphates and bioglasses [4]. Alumina and zirconia, due to their outstanding wear resistance and low friction, are used in the head of hip prostheses, generally matched with a UHMWPE acetabular cup. Such oxide ceramics are completely inert inside the human body and do not degrade and can be also safely used in contact with living tissues in dental implants [23]. We described bone as a natural composite, made of a collagen matrix with a dispersed ceramic phase (a calcium phosphate known as calcium hydroxyapatite, HA): it is thus not surprising that HA has good osteoconductivity and can achieve osseintegration. Indeed, calcium phosphates are mainly used to coat metallic implants to improve their biocompatibility [4]. Bioglasses are glass-ceramics (polycrystalline material) made of SiO_2 with a variable amount of other oxides, phosphates and fluorides that are important for the in vivo formation of bone. After implantation, bioglass starts to dissolve and to provide the adequate nutrients for the growing bone tissue. The result is a very stable bond which produces a bone/implant interfacial strength considerably superior to that achieved with other materials. For this reason, they are defined *bioactive* [13,24]. The adhesion of bone to bioglass does not depend on roughness, indicating a predominantly chemical nature of the

bond [25]. The main drawback of ceramic materials is that they are brittle, which can lead to sudden failures [4].

1.1.3.3 Metals

Metals have very good stiffness, strength, toughness, and fatigue resistance, making them suitable for the most demanding load bearing applications. The main applications are in orthopedics: for example, bone fixation devices, such as screws, nails and fracture plates, joint replacement implants and scaffolds. The main issue with metals placed inside the human body is corrosion and the release of potentially harmful elements, especially if in large quantities [25]. Corrosion in vivo can result in local pain and swelling without evidence of infection, and cause persistent inflammation [13]. Indeed, metals currently usable for biomedical applications form a very thin but stable passivating oxide layer that protects the bulk from corrosion: these are stainless steel, cobalt-chromium (Co-Cr) alloys and titanium alloys. Among stainless steels, the most commonly used is grade 316L. Due to its high density (8000 kg/m^3) and tendency to corrode via pitting in the physiological environment, it is best suited for small temporary implants such as screws and plates [13,25]. Co-Cr alloys show a better corrosion resistance than stainless steel and they can be used to produce permanent implants. Two types of Co-Cr alloy are used, the CoCrMo alloy and the CoNiCrMo alloy. The first is usually cast to produce dental or joint implants, while the second is usually forged to produce heavily loaded components, such as stems for hip joint implants, thanks to its superior fatigue resistance and strength. These alloys are not appropriate for bearing surfaces (especially in metal-on-metal applications) because they have poor wear resistance and can thus release Cr particles. They are stiffer than steels (220-234 GPa), [13] and also denser than steels (8300 kg/m^3, cast, and 9.2 kg/m^3, wrought) . A detailed summary of the classification and properties of biomedical Co-Cr alloys can be found in [26]. Titanium alloys are the most used metals for biomedical implants thanks to their excellent specific mechanical properties (the density is very low, 4.3 kg/m^3) and their remarkable corrosion resistance (due to the formation of thin and adherent TiO_2 oxide layer). Among the various Ti alloys, Ti-6Al-4V and Nitinol (shape memory alloy) are the most common [13,25]. Titanium alloys will be discussed more in depth in Section 1.4. The passivating oxide layers formed on these alloys are inert towards the surrounding tissue and thus fixation is prevalently achieved via mechanical integration. Such inert surfaces are normally not osseoinductive but can be osseoconductive, i.e. they support the adhesion and spread of cells but do not induce cell differentiation. Nevertheless, the formation of calcium phosphate on the surface of untreated titanium and 316L stainless steel has been observed in vivo, which indicates a degree of osseointegration.

The surface of the metallic implant can be modified to improve its in vivo performance. Physical modifications of the oxide layer, like the creation of nano-

sized trabeculae or protruding structures, or increasing the roughness was observed to increase the adhesion force. A macroscopically porous or trabecular coating can also be effective in improving bone ingrowth and subsequently increasing fixation [25]. Implanted metals can also be coated with substances that improve their biocompatibility and stability by promoting osseointegration. Hydroxyapatite (HA) has been used for thin (30-100 μm) coatings on implants with both smooth and porous surface. HA is chemically compatible with the mineral part of bone and, can provide the growing tissue with the necessary phosphates and calcium. Such coatings are thought to be both osseoinductive and osseoconductive and can osseointegrate by promoting the growth of mature bone tissue and by establishing chemical bonds with the bone, thus improving the long term stability of the implant [27]. It is appropriate to note that, despite the encouraging results both in vivo and clinically shown by many studies, there are conflicting opinions in the literature about the real effectiveness of HA coatings in improving the fixation of cementless implants [28,29]. While early fixation is generally promoted, clear long-term positive effects compared to uncoated devices, are not always shown. Indeed, it is difficult to precisely evaluate the performance of HA coatings on the overall success of the implant because it is strongly dependent on many factors such as the morphology of the coating (thickness, roughness, porosity), the chemical composition, the design of the implant, the anatomic site, and the condition of the patient [30–32].

1.1.4 Tissue response to implant

The biocompatibility of an implant is qualified based on the response of the tissue. In general, the reaction of the body to a foreign object (the implant) is to reject it [13]. It should not be forgotten that when an implant is inserted into the body, normally an injury is also present (it could be due to the trauma or simply due to the surgical procedure). The normal healing process of an injury consists of an inflammatory reaction which basically is followed by the formation of a fibrin (an insoluble protein) scaffold around the injured site which is then used by fibroblast (collagen producing cells) to deposit collagen and, at the same time, new capillaries form. Finally, the wound remodels and the production of collagen decreases until complete healing [13]. Bone tissue is different from other tissues because it regenerates instead of simply repairing [6,13]: bone-building cells (osteogenic cells) and fibroblast migrate towards the injury and form a collagenous matrix (callus). Osteogenic cells evolve into osteoblasts and start to calcify the collagen of the callus. First trabecular bone is formed, which then further densifies, depending on the mechanical stimuli, to form compact bone.

The implanted material induces the following processes in the host [13,17,28,33,34]:

- Protein adsorption
  The implant, as soon as it meets the living tissue, is covered with a layer of adsorbed proteins which then regulate the response of the surrounding cells. The characteristics of this layer (types of proteins, concentration, and conformations) depends on the composition, size, shape, surface roughness, surface chemistry, hydrophobicity, and surface charge of the implant.
- Material degradation
  Simultaneously to the host response, the material of the implant starts to degrade because of the aggressive physiological environment and/or mechanical loading. Polymeric materials degrade (generally through hydrolysis), while metals corrode. The degradation products influence the cellular behavior: whether in a positive or negative manner depends on the biocompatibility of the implant. Degradation products can stimulate healing or can induce adverse reactions, such as inflammation. Solid particles (metallic or polymeric) can form as a result of implant wear which can induce chronic inflammation. The effect of a continuous inflammation stimulated by implant degradation is bone resorption and subsequent implant loosening. Moreover, if particles are in the nanometric range, they can also stimulate immunogenic responses.
- Evolution of the local host response
  The implant affects the normal healing process to different degrees depending on the implant (material, shape, surface characteristics) and on the implantation technique. In the case of an inert material, the only response is the deposition by fibroblasts of a fibrous collagen envelop around the implant. In the case of a reactive implant (chemically or mechanically unstable, or contaminated with organisms), a persistent inflammation will be induced. This can lead to a much thicker fibrous envelop, or, in the worst case, to local necrosis. It is worth to highlight that the host tissue reacts not only to the changed chemical composition of the environment but also to mechanical effects such as micromotions of the implants and sharp edges, which lead to variations in the fibrous capsule thickness.
- Systemic effects
  The effect of the implant can also extend to the entire body. This can be due to leaked substances (ions or monomers, for example) that are carried to other organs by the circulatory system and interfere with the normal metabolic functions. Other effects could include immune responses or carcinogenicity.

The reader that wishes to further study the complex matter of body response to wounds and implantation of a foreign body is referred to the following detailed although not overly complex books [13,26,35] and a review [6].

1.1.5 Joint replacement implants and their performance in the living tissue

Severe traumas to joints or their degeneration are heavily debilitating because, contrary to bone, cartilage has a very limited ability to repair. In such cases, a total joint replacement implant may be needed. This kind of implants is permanent and irreversible due to the invasive nature of the surgical procedure.

1.1.5.1 Requirements and issues of joint replacement prostheses

The design of joint prosthesis requires the knowledge of the biomechanics (kinematics and loads) of the joint, the physiology of the living tissue to be replaced (bone and cartilage), the possible reactions of the host to the implant, and the engineering properties of the implant material. It is especially important to adequately design the fixation method (with or without cement and the morphology and chemical composition of the surface) because it determines the load transfer characteristics and ultimately the long-term survival of the bone-implant system [32]. Indeed, bone adapts to the mechanical stimuli by remodeling: it densifies where the load is higher, and it resorbs where the loads are lower. Thus, an inappropriate load transfer can lead to implant loosening or at least to a local weakening of the bone which can lead to fractures or jeopardize the outcome of revision surgery. The main design requirements of bone prostheses are the following [4,32]:

- The implant should be properly fixed and no micromotions should occur, but it should also be removable without excessive damage to the surrounding tissues
- The implant should allow a functional range of motion and adequate kinematic stability

Three methods of fixation are effective in permanent implants [32]:

- Mechanical interlock: it can be achieved by using a cement (PMMA) that flows into the porosity of the bone and the implant, by threaded joints or by press-fitting the implant.
- Biological fixation (bone ingrowth): bone grows into the asperities and the porosity of the implant to realize a sort of mechanical interlocking.
- Direct chemical bonding between bone and implant (osseointegration): this occurs when there is a strong chemical affinity between the bone tissue and the implant surface (suche as with HA or bioglass coatings).

Failure of permanent joint implants is related to the following scenarios [4]:

- Fatigue failure of the prosthesis material.
  Daily life generates cyclic loads on the joint implant that can lead to the failure of the bone/implant interface (cement failure or debonding) or of the implant itself.
- Reaction to wear debris
  Wear debris can be generated due to metal-on-metal contacts, abrasion of the PMMA cement (in cemented implants) or wear of the UHMWPE bearing surface. Such debris can cause persistent inflammation, bone resorption and subsequent implant loosening.
- Failed fixation
  Excessive micromotion (due to an inadequate preliminary fixation) or large gaps can prevent bone ingrowth and/or osseointegration and thus the implant is unstable form the start.
- Stress shielding
  Bone tends to become denser if loaded while it resorbs if underloaded. If the implant is stiffer than the surrounding bone it takes on most of the physiological load that was originally carried by the bone. Over time, this can cause the bone tissue to lose mass density and weaken. Stress shielding to the extreme is known as “stress bypass” and occurs when parts of the bone are completely unloaded due to bad prosthesis design.
- Destructive wear
  The bearing surfaces (usually made of UHMWPE) can completely wear out until the function of the implant is compromised

There are two approaches to fixate the implant to the bone: with cement and without cement. In the former case, the implant is secured to the bone with a PMMA cement, which is injected into the bone during surgery to permeate the pores in the bone and then polymerized in situ. Cementless implants, on the other hand, exploit fixation of the bone tissue with the surface of the implant without any intermediate layer of cement [4].

1.1.5.2 Cemented implants

Using a cement to fixate the implant provides almost immediate stability and the device can bear full weight after a few hours. PMMA cement works like a grout: it flows inside the surface porosity of the bone and the implant and it hardens, thus locking the implant by interdigitation. Besides its rapid action, it has the advantage of absorbing shocks and of redistributing loads avoiding stress concentrations thanks to its viscoelastic behavior [32]. The problem with cement is that it is known to be toxic and this, together with the strongly exothermic polymerization reaction, causes the death of a layer (up to a few millimeters) of bone tissue around the implant.

Paradoxically, this necrotic layer is the reason why cemented implants work: this interface does not change with time (no resorption) and thus guarantees long implant life (10-15 years), particularly in older patients [4,22,28]. Anyway, given the low biocompatibility of cement, the body surrounds it with a fibrous layer which, if it becomes too thick due to a persistent inflammatory reaction, can lead to implant loosening [32]. In general, cemented implants work well in older patients or in cases where bone has a limited ability to regenerate, because fixation does not require bone growth [32].

1.1.5.3 Cementless implants

This type of implants was developed to avoid the issues associated to the use of cement (toxicity and necrosis) which could lead to adverse foreign body reaction and subsequent implant loosening [32], because of the early failure of the first generation (1960s) of cemented implants [36], and because of the lower revision rates compared to cemented implants, especially in younger and more active patients [37]. In principle, this solution should be the best because it allows the bone to fixate "naturally" to a biocompatible surface, but in practice, several issues have to be coped with. First, a long recovery time is needed before the implant can be safely loaded (3-4 up to 12 weeks) [22,32]. To achieve long term fixation, after an initial "press fit" constraint that prevents micromotions that could inhibit bone growth [28,32], two not mutually exclusive processes are possible: bone ingrowth and osseointegration. In the former, bone grows into macroscopic irregularities of the surface such as pores of the order of a few hundred microns and creates a geometrical interlocking, in the latter, bone directly grows into the microscopic irregularities of the surface or even achieves direct chemical bonding [22]. Fixation by bone ingrowth depends on the characteristics of the surface of the implant (biocompatibility, porosity and roughness), the state of the bone tissue, the surgical technique and the post-operation loading pattern. It has been observed that the tissue that grows inside macroscopic porosity is in majority fibrous and not mature bone [28]. Unfortunately, implants fixed by only ingrowth can be unstable and even migrate over time: a higher frequency of failure compared to cemented implants has been observed. Nevertheless, modern implants coated with a highly porous mesh have shown improved fixation [22].

Fixation by *osseointegration*, on the other hand, requires a complete maturation of bone tissue on the bone-implant interface (reaching a density equal to the surrounding healthy bone) and implies a more intimate contact with the surface. In such way, a rigid fixation is obtained, which is stable in time. A wider contact surface increases the strength of the bond, so a rough surface can improve fixation, and it has been observed that there is an optimal value of roughness [22,28,38]. A direct chemical bond between bone and implant can be obtained only in the case of a very high affinity, such as in the case of calcium hydroxyapatite (HA) or bioglass (which

can also be coatings on other materials, such as metals [28]). Osseointegration occurs only if osteoinduction and osteoconduction preexist [38]. *Osteoinduction* is the recruitment of undifferentiated mesenchymal cells and their transformation to preosteoblasts (the cells which then differentiate to bone-building cells, the osteoblasts). This process occurs regularly during natural healing of an injured bone and is essential to guarantee proper healing and fixation of an implant. *Osteoconduction* is the growth of bone on a surface, like that of the implant, and it is related to the presence of differentiated bone cells, so it follows the process of osteoinduction. Its effectiveness depends obviously on the type of surface: biomaterials show better performance compared to other materials [38]. Fixation, in the ideal case, is achieved by a combination of the two processes: bone ingrowth in the surface macroporosity and subsequent osseointegration thanks to a bioactive surface. This can be achieved, for instance, with a HA coating on a porous titanium surface [32]. Figure I - 7 summarizes the different bone-implant interaction mechanisms.

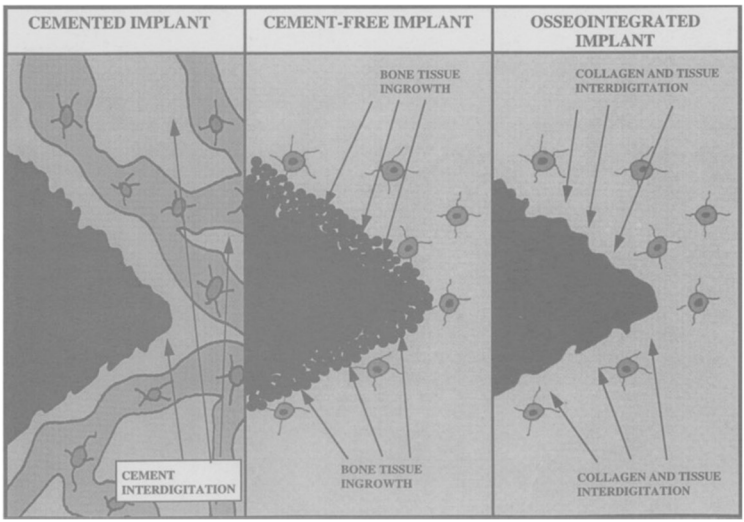

Figure I - 7. Different bone-implant fixation processes (the implant surface is represented by the dark ridge). Cemented implants are fixated by cement interdigitation in bone porosity; cement free implants are fixated via bone ingrowth into implant porosity or osseointegration [22].

1.1.5.4 Total hip arthroplasty: an example of permanent implant

Total hip arthroplasty is one of the greatest achievements in orthopaedic surgery [36] and the most frequent type of joint replacement surgery [13,39]. Moreover, the hip joint it is probably the most studied joint regarding its biomechanics and the issues associated to its replacement with an implant, so it is relatively easy to write a well-

documented review. Finally, it is safe to say that many of its features apply also to other joint replacement implants, such as the knee [4,13,32]. Among the joints of the human body, the hip is one of the most critical due to the high loads it must bear and its fundamental role in guaranteeing ambulation. The biomechanical loads of the hip-femur system, although quite complex, have been studied since Galileo, but the first in depth study was carried out by Wolff at the end of the XIX century. The main difficulty in studying the loads and the consequent stresses in the femur is that they vary considerably depending on the activity (walking, jogging, etc.) and on the subject (health, age, sex, condition, life-style) considered. Moreover, from the point of view of the femur, each activity can be regarded as a cycle during which the forces and their directions can vary. Finally, exceptional loads can also occur, for example in the case of a fall. It is thus impossible to describe the loads that a femur has to carry with a single load scheme. Anyway, a detailed discussion of the loads acting in the femur and on the hip-femur contact surface is not within the scopes of this work, and the interested reader can find some basic information in [40–44]. Nevertheless, just to give an idea of the loads a hip implant must bear, we can observe that, for example, due to dynamic effects and the systems of leverage of the kinetic chain, by fast walking the femur head feels almost eight times the weight of the body, as shown in Table I - 3. These loads are cyclic and over a period of 10 years can be repeated 17 million times [32]. Stumbling on the other hand, can cause a peak in the hip contact force of roughly 13 times body weight [41]. A hip joint implant has to be designed by considering both high peak loads and high cycle fatigue loading. Moreover, the hip contact load is not the only load acting on the femur (although it is undoubtedly the most intense), but also muscles are attached and thus transmit loads [44,45]. The effect of these muscular forces is to ensure a prevalent compressive load in the femur, thus avoiding dangerous tensile stresses (bone is stronger in compression than in tension).

Table I - 3. Indicative contact loads at the hip and knee joints for selected daily activities [13].

Activity	Maximum joint force (times body weight)	
	Hip	Knee
Slow walking	4.9	2.7
Normal walking	4.9	2.8
Fast walking	7.6	4.3
Stairs (up)	7.2	4.4
Stairs (down)	7.1	4.4
Ramp (up)	5.9	3.7
Ramp (down)	5.1	4.4

The hip, from the mechanical point of view, is a ball-in-socket joint: the head of the femur is the ball, while the acetabulum (located in the hip) is the socket (Figure I - 8a). In the same way, the implant for total hip replacement is made of an acetabular component and a femoral component [32], as shown in Figure I - 8b. The femoral component is divided into a stem and a head, connected by the neck. The stem, which should strong and tough, is made of metal (Ti alloy, CoCr alloy, or, more rarely, 316L stainless steel) and it is fixed in the intramedullary cavity of the femur by cementation or press-fitting (and subsequent bone ingrowth/osseointegration). The head should be wear-resistant and is generally made of CoCr or, in more modern implants, of zirconia or alumina. The acetabular component should have low friction with the femur head and be shock absorbers, so usually it is made of UHMWPE (which can be also cross-linked to further improve its wear resistance). The cup can be a single piece, or an UHMWPE insert to a metallic shell then placed into the prepared cavity of the hip. The second method improves fixation (the metal part is coated with a porous layer, as previously discussed) and it reduces the deformation of the plastic cup. Despite its advantages, the UHMWPE insert is a potential source of wear debris not only on the interface with the femoral head, but also on the interface with the shell [13,32].

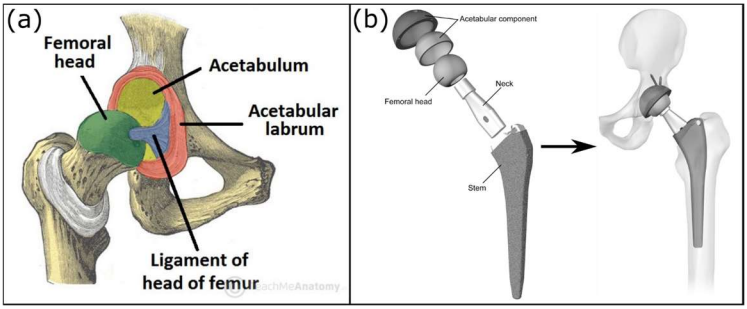

Figure I - 8. (a) Anatomy of the human hip joint [www.teachmeanatomy.info] (b) structure and components of hip joint replacement implants [46].

1.1.6 Stress shielding

Bone is a living tissue and has the remarkable property of adapting to external mechanical stimuli to provide an adequate structural response with the fewest resources possible. This phenomenon is called bone remodeling and it is a sort of topological optimization: tissue densifies where the strains are more intense, and it resorbs where the strains are lower. Variations in functional loading of bones can be general, like those caused by changes in lifestyle (for example, it is known well-conditioned individuals tend to have stronger bones then those conducting a

sedentary life), or localized. The second scenario occurs in the case of an immobilized limb due to plaster or in the case of devices directly attached to the bone, such as orthopaedic implants. Whether they are fracture fixation devices (plates) or joint replacement implants, the effect is to locally reduce the load carried by the bone, i.e. stress shielding occurs. In the case of joint implants, stress shielding is a major issue because such devices are intended to stay in place for many years and so the change in functional loading is permanent. An invasive system such as the hip implant causes a considerable change in the stress distribution of the femur and subsequent bone remodeling [47,48]. Although it is generally not associated with pain and functional limitations and there are not identifiable clinical consequences, biomechanical engineers and orthopaedic surgeons have put considerable effort in trying to avoid stress shielding or at least compensate it. The bone mass density loss that stress shielding implicates, and the subsequent weaker bone, can jeopardize implant revision surgery that the patient will most likely need. Indeed, a progressively weakening of the bone tissue can reduce the implant stability in the first place and lead to loosening or migration [48,49]. The key factor determining stress shielding is the relative stiffness difference between bone and the implant (the stiffness of the implant depends on the material, but also on its geometry), but also the stiffness of the bone-implant interface and the direction of the applied loads have an influence [48,49]. The bone-implant system can be approximated to two springs in parallel: the stiffer component carries a higher fraction of the load, thus *shielding* the other one. In other words, the load normally carried by the bone is in part carried by the implant. The higher the elastic modulus of the stem material and/or the thicker the stem, the more load it carries. Paradoxically, the better is fixation, the more load is transferred to the implant: non-cemented implants with extensive bone ingrowth and osseointegration have shown a considerable degree of bone resorption due to stress-shielding. For the same reason, cemented implants are less affected: the viscoelastic cement tends to distribute more uniformly the loads. The initial bone mass density (and thus the stiffness) of the patient is a factor to consider: in the case of a dense bone the stiffness mismatch with the implant is lower. Indeed, we should not forget that the characteristics of the individual are extremely important, so the implantation of the same device into two patients can have very different outcomes [48]. The proximal part of the femur is the most affected by stress shielding due to the local greater thickness of the stem and, in some instances, bone resorption can easily reach 30% (Figure I - 9). Notably, the process is quite fast: the greatest amount of bone loss occurs in the first 6 months to 2 years after surgery [50].

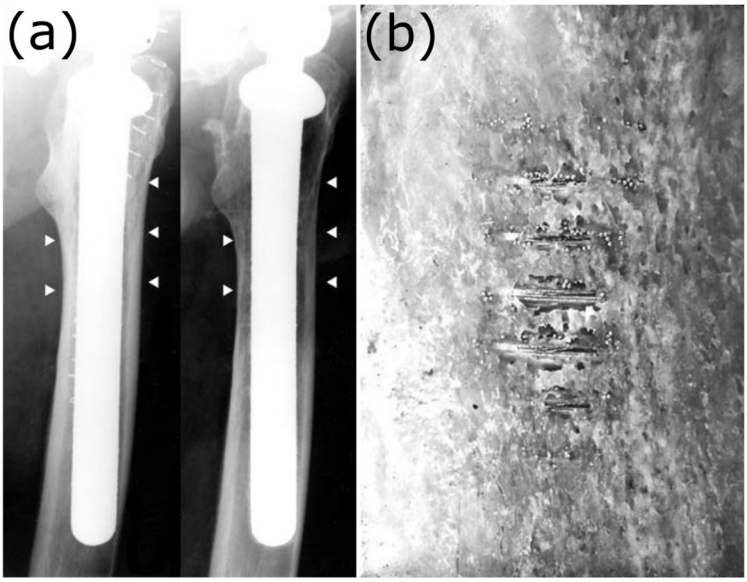

Figure I - 9. Stress shielding induced by bone-implant stiffness mismatch: (a) the comparison between radiographs immediately after surgery and after five years show considerable bone density loss after five years (arrows) in human total hip arthroplasty; (b) bone resorption in the proximity of a screw in a canine femur [48].

Several designs of hip implant stems have been proposed to reduce stress shielding [48,50]: the general strategy is to increase load transfer in the proximal region by increasing bone ingrowth with porous coatings and to reduce the stiffness of the stem by modifying its geometry or by applying a compliant coating (polymer or porous metal). Recall that we are talking about fully dense metallic stems made of CoCr alloy (E=230 GPa) or Ti alloy (E=110 GPa), both considerably stiffer than bone (cortical bone can barely reach 20 GPa). Unfortunately, neither of the two solutions is optimal. A low modulus material (or the presence of cement), although effective in considerably reducing bone mass density loss, induces high interfacial stresses at the bone/implant boundary that can lead to interface failure and subsequent implant micromotion and possibly loosening [39,49]. On the other hand, concentrating load transfer in the proximal region does not achieve a uniform stress distribution [39]. A stiff stem will concentrate the loads distally leaving the proximal region under-loaded. A compliant stem will increase the loads proximally, but it will also increase interface shear. The stress-shielding issue is thus even more complex because the ideal implant should compromise between these two conflicting objectives: reduce stress shielding (i.e. decrease implant stiffness) and reduce interfacial shear stresses (i.e increase implant stiffness) [39,51,52]. Kuiper et al. [52] showed computationally that

the optimal compromise can be obtained only with a non-homogeneous stem that has locally variable elastic modulus. In other words, they suggested that a functionally graded stem can reduce bone loss while avoiding shear stress spikes in the proximal region. Functionally graded materials are materials, designed for a specific application (or function), that have a continuous transition in properties from one location to the another. Notably, also bone is a functionally graded material (continuous transition from cortical to trabecular bone). The use of functionally graded materials for orthopaedic applications has been reviewed by Sola et al. [53]. Fully porous functionally graded metallic implants, with optimized relative density, have been designed in [54–56]. A detailed analysis of the stress shielding phenomenon is beyond the scopes of this thesis and the aim of this discussion was only to educate the reader on the complexity of the issue and on the possible strategies to confront it. Who is interested to take a deeper look into the matter should start from some excellent reviews [49,50,57] and book chapters [39,47,48].

1.1.6.1 Porous materials in orthopaedic implants

The use of porous structures in orthopaedic implants was mentioned several times in the previous discussion and, in fact, it is not new in the orthopaedical field. Porous metallic coatings in orthopaedic implants were developed to improve cement adhesion to the implant or to promote bone ingrowth in cementless stems [58]. Moreover, interfacing bone with a more compliant material is beneficial for stress shielding [7,15]. Highly porous polymeric or ceramic porous coatings are not used in load bearing applications due to a lack of reliability of the mechanical properties [15], but ceramic (HA, bioglass) coatings can be applied over a porous metal surface to improve its biocompatibility [27,30]. Several types of porous metallic coatings have been developed and successfully used clinically in the last three decades [58,59]: (i) fiber metal coatings, which are randomly oriented titanium or CoCrMo thin wires pressed and diffusion bonded on the surface of the implant; (ii) bead coatings, that are obtained by sintering layers of Ti or CoCrMo beads on the surface of the Ti or CoCr alloy implant, respectively; (iii) plasma spray coatings of CP Ti or Ti-6Al-4V alloy; (iv) open-cell porous tantalum coating obtained by chemical vapor deposition (CVD) of Ta on a reticulated vitreous carbon foam (known as Trabecular Metal). The porous coatings that were previously described have pore sizes of ranging from 100 to 1000 μm and a pore volume of 40-50%, apart from porous tantalum which has a much higher porosity (75-85%) and a more regular pore size of 550 μm on average, which make it very similar to trabecular bone [58]. Moreover, its elastic modulus is approximately 3 GPa, which is between the values of trabecular bone and cortical bone. Due to its properties, Trabecular Metal has excellent bone ingrowth characteristics compared to the other coatings and has been used since 1995. Remarkably, it can also be produced and used as a stand-alone implant in spinal

fusion cages, showing that porous metals can be used in load bearing orthopaedic applications [7,58,59].

Despite the positive results showed by porous metal coatings, there are some issues to consider. First, the application of a porous coating on a dense substrate introduces notches on the surface that act as stress concentrators and can reduce the fatigue strength of the implant if not accounted for. Second, coatings can detach or fail [58]. Moreover, implant designs based on fully dense stems seem unable to avoid a considerable degree of stress-related bone resorption (due to their high elastic modulus) and at the same time avoid the increase of high tangential stresses (if compliant coatings are applied). A promising idea that could considerably improve the performance of joint implants is that of using a fully porous device instead of only a porous coating [60–62]. A more accurate term than “porous materials” would be “cellular”, given that the degree of porosity of these materials is quite high. If adequately designed, a fully cellular hip implant stem could reduce stress shielding and high interfacial stresses and at the same time achieve excellent fixation via bone ingrowth and osseointegration [49,61]. Moreover, modern additive manufacturing techniques for metallic materials, such as Selective Laser Melting (SLM) and Electron Beam Melting (EBM), make possible to produce even the most complex geometries (even locally variable, as for the case of functionally graded materials) without additional effort (Figure I - 10) [54,61].

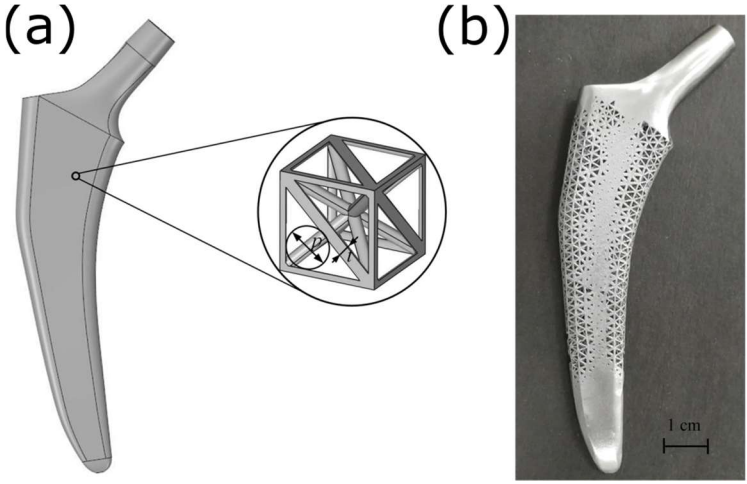

Figure I - 10. Fully porous hip implant stem: (a) dense hip implant stem to be replaced with a cellular architecture; (b) functionally graded cellular stem built by SLM in Ti alloy [56].

In the next Section, a basic introduction on cellular materials will be presented to provide the reader with the fundamental concepts regarding the mechanical behavior of this class of materials.

1.2 Mechanical behavior of cellular materials

Cellular materials differentiate from traditional materials because their properties do not depend only on their chemical composition and microstructure, but also on their micro-architecture. This peculiar class of materials is indeed a structure on the small scale, as it is made up of a network of struts and/or plates of a size considerably smaller than the characteristic dimension of the part. For the sake of clarity, in this context, with the term *lattice (or cellular) materials* we indicate materials with a high degree of porosity and a regular structure, composed of a structural unit regularly repeated in space: this unit is called *unit cell*. These are also known as regular lattices or periodic lattices. On the other hand, highly porous materials with a disordered (stochastic) structure will be called *foams* (a comparison is shown in Figure I - 11). Nevertheless, in the literature the two terms are often used interchangeably and sometimes the differences are quite subtle. The micro-architecture of cellular materials provides the designer with an additional level of design, besides the material of the struts (often called *base material* and it can be metallic, ceramic, polymeric) and the shape of the macroscopic part (for instance, a femoral stem). Cellular materials behave as structures on the small scale and as homogenous materials on the macroscopic scale. In other words, there is a length scale separation between the lattice scale and the macroscopic scale. Consequently, their behavior on the macroscopic scale can be described in terms of effective homogeneous properties (elastic modulus, for instance) that depend on the base material and the unit cell and compared with that of traditional materials. By only tailoring the geometry of the unit cell, while keeping constant the base material, it is possible to range between far extremes of the material properties space, such as stiffness, strength, density, permeability, thermal conductivity [9,63,64].

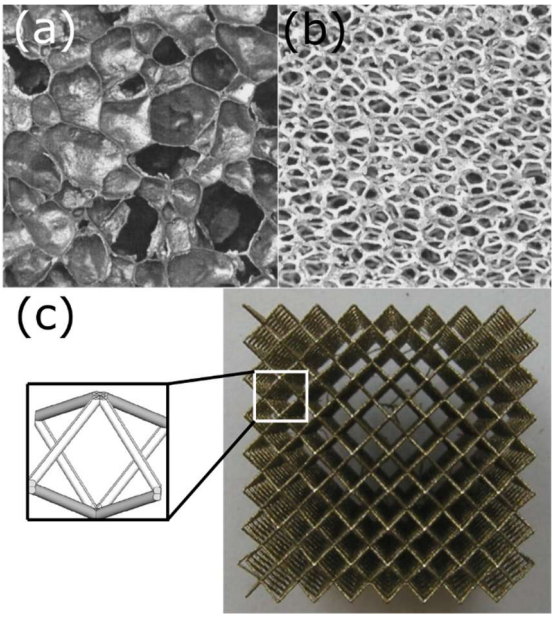

Figure I - 11. Examples of cellular materials: (a) closed cell foam [65]; (b) open cell foam [65]; (c) regular cellular material (BCC unit cell) [66].

1.2.1 Morphology and relative density

There are several classifications of cellular materials based on their structure. We already discussed the first, based on whether the structure is periodic or stochastic. Another criterion is based on cell, that can be open or closed, depending on whether only the cell edges are solid or both the edges and faces, respectively (Figure I - 11a and Figure I - 11b). Open-celled cellular materials are permeable to the flow of fluids, which is normally a necessary requirement in biomedical applications, and thus constitute the totality of the lattice materials found in load bearing biomedical implants. On the other hand, closed cell cellular materials are more common where insulating (thermal, sound) properties are requested [9,63,64]. A very useful classification criterion, which has important consequences on the mechanical behavior of the lattice, distinguishes between *bending*- and *stretching*- dominated structures by analyzing the nodal connectivity of the structure. If we imagine replacing the rigid (welded) junctions between the struts with pins, depending on the nodal connectivity of the lattice, the structure can collapse due to the rotation of the struts about the joints (i.e. it becomes a mechanism) or not (i.e. it becomes simply a truss frame) (compare Figure I - 12a and Figure I - 12). The former structure is defined as bending dominated, because the struts of the frame with welded joints *bend* when

loaded externally (the joint resists rotation), while the latter structure is defined as stretching dominated because the struts are loaded mainly axially even with welded joints. An example of the two types of unit cells is shown in Figure I - 12c and Figure I - 12d. This classification is expressed mathematically by the Maxwell stability criterion. Stretching-dominated structures are structurally more efficient than bending-dominated structures because struts are loaded almost exclusively in tension or compression [63,64,67].

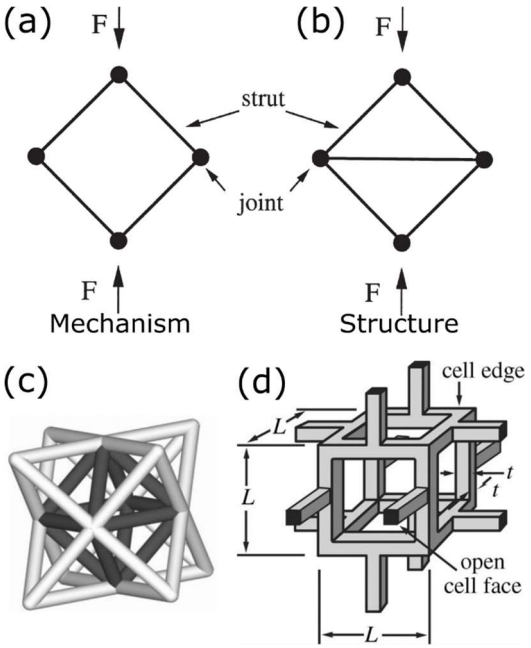

Figure I - 12. (a) A bending-dominated structure becomes a mechanism if the joints are substituted by pins, while (b) a stretching-dominated structure stays a structure. Examples of (c) stretching dominated and (d) bending dominated unit cells [63].

The single most important parameter of cellular materials, that any property can be related to, is the relative density $\overline{\rho}$ [9], defined as the ratio of the density of the cellular material ρ^* to the density of the base (solid) material ρ_s:

$$\overline{\rho} = \frac{\rho^*}{\rho_s}$$

If the mass of the substance filling the cells is negligible with respect to the mass *m* of the solid material making up the struts (a very common practical situation), and

being V_s the volume of the struts and V^* the volume occupied by the cellular lattice, we obtain:

$$\overline{\rho} = \frac{\rho^*}{\rho_m} = \frac{\frac{m}{V^*}}{\frac{m}{V_m}} = \frac{V_m}{V^*}$$

The relative density essentially says how much solid material is there in the volume overall occupied by the cellular material. The opposite of the relative density is porosity, calculated as $1 - \bar{\rho}$. Generally cellular materials have relative densities less than 0.3. This parameter can be calculated with geometrical considerations: models to calculate the relative density of several different types of cellular materials are discussed in [9]. Despite being a powerful concept, the relative density alone is not sufficient to characterize the morphology of a cellular material. It is very important to consider also the type of unit cell: having same relative density, a triangular lattice has different properties than a Kagome lattice or a hexagonal lattice. For instance, a bending and a stretching dominated structure with the same relative density have completely different mechanical properties and failure mechanisms, as will be discussed in the next paragraph. Moreover, even two lattices of the same type can have a different mechanical behavior depending on the relative distribution of material between the center of the struts and the struts (Figure I - 13) [68].

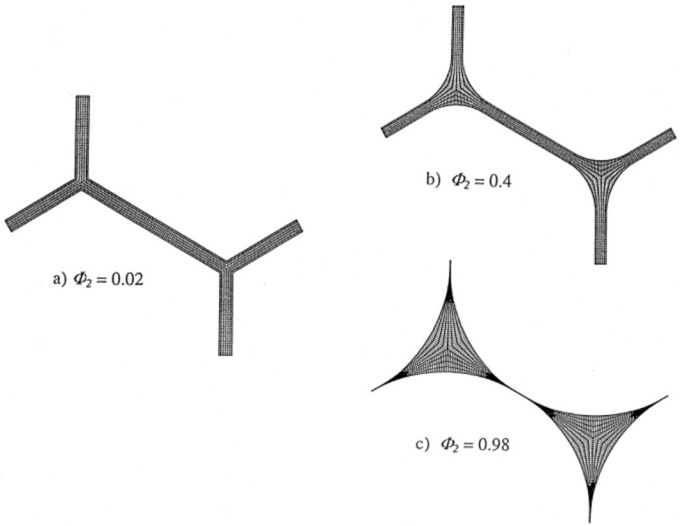

Figure I - 13. Planar lattices with the same relative density, but different fraction Φ of material at the joints [68].

1.2.2 Mechanical behavior of cellular materials

The mechanical behavior of cellular materials is illustrated by the compressive stress-strain curves in Figure I - 14. The curves can be divided into three parts: a linear elastic regime until struts yield due to bending or stretching, a plateau regime during which the cells start to progressively collapse because of buckling, brittle crushing or yielding depending on the base material and the morphology and finally a densification phase, that corresponds to the collapse of the cells one against the other (the struts reach contact). The slope of the densification regime tends to the elastic modulus of the base material, which is considerably higher. The stress-strain curves of the stretching-dominated lattices are generally characterized by higher stiffness and yield strength than a bending-dominated lattice of the same relative density. Moreover, a post-yield softening is also observed, due to the sudden failure by buckling or brittle crush of a layer of cells, and the subsequent plateau is made of peaks and valleys that indicate the progressive failure of the layers. Stretching dominated structures are therefore more structurally efficient but are prone to sudden failures and are not effective at dissipating deformation energy. On the other hand, bending-dominated structures are more compliant, have a more progressive transition to the stress plateau due to the bending of the struts and have a relatively flat plateau [7,63]. In their numerical study, Kadkhodapur et al. [69] correlated the stress-strain curve with the failure mechanism of bending- and stretching-dominated lattices and they observed that stretching-dominated lattices tend to fail layer-by-layer (the failure of the first layer is indicated by post-yield softening), while bending-dominated lattices fail in shear bands, matched by a smaller fluctuations in the stress-strain curve. Several experimental works have also confirmed these results, see for instance [70,71].

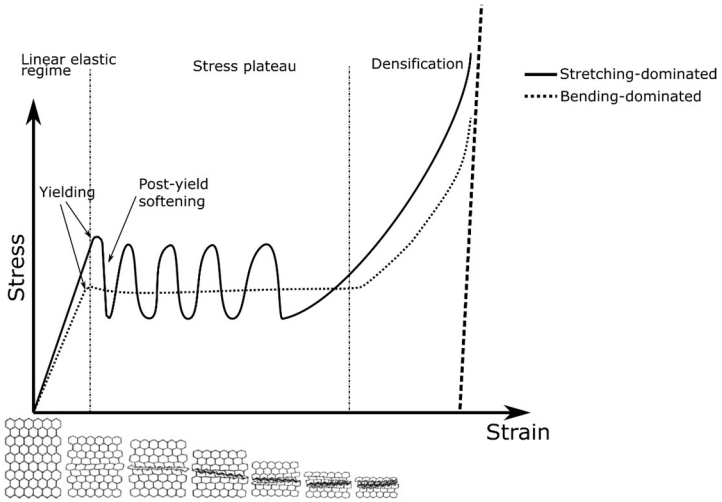

Figure I - 14. Typical compressive strain-stress curves for stretching- and bending-dominated cellular materials with same relative density and corresponding compression of a bending-dominated honeycomb [adapted from [63]].

Tensile stress-strain curves are the same as compressive curves in the elastic region, but after yielding the struts tend to progressively orient in the loading direction, without any buckling, until failure. Elasto-plastic materials, after yielding, can display a short plateau until all struts are yielded, followed by densification. In tension, cellular materials fail by yield or brittle fracture, depending on the base material [9].

1.2.3 Modelling of the mechanical behavior of cellular materials

The high number of cells in a lattice structure makes it often practically impossible to model the entire cellular component in full detail, even by using advanced finite elements softwares combined with powerful calculators. Consequently, in the last decades, several theoretical and numerical approaches have been specifically developed to model the mechanical properties of materials with a repetitive nature, which will be now very briefly reviewed. The aim of these approaches is to determine the effective properties of the lattice as a function of properties of the base material and the morphology of the cells. The effective properties can then be used as the properties of any regular material in the design process. A fundamental concept in the mechanical modelling of cellular materials is the Representative Volume Element (RVE), which is a fraction of the volume of the lattice that is representative of the properties of the entire structure. In other words, this element should be small

enough to reduce the complexity of the problem, but big enough to approximate with the requested accuracy the behavior of the lattice. In the case of regular periodic structures, the most logic choice for the RVE is the unit cell of the lattice. On the other hand, identifying the correct size of the RVE is not immediate in the case of cellular materials that are not regular periodic, such as, for instance, fully random foams, lattices affected by some degree of irregularity, or lattices with fabrication defects. In such cases, the simplest approach is to progressively increase the size of the RVE and choose the size at which the properties converge to a constant value [72–74].

Closed form models for the effective elastic constants and the yield strength of 2D and 3D regular lattices made of simple unit cells have been first devised by Gibson et al. [9,75], assuming the cell walls behave like Euler-Bernoulli beams. The elastic constants are calculated from the stresses and strains produced by applying uniform loads to the unit cell. Moreover, they observed that it is possible to correlate the elastic modulus of the lattice with its relative density in the form of a power law:

$$\frac{E}{E_m} = C\left(\frac{\rho^*}{\rho_m}\right)^n$$

Where C and n are constants that depend on the type of unit cell and can be determined theoretically (closed form solution) or fitted to experimental data. n is equal to 1 in an ideal stretching dominated structure and to 2 in an ideal bending dominated structure, as shown in Figure I - 15.

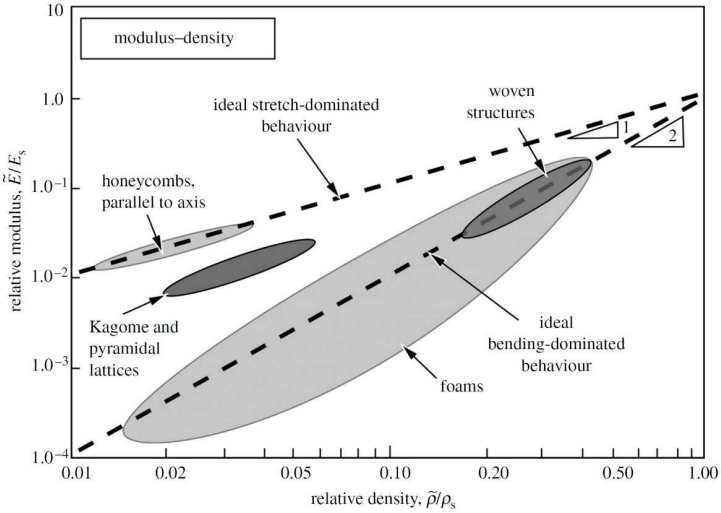

Figure I - 15. Relative modulus plotted against relative density for various topologies of cellular materials [63].

Equations of the same type were derived also for the other elastic constants, the collapse stress, the fracture toughness and the plastic buckling stress and where proven to correlate well with experimental results [9]. Closed form equations based on classical beam theory for the elastic properties and the yield strength of several types of 2D regular cellular lattices are also derived in [76]. This approach is ideal because it provides equations that directly provide the properties of a lattice as a function of the geometrical parameters, but unfortunately there are several limitations. First, assuming the cell walls to behave as beams provides good results only if they are sufficiently slender, i.e. these models progressively lose in accuracy as the relative density increases (generally it should be less than 0.3 [77]). Second, the derivation of closed form equations becomes impractical for very complex lattices. Third, these models often assume a uniform section of the beam, which is not generally the case in real cellular lattices, although it is possible to derive closed form equations also for cell walls of variable cross-section, provided the variation can be described by simple functions [78,79]. Finally, classical beam theory cannot accurately capture the stress-strain state at stress concentrators (such as at cell joints).

More advanced numerical modelling techniques, such as numerical homogenization methods, are able to overcome these limitations [80]. Homogenization techniques replace the cellular structure with the appropriate RVE, that can also include any possible irregularity of the lattice and does not have any limitation on the relative density value. The only two assumptions are that there exists a length scale separation between the microstructure and the domain of interest and that there is a spatial periodicity in the lattice (i.e. the field variables depend on multiple spatial scales and are periodic on the small scale and smooth on the macroscopic scale) [72,74]. Among the various homogenization techniques (reviewed in [72,80–82]), asymptotic homogenization has been successfully applied in many instances to the modelling of cellular media [77,83], including the solution of topology optimization problems [84], and manufacturing irregularities [55]. Asymptotic homogenization assumes that any field quantity, such as displacement, can be described as an asymptotic expansion of the periodically varying function in the equations of equilibrium. This is possible given the assumption of scale length separation: the very rapidly varying function on the small scale becomes near-smooth on the macroscopic scale [81]. Nevertheless, the homogenization method has some limitations, which are due to the assumptions it is based on. Several situations arise in which, for instance, the length scale separation is not verified due to the small number of unit cells that make up the domain considered, or the accurate stresses in some specific location need be known (homogenization techniques capture the homogenized stress state while they are inaccurate regarding the local stress state), or the effect of defects on the local stress state is investigated. The FE method, on the other hand, does not have these limitations and it is thus a valid alternative in

such situations. Indeed, potentially, with the FE method it is possible to study the mechanical behavior of the most complex cellular materials including the finest details without the necessity of any simplifying assumption, the only limitation being the computational power of the computer. FE models of cellular lattices can be divided into two classes: models based on beam elements and models based on continuum elements [80]. The former are computationally faster and are useful to calculate the effective properties of the lattice and can also correctly capture failure mechanisms [85,86]. Beam elements are quite versatile and can be used also to take into account material heterogeneities, irregularities in the strut cell wall thickness [87–89] and the effect of fillets at strut joints on the elastic properties [90]. Alkhader and Vural [91] used beam elements to show that the loss of periodicity in the structure of a stretching dominated cell results into a shift towards a bending-dominated mechanical behavior and thus a decrease in stiffness. Also, the study of the fatigue behavior of cellular materials gained considerably from the use of beam elements: in [92] the effect of cell geometry and relative density on the fatigue behavior was investigated, while in [93] a computational approach to predict the fatigue behavior was proposed, including also manufacturing irregularities. On the downside, beam models are accurate only for low relative densities (slender cell walls) and they do not provide the local stress-strain state. Continuum models provide the highest accuracy and the most faithful reproduction of any morphological feature at the expense of long computation times [80]. Several examples of complex analyses carried out using 2D and 3D continuum elements can be found in the literature. The effective elastic constants of planar lattices with stout cell walls were calculated in [94,95], while in [68,96] the influence of material distribution between the center of the cell walls and the junctions on the elastic constants of planar lattices was studied. The effect of surface irregularities on the elastic modulus was investigated in [97] regarding polymeric regular lattices using SEM measurements and in [98] regarding SLM CoCr lattices. More recently, the failure mechanisms of stretching and bending dominated lattices were simulated using 3D continuum models and successfully compared with experimental tests in [69], while Cuadrado et al. [99] also investigated the effect of load orientation. Multi-material analyses can also be completed, for instance to study the effect of tissue ingrowth in SLM Ti-6Al-4V biomedical scaffolds [100]. The FE method and accurate geometrical measurement techniques, such as X-ray Computed Tomography (CT), form a very powerful tool to interpret experimental results because, for the first time, it becomes possible to simulate the mechanical behavior of as-fabricated lattices [101,102].

There are several techniques to manufacture cellular materials, depending on the base material and on the type of structure [9]. For instance, foams can be produced by introducing gas into molten metal, glass or liquid monomers prior to polymerization. Periodic cellular structures, on the other hand, are more complex to

produce and require advanced manufacturing techniques, such as additive manufacturing, which will be briefly reviewed in the next Section.

1.3 Additive manufacturing of metals

Additive manufacturing (AM) is a novel manufacturing technology that creates an object by adding material layer by layer, only where it is needed. This technology stands out for its near-net-shape capability and the ability to produce complex geometries such as cellular structures without added cost or time. Moreover, it makes possible to considerably reduce the amount of waste material compared to more traditional technologies such as machining. The manufacturing process starts from a CAD model of the object as an input, which is then divided in layers (sliced) by a dedicated software and thus fed to the machine (printer). This technology started as a method to rapidly produce polymeric prototypes (hence AM is also called Rapid Prototyping) for visualization purposes, but nowadays it is regularly used to manufacture actual products. Many different AM techniques exist and all classes of materials (metals, ceramics, polymers) can be printed using the appropriate method [103,104]. Here, only the two most relevant AM technologies for biomedical metallic materials will be reviewed: Selective Laser Melting (SLM) and Electron Beam Melting (EBM). For a complete review of AM processes, the reader should refer to [103,105,106].

SLM and EBM belong to the class of Powder Bed Fusion (PBF) methods. The PBF process consists of building up a solid metal part layer by layer starting from a metal powder. A laser (SLM) or an electron (EBM) beam scans the powder bed and melts the particles in the locations where it is needed, which subsequently solidify. The bed is then lowered, and a new layer of powder is deposited by a recoating blade, and the energy beam repeats the scanning. The process continues until the part is finished. To print complex shapes with overhanging parts it is necessary to add support structures, which are lattice structures that avoid the collapse of the growing solid, reduce deformations related to thermal stresses and contribute to dissipate heat.

1.3.1 Selective Laser Melting

In SLM, the energy that melts the powder is provided by a laser (commonly a single mode fiber laser emitting light in the near infrared) of 20-1000 W of power (P_L) scanned with a speed (v_s) up to 15 m/s and a spot size varying from 50 μm to 180 μm. The thickness (D_s) of the powder layer deposited each time can range between 20 μm and 100 μm, which corresponds to the thickness of a few powder particles (generally 20-60 μm of diameter [107]). There are different possible scanning

strategies (i.e. the path of the laser) and the distance between two adjacent paths is called hatch distance (h_s) [104]. The specific energy E_v transferred to the volume of powder, responsible for the melting of the powder and for the heating of the adjacent areas, is defined as

$$E_V = \frac{P_L}{v_S h_S D_S}$$

The high thermal gradients caused by the concentrated energy source and the solidification of one layer over the other can generate considerable distortions during fabrication. Apart from the support structures, the strategy to reduce them is to pre-heat the build plate on which the part grows to reduce thermal gradients (for Ti-6Al-4V, pre-heating temperatures are usually about 200°C), but this is not sufficient to avoid considerable residual stresses [104]. An inert atmosphere of N_2 or Ar (Ar only for Ti) is maintained inside the closed process chamber to reduce the amount of O_2 present, which would cause the formation of impurities due to very high reactivity of Ti [107,108]. Given the low temperatures of the chamber, the cooling rates are typically high, which has important consequences on the microstructure of the product. A scheme of the SLM system is shown in Figure I - 16.

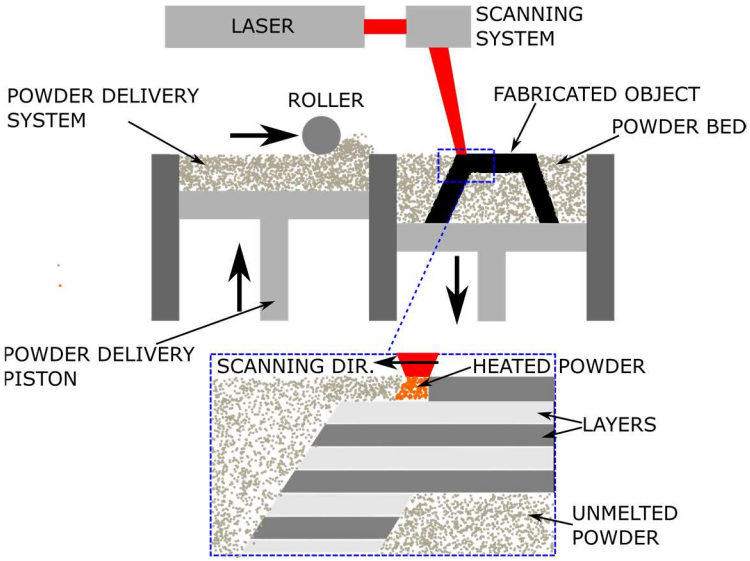

Figure I - 16. Schematic of the SLM system.

1.3.2 Electron Beam Melting

Conceptually, EBM is quite similar to SLM (Figure I - 17): the main difference being the energy source, which is an electron beam in this case, and subsequently the necessity for a high vacuum process chamber (~ 1 Pa of helium). The electrons are produced by a tungsten filament electron gun and accelerated by a 60 kV voltage. The beam is focused by a series of electromagnetic lenses and directed to the desired location by a magnetic scan coil. A powder layer of 50 µm – 200 µm is deposited and, differently from SLM, it is preheated with the electron beam to temperatures enough to sinter the powder particles (0.8 Tm, ~700°C for Ti-6Al-4V). The powder is then scanned with beam of 5 mA – 10 mA of current and 0.1 m/s of scanning speed [104,108].

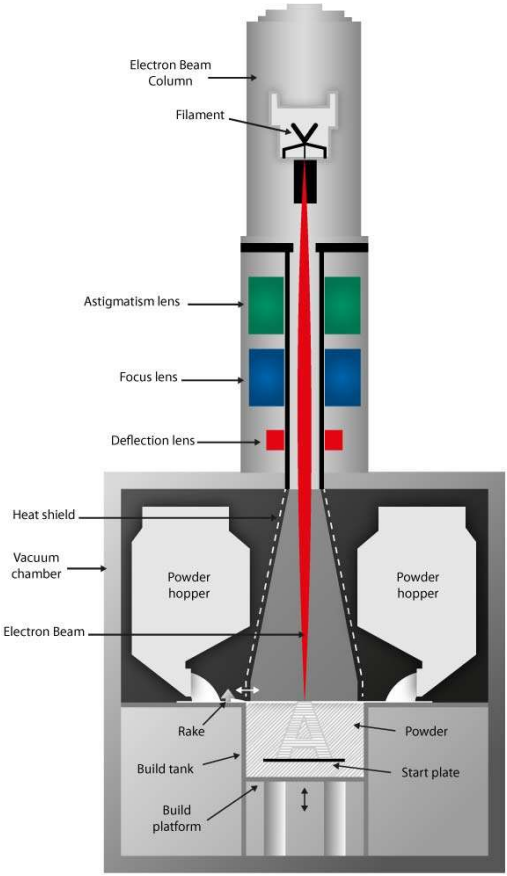

Figure I - 17. Schematic of an EBM system [www.arcam.com].

1.3.3 Comparison between SLM and EBM

The main differences between the SLM and the EBM systems are essentially related to the different energy source of the beams, laser and electrons, respectively. The electron beam negatively charges the powder particles, thus a repulsive force between the particles and between the particles and the electrons will arise. Therefore, the particles cannot be too small (45-105 μm [107]), otherwise their low mass and friction forces would allow their expulsion from the melting region. Moreover, the electrons tend to be diffused. This issue is mitigated with increasing conductivity of the powder, but anyway EBM is limited to conductive powders (metals). Nevertheless, the EBM spot size has to be larger than that of the SLM to avoid an excessive local charge buildup, and, consequently, the melt pool is larger, reducing the geometrical accuracy [103]. Electrons need vacuum to travel, which adds to the technological complexity of the EBM, but on the other hand it ensures a cleaner environment, reducing impurities in the fabricated part [107,109]. The high energy electron beam heats the powder surrounding the melt to a high temperature, thus, in order to avoid high gradients, the powder layer is heated to a higher temperature than SLM, leading to a slower cooling rate of the build and consequently lower residual stresses. Moreover, depending on the material, the final microstructure can also be different between the two technologies, SLM producing a martensitic microstructure [103,108]. The scan coil is much faster in directing the electron beam than the galvanometers used to direct the laser, so the scan speeds in EBM is higher, meaning higher build rates [103,110].

Parts fabricate by SLM or EBM, typically need post-fabrication processing to remove support structures and heat treatments to reduce residual stresses (only SLM). Depending on the requirements, it may be necessary to carry out further heat treatments to improve the microstructure and surface treatments (shot peening, sand blasting, machining) to remove loose powder, reduce surface roughness and respect geometric tolerances [111].

To summarize (Table I - 4), the main advantage of SLM is geometrical accuracy, while EBM is faster and can avoid the need of post fabrication heat treatments to reduce residual stresses. In the case of lattice structure, geometrical accuracy is an issue (as will be thoroughly discussed in the last Section of the Introduction), so SLM has a clear advantage.

Table I - 4. Comparison between EBM and SLM systems (adapted from [103,104,107,108]).

Characteristic	EBM	SLM
Power source	Electron beam (up to 3kW)	Laser (up to 1kW)
Atmosphere	Inert gas (N_2, Ar)	High vacuum (~ 1 Pa of helium)
Scanning	Deflection coils	Galvanometers
Energy absorption	Conductivity-limited	Absorptivity-limited
Powder preheating	High, using beam ($0.8T_m$)	Low, using heaters (~200°C)
Scan speeds	Very fast, magnetically driven (up to 10 m/s during pre-heat, 0.1 m/s during melting)	Limited by galvanometer inertia (up to 0.8-1.2 m/s)
Energy costs	Moderate	High
Spot size	50-180 µm	
Surface finish	Moderate to poor	Excellent to moderate
Feature resolution	Moderate	Excellent
Materials	Metals, polymers, ceramics	Metals (must be conductive)
Powder particle size	Medium (45-105 µm)	Fine (20-60 µm)
Powder layer thickness	50 µm	20-100 µm
Build rate	Fast	Slow
Residual stresses	Low	High

1.4 Titanium and its alloys for biomedical applications

Pure Ti and its alloys (essentially Ti-6Al-4V) are the most used metals in biomedical applications due to their superior biocompatibility and corrosion resistance in the human body, excellent mechanical properties-to-weight ratio, and low elastic modulus (Table I - 5). The only drawback of Ti alloys is that, compared to CoCr, they have a lower wear resistance [112]. Commercially pure titanium, although it has better biocompatibility than its Ti-6Al-4V alloy (there are concerns about the possible cytotoxicity of V [112]), is not strong enough for load bearing applications [113]. Moreover, the TiO_2 oxide layer on the surface normally prevents any ion release, thus granting a high biocompatibility also to Ti-6Al-4V [114]. Given these considerations, it is no surprise that Ti-6Al-4V is the most common choice for the manufacturing of load bearing biomedical implants [113].

Table I - 5. Comparison of the mechanical properties of the principal biomedical alloys [114], density [115].

Metal	E [GPa]	YS [MPa] (YS/density)	Fatigue strength [MPa]	% El.	Density [g/cm^3]
316L SS	210	450 (57)	250	40	7.9
CoCr (as cast)	200	500 (60)	300	8	8.3
CoNiCrMo (as wrought)	220	850 (92)	500	20	9.2
Ti-6Al-4V	105	900 (200)	500	13	4.5
Cp-Ti	100	300 (67)	200	40	4.5

To summarize, in Table I - 6 the three principal metals for biomedical implants are compared. In the next paragraphs, the discussion will focus on the microstructural, mechanical, and biological properties of Ti-6Al-4V alloy, for more information on Ti and its alloys the reader is referred to [116–118].

Table I - 6. Summary of the characteristics of the most common biomedical alloys [112].

	Stainless steels	CoCr alloys	Ti alloys
Designation	ASTM F-138 (316L)	ASTM F-75 ASTM F-799 ASTM F-1537	ASTM F-67 ASTM F-136 ASTM F-1295
Principal alloying elements (wt%)	Fe (bal.); Cr (17-20); Ni (12-14); Mo (2-4)	Co (bal.); Cr (19-30); Mo (0-10); Ni (0-37)	Ti (bal.); Al (6); V (4); Nb (7)
Advantages	Cost, availability processing	wear resistance corrosion resistance fatigue strength	biocompatibility corrosion minimum modulus fatigue strength
Disadvantages	long term behavior high modulus	high modulus biocompatibility	power wear resistance low shear strength
Primary utilisations	Temporary devices (fracture plates, screws, hip nails)	Dentistry castings; prostheses stems; load bearing components	THRs with modular (CoCrMo or ceramic) femoral heads; Long-term, permanent devices

1.4.1 Ti-6Al-4V: metallurgy

Depending on the composition, two types of Ti-6Al-4V (Tm = 1650°C) alloys exist: the standard, named Grade 5 (composition listed in Table I - 7), and the Extra Low Interstitial (ELI), known as Grade 23. The only difference between the two is the maximum allowable quantity of oxygen, which is 0.2% wt. for grade 5 and 0.13% wt. for grade 23. The effect of the lower concentration of oxygen is to increase ductility and fracture toughness [119].

Table I - 7. Composition of Ti-6Al-4V (grade 5) in %wt [120].

Alloy	Al	V	N	C	H	Fe	O	Others	
								Single	Sum
Ti-6Al-4V (Grade 5)	5.50-6.50	3.50-4.50	<0.05	<0.08	<0.0125	<0.25	<0.2	0.1	0.4

Titanium exists in two allotropic forms: α (hexagonal close packed structure, hcp) and β (body-centered cubic structure, bcc). α-Ti is stable up to 882°C, then it transforms to β-Ti. The addition of alloying elements to pure titanium can alter the transition temperature: some elements, known as α stabilizers (Al, O, N, C), increase the α→β transition temperature, while others, known as β stabilizers (V, Mo, Nb, Ta, Fe, W, Cr, Si, Ni, Co, Mn, H) decrease the transition temperature [112,115]. Depending on the chemical composition and thus on the microstructure at room temperature, Ti alloys can be classified as α, near-α, α+β, metastable β, or stable β. For instance, this behavior is illustrated by the Ti6Al-V phase diagram Figure I - 18: Al increases β-transus temperature, while an increasing concentration of V progressively increases the stability of phase β in the microstructure. β alloys are defined as Ti alloys with a composition that produces 100% β when quenching from above β-transus (although in the metastable region β can decompose to α+β upon aging). On the other hand, α+β alloys, upon fast cooling (quenching), transform into a metastable martensitic *α′* phase.

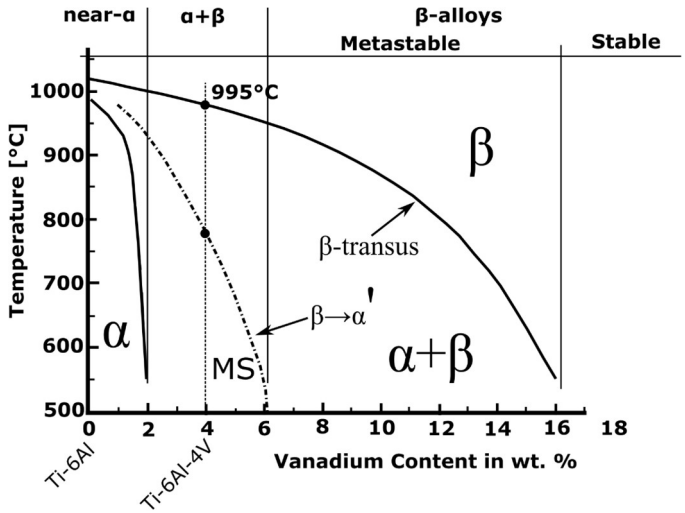

Figure I - 18. Pseudo-binary phase diagram of a Ti-6Al alloy with variable V content. The vertical dashed line indicates the Ti-6Al-4V (standard) composition with the β-transus and martensite start (MS) temperatures [Adapted from [121]].

Ti-6Al-4V is an α+β Ti alloy (Figure I - 18) and is a well-balanced compromise between mechanical and corrosion properties between the single-phase alloys due to the presence of both phases (a qualitative comparison is shown in Table I - 8), although the mechanical properties strongly depend on the thermal or thermo-mechanical treatment [112,121].

Table I - 8. Comparison of the properties of α , α+β and β Ti alloys [121].

	α	α+β	β
Density	+	+	-
Strength	-	+	++
Ductility	-/+	+	+/-
Fracture toughness	+	-/+	+/-
Creep strength	+	+/-	-
Corrosion behavior	++	+	+/-
Oxidation behavior	++	+/-	-
Weldability	+	+/-	-
Cold formability	--	-	-/+

The properties of the alloy depend on the microstructure, which is defined by the arrangement of the α and β phases, determined by the thermal or thermo-

mechanical treatment applied. In Ti alloys, these treatments are normally a sequence of deformation, solution heat treatment, and ageing. Two basic types of microstructure exist: lamellar and equiaxial, which can be coarse or fine depending on the thermo-mechanical history and on the starting microstructure. Given a specific composition, the most important parameter for the thermomechanical treatments is the β-transus temperature (995°C and 975°C for the standard and the ELI Ti-6Al-4V compositions, respectively [117]). *Lamellar microstructure* results from cooling from temperatures above β-transus: below the critical temperature, α lamellae nucleate at the previous β brain boundaries and then grows inside those grains (Figure I - 19 (a)). The faster the cooling, the finer become the lamellae: if quenched, the very fine needle-like microstructure (normally indicated as α') of (Figure I - 19 (d)) is obtained after a martensitic transformation. On the other hand, the *equiaxed microstructure* (Figure I - 19 (b)) is obtained after recrystallization: the alloy is highly deformed at low temperatures and then recrystallized in the α+β field. If the recrystallization temperature is close to the β-transus, the bimodal (also called duplex) microstructure shown in Figure (Figure I - 19 (c)) is obtained, which consists of primary equiaxed α grains in a lamellar α+β matrix [121]. A final annealing treatment is usually performed at variable temperatures to relieve stresses or to age the alloy (by precipitation) [117].

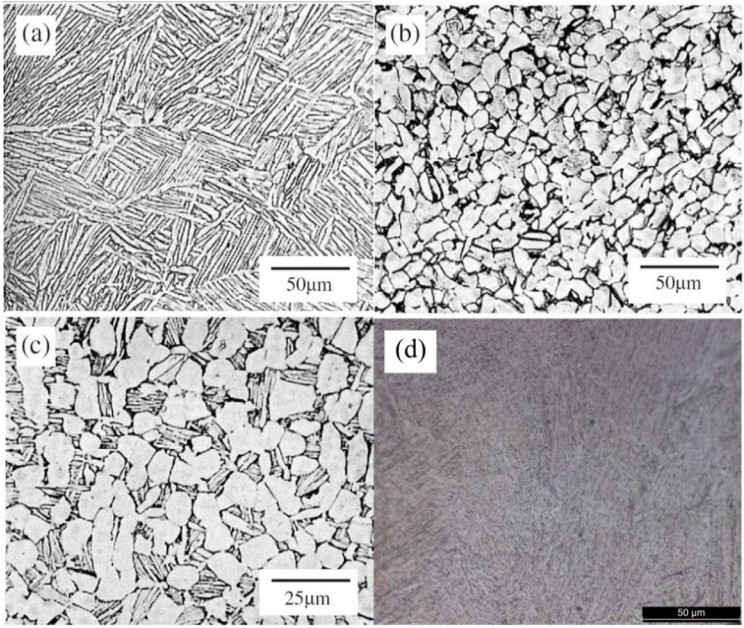

Figure I - 19. Typical microstructures found in α+β Ti alloys (α is light colored phase, while β is the darker) [(a-c) from [113], (d) from [122]].

The effect of the microstructure is qualitatively illustrated in Table I - 9. In general, a finer microstructure tends to improve strength, ductility and retards fatigue fracture initiation. On the other hand, a coarser microstructure is tougher, more resistant to creep and slows the propagation of fatigue cracks [121]. An equiaxed microstructure is sought for when strength and ductility are desired, while a lamellar microstructure when toughness is requested. The bimodal microstructure is a balanced compromise between the lamellar and equiaxed microstructures, but has superior high cycle fatigue resistance (lamellar microstructure has the lowest fatigue resistance while the equiaxed microstructure is intermediate) [113,121]. A detailed account on the thermomechanical treatments and their effect on the microstructure of α+β alloys can be found in [117], Chapter 5.

Table I - 9. Effect of the microstructure of Ti alloys on their properties (◯ uninfluential, + increase, - decrease) [121].

fine	coarse	Property	lamellar	equiaxed
◯	◯	Elastic modulus	◯	+/- (texture)
+	-	Strength	-	+
+	-	Ductility	-	+
-	+	Fracture toughness	+	-
+	-	Fatigue crack initiation	-	+
-	+	Fatigue crack propagation	+	-
-	+	Creep strength	+	-
+	-	Superplasticity	-	+
+	-	Oxidation behavior	+	-

1.4.2 Ti-6Al-4V: mechanical properties

In the previous paragraph, we discussed qualitatively the effect of the microstructure on the mechanical properties. Given the variety and complexity of the possible thermomechanical treatments and of the microstructures obtained, it is difficult to indicate precise values of the mechanical properties and, in the literature, there is a considerable scatter. Moreover, for the values found it is not always specified the microstructure or the thermomechanical process. Nevertheless, some representative values for the main mechanical properties measured for different microstructures are listed in Table I - 10. The trends discussed in the previous Paragraph are confirmed: the equiaxed microstructure is stronger and more ductile, but it is less tough compared to the lamellar. The bimodal has intermediate strength, but it is considerably tougher. On the other hand, the elastic modulus is very weakly

dependent on the microstructure. As a comparison, the properties of a martensitic microstructure are also listed, which is stronger and harder than the others, but less ductile.

Table I - 10. Indicative values of the mechanical properties of Ti-6Al-4V for various microstructures. (Notes: [d] reports data for mill annealed condition, which is approximately an equiaxed microstructure).

	E [GPa]	YS [MPa]	UTS [MPa]	A (%)	Hardness	K_{IC} [MPa·m$^{0.5}$]
Ti-6Al-4V ELI (equiaxed)	101-110[d]	830[b]; 795-875[d];	903[b]; 860-965[d]	17[b]; 10-15[d]	-	91[b]
Ti-6Al-4V ELI (SLM, α' martensitic)	113[c]	1015[c]	1090[c]	10[c]	380HV[c]	-
Ti-6Al-4V (equiaxed)	-	910[a]; 951[b]	1020[b]	15[b]	-	44-66[a]; 61[b]
Ti-6Al-4V (bimodal)	-	875[a]	-	-	-	88-110[a]
Ti-6Al-4V (lamellar)	110-114[d]	884[b]	949[b]	13[b]	-	78[b]

[a][123]; [b][113]; [c][124]; [d][119]

The fatigue resistance of Ti-6Al-4V is very sensitive to the microstructure (grain size or lamellae width, and arrangement of the phases), previous thermomechanical treatments and oxygen content (increases crack propagation rate). Moreover, the quality of the surface is also very important given the high notch sensitivity of this alloy [112,125].

The results regarding the effect of the microstructure on the fatigue behavior are contradictory, but in very general terms it is possible to say that a finer microstructure (thinner lamellae for lamellar microstructure or smaller grains for equiaxed microstructure) increases crack initiation time and has lower short crack propagation rates. On the other hand, a coarser microstructure reduces crack propagation rate [125]. To summarize, in the case of high cycle fatigue life, which depends on the resistance to crack nucleation, we find in order of performance the bimodal, the fine

equiaxed, the fine lamellar, the coarse equiaxed, and the coarse lamellar microstructure (Figure I - 20) [112].

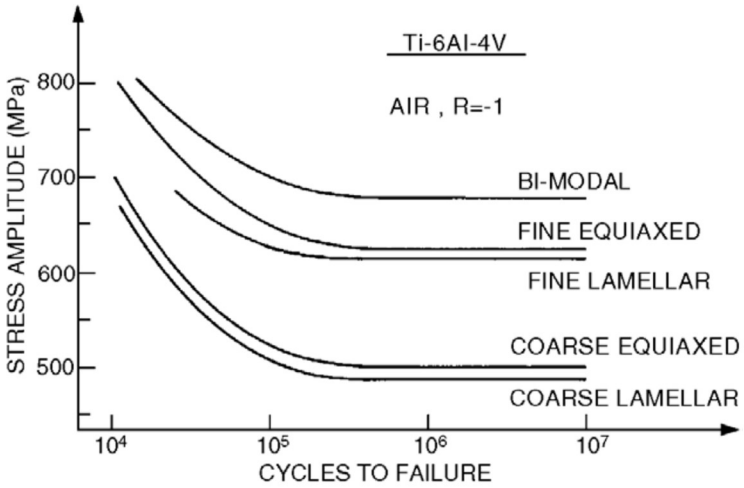

Figure I - 20. Fully reversed fatigue curves for various Ti-6Al-4V microstructures [113].

The fatigue behavior of Ti alloys, besides the microstructure, can be tailored by surface treatments. Ti has a high notch sensitivity, so the presence of surface notches or roughness is strongly detrimental to fatigue life. This is the reason why porous coatings (such as those to enhance biocompatibility) considerably affect the long-term mechanical performance of implants and their effect on fatigue should be taken into account in the design phase. Fatigue resistance can be improved by reducing defects on the surface by polishing (reduces crack nucleation), by inducing a compressive state of stress and by cold working the surface (slows short crack propagation). Shot peening is a surface treatment that consists in bombarding the surface with small hard beads that cold work the surface and induce a state of compressive residual stresses. This process should be controlled carefully because it also increases surface roughness: indeed, stress relieving can relax residual stresses produced by shot peening, which causes a drop of fatigue resistance with respect to the polished surface due to the increased roughness (Table I - 11). Polishing after shot peening can further improve fatigue resistance by removing roughness [112,125].

Table I - 11. Rotating bending fatigue strength (R=-1) of Ti-6Al-4V with fine equiaxed microstructure.

Surface condition	Fatigue strength [MPa]
Electrically polished	610
Shot peened	710
Shot peened + 1 h 500 °C	390
Shot peened + 1 h 500 °C + 20µm removed	800
Shot peened + 20µm removed	820

More information on the fatigue behavior of Ti alloys can be found in [112,117,120,125].

1.4.3 Ti-6Al-4V: corrosion resistance

An implant placed inside the human body is surrounded by a solution of roughly 0.9% NaCl at a pH of 7.4 (during an inflammatory response the pH decreases to 5.5). The breakdown potential of Ti-6Al-4V in physiological solution is +2.0 V, which is higher than the respective values for CoCr alloys and stainless steel (Table I - 12). Ti-6Al-4V (and metals with a higher breakdown potential) cannot undergo a breakdown of passivity. On the other hand, the passivating layer can be damaged mechanically, so the time for repassivation (t_e) and for oxide growth ($t_{0.05}$) are critical. Referring again to Table I - 12, we can recognize that oxides form very quickly on the surface of Ti, preserving the integrity of the bulk metal [114]. The passivating layer on the surface of Ti-6Al-4V is TiO_2 with small amounts of Al_2O_3 [112].

Table I - 12. Breakdown potentials (in Hank's solution) and repassivation times (in 0.9% NaCl solution, pH=7.4) for the most common biomedical metals [114].

Material	Breakdown potential [V]	Repassivation time [10^{-3} s] t_e		$t_{0.05}$	
		-0.5 V	+0.5 V	-0.5 V	+0.5 V
316L	0.2-0.3	> 72000	35	>> 7200	> 6000
CoCr (as cast)	+0.42	44.4	36	>> 6000	> 6000
CoNiCr (as wrought)	+0.42	35.5	41	> 6000	5300
Ti-6Al-4V	+2.0	37	41	43.4	45.8
cp-Ti	+2.4	43	44.4	47.4	49
cp-Ta	+2.25	41	40	43	45
cp-Nb	+2.5	47.6	43.1	47	85

Titanium has a very high affinity with oxygen (this is the reason for low passivation times) and, during the formation of the surface oxide, oxygen atoms tend to diffuse into the surface layer. The consequence is the formation of an oxygen-rich α layer, known as α-case because it forms a continuous oxygen stabilized α phase along the surface of the component. The issue with this is that this phase is harder and less ductile than the bulk metal and thus prone to crack initiation. The formation of the α-case occurs at temperatures above 550°C, where oxygen diffusion is fast [117].

1.4.4 Ti-6Al-4V: biocompatibility

Ti-6Al-4V and Ti in general have good biocompatibility thanks to the thin (~10 nm) oxide layer on the surface that prevents corrosion and the subsequent increased inflammatory response of the body that could lead to implant loosening [115]. Bone growth directly on the surface of the implant was observed and an increase in tear off force with time was measured. Indeed, Ti alloys can osseointegrate also without any bioactive coating (such as HA or bioglass), although coatings can certainly improve performance. It has been suggested, that the OH- groups that exist on the surface can bond with the Ca and P ions present in the living tissue and favor an attachment of the mineralized collagen fibrils [114]. The effect of the microstructure and of the surface topography is complex. It has been observed that a finer microstructure enhances osteoblast adhesion on the surface [113]. Moreover, a certain degree of surface roughness is beneficial to osseointegration (<22μm) because it enlarges the contact surface [114].

1.4.5 Ti-6Al-4V fabrication via SLM for biomedical applications

In this Paragraph, the characteristic and properties of SLM fabricated Ti-6Al-4V parts will be discussed because SLM was the technology use to fabricate the cellular structures studied in this Thesis. For a more general discussion including also EBM, the reader should refer to [104,107–109,111,126,127].

Parts fabricated by PBF methods are characterized by fast cooling rates, directional heat flow and repeated thermal cycles. These factors have a strong influence on the microstructure, thus PBF parts are characterized by the formation of metastable phases induced by rapid cooling rates (i.e. martensite) and preferential grain growth direction produced by the directional heat flow [106]. The pre-heating in SLM is considerably lower for SLM than for EBM (200°C vs 700°C for Ti-6Al-4V) leading to more rapid cooling rates. As a consequence, the microstructure typically obtained after SLM is an α' fine acicular martensitic (Figure I - 21a and Figure I - 21b), while after EBM normally is lamellar α+β [108]. More precisely, during scanning we assist

to the formation of columnar β grains aligned with the build direction that can encompass several layers due to epitaxial growth and, by cooling, these grains are filled by martensitic needles during the β→α' decomposition (Figure 1.22a). The final microstructure depends on the volume energy, i.e. the amount of heat received by the melt and the surrounding powder: less heat means faster cooling rates and thus a finer structure [104,128]. Due to melting of successive layers one on top of the other, precipitation of Ti_3Al can occur, as with ageing [104]. In general, the microstructures obtained with PBF methods reflects a more or less fast cooling from a melt. We have also to consider that the actual amount of material melted and solidified each time is quite small, thus the microstructure resembles more that of small cast parts, but in general it is much finer, especially in SLM. It is quite unlikely to find equiaxed grains as in wrought bulk parts, even in the α+β EBM microstructure [111].

The SLM as-built martensitic microstructure is normally not suitable for biomedical applications because, despite being hard and strong, displays low ductility. Moreover, there are high residual stresses that can cause distortions or even cracks. Post manufacturing stress relieving heat treatments are commonly carried out, from about 700°C (only stress relieve) to 1000°C (solution annealing). The latter completely decomposes the martensitic microstructure into the equilibrium α+β phases, and considerably coarsens the grains (Figure I - 21c). Hot isostatic pressing (HIP) is another common process, that consists in applying an hydrostatic pressure (by the means of a fluid, like oil) and simultaneously a high temperature (about 920°C): the effect is to transform the martensite into α+β and to close surface porosity and, consequently, increase ductility and fatigue resistance at the expense of a small decrease in strength [104].

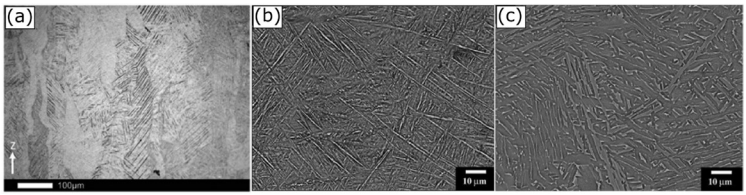

Figure I - 21. Microstructure of SLM Ti-6Al-4V: a) needle-like martensitic microstructure in prior elongated β grains (*z* is the build direction) ; b) as built needle-like martensitic, c) lamellar α+β after HIP at 920°C and 103 MPa [104]

The mechanical properties of SLM parts in relation to other manufacturing technologies can be understood by considering the microstructural features discussed above and the porosity. Indeed, given that the starting materials is a powder, a characteristic of any PBF process is the presence of closed porosity, although densities higher than 99.5% are normally requested. Pores can be the

result of trapped gases (spherical shape) or lack of melting (elongated shape). The former are usually caused by excessive volume energy (more intense melt dynamics), the latter by too little volume energy [104,129,130]. Pores are detrimental because can act as stress concentrators. Due to their finer microstructure, SLM parts have higher tensile strength compared to cast or wrought parts, but they are less ductile. Nevertheless, as discussed, heat treatments can be applied to tailor mechanical properties: for instance, HIPing. A certain degree of anisotropicity is observed in AM parts, because microstructure and porosity are affected by the layer-by-layer build strategy, although the dependence of the mechanical properties on the build direction are somewhat contradictory. Fatigue strength is particularly sensitive to porosity and surface roughness, so as built SLM parts have normally shorter fatigue lives than wrought or cast parts with the same loads. For the same reason, HIPing and surface treatments can considerably improve their performance. EBM parts have poorer surface finish, but are less porous (more homogenous heating) and more ductile, so in the as built condition have higher fatigue resistance than SLM parts [104,126]. Herzog et al. in [104] carry out an in depth literature review to compare the mechanical properties of SLM, EBM, wrought and cast Ti-6Al-4V specimens, while [126] discuss their interesting experimental results of static and fatigue tests of SLM and EBM Ti-6Al-4V specimens printed in different orientations to the build direction and having applied different heat treatments.

1.5 SLM Ti-6Al-4V cellular lattices for load bearing biomedical implants

In the previous Sections, we introduced the fact that cellular materials are increasingly used in the biomedical field, both as tissue engineering scaffolds and as permanent metallic biomedical implants. The qualities that make cellular materials attractive for load bearing implants are:

- High degree of porosity: porosity provides space for the growth of bone tissue and the flow of nutrients and, given the same volume, more surface for the bone to attach to.
- Low modulus: given its lower density, a porous material has a lower modulus than a bulk material. If appropriately designed, the elastic modulus of the artificial lattice can match that of the bone, even if the base material is very stiff as is the case for metals, decreasing stress shielding and the related issues.
- Tailorable properties: the properties of a cellular material depend on the base material and on the micro-architecture (unit cell type, strut thickness and junction geometry). Thus, by keeping the same base material

(chosen for its biocompatibility, for instance) it is still possible to obtain materials with a wide range in the mechanical properties by changing their geometry. Moreover, the structure can be made to progressively change form one area of the part to another, i.e. a functionally graded structure is also practically achievable.

Manufacturing of cellular structures with traditional technologies is not feasible given the complexity of their structure, especially when a big number of unit cells are necessary [131]. Fabricating foams is less demanding, but their applicability to load bearing implants is limited because their structure is less controllable. Little control over the micro-architecture has detrimental consequences on both the biological and the mechanical performances of the implant. Indeed, pores that are too big or too small are not effective for bone ingrowth. On the other hand, the great number of defects typically present in a foam decrease its strength (fatigue and static) and its reliability. Additive manufacturing, being a layer-by-layer process, it is the most promising technology to fabricate cellular materials with a highly controlled structure. EBM and SLM share some common advantages regarding the manufacturing of orthopaedic implants [109,132]:

- Possibility to fabricate complex shapes, hollow parts, cellular structures, and functionally graded materials unfeasible with other technologies.
- Increasing the complexity of the part does not substantially increase manufacturing time.
- Reduced production time and cost for small batches compared to traditional methods
- The geometry of the part can be easily changed by simply modifying the CAD without added costs (easy customization of implants)

Ti-6Al-4V combines excellent biocompatibility with good mechanical properties and low weight and it is the first choice for fabricating permanent load bearing implants. Given also its use in the aeronautical sector, it has been extensively studied, also regarding fabrication via AM technologies. SLM, compared to EBM, is more accurate and produces a better surface finish, thus it has a considerable advantage in producing structures that should have reliable and predictable properties. Nevertheless, several aspects have to be addressed and understood regarding the development of additively manufactured SLM Ti-6Al-4V cellular materials for load bearing biomedical implants. Such aspects, like the mechanical properties, the biological properties and the morphological accuracy, will be now briefly reviewed.

1.5.1 Mechanical properties

The mechanical properties of SLM cellular lattices have been studied via experimental [71,133], analytical [134], and computational approaches [69]. In Section 1.2, we discussed the mathematical models used to predict the mechanical properties of cellular materials in general. Analytical relationships are the easiest and fastest to use, but such models are limited to the nominal geometry (i.e., the CAD) because, unfortunately, it is very difficult to include defects and irregularities [134]. Indeed, predictions based only on the nominal geometry of the unit cell and on the isotropic mechanical properties of the metal are affected by a degree of inaccuracy because the manufacturing method strongly affects the mechanical properties of the lattice [80,135,136]. There are several studies regarding the mechanical behavior of SLM Ti-6Al-4V cellular structures and the influence of the manufacturing process [89,122,137–141] and even more data is available if we include studies carried out using EBM [102,142,143] or other materials (among several, steels, CoCr alloys, AlMgSi alloys, other Ti alloys) [70,85,88,144–147]. The most accurate and simple approach to study the effect of process parameters on the mechanical properties is obviously the experimental approach [70,138,141,144,148], but it requires a lot of time and resources because a large number of specimens should be manufactured to obtain a reliable statistic. Moreover, each time the structure or the AM process parameters are modified, the experiments should be repeated. Computational approaches can bridge the gap between empirical studies and purely theoretical models. For instance, FE models that include manufacturing defects (evaluated with μCT scans or SEM observations) have been reported in the literature [88,89,98,102]. These models have been used to interpret the experimental results, to estimate the effect of such defects on the mechanical properties and, moreover, to classify defects and separate the respective contributions. Recently, advanced predictive computational models of the stiffness and strength of SLM lattices that include manufacturing imperfections have been devised with good success [88,145,149]. This approach has great potentiality because, once the model is calibrated, it can be used to accurately predict the mechanical behavior of fully cellular parts (e.g. hip implant stem) reducing considerably the resources for experimental verification [55,56].

The effect of manufacturing on the mechanical properties is due to influence of process parameters on the microstructure and the micro-architecture of the lattice [80,136]. Firstly, the microstructure of as-built SLM parts can be quite different from that obtained by casting or forging and, subsequently, the mechanical properties of the base metal differ from those normally [137–139]. Second, several types of geometrical defects and irregularities are introduced that can also considerably alter the mechanical behavior [138,141,147,148,150]. The microstructure of SLM Ti-6Al-4V parts was already discussed in Section 1.4. Its effect on the mechanical behavior

is essentially due to the directionality of grain growth (normally aligned parallel to the printing direction) and to the very fine grain size. In other words, there is a certain degree of anisotropicity of the base material and, moreover, the base material is stronger but less ductile than the cast or forged. In practice this means that interpreting the experimental results for cellular lattices using, for instance, isotropic mechanical properties should be done with care because it can lead to errors [80]. Nevertheless, this practice is quite common in the literature and it is often justified due to its simplicity and because the microstructural effects in cellular materials are secondary to the morphological quality [100,102,149].
There are several different types of morphological defects and irregularities found in SLM metallic lattices [88,89,145,151] that can be essentially classified as following.

1.5.1.1 Porosity

Two types of pores can be found in SLM parts, spherical pores and irregular-shaped pores: the former are due to trapped gases, while the latter are due to incomplete melting of powder particles. The formation of spherical pores is promoted by a high specific energy that increases melt dynamics while irregular pores form more often when the specific energy is low [104]. The amount of porosity in bulk parts is normally very low, about 0.5%-0.1%, but it can be considerably higher in lattice structures (Figure I - 22). Porosity can be reduced by HIPing [122,152]. The inclination of the struts to the printing direction has been observed to influence porosity: as the inclination of the struts increases so does porosity [139,152].

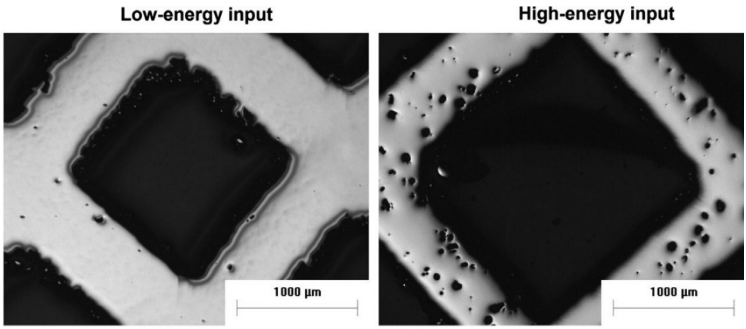

Figure I - 22. Spherical pores at different laser energy inputs in SLM Ti-6Al-4V lattice structures: excessive energy can create high volume of pores [140].

1.5.1.2 Unmelted attached particles

As the melt solidifies, nearby unmelted powder particles are inevitably attached to the surface of the solid and, depending on the amount of melt wetting them, they can be strongly attached or loose. In any case, the effect is to increase the roughness of the surface, depending on the size of the particles [80]. The number of attached

particles depend on the orientation of the surface (Figure I - 23): downward surfaces are characterized by more particles than lateral surfaces, while upward surfaces are almost free of particles [148,153]. This effect is related to the thermal behavior of the solid/powder system, as will be discussed in the next Paragraph. The layer of partially melted particles can be removed by chemical etching [142,148,151]. Higher laser power seems to increase the number of adhered particles [70].

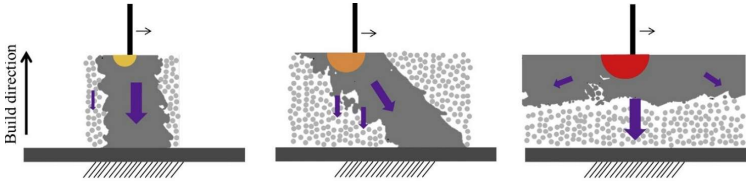

Figure I - 23. Effect of the build orientation of the struts on the surface appearance. The arrows indicate the amount of heat flow: if more heat is transmitted to the powder (horizontal strut), more particles tend to melt and attach to the surface [154].

1.5.1.3 As-built/as-designed mismatch

It is well known that there can be a considerable deviation between the as-designed geometry (CAD) and the as-built geometry for AM parts and this issue is particularly relevant in parts with fine details such as cellular lattices [80]. Ultimately, the accuracy of SLM is determined by the size of the melt pool: the bigger it is, the more difficult it becomes to reproduce fine details. The size of the melt pool is determined by the local thermal properties of the powder/solid system and by the energy provided by the scanning laser: if high amount of heat is provided and/or it is not carried away quickly, a large melt pool will form, otherwise, a smaller melt pool is obtained. The energy provided by the laser is the specific energy and it is determined by the process parameters such as the laser power, the scanning speed, the layer thickness and the hatch distance [70,144,155].

The local heat transfer properties of the solid/powder system are a complex issue, but they mainly depend on the spatial orientation of the already solid material, on the quantity of solid in respect to the powder and on the packing density of the powder (Figure I - 24a). The powder, regardless of its packing, is less conductive than the solid, so heat will be mainly carried away by the already solidified part. For instance, a horizontal strut is supported only by the less conductive powder below and thus the melt pool will tend to be large [141,148]. Moreover, due to gravitational and capillary effects, the melt will tend to flow into the powder, leading to an oversized strut with an irregular surface, particularly on the lower side where many loose particles are found [153,155]. On the other hand, in the case of a vertical strut, the melt pool is supported only by solid material and it is thus smaller, leading to a much more faithful reproduction of the CAD. In other words, the morphological quality of a horizontal strut is the lowest and it progressively improves with increasing angle [135,156]. This phenomenon is not limited to the struts of cellular lattices but is a

characteristic of any overhanging part [157,158]. Inclined struts can show the so called “staircase effect” (Figure I - 24c), which is caused by the strut being made of small layers welded one to the other with a small axial offset due to the inclination [148,153]. The complexity of the as-built/as-designed mismatch issue is increased by material shrinkage during solidification and cooling [159].

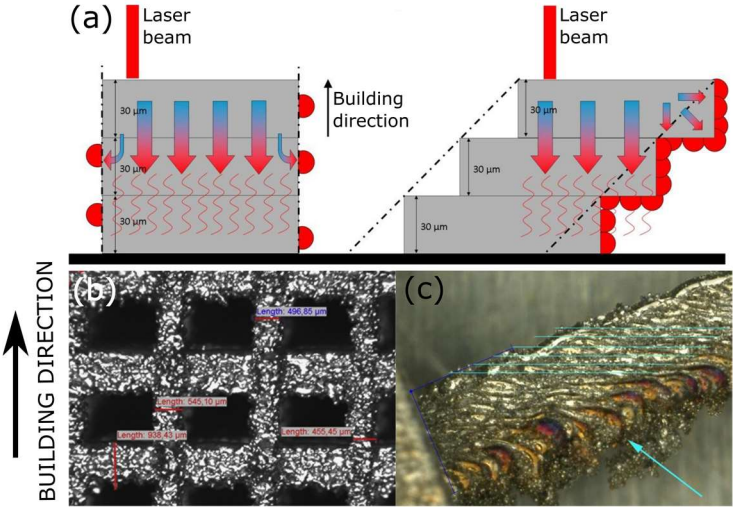

Figure I - 24. Effect of strut orientation on strut morphology: (a) heat (arrows) is carried away more efficiently by vertical struts then horizontal struts, improving surface appearance and geometrical accuracy compared to (b) horizontal and (c) inclined struts. The formation of the staircase effect is shown in (a) and (c) [(a) [148]; (b) [99]; (c) [156]].

The aspects discussed above are responsible for the as-built/as-designed mismatch, which can be decomposed into several contributes, useful mainly for modelling purposes [88,89]:

- Strut waviness
  The barycenter of the cross-sections along the length of the strut do not typically lie on the nominal axis but there is some degree of offset which produces a wavy effect (Figure I - 25) [88,141].
- Strut section irregularity
  The as-built shape of the cross-section tends to deviate from the designed shape due to the irregular distribution of material (Figure I - 25) [88,156].
- Strut thickness variation
  The average thickness (or diameter, depending on the geometry of the cross-section) of the cross-section can be higher or lower than the as-

designed value depending on the inclination of the struts to the printing direction and on the process parameters [70,71,135,141]. The thickness of struts with small angles to the building plane tend to be considerably thicker than struts parallel to the printing direction (Figure I - 24b) [135].

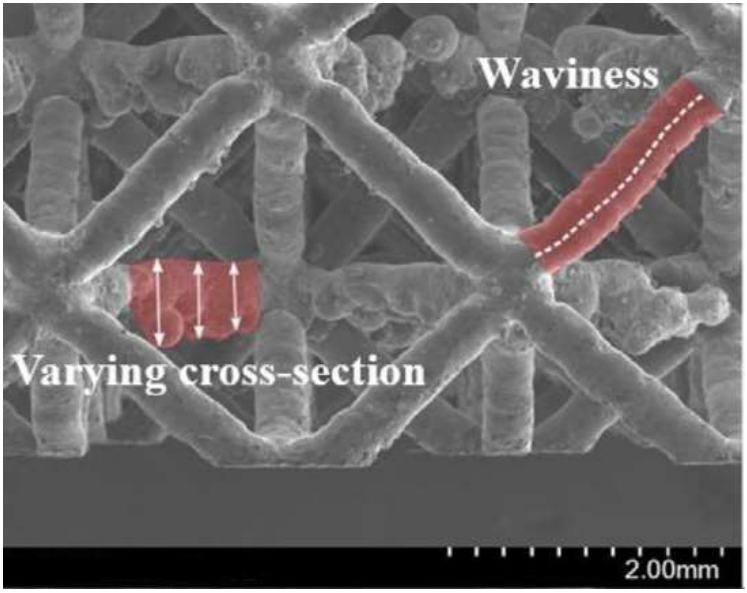

Figure I - 25. Examples of geometrical irregularities in an SLM lattice: strut waviness and strut cross-section variation on a horizontal strut [88].

The rapid cooling typical of SLM induces residual stresses in the cellular lattice which are not always completely released with post-manufacturing stress relieving. These stresses, apart from possibly inducing distortions in the lattice, can also affect the mechanical properties. More specifically, tensile residual stresses are particularly detrimental for fatigue resistance [136]. Anyway, it is very difficult to quantify this effect given the complexity of the structure and the technical challenge of measuring the residual stresses in the struts.

In orthopaedic implants, the elastic modulus is often the single most important parameter to determine the suitability of the material, given its relation to stress shielding and bone regeneration (see Section 1.1). The yield stress and the strength of the lattice are also important, because the implant should strong enough to carry the physiological loads. These parameters are relatively easy to measure with compressive or, more rarely, tensile tests and need fewer specimens compared to,

for instance, fatigue analyses. The quasi-static properties depend on the type of unit cell, on the thickness of the struts, on the properties of the base material (see Section 1.2), on the manufacturing defects (geometric irregularities and surface condition). The effect of the manufacturing defects is in general to decrease the mechanical performance of the lattice, although it is difficult to identify general trends and the effect of defects should be analyzed case by case. Moreover, the orientation of the struts has to be taken into account: struts oriented in the direction of the applied load give a higher contribution to the overall mechanical performance of the lattice. In other words, the defects of these struts have a stronger influence than those affecting struts that carry a lower fraction of the load [80]. As a general rule, struts laying in the building plane should be avoided because, especially if oriented in loading direction, can considerably alter the mechanical properties of the lattice [139]. Given the strong aleatory component of manufacturing defects, as-built lattice structures can show a considerable scatter in mechanical performance [89,160].

1.5.1.4 Elastic modulus

Strut waviness is the defect that affects the most the elastic modulus by decreasing it because it makes the strut more prone to bending [88,145]. Nominally stretching dominated structures are remarkably sensitive to strut waviness because such structures are very stiff given that the struts are loaded only axially: waviness introduces bending moments that cause a drop in the stiffness of the strut promoting in fact a transition to a quasi-bending dominated behavior. The deviation of the cross-section shape and size for the design has also a strong effect on the elastic modulus both in the case of stretching and bending dominated structures because it changes the moment of inertia and the load bearing area of the struts. The effect can be both to increase or decrease the modulus, depending whether the section is bigger or smaller. Internal porosity and surface roughness decrease the elastic modulus, but their effect is generally small compared to the other morphological defects, unless, for instance, the pores are unusually big [89].

1.5.1.5 Strength

Strut waviness decreases strength, although to a less extent than the elastic modulus. Variations in the shape and size of the cross-section strongly affect strength, increasing it or decreasing it depending on whether the as-built section is bigger or smaller than the designed section [70,88]. Both yield stress and ultimate tensile strength are more sensitive than the elastic modulus to internal porosity, surface roughness and surface irregularities because they create weak spots where stresses increase locally, inducing premature plasticization and subsequent rupture [80,89].

1.5.1.6 Fatigue resistance

Fatigue resistance is critical in load bearing biomedical implant materials because cyclic loads are produced by regular daily activities such as walking, for instance. Bones and joints are normally loaded in pure compression (i.e. compression-compression fatigue) thanks to synergic actions of muscles. For this reason, in the literature the compression-compression fatigue behavior of cellular lattices [161–165] is considerably more studied than the tensile-compression or tensile-tensile fatigue [166]. Nevertheless, it is not excluded that tensile loads could arise in some parts of complex implants, such as hip prostheses. Moreover, even compressive remote loads can induce tensile stresses in individual struts (for instance, if subjected to bending actions), depending on the type of unit cell [167]. To be safely used in implants, cellular materials should possess high fatigue resistance. The fatigue life of cellular structures is usually divided into three stages [167–169]. The first stage is the crack initiation life and consists in a progressive accumulation of plastic strain in correspondence of some weak spot where the stresses are intensified, that in SLM cellular structures are usually surface irregularities (roughness, notches, pores) or geometric stress raisers such as the strut junctions [161,162,164,170]. The second stage consists in crack initiation and propagation across single struts in different locations of the lattice, while during the third stage crack the cracks coalesce across several unit cells leading to rapid failure. The second and the third stage represent the crack propagation life. The propagation of the crack is matched by a progressive decrease in stiffness.

The morphology of the unit cell strongly influences the fatigue behavior of the lattice: structures with struts prevalently loaded axially are more resistant than structures where bending actions are not neglectable, provided that the relative densities are the same [162,165]. Notably, Amin Yavari et al. [161,165] showed that if the fatigue strength is normalized by the yield strength, the S-N curves for different levels of relative density for the same type of unit cells practically overlap. This interesting result suggest that, given a unit cell type, it is enough to characterize the fatigue behavior for one value of relative density, while the S-N curves for any other relative density can be computed from the yield stress measured with much faster quasi-static tests.

Fatigue, contrary to the elastic modulus and other monotonic properties, is a highly localized phenomenon and it is thus very sensitive to the microstructural and morphological quality of the part [171]. In other words, fatigue, more than anything else, is affected by the manufacturing process. Thus, understanding the effect of manufacturing on fatigue properties is of paramount importance. For instance, Vayssette et al. [172] report the fully reversed fatigue resistance at 2×10^6 cycles of a hot rolled Ti-6Al-4V bulk specimens to be 640 MPa, that of a machined HIPed SLM specimen to be 512 MPa and finally that of a HIPed SLM specimen in as-built surface conditions to be only 222 MPa. The better performance of the hot rolled

specimens is due to the microstructure (fine equiaxed vs fine lamellar), but the strong negative effect of surface roughness and irregularities is demonstrated by the superior performance of the machined SLM specimen compared to the as-built SLM specimen. The effect of manufacturing is even more evident in cellular SLM Ti-6Al-4V: the limit fatigue strength of cellular materials has been reported to be 25-35% of the yield (plateau) strength of the lattice [161,165] or as low as 16% [162]. Ti alloys are especially sensitive to surface defects such as roughness, porosity and notches due their high notch sensitivity [119]. Apart from stress raiser defects, also residual stresses and the microstructure determine the fatigue behavior [168,169,173]. The effect of the stress ratio *R* on compression-compression fatigue strength was investigated by de Krijger et al. [164] who observed that loading under high R-ratios resulted in greater number of cycles to failure. They observed a strong influence of the load amplitude, while the effect of the mean stress was weak. The presence of notches and geometrical irregularities appears to be the most likely explanation, given that in bulk Ti notches reduce the fatigue strength but also the sensitivity to the mean stress.

FE tools have been proven to be very useful in the interpretation of the effect of the unit cell morphology and type of defects on the results of fatigue tests on cellular materials [92,162,166,174]. Moreover, the high cost of fatigue characterization in terms of time and number of specimens draw towards the development of computational techniques to predict the fatigue behavior of AM lattice structures [175].

Treatments that improve the surface conditions, close internal porosity, remove tensile residual stresses or increase the ductility of the microstructure can act positively on the fatigue performance of SLM Ti-6Al-4V [160,168]. HIPing has been proved an effective treatment as it increases the ductility of the as-built microstructure. The effect of the reduction of internal porosity, although very effective in bulk specimens [173,176], is small in cellular structures because of the prevalence of surface defects which are not affected by HIPing [163]. In [163] it was shown that HIPing followed by chemical etching is the most effective treatment because it also removed surface stress raisers.

Struts often fail due to fatigue in the proximity of the strut junctions [163,166]. Indeed, at the junctions stresses are generally higher due to the combined effect of surface irregularities and the stress concentration effect of the junction [164,175]. This suggest that the fatigue resistance of lattice structures could be increased by placing fillets at the junctions to reduce stress concentration [83,90,174].

1.5.2 Biological performance: unit cell size and surface

The spread of cellular materials in the biomedical field is due to the versatility of their mechanical and morphological properties. Indeed, the reduction of stress shielding

and the enhanced bone ingrowth and osseointegration are related to their high interconnected porosity. Moreover, the surface condition of the struts is also a factor of paramount importance because, as the implant is placed into the body, the first thing the living tissue meets is indeed the surface of the struts. In the literature, there is little agreement on the optimal value of the pore size for bone ingrowth and fixation and pore sizes as small as 50 μm are reported to be effective in animals [15], but generally bigger sizes of 400-1000 μm are more frequent [15,109,110,177,178]. For instance, Taniguchi et al. [179] have compared the bone ingrowth of SLM Ti-6Al-4V lattices with different pore sizes and observed that the best performance was shown by pores of 600 μm. In their review on metallic scaffolds for biomedical applications, Tan et al. [110] suggest that smaller pores (~500 μm) favor bone cell growth but larger pores (~1000 μm) provide a better flow of nutrients. Pores bigger than 1 mm may be ingrown by fibrous tissue rather than mineralized bone [15]. On the other hand, apparently there is no correlation between pore shape and bone ingrowth [177].

Surface roughness increases the surface of the implant available for bone cells to attach too and it is thus generally viewed as necessary for the biological performance. Nevertheless, if the surface is too rough, cell proliferation is hindered [109]. Ponader et al. [180] found a threshold equal to 24.9 μm for the mean roughness amplitude below which roughness has a positive effect on cell proliferation. If the surface roughness of the as built lattice exceeds this value, surface treatments such as chemical etching can be beneficial [109].

1.5.3 Design for Additive Manufacturing

The morphological characterization of cellular lattices is very useful to classify and quantify the defects and to interpret a-posteriori the mechanical behavior of a specific structure. Moreover, understanding the correlation of the morphological features with the principal process parameters (laser power, scan speed, layer thickness) and the orientation of the struts can lead to a considerable reduction of the mismatch between the as-built and the as-designed structure, although not to eliminate it completely. Indeed, given the complexity of cellular structures that normally have struts oriented in several directions, it seems unlikely that it is possible to optimize the process parameters to achieve a perfect as-built/as-designed match in every location of the lattice. Nevertheless, it has been observed that there is a well-defined linear correlation between the as-designed strut thickness and the as-built thickness [138,141,148], which suggests that the as-built/as-designed deviation has systematic component that should be possible to adjust. Two different strategies have been proposed in the literature: post-manufacturing chemical etching to remove the material in excess [142,148,151] and a modification of the input CAD to account for the material in excess (or lacking) [135]. The second approach is essentially a

compensation of the “inevitable” manufacturing deviation and its advantages consists in the absence of additional post-manufacturing treatments and in the possibility to easily apply separate degrees of compensation to different struts of the lattice depending on their inclination and as-designed thickness. The compensation model is calibrated with a first set of experiments to calculate the mathematical relationship between the as-built thickness and the as-designed thickness. Once this correlation is available, it is possible to adjust the mismatch of any subsequent lattice produced with the same process parameters and thus improve the correspondence between the mechanical properties of the as-built lattice and the required properties. In other words, by compensating the manufacturing error the mechanical properties of the lattice can be predicted with improved accuracy. The error compensation model can be integrated into an FE procedure [149] which can be used, for instance, to design fully porous load bearing biomedical implants via topology optimization [55,56].

Considering manufacturing aspects already in the design phase of the structure to improve the morphological and functional quality of the part is known as *design for additive manufacturing of cellular structures* [80,181]. This approach relies on advanced metrological techniques such as the μCT system to evaluate the morphology of the fabricated structures. The acquired data can be analyzed statistically to measure the defects [88] and imported into powerful simulation tools such as FE and CAD softwares to calculate the mechanical properties to be compared with the expected properties to quantify the effect of defects [149].

1.6 References

[1] Wang X, Xu S, Zhou S, Xu W, Leary M, Choong P, Qian M, Brandt M, Min Y. Biomaterials Topological design and additive manufacturing of porous metals for bone scaffolds and orthopaedic implants : A review. Biomaterials 2016;83:127–41. doi:10.1016/j.biomaterials.2016.01.012.

[2] Wu S, Liu X, Yeung KWK, Liu C, Yang X. Biomimetic porous scaffolds for bone tissue engineering. Mater Sci Eng R 2014;80:1–36. doi:10.1016/j.mser.2014.04.001.

[3] Wang X, Nyman JS, Dong X, Leng H, Reyes M. Fundamental Biomechanics in Bone Tissue Engineering. Morgan & Claypool; 2010.

[4] Cowin SC. Bone Mechanics Handbook. Second. CRC press; 2001.

[5] Tortora GJ, Derrickson B. Principles of anatomy & physiology. 13th ed. John Wiley & Sons, Inc.; 2012.

[6] Hing KA. Bone repair in the twenty − first century : biology , chemistry or engineering ? Philos Trans R Soc A Math Phys Eng Sci 2004;362:2821–50. doi:10.1098/rsta.2004.1466.

[7] Gibson LJ, Ashby MF, Harley BA. Cellular materials in nature and medicine. Cambridge University Press; 2010.

[8] Marieb EN, Hoehn K. Human Anatomy & Physiology. 9th ed. Pearson

Education; 2013.
[9] Gibson LJ, Ashby MF. Cellular Solids - Structure and Properties. Cambridge University Press; 2 edition; 1999.
[10] Currey JD. The structure and mechanics of bone. J Mater Sci 2012;47:41–54. doi:10.1007/s10853-011-5914-9.
[11] Voo L, Armand M, Kleinberger M. Stress fracture risk analysis of the human femur based on computational biomechanics. Johns Hopkins APL Tech Dig (Applied Phys Lab 2004;25:223–30.
[12] Williams DF. On the mechanisms of biocompatibility. Biomaterials 2008;29:2941–53. doi:10.1016/j.biomaterials.2008.04.023.
[13] Park J, Lakes RS. Biomaterials. Third Edit. Springer; 2007.
[14] Zhao P, Gu H, Mi H, Rao C, Fu J, Turng L sheng. Fabrication of scaffolds in tissue engineering: A review. Front Mech Eng 2018;13:107–19. doi:10.1007/s11465-018-0496-8.
[15] Ryan G, Pandit A, Apatsidis DP. Fabrication methods of porous metals for use in orthopaedic applications. Biomaterials 2006;27:2651–70. doi:10.1016/j.biomaterials.2005.12.002.
[16] Williams DF. On the nature of biomaterials. Biomaterials 2009;30:5897–909. doi:10.1016/j.biomaterials.2009.07.027.
[17] Williams DF. General concepts of biocompatibility. In: Murphy W, Black J, Hastings G, editors. Handb. Biomater. Prop. 2nd Editio, Springer; 2016.
[18] Vert M. Polymeric biomaterials: Strategies of the past vs. strategies of the future. Prog Polym Sci 2007;32:755–61. doi:10.1016/j.progpolymsci.2007.05.006.
[19] Teo AJT, Mishra A, Park I, Kim YJ, Park WT, Yoon YJ. Polymeric Biomaterials for Medical Implants and Devices. ACS Biomater Sci Eng 2016;2:454–72. doi:10.1021/acsbiomaterials.5b00429.
[20] Wang X, Nyman JS, Dong X, Leng H, Reyes M. Fundamental Biomechanics in Bone Tissue Engineering. vol. 2. 2010. doi:10.2200/S00246ED1V01Y200912TIS004.
[21] Ambrose CG, Harline BE, Clanton TO, Lowe WR, McGarvey WC. Polymers in Orthopaedic Surgery. In: Puoci F, editor. Adv. Polym. Med., Springer; 2015, p. 129–45.
[22] Albrektsson TO. Hard tissue response. In: Murphy W, Black J, Hastings G, editors. Handb. Biomater. Prop. 2nd Editio, Springer; 2016.
[23] Li J, Hastings GW. Oxide Bioceramics: Inert Ceramic Materials in Medicine and Dentistry. In: Murphy W, Black J, Hastings G, editors. Handb. Biomater. Prop. 2nd Editio, Springer; 2016.
[24] Hench LL, Kokubo T. Properties of Bioactive Glasses and Glass-ceramics. In: Murphy W, Black J, Hastings G, editors. Handb. Biomater. Prop. 2nd Editio, Springer; 2016.
[25] Breme H, Biehl V, Reger N, Gawalt E. Metallic Biomaterials: Introduction. In: Murphy W, Black J, Haastings G, editors. Handb. Biomater. Prop., Elsevier; 2016.
[26] Murphy W, Black J, Hastings G, editors. Handbook of Biomaterial Properties. Second Edi. Springer; 2016. doi:10.1016/S0168-3659(99)00208-4.
[27] Epinette J-A, Manley MT, editors. Fifteen Years of Clinical Experience with

Hydroxyapatite Coatings in Joint Arthroplasty. Springer; 2007.
[28] Yao Z, Lin T-H, Pajarinen J, Sato T, Goodman S. Host Response to Orthopedic Implants (Metals and Plastics). In: Badylak S, editor. Host Response to Biomater., Elsevier; 2015.
[29] Goosen JHM, Kums AJ, Kollen BJ, Verheyen CCPM. Porous-coated femoral components with or without hydroxyapatite in primary uncemented total hip arthroplasty: A systematic review of randomized controlled trials. Arch Orthop Trauma Surg 2009;129:1165–9. doi:10.1007/s00402-008-0749-9.
[30] Bose S, Tarafde S, Bandyopadhyay A. Hydroxyapatite coatings for metallic implants. In: Mucalo M, editor. Hydroxyapatite Biomed. Appl., Elsevier Ltd; 2015.
[31] Manley MT, Sutton K, Dumbleton J. Calcium Phosphates: A Survey of the Orthopaedic Literature. In: Epinette J-A, Manley MT, editors. Fifteen Years Clin. Exp. with Hydroxyapatite Coatings Jt. Arthroplast., Springer; 2004.
[32] Park S-H, Llinás A, Goel VK, Keller JC. Hard Tissue Replacement. In: Bronzino JD, editor. Biomed. Eng. Fundam. 3d Edition, Taylor & Francis; 2006.
[33] Anderson JM. Soft tissue response. In: Murphy W, Black J, Hastings G, editors. Handb. Biomater. Prop. 2nd Editio, Springer; 2016.
[34] Ratner BD. The Biocompatibility of Implant Materials. In: Badylak SF, editor. Host Response to Biomater., Elsevier Inc.; 2015.
[35] Badylak SF, editor. HOST RESPONSE TO BIOMATERIALS. Elsevier Inc.; 2015.
[36] Learmonth ID, Young C, Rorabeck C, Bs B. The operation of the century : total hip replacement. Lancet 2007;370:1508–19. doi:10.1016/S0140-6736(07)60457-7.
[37] Wechter J, Comfort TK, Tatman P, Mehle S, Gioe TJ. Improved survival of uncemented versus cemented femoral stems in patients aged < 70 years in a community total joint registry. Clin Orthop Relat Res 2013;471:3588–95. doi:10.1007/s11999-013-3182-5.
[38] Albrektsson T, Johansson C. Osteoinduction, osteoconduction and Osseointegration. J Eur Spine 2001;10:96–101. doi:10.1007/s005860100282.
[39] Huiskes R, Stolk J. Biomechanics and Preclinical Testing of Artificial Joints: The Hip. In: Mow VC, Huiskes R, editors. Basic Orthop. Biomech. Mechano-biology. 3d Edition, Lippincott Williams & Wilkins; 2005.
[40] Mow VC, Huiskes R, editors. Basic Orthopaedic Biomechanics and Mechano-Biology. 3d Edition. Lippincott Williams & Wilkins; 2005.
[41] Bergmann G, Graichen F, Rohlmann A, Bender A, Heinlein B, Duda GN, Heller MO, Morlock MM. Realistic loads for testing hip implants 2010;20:65–75. doi:10.3233/BME-2010-0616.
[42] Taylor SJG, Walker PS. Forces and moments telemetered from two distal femoral replacements during various activities 2001;34:839–48.
[43] Duda GN, Schneider E, Chaot EYS, Section B. Internal forces and moments in the femur during walking. Brand 1997;30:933–41.
[44] Taylor M, Tanner K, Freeman M, Yettram A. Stress and strain distribution within the intact femur: compression or bending? Med Eng Phys

1996;18:122–31. doi:1350453395000313 [pii].
[45] Lu T, Taylor SJG, Connor JJO, Walker PS. Influence of muscle activity on the forces in the femur: an in-vivo study. J Biomech 1997;30:1101–6.
[46] Affatato S. Perspectives in Total Hip Arthroplasty. Elsevier; 2014.
[47] Goodship AE, Cunningham JL. Pathophysiology of Functional Adaptation of Bone in Remodeling and Repair in Vivo. In: Cowin SC, editor. Bone Mech. Handb. 2nd Editio, CRC press; 2001.
[48] Bobyn JD, Tanzer M, Glassman AH. Stress-Related Bone Resorption. In: Shanbhag A, Rubash HE, Jacobs JJ, editors. Jt. Replace. Bone Resorpt. Pathol. Biomater. Clin. Pract., Taylor & Francis; 2005.
[49] Sumner DR. Long-term implant fi xation and stress-shielding in total hip replacement. J Biomech 2015;48:797–800. doi:10.1016/j.jbiomech.2014.12.021.
[50] Glassman AH, Bobyn JD, Tanzer M. New femoral designs: Do they influence stress shielding? Clin Orthop Relat Res 2006:64–74. doi:10.1097/01.blo.0000246541.41951.20.
[51] Huiskes R, Weinans H, Dalstra M. Adaptive bone remodeling and biomechanical design considerations : for noncemented total hip arthroplasty. Orthopedics 1989;12:1255–67.
[52] Kuiper JH, Huiskes R. Mathematical Optimization of Elastic Properties : Application to Cementless Hip Stem Design 1997;119:166–74.
[53] Sola A, Bellucci D, Cannillo V. Functionally graded materials for orthopedic applications – an update on design and manufacturing 2016;34:504–31. doi:10.1016/j.biotechadv.2015.12.013.
[54] Arabnejad S, Johnston B, Tanzer M, Pasini D. Fully Porous 3D Printed Titanium Femoral Stem to Reduce Stress-Shielding Following Total Hip Arthroplasty 2016:29–31. doi:10.1002/jor.23445.
[55] Moussa A, Tanzer M, Pasini D. Cervical fusion cage computationally optimized with porous architected Titanium for minimized subsidence. J Mech Behav Biomed Mater 2018;85:134–51. doi:10.1016/j.jmbbm.2018.05.040.
[56] Wang Y, Arabnejad S, Tanzer M, Pasini D. Hip Implant Design With Three-Dimensional Porous Architecture of Optimized Graded Density. J Mech Des 2018;140:1–13. doi:10.1115/1.4041208.
[57] Cristofolini L. A critical analysis of stress shielding evaluation of hip prosthesis. Crit Rev Biomed Eng 1997;25:409–83.
[58] Blanchard CR, Medlin DJ, Shetty R. Advances in Metals. In: Shanbhag A, Rubash HE, Jacobs JJ, editors. Jt. Replace. Bone Resorpt. Pathol. Biomater. Clin. Pract., Taylor & Francis; 2005.
[59] Levine B. A new era in porous metals: Applications in orthopaedics. Adv Eng Mater 2008;10:788–92. doi:10.1002/adem.200800215.
[60] Murr LE, Gaytan SM, Medina F, Lopez MI, Martinez E, Wicker RB. Additive Layered Manufacturing of Reticulated Ti-6Al-4V Biomedical Mesh Structures by Electron Beam Melting 2009:23–8.
[61] Murr LE, Gaytan SM, Medina F, Lopez H, Martinez E, MacHado BI, Hernandez DH, Martinez L, Lopez MI, Wicker RB, Bracke J. Next-generation biomedical implants using additive manufacturing of complex cellular and functional mesh arrays. Philos Trans R Soc A Math Phys Eng

Sci 2010;368:1999–2032. doi:10.1098/rsta.2010.0010.
[62] Harrysson OLA, Cansizoglu O, Marcellin-Little DJ, Cormier DR, West HA. Direct metal fabrication of titanium implants with tailored materials and mechanical properties using electron beam melting technology. Mater Sci Eng C 2008;28:366–73. doi:10.1016/j.msec.2007.04.022.
[63] Ashby MF. The properties of foams and lattices. Philos Trans R Soc A Math Phys Eng Sci 2006;364:15–30. doi:10.1098/rsta.2005.1678.
[64] Fleck NA, Deshpande VS, Ashby MF. Micro-architectured materials: Past, present and future. Proc R Soc A Math Phys Eng Sci 2010;466:2495–516. doi:10.1098/rspa.2010.0215.
[65] Gibson LJ. Mechanical behavior of metallic foams. Annu Rev Mater Sci 2000;30:191–227.
[66] Smith M, Guan Z, Cantwell WJ. Finite element modelling of the compressive response of lattice structures manufactured using the selective laser melting technique. Int J Mech Sci 2013;67:28–41. doi:10.1016/j.ijmecsci.2012.12.004.
[67] Deshpande VS, Ashby MF, Fleck NA. Foam topology: Bending versus stretching dominated architectures. Acta Mater 2001;49:1035–40. doi:10.1016/S1359-6454(00)00379-7.
[68] Simone AE, Gibson LJ. Effects of solid distribution on the stiffness and strength of metallic foams. Acta Mater 1998;46:2139–50. doi:10.1007/s11069-011-9918-1.
[69] Kadkhodapour J, Montazerian H, Darabi AC, Anaraki AP, Ahmadi SM, Zadpoor AA, Schmauder S. Failure mechanisms of additively manufactured porous biomaterials: Effects of porosity and type of unit cell. J Mech Behav Biomed Mater 2015;50:180–91. doi:10.1016/j.jmbbm.2015.06.012.
[70] Qiu C, Yue S, Adkins NJE, Ward M, Hassanin H, Lee PD, Withers PJ, Attallah MM. Influence of processing conditions on strut structure and compressive properties of cellular lattice structures fabricated by selective laser melting. Mater Sci Eng A 2015;628:188–97. doi:10.1016/j.msea.2015.01.031.
[71] Ahmadi SM, Yavari SA, Wauthle R, Pouran B, Schrooten J, Weinans H, Zadpoor AA. Additively manufactured open-cell porous biomaterials made from six different space-filling unit cells: The mechanical and morphological properties. Materials (Basel) 2015;8:1871–96. doi:10.3390/ma8041871.
[72] Hollister SJ, Kikuchi N. A comparison of homogenization and standard mechanics analyses for periodic porous composites. Comput Mech 1992;10:73–95.
[73] Shahzamanian MM, Tadepalli T, Rajendran AM, Hodo WD, Mohan R, Valisetty R, Chung PW, Ramsey JJ. Representative Volume Element Based Modeling of Cementitious Materials. J Eng Mater Technol 2014;136:1–16. doi:10.1115/1.4025916.
[74] Hashin Z. Analysis of Composite Materials — A Survey. J Appl Mech 1983;50:481–505.
[75] Gibson LJ, Ashby MF, Schajer GS, Robertson CI. The mechanics of two-dimensional cellular materials. Proc R Soc A Math Phys Eng Sci 1982;382:25–42.

[76] Wang A, Mcdowell DL. In-Plane Stiffness and Yield Strength of Periodic Metal. J Eng Mater Technol 2004;126:137–56. doi:10.1115/1.1646165.
[77] Arabnejad S, Pasini D. Mechanical properties of lattice materials via asymptotic homogenization and comparison with alternative homogenization methods. Int J Mech Sci 2013;77:249–62. doi:10.1016/j.ijmecsci.2013.10.003.
[78] Kim HS, Al-hassani STS. A morphological elastic model of general hexagonal columnar structures. Int J Mech Sci 2001;43:1027–60.
[79] Warren WE, Kraynik AM. Foam mechanics: the linear elastic response of two-dimensional spatiallly periodic cellular materials. Mech Mater 1987;6:27–37. doi:10.1016/0167-6636(87)90020-2.
[80] Dong G, Tang Y, Zhao YF. A Survey of Modeling of Lattice Structures Fabricated by Additive Manufacturing. J Mech Des 2017;139:1–13. doi:10.1115/1.4037305.
[81] Hassani B, Hinton E. A review of homogenization and topology optimization IÐhomogenization theory for media with periodic structure 1998;69:707–17.
[82] Hassani B, Hinton E. A review of homogenization and topology opimization II - analytical and numerical solution of homogenization equations. Comput Struct 1998;69:719–38.
[83] Masoumi Khalil Abad E, Arabnejad Khanoki S, Pasini D. Fatigue design of lattice materials via computational mechanics: Application to lattices with smooth transitions in cell geometry. Int J Fatigue 2013;47:126–36. doi:10.1016/j.ijfatigue.2012.08.003.
[84] Khanoki SA, Pasini D. Multiscale Design and Multiobjective Optimization of Orthopedic Hip Implants with Functionally Graded Cellular Material. J Biomech Eng 2012;134:1–10. doi:10.1115/1.4006115.
[85] Smith M, Guan Z, Cantwell WJ. Finite element modelling of the compressive response of lattice structures manufactured using the selective laser melting technique. Int J Mech Sci 2013;67:28–41. doi:10.1016/j.ijmecsci.2012.12.004.
[86] Luxner MH, Stampfl J, Pettermann HE. Finite element modeling concepts and linear analyses of 3D regular open cell structures. J Mater Sci 2005;40:5859–66. doi:10.1007/s10853-005-5020-y.
[87] Zhu HX, Thorpe SM, Windle AH. The effect of cell irregularity on the high strain compression of 2D Voronoi honeycombs. Int J Solids Struct 2006;43:1061–78. doi:10.1016/j.ijsolstr.2005.05.008.
[88] Liu L, Kamm P, García-Moreno F, Banhart J, Pasini D. Elastic and failure response of imperfect three-dimensional metallic lattices: the role of geometric defects induced by Selective Laser Melting. J Mech Phys Solids 2017;107:160–84. doi:10.1016/j.jmps.2017.07.003.
[89] Campoli G, Borleffs MS, Amin Yavari S, Wauthle R, Weinans H, Zadpoor AA. Mechanical properties of open-cell metallic biomaterials manufactured using additive manufacturing. Mater Des 2013;49:957–65. doi:10.1016/j.matdes.2013.01.071.
[90] Latture RM, Rodriguez RX, Holmes LR, Zok FW. Effects of nodal fillets and external boundaries on compressive response of an octet truss. Acta Mater 2018;149:78–87. doi:10.1016/j.actamat.2017.12.060.

[91] Alkhader M, Vural M. Mechanical response of cellular solids: Role of cellular topology and microstructural irregularity. Int J Eng Sci 2008;46:1035–51. doi:10.1016/j.ijengsci.2008.03.012.

[92] Zargarian A, Esfahanian M, Kadkhodapour J, Ziaei-Rad S. Numerical simulation of the fatigue behavior of additive manufactured titanium porous lattice structures. Mater Sci Eng C 2016;60:339–47. doi:10.1016/j.msec.2015.11.054.

[93] Hedayati R, Hosseini-toudeshky H, Sadighi M, Mohammadi-aghdam M, Zadpoor AA. Computational prediction of the fatigue behavior of additively manufactured porous metallic biomaterials 2016;84:67–79. doi:10.1016/j.ijfatigue.2015.11.017.

[94] Kim HS, Al-hassani STS. Effective elastic constants of two-dimensional cellular materials with deep and thick cell walls. Int J Mech Sci 2003;45:1999–2016. doi:10.1016/j.ijmecsci.2004.02.002.

[95] Webb DC, Kormi K, Al-Hassani STS. Use of FEM in performance assessment of perforated plates subject to general loading conditions. Int J Press Vessel Pip 1995;64:137–52. doi:10.1016/0308-0161(94)00078-W.

[96] Zargarian A, Esfahanian M, Kadkhodapour J, Ziaei-Rad S. Effect of solid distribution on elastic properties of open-cell cellular solids using numerical and experimental methods. J Mech Behav Biomed Mater 2014;37:264–73. doi:10.1016/j.jmbbm.2014.05.018.

[97] Cahill S, Lohfeld S, McHugh PE. Finite element predictions compared to experimental results for the effective modulus of bone tissue engineering scaffolds fabricated by selective laser sintering. J Mater Sci Mater Med 2009;20:1255–62. doi:10.1007/s10856-009-3693-5.

[98] Hazlehurst K, Wang CJ, Stanford M. Evaluation of the stiffness characteristics of square pore CoCrMo cellular structures manufactured using laser melting technology for potential orthopaedic applications. J Mater 2013;51:949–55. doi:10.1016/j.matdes.2013.05.009.

[99] Cuadrado A, Yánez A, Martel O, Deviaene S, Monopoli D. Influence of load orientation and of types of loads on the mechanical properties of porous Ti6Al4V biomaterials. Mater Des 2017;135:309–18. doi:10.1016/j.matdes.2017.09.045.

[100] Hedayati R, Janbaz S, Sadighi M, Mohammadi-Aghdam M, Zadpoor AA. How does tissue regeneration influence the mechanical behavior of additively manufactured porous biomaterials? J Mech Behav Biomed Mater 2017;65:831–41. doi:10.1016/j.jmbbm.2016.10.003.

[101] Veyhl C, Belova I V., Murch GE, Fiedler T. Finite element analysis of the mechanical properties of cellular aluminium based on micro-computed tomography. Mater Sci Eng A 2011;528:4550–5. doi:10.1016/j.msea.2011.02.031.

[102] Xiao L, Song W, Wang C, Tang H, Fan Q, Liu N, Wang J. Mechanical properties of open-cell rhombic dodecahedron titanium alloy lattice structure manufactured using electron beam melting under dynamic loading. Int J Impact Eng 2017;100:75–89. doi:10.1016/j.ijimpeng.2016.10.006.

[103] Gibson I, Rosen D, Stucker B. Additive manufacturing technologies: 3D printing, rapid prototyping, and direct digital manufacturing, second edition.

2015. doi:10.1007/978-1-4939-2113-3.
[104] Herzog D, Seyda V, Wycisk E, Emmelmann C. Additive manufacturing of metals. Acta Mater 2016;117:371–92. doi:10.1016/j.actamat.2016.07.019.
[105] Milewski JO. Additive Manufacturing of Metals. Springer; 2017. doi:10.1007/978-3-319-58205-4.
[106] Frazier WE. Metal additive manufacturing: A review. J Mater Eng Perform 2014;23:1917–28. doi:10.1007/s11665-014-0958-z.
[107] Tan XP, Tan YJ, Chow CSL, Tor SB, Yeong WY. Metallic powder-bed based 3D printing of cellular scaffolds for orthopaedic implants: A state-of-the-art review on manufacturing, topological design, mechanical properties and biocompatibility. Mater Sci Eng C 2017;76:1328–43. doi:10.1016/j.msec.2017.02.094.
[108] Murr LE, Gaytan SM, Ramirez DA, Martinez E, Hernandez J, Amato KN, Shindo PW, Medina FR, Wicker RB. Metal Fabrication by Additive Manufacturing Using Laser and Electron Beam Melting Technologies. J Mater Sci Technol 2012;28:1–14. doi:10.1016/S1005-0302(12)60016-4.
[109] Sing SL, An J, Yeong WY, Wiria FE. Laser and electron-beam powder-bed additive manufacturing of metallic implants: A review on processes, materials and designs. J Orthop Res 2016;34:369–85. doi:10.1002/jor.23075.
[110] Tan XP, Tan YJ, Chow CSL, Tor SB, Yeong WY. Metallic powder-bed based 3D printing of cellular scaffolds for orthopaedic implants: A state-of-the-art review on manufacturing, topological design, mechanical properties and biocompatibility. Mater Sci Eng C 2017;76:1328–43. doi:10.1016/j.msec.2017.02.094.
[111] Dutta B, Froes FH. Additive manufacturing of titanium alloys. Addit Manuf Handb Prod Dev Def Ind 2017;00:263–74. doi:10.1201/9781315119106.
[112] Long M, Rack HJ. Titanium alloys in total joint replacement - A materials science perspective. Biomaterials 1998;19:1621–39. doi:10.1016/S0142-9612(97)00146-4.
[113] Rack HJ, Qazi JI. Titanium alloys for biomedical applications. Mater Sci Eng C 2006;26:1269–77. doi:10.1007/978-3-662-46836-4_8.
[114] Breme J, Eisenbarth E, Biehl V. Titanium and its Alloys for Medical Applications. In: Leyens C, Peters M, editors. Titan. Titan. Alloy. Fundam. Appl., Wiley; 2003.
[115] Park JB, Kim YK. Metallic Biomaterials. In: Bronzino JD, editor. Biomed. Eng. Fundam. 3d Edition, Taylor & Francis; 2006.
[116] Leyens C, Peters M, editors. Titanium and Titanium Alloys. WILEY-VCH; 2003.
[117] Luetjering G, Williams JC. Titanium. 2nd editio. Springer; 2007.
[118] Brunette DM, Tengvall P, Textor M, Thomsen P, editors. Titanium in Medicine. Material Science, Surface Science, Engineering, Biological Responses and Medical Applications. Springer; 2001.
[119] Niinomi M. Mechanical properties of biomedical titanium alloys. Mater Sci Eng A 1998;243:231–6. doi:10.1016/S0921-5093(97)00806-X.
[120] Breme H, Biehl V, Reger N, Gawalt E. Metallic Biomaterials: Titanium and Titanium Alloys. In: Murphy W, Black J, Hastings G, editors. Handb. Biomater. Prop. 2nd Editio, Springer; 2016.

[121] Peters M, Hemptenmacher J, Kumpfert J, Leyens C. Structure and Properties of Titanium and Titanium Alloys. In: Leyens C, Peters M, editors. Titan. Titan. Alloy. Fundam. Appl., Wiley; 2003.
[122] Dallago M, Fontanari V, Torresani E, Leoni M, Pederzolli C, Potrich C, Benedetti M. Fatigue and biological properties of Ti-6Al-4V ELI cellular structures with variously arranged cubic cells made by selective laser melting. J Mech Behav Biomed Mater 2018;78:381–94. doi:10.1016/j.jmbbm.2017.11.044.
[123] Freese HL, Volas MG, Wood JR. Metallurgy and Technological Properties of Titanium and Titanium Alloys. In: Brunette D, Tengvall P, Textor M, Thomsen P, editors. Titan. Med., Springer; 2001.
[124] Benedetti M, Torresani E, Leoni M, Fontanari V, Bandini M, Pederzolli C, Potrich C. The effect of post-sintering treatments on the fatigue and biological behavior of Ti-6Al-4V ELI parts made by selective laser melting. vol. 71. 2017. doi:10.1016/j.jmbbm.2017.03.024.
[125] Wagner L, Bigoney JK. Fatigue of Titanium Alloys. In: Leyens C, Peters M, editors. Titan. Titan. Alloy. Fundam. Appl., WILEY-VCH; 2003.
[126] Zhao X, Li S, Zhang M, Liu Y, Sercombe TB, Wang S, Hao Y, Yang R, Murr LE. Comparison of the microstructures and mechanical properties of Ti-6Al-4V fabricated by selective laser melting and electron beam melting. Mater Des 2016;95:21–31. doi:10.1016/j.matdes.2015.12.135.
[127] Murr LE. Metallurgy of additive manufacturing: Examples from electron beam melting. Addit Manuf 2015;5:40–53. doi:10.1016/j.addma.2014.12.002.
[128] Zhao S, Li SJ, Hou WT, Hao YL, Yang R, Murr LE. Microstructure and mechanical properties of open cellular Ti–6Al–4V prototypes fabricated by electron beam melting for biomedical applications. Mater Technol 2016;7857:1–10. doi:10.1179/1753555715Y.0000000056.
[129] Thijs L, Verhaeghe F, Craeghs T, Humbeeck J Van, Kruth JP. A study of the microstructural evolution during selective laser melting of Ti-6Al-4V. Acta Mater 2010;58:3303–12. doi:10.1016/j.actamat.2010.02.004.
[130] Vilaro T, Colin C, Bartout JD. As-fabricated and heat-treated microstructures of the Ti-6Al-4V alloy processed by selective laser melting. Metall Mater Trans A Phys Metall Mater Sci 2011;42:3190–9. doi:10.4997/JRCPE.2017.305.
[131] Rashed MG, Ashraf M, Mines RAW, Hazell PJ. Metallic microlattice materials: A current state of the art on manufacturing, mechanical properties and applications. Mater Des 2016;95:518–33. doi:10.1016/j.matdes.2016.01.146.
[132] Zadpoor AA. Design for Additive Bio-Manufacturing : From Patient-Specific Medical Devices to Rationally Designed Meta-Biomaterials. Int J Mol Sci 2017;18:1–18. doi:10.3390/ijms18081607.
[133] Campanelli SL, Contuzzi N, Ludovico AD, Caiazzo F, Cardaropoli F, Sergi V. Manufacturing and characterization of Ti6Al4V lattice components manufactured by selective laser melting. Materials (Basel) 2014;7:4803–22. doi:10.3390/ma7064803.
[134] Zadpoor AA, Hedayati R. Analytical relationships for prediction of the mechanical properties of additively manufactured porous biomaterials. J

Biomed Mater Res - Part A 2016;104:3164–74. doi:10.1002/jbm.a.35855.
[135] Bagheri ZS, Melancon D, Liu L, Johnston RB, Pasini D. Compensation strategy to reduce geometry and mechanics mismatches in porous biomaterials built with Selective Laser Melting. J Mech Behav Biomed Mater 2017;70:17–27. doi:10.1016/j.jmbbm.2016.04.041.
[136] Zadpoor AA. Mechanics of additively manufactured biomaterials. J Mech Behav Biomed Mater 2017;70:1–6. doi:10.1016/j.jmbbm.2017.03.018.
[137] Weißmann V, Bader R, Hansmann H, Laufer N. Influence of the structural orientation on the mechanical properties of selective laser melted Ti6Al4V open-porous scaffolds. Mater Des 2016;95:188–97. doi:10.1016/j.matdes.2016.01.095.
[138] Weißmann V, Drescher P, Bader R, Seitz H, Hansmann H, Laufer N. Comparison of Single Ti6Al4V Struts Made Using Selective Laser Melting and Electron Beam Melting Subject to Part Orientation. Metals (Basel) 2017;7:91. doi:10.3390/met7030091.
[139] Wauthle R, Vrancken B, Beynaerts B, Jorissen K, Schrooten J, Kruth JP, Van Humbeeck J. Effects of build orientation and heat treatment on the microstructure and mechanical properties of selective laser melted Ti6Al4V lattice structures. Addit Manuf 2015;5:77–84. doi:10.1016/j.addma.2014.12.008.
[140] Sallica-Leva E, Jardini AL, Fogagnolo JB. Microstructure and mechanical behavior of porous Ti-6Al-4V parts obtained by selective laser melting. J Mech Behav Biomed Mater 2013;26:98–108. doi:10.1016/j.jmbbm.2013.05.011.
[141] Van Bael S, Kerckhofs G, Moesen M, Pyka G, Schrooten J, Kruth JP. Micro-CT-based improvement of geometrical and mechanical controllability of selective laser melted Ti6Al4V porous structures. Mater Sci Eng A 2011;528:7423–31. doi:10.1016/j.msea.2011.06.045.
[142] de Formanoir C, Suard M, Dendievel R, Martin G, Godet S. Improving the mechanical efficiency of electron beam melted titanium lattice structures by chemical etching. Addit Manuf 2016;11:71–6. doi:10.1016/j.addma.2016.05.001.
[143] Parthasarathy J, Starly B, Raman S, Christensen A. Mechanical evaluation of porous titanium (Ti6Al4V) structures with electron beam melting (EBM). J Mech Behav Biomed Mater 2010;3:249–59. doi:10.1016/j.jmbbm.2009.10.006.
[144] Sing SL, Wiria FE, Yeong WY. Selective laser melting of lattice structures: A statistical approach to manufacturability and mechanical behavior. Robot Comput Integr Manuf 2018;49:170–80. doi:10.1016/j.rcim.2017.06.006.
[145] Takano N, Takizawa H, Wen P, Odaka K, Matsunaga S, Abe S. Stochastic prediction of apparent compressive stiffness of selective laser sintered lattice structure with geometrical imperfection and uncertainty in material property. Int J Mech Sci 2017;134:347–56. doi:10.1016/j.ijmecsci.2017.08.060.
[146] Speirs M, Van Humbeeck J, Schrooten J, Luyten J, Kruth JP. The effect of pore geometry on the mechanical properties of selective laser melted Ti-13Nb-13Zr scaffolds. Procedia CIRP 2013;5:79–82. doi:10.1016/j.procir.2013.01.016.

[147] Yan C, Hao L, Hussein A, Raymont D. Evaluations of cellular lattice structures manufactured using selective laser melting. Int J Mach Tools Manuf 2012;62:32–8. doi:10.1016/j.ijmachtools.2012.06.002.
[148] Pyka G, Kerckhofs G, Papantoniou I, Speirs M, Schrooten J, Wevers M. Surface roughness and morphology customization of additive manufactured open porous Ti6Al4V structures. Materials (Basel) 2013;6:4737–57. doi:10.3390/ma6104737.
[149] Melancon D, Bagheri ZS, Johnston RB, Liu L, Tanzer M, Pasini D. Mechanical characterization of structurally porous biomaterials built via additive manufacturing: experiments, predictive models, and design maps for load-bearing bone replacement implants. Acta Biomater 2017;63:350–68. doi:10.1016/j.actbio.2017.09.013.
[150] Gong H, Rafi K, Gu H, Janaki Ram GD, Starr T, Stucker B. Influence of defects on mechanical properties of Ti-6Al-4V components produced by selective laser melting and electron beam melting. Mater Des 2015;86:545–54. doi:10.1016/j.matdes.2015.07.147.
[151] Lhuissier P, de Formanoir C, Martin G, Dendievel R, Godet S. Geometrical control of lattice structures produced by EBM through chemical etching: Investigations at the scale of individual struts. Mater Des 2016;110:485–93. doi:10.1016/j.matdes.2016.08.029.
[152] Qiu C, Adkins NJE, Attallah MM. Microstructure and tensile properties of selectively laser-melted and of HIPed laser-melted Ti-6Al-4V. Mater Sci Eng A 2013;578:230–9. doi:10.1016/j.msea.2013.04.099.
[153] Yan C, Hao L, Hussein A, Young P, Raymont D. Advanced lightweight 316L stainless steel cellular lattice structures fabricated via selective laser melting. Mater Des 2014;55:533–41. doi:10.1016/j.matdes.2013.10.027.
[154] Suard M, Martin G, Lhuissier P, Dendievel R, Vignat F, Blandin JJ, Villeneuve F. Mechanical equivalent diameter of single struts for the stiffness prediction of lattice structures produced by Electron Beam Melting. Addit Manuf 2015;8:124–31. doi:10.1016/j.addma.2015.10.002.
[155] Mullen L, Stamp RC, Brooks WK, Jones E, Sutcliffe CJ. Selective laser melting: A Regular Unit Cell Approach for the Manufacture of Porous, Titanium, Bone In-Growth Constructs, Suitable for Orthopedic Applications. J Biomed Mater Res - Part B Appl Biomater 2009;89B:325–34. doi:10.1002/jbm.b.31504.
[156] Kessler J, Balc N, Gebhardt A, Abbas K. Basic design rules of unit cells for additive manufactured lattice structures. MATEC Web Conf 2017;137. doi:10.1007/BF01171954.
[157] Kranz J, Herzog D, Emmelmann C. Design guidelines for laser additive manufacturing of lightweight structures in TiAl6V4. J Laser Appl 2015;27:S14001. doi:10.2351/1.4885235.
[158] Calignano F. Design optimization of supports for overhanging structures in aluminum and titanium alloys by selective laser melting. J Mater 2014;64:203–13. doi:10.1016/j.matdes.2014.07.043.
[159] Zhu Z, Anwer N, Mathieu L. Deviation Modeling and Shape Transformation in Design for Additive Manufacturing. Procedia CIRP 2017;60:211–6. doi:10.1016/j.procir.2017.01.023.
[160] Torries B, Imandoust A, Beretta S, Shao S, Shamsaei N. Overview on

Microstructure- and Defect-Sensitive Fatigue Modeling of Additively Manufactured Materials. Jom 2018;70:1853–62. doi:10.1007/s11837-018-2987-9.

[161] Amin Yavari S, Wauthle R, Van Der Stok J, Riemslag AC, Janssen M, Mulier M, Kruth JP, Schrooten J, Weinans H, Zadpoor AA. Fatigue behavior of porous biomaterials manufactured using selective laser melting. Mater Sci Eng C 2013;33:4849–58. doi:10.1016/j.msec.2013.08.006.

[162] Zhao S, Li SJ, Hou WT, Hao YL, Yang R, Misra RDK. The influence of cell morphology on the compressive fatigue behavior of Ti-6Al-4V meshes fabricated by electron beam melting. J Mech Behav Biomed Mater 2016;59:251–64. doi:10.1016/j.jmbbm.2016.01.034.

[163] Van Hooreweder B, Apers Y, Lietaert K, Kruth JP. Improving the fatigue performance of porous metallic biomaterials produced by Selective Laser Melting. Acta Biomater 2017;47:193–202. doi:10.1016/j.actbio.2016.10.005.

[164] de Krijger J, Rans C, Van Hooreweder B, Lietaert K, Pouran B, Zadpoor AA. Effects of applied stress ratio on the fatigue behavior of additively manufactured porous biomaterials under compressive loading. J Mech Behav Biomed Mater 2017;70:7–16. doi:10.1016/j.jmbbm.2016.11.022.

[165] Amin Yavari S, Ahmadi SM, Wauthle R, Pouran B, Schrooten J, Weinans H, Zadpoor AA. Relationship between unit cell type and porosity and the fatigue behavior of selective laser melted meta-biomaterials. J Mech Behav Biomed Mater 2015;43:91–100. doi:10.1016/j.jmbbm.2014.12.015.

[166] Lipinski P, Barbas A, Bonnet AS. Fatigue behavior of thin-walled grade 2 titanium samples processed by selective laser melting. Application to life prediction of porous titanium implants. J Mech Behav Biomed Mater 2013;28:274–90. doi:10.1016/j.jmbbm.2013.08.011.

[167] Zadpoor AA. Mechanics of additively manufactured biomaterials. J Mech Behav Biomed Mater 2017;70:1–6. doi:10.1016/j.jmbbm.2017.03.018.

[168] Ren D, Li S, Wang H, Hou W, Hao Y, Jin W, Yang R. Fatigue behavior of Ti-6Al-4V cellular structures fabricated by additive manufacturing technique. J Mater Sci 2019;35:285–94.

[169] Fotovvati B, Namdari N, Dehghanghadikolaei A. Fatigue performance of selective laser melted Ti6Al4V components: State of the art. Mater Res Express 2019;6. doi:10.1088/2053-1591/aae10e.

[170] Ahmadi SM, Hedayati R, Li Y, Lietaert K, Tümer N, Fatemi A, Rans CD, Pouran B, Weinans H, Zadpoor AA. Fatigue performance of additively manufactured meta-biomaterials: The effects of topology and material type. Acta Biomater 2018;65:292–304. doi:10.1016/j.actbio.2017.11.014.

[171] Dowling NE. Mechanical Behavior of Materials. Fourth edi. Pearson Education; 2013.

[172] Vayssette B, Saintier N, Brugger C, Elmay M, Pessard E. Surface roughness of Ti-6Al-4V parts obtained by SLM and EBM: Effect on the High Cycle Fatigue life. Procedia Eng 2018;213:89–97. doi:10.1016/j.proeng.2018.02.010.

[173] Leuders S, Thöne M, Riemer A, Niendorf T, Tröster T, Richard HA, Maier HJ. On the mechanical behaviour of titanium alloy TiAl6V4 manufactured

by selective laser melting: Fatigue resistance and crack growth performance. Int J Fatigue 2013;48:300–7. doi:10.1016/j.ijfatigue.2012.11.011.

[174] Savio G, Rosso S, Curtarello A, Meneghello R, Concheri G. Implications of modeling approaches on the fatigue behavior of cellular solids. Addit Manuf 2019;25:50–8. doi:10.1016/j.addma.2018.10.047.

[175] Hedayati R, Hosseini-Toudeshky H, Sadighi M, Mohammadi-Aghdam M, Zadpoor AA. Computational prediction of the fatigue behavior of additively manufactured porous metallic biomaterials. Int J Fatigue 2016;84:67–79. doi:10.1016/j.ijfatigue.2015.11.017.

[176] Benedetti M, Torresani E, Leoni M, Fontanari V, Bandini M, Pederzolli C, Potrich C. The effect of post-sintering treatments on the fatigue and biological behavior of Ti-6Al-4V ELI parts made by selective laser melting. J Mech Behav Biomed Mater 2017;71:295–306. doi:10.1016/j.jmbbm.2017.03.024.

[177] Singh R, Lee PD, Dashwood RJ, Lindley TC. Titanium foams for biomedical applications : a review 2010;25:127–36. doi:10.1179/175355510X12744412709403.

[178] Van Bael S, Chai YC, Truscello S, Moesen M, Kerckhofs G, Van Oosterwyck H, Kruth JP, Schrooten J. The effect of pore geometry on the in vitro biological behavior of human periosteum-derived cells seeded on selective laser-melted Ti6Al4V bone scaffolds. Acta Biomater 2012;8:2824–34. doi:10.1016/j.actbio.2012.04.001.

[179] Taniguchi N, Fujibayashi S, Takemoto M, Sasaki K, Otsuki B, Nakamura T, Matsushita T, Kokubo T, Matsuda S. Effect of pore size on bone ingrowth into porous titanium implants fabricated by additive manufacturing: An in vivo experiment. Mater Sci Eng C 2016;59:690–701. doi:10.1016/j.msec.2015.10.069.

[180] Ponader S, Vairaktaris E, Heinl P, Wilmowsky C, Rottmair A, Singer RF, Holst S, Schlegel KA, Neukam FW, Nkenke E. Effects of topographical surface modifications of electron beam melted Ti-6Al-4V titanium on human fetal osteoblasts 2007. doi:10.1002/jbm.a.31540.

[181] Rosen DW. Computer-Aided Design for Additive Manufacturing of Cellular Structures 2007;4:585–94. doi:10.1080/16864360.2007.10738493.

Chapter II

The effect of filleted wall junctions on the elastic constants and on the stress concentration factors of 2D cellular structures

In this Chapter, the elastic constants and the stress concentration factor (SCF) for 2D square cell honeycombs with filleted junctions are calculated.
The elastic constants are derived for two lattices, a lattice with regular square cells and a lattice with square cells staggered of half-length of the cell wall. An analytical model based on classical beam theory is proposed to identify the effect of stretching and bending actions on the elastic constants of a single cell by applying the periodic boundary conditions. The theoretical beam model is fitted on the results from a 2D Finite Elements (FE) model based on plane elements via an extensive parametric analysis. In this way, semi-analytical formulas are proposed to calculate the elastic constants in large domains of the geometric parameters, namely the cell-wall diameter t_0 and the fillet radius R at the joints.
A numerical method is proposed for the estimation of the Stress Concentration Factors at the cell wall junctions of a 2D regular square cellular lattice. The aim is to obtain a model capable of calculating the values of the SCF as a function of the unit cell geometrical parameters. This was achieved by applying the Finite Elements (FE) method to the unit cell for wide intervals of t_0 and R to calculate the SCF for each couple of the parameters. The values of the SCFs were then fitted with some functions.
The models developed in this Chapter will be used in the next chapters as a support in the design of 3D regular square lattices and in the interpretation of the mechanical characterization.

Part of this chapter has been published in:

M. Dallago, M. Benedetti, V. Luchin and V. Fontanari,

"***Orthotropic elastic constants of 2D cellular structures with variously arranged square cells: the effect of filleted wall junctions***",
International Journal of Mechanical Sciences 122 (2017), pp. 63–78

2.1 Introduction

The advent of Additive Manufacturing gave a considerable boost to the study of cellular materials because the new 3D printing processes, such as SLM, permit to obtain products with dimensional accuracy less than 0.1 millimeter, giving the possibility of designing complex components such as lattice materials in minute details. In this way, it is possible to accurately control the local geometry of each single cell. For instance, cellular materials for structural applications require a strict control of the geometrical parameters to tailor stiffness as well as static and fatigue resistance to the specific application. While the effect of the wall thickness on these properties is often considered in the study of this material class, most authors have often neglected the fillet at the conjunction among cell walls.

The study of filleted joints in cellular materials is relevant for multiple reasons. On one hand, fillets can be unwanted, but generated due to the accumulation of parasitic mass at the joints strut in some AM processes such as SLM [1,2]. On the other, fillets can be part of the design, aimed at reducing stress concentrations [3,4]. Regardless, additional material at the joints is demonstrated [5] to affect the stiffness of the cellular solids. Shifting material away from the cell edges to the vertices increases the modulus and peak stress of the lattice by increasing the moment of inertia at the ends of the members where the bending moments are the highest.

Despite these premises, in the literature few works are aimed at developing simple design models to account for the non-uniform material distribution in the cell walls of lattice materials. To the author's best knowledge, the first to consider also cell walls of non-uniform thickness in the calculation of the elastic constants of the cellular structure were Warren et al. [6], who modeled the cell walls as tapered struts with a discontinuity in slope at the mid-span, including axial and bending deformations. Kim et al. [7] improved on the previous study by developing an analytical model based on classical beam theory to predict the elastic constants of 2D and 3D honeycombs with a continuous change in strut section thickness and by taking into account axial, bending and shear deformations. They highlight the importance of strut morphology in the calculation of the elastic constants of a cellular structure. The same authors, in a subsequent paper [8], introduce a joint stiffening factor, calculated via FE analyses, which accounts for the stiffening effect introduced by the joints between the cell walls. This factor is used to correct the analytical models based on beam theory, but in this work the struts are uniform.

Even less theoretical works on the fatigue of cellular materials can be found in the literature and thus the development of theoretical and numerical approaches is much needed to avoid the high costs of experimentation. Of the theoretical publications, most [9–11] use beam theory combined with linear elastic fracture mechanics to model the fatigue failure of open cell cellular materials. This approach is limited by the fact that it does not consider the presence of stress raisers in the structure which

are always present, at least where the cell walls are joint. Fatigue is in fact caused by the accumulation of damage at spots were concentration of stresses occurs and thus to be able to accurately predict the fatigue resistance of a structure the focus must be shifted to the local variations of the geometry [12]. The effect of the joints of the cell-wall on the stress field and their effect on the fatigue resistance of cellular structures were considered in [4]. In these papers, the curvature of the fillet at the joint was optimized to minimize the local stresses and then asymptotic homogenization was used to obtain the homogenized stiffness matrix and the fatigue strength. The stress concentration factor due to the joints and geometrical irregularities in general (roughness and variations in the cross-section of the cell-walls) was included in the approach based on numerical simulations described in [13] to estimate the fatigue life of cellular structures. This latter work is not entirely theoretical as the stress concentration factors are calculated by calibrating the numerical model on experimental results. The detrimental effect of geometrical irregularities as stress raisers on the fatigue resistance of AM metallic cellular structures has been discussed from the experimental point of view for instance in [14] and [15].

In this Chapter, the elastic constants of 2D square cell cellular materials are calculated, taking into account also the fillet radius. Two versions of this morphology have been studied: the regular square structure and the staggered square structure, which is derived from the regular square structure by offsetting every other line of squares of half the length of the cell side. These cell geometries have been selected because, in contrast to other 2D cell geometries, they have a very simple shape that allows a relatively easy transition from 2D to a 3D structure. The study is conducted by varying two cellular parameters, namely the cell wall thickness t_0 and the internal fillet radius R. Both parameters are normalized to the cell wall length L: $t_0^* = \frac{t_0}{L}$ and $R^* = \frac{R}{L}$. A mixed analytical-numerical model is developed as a mean to predict the elastic behavior of the structures. This model was obtained by fitting a beam model of the structure on the results from the FE analyses. The radius R of the fillet between each cell wall was taken into account in the analytical model by recognizing that the section t_0 of the beam modeling the cell wall is not constant in the fillet zone, but it varies along the beam axis according continuous functions. This approach was inspired by the work of Lobontiu [16–18] who studied the stiffness of corner-filleted hinges with Euler-Bernoulli beam theory successfully.

Similarly, a numerical method is proposed for the estimation of the stress concentration factors (SCF) at the cell wall junctions of 2D regular square cell cellular structures. The aim is to obtain a model capable of calculating the values of the SCFs as a function of the unit cell geometrical parameters, namely the cell-wall diameter t0 and the fillet radius R at the joints. This was achieved by applying the Finite Elements (FE) method to the unit cell for wide intervals of $t_0^* = \frac{t_0}{L}$ and $R^* =$

$\frac{R}{L}$ to calculate the SCF for each couple of the parameters. The values of the SCF were then fitted with some functions. This work is an effort to provide a useful instrument that allows the designer to estimate the maximum stress in a structure by avoiding lengthily numerical simulations.

2.2 Model development: Elastic constants

2.2.1 Orthotropic elasticity

An orthotropic material is defined as a material having three mutually orthogonal symmetry planes at each point. The generalized stress-strain relationship for linear elastic solids is expressed in Einstein's notation by the following equation:

$$\varepsilon_{ij} = S_{ijkl}\,\sigma_{kl} \qquad \text{(II - 1)}$$

Where S_{ijkl} represents the 81 components of the compliance matrix (fourth rank tensor), ε_{ij} the 9 components of the strain tensor (second rank tensor) and σ_{ij} represents the 9 components of the stress tensor (second rank tensor). Given that the strain and stress tensors are symmetric, respectively because of the assumption of small deformations and because of equilibrium, the number of independent constants of the compliance tensor can be reduced to 36. Further considerations on the strain energy allow reducing the number of independent components of S_{ijkl} to 21, which completely characterize the elastic behavior of an *anisotropic* material. In the case of an orthotropic material, the independent elastic constants can be further reduced to 9 by applying the appropriate coordinate transformations. The stress-strain relationship for orthotropic materials is shown explicitly by Eq. II - 2 using the contracted notation, where subscripts 1, 2 and 3 indicate the material principal directions (directions perpendicular to the symmetry planes):

$$\begin{bmatrix}\varepsilon_1\\ \varepsilon_2\\ \varepsilon_3\\ \gamma_{23}\\ \gamma_{31}\\ \gamma_{12}\end{bmatrix} = \begin{bmatrix} \frac{1}{E_1} & -\frac{\nu_{21}}{E_2} & -\frac{\nu_{31}}{E_3} & 0 & 0 & 0\\ -\frac{\nu_{12}}{E_1} & \frac{1}{E_{22}} & -\frac{\nu_{32}}{E_3} & 0 & 0 & 0\\ -\frac{\nu_{13}}{E_1} & -\frac{\nu_{23}}{E_2} & \frac{1}{E_3} & 0 & 0 & 0\\ 0 & 0 & 0 & \frac{1}{G_{23}} & 0 & 0\\ 0 & 0 & 0 & 0 & \frac{1}{G_{31}} & 0\\ 0 & 0 & 0 & 0 & 0 & \frac{1}{G_{12}} \end{bmatrix} \begin{bmatrix}\sigma_1\\ \sigma_2\\ \sigma_3\\ \tau_{23}\\ \tau_{31}\\ \tau_{12}\end{bmatrix} \qquad \text{(II - 2)}$$

Where $\gamma_{ij} = 2\varepsilon_{ij}$ is the engineering shear strain and τ has been used to represent shear stresses instead of *σ*. The engineering constants are defined as follows:

- E_i is the elastic modulus in the *i*-th principal direction
- G_{ij} is the shear modulus in the *ij* plane
- ν_{ij} is Poisson's coefficient which is defined as $\nu_{ij} = -\frac{\varepsilon_j}{\varepsilon_i}$, i.e. the negative of the ratio between the strain induced in the transverse direction *j* to the *i*-direction in which the stress is applied and the strain in the *i*-direction.

For orthotropic materials there is no coupling between shear strains and normal stresses and between normal strains and shear stresses in the principal directions. From the symmetry of the compliance matrix, we immediately obtain that:

$$\frac{\nu_{ij}}{E_i} = \frac{\nu_{ji}}{E_j} \quad for\ i,j = 1 \dots 3 \qquad \text{(II - 3)}$$

In the present work, only a 2D analysis is discussed, that is loads are applied only in the plane defined by directions 1-2, so the independent elastic constants to consider are only 4: E_1, E_2, G_{12} and ν_{12}. The stress-strain relationship can be thus simplified to obtain Eq. 4:

$$\begin{bmatrix}\varepsilon_1\\ \varepsilon_2\\ \gamma_{12}\end{bmatrix} = \begin{bmatrix} \frac{1}{E_1} & -\frac{\nu_{21}}{E_2} & 0\\ -\frac{\nu_{12}}{E_1} & \frac{1}{E_2} & 0\\ 0 & 0 & \frac{1}{G_{12}} \end{bmatrix} \begin{bmatrix}\sigma_1\\ \sigma_2\\ \tau_{12}\end{bmatrix} \qquad \text{(II - 4)}$$

Since a material can be loaded in any direction and not just in the principal directions, it is useful to have the relationships that allow expressing the in-plane

elastic properties in any *x-y* reference system inclined of an angle α to the principal directions 1-2, as shown in Figure II - 1.

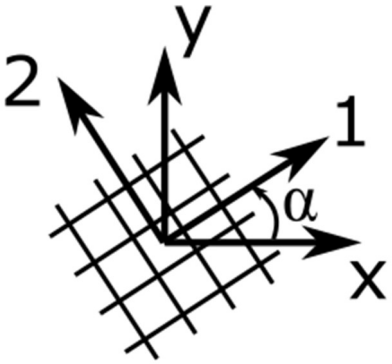

Figure II - 1. Positive rotation α of the principal (material) axes 1-2 with respect to the x-y axes.

In the generic x-y reference system, coupling occurs between shear strains and normal stresses and between shear stresses and normal strains also for orthotropic materials as for anisotropic ones, thus Eq. (II – 4) can be rewritten in the x-y reference system as:

$$\begin{bmatrix}\varepsilon_x\\ \varepsilon_y\\ \gamma_{xy}\end{bmatrix}=\begin{bmatrix}\frac{1}{E_x} & -\frac{\nu_{yx}}{E_y} & -\frac{\eta_{x,xy}}{G_{xy}}\\ -\frac{\nu_{xy}}{E_x} & \frac{1}{E_y} & -\frac{\eta_{y,xy}}{G_{xy}}\\ -\frac{\eta_{xy,x}}{E_x} & -\frac{\eta_{xy,y}}{E_y} & \frac{1}{G_{xy}}\end{bmatrix}\begin{bmatrix}\sigma_x\\ \sigma_y\\ \tau_{xy}\end{bmatrix} \qquad \text{(II – 5)}$$

Where, because of symmetry, we have that $\frac{\eta_{x,xy}}{G_{xy}}=\frac{\eta_{xy,x}}{E_x}$ and $\frac{\eta_{y,xy}}{G_{xy}}=\frac{\eta_{xy,y}}{E_y}$. The coefficients of mutual influence $\eta_{i,ij}$ and $\eta_{ij,i}$ are defined as follows:

- $\eta_{i,ij}$ is the coefficient of mutual influence of the first kind and accounts for the normal strain in the *i*-direction induced by a shear stress in the *ij* plane: $\eta_{i,ij}=\frac{\varepsilon_i}{\gamma_{ij}}$.
- $\eta_{ij,i}$ is the coefficient of mutual influence of the second kind and accounts for the shear strain in the *ji* plane induced by a normal stress in the *i*-direction: $\eta_{ij,i}=\frac{\gamma_{ij}}{\varepsilon_i}$.

The engineering constants in the *xy* reference frame depend only on the engineering constants in the principal directions (and of course the angle α), so four constants are still sufficient to describe the in-plane behavior of an orthotropic material:

$$\frac{1}{E_x} = \frac{1}{E_1} cos^4\alpha + \left(\frac{1}{G_{12}} - \frac{2\nu_{12}}{E_1}\right) sin^2\alpha\, cos^2\alpha + \frac{1}{E_2} sin^4\alpha \quad \text{(II – 6a)}$$

$$\frac{1}{E_y} = \frac{1}{E_1} sin^4\alpha + \left(\frac{1}{G_{12}} - \frac{2\nu_{12}}{E_1}\right) sin^2\alpha\, cos^2\alpha + \frac{1}{E_2} cos^4\alpha \quad \text{(II – 6b)}$$

$$\nu_{xy} = E_x \left[\frac{\nu_{12}}{E_1}(sin^4\alpha + cos^4\alpha) - \left(\frac{1}{E_1} + \frac{1}{E_2} - \frac{1}{G_{12}}\right) sin^2\alpha\, cos^2\alpha\right] \quad \text{(II – 6c)}$$

$$\frac{1}{G_{xy}} = 2\left(\frac{2}{E_1} + \frac{2}{E_2} + \frac{4\nu_{12}}{E_1} - \frac{1}{G_{12}}\right) sin^2\alpha\, cos^2\alpha + \frac{1}{G_{12}}(sin^4\alpha + cos^4\alpha) \quad \text{(II – 6d)}$$

$$\eta_{xy,x} = E_x \left[\left[\frac{2}{E_1} + \frac{2\nu_{12}}{E_1} - \frac{1}{G_{12}}\right] sin\alpha\, cos^3\alpha - \left[\frac{2}{E_2} + \frac{2\nu_{12}}{E_1} - \frac{1}{G_{12}}\right] sin^3\alpha\, cos\alpha\right] \quad \text{(II – 6e)}$$

$$\eta_{xy,y} = E_y \left[\left[\frac{2}{E_1} + \frac{2\nu_{12}}{E_1} - \frac{1}{G_{12}}\right] sin^3\alpha\, cos\alpha - \left[\frac{2}{E_2} + \frac{2\nu_{12}}{E_1} - \frac{1}{G_{12}}\right] sin\alpha\, cos^3\alpha\right] \quad \text{(II – 6f)}$$

These relationships are very useful because they allow writing an expression for each elastic constant as a function of α once the elastic properties of the orthotropic material are established in the principal directions.

2.2.2 General procedure to calculate the elastic constants in the principal directions

The approach to calculate the elastic constants of the lattice structures can be summarized in the following steps:

(1) Identify the unit cell of the cellular structure based on periodicity considerations. If appropriate, further simplify the structure based on symmetry considerations [19]

(2) Analytical solution of the unit cell with beam theory to find the in-plane elastic constants in the principal directions 1 and 2
(3) Numerical (FE) solution of the unit cell to find the in-plane elastic constants in the principal directions 1 and 2 for various combinations of the geometrical parameters inside the chosen interval
(4) The analytic model obtained at point (4) is fitted to the numerical results by introducing an additional coefficient into the analytical equation, named effective thickness t_{eff}, that accounts for the joint stiffening effect [8].

The generic 2D cell is shown in Figure II - 2, with each side identified by a number. The elastic constants E_1, E_2, G_{12} and v_{12} in the principal directions are calculated by applying the appropriate boundary conditions to the unit cell, according to the *compliance matrix* and *stiffness matrix* methods, described in [20] and [8], which will be now briefly described.

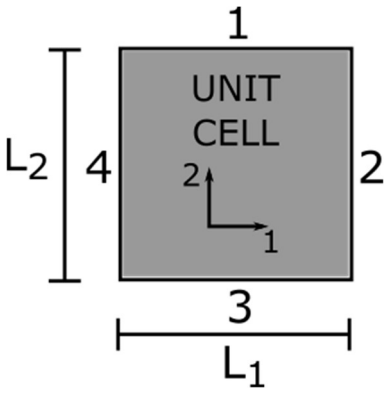

Figure II - 2. Scheme of the unit cell for the application of the stiffness and compliance matrix methods, with the 1-2 principal reference system.

2.2.2.1 Stiffness matrix method

This method is based on the stress-strain relationship expressed by the stiffness matrix ***K*** of Eq. (II – 7).

$$\begin{Bmatrix}\sigma_{11}\\ \sigma_{22}\\ \tau_{12}\end{Bmatrix} = \begin{bmatrix}K_{11} & K_{12} & K_{13}\\ K_{21} & K_{22} & K_{23}\\ K_{31} & K_{32} & K_{33}\end{bmatrix}\begin{Bmatrix}\varepsilon_{11}\\ \varepsilon_{22}\\ \gamma_{12}\end{Bmatrix} = \begin{bmatrix}\frac{E_{11}}{1-\nu_{12}\nu_{21}} & \frac{\nu_{21}E_{22}}{1-\nu_{12}\nu_{21}} & 0\\ \frac{\nu_{12}E_{11}}{1-\nu_{12}\nu_{21}} & \frac{E_{22}}{1-\nu_{12}\nu_{21}} & 0\\ 0 & 0 & G_{12}\end{bmatrix}\begin{Bmatrix}\varepsilon_{11}\\ \varepsilon_{22}\\ \gamma_{12}\end{Bmatrix} \qquad (II-7)$$

The procedure of calculating the elastic constants via the *stiffness matrix* method consists of applying the constraints and the loads reported for each line of Table II - 1 to the corresponding side of the unit cell (Figure II - 3) and solving the structural

problem via FE or beam theory. It is actually equivalent to apply the loads in terms of displacements (and then calculate the reaction forces at the constraints) or in terms of forces (and then calculate the displacements of the sides to which the forces are applied). Thus, each component of the stiffness matrix can be easily obtained after the stresses and the strains have been substituted into Eq. (II – 7).

Table II - 1. Boundary conditions defining the stiffness matrix method.

STIFFNESS MATRIX METHOD					
K matrix components	Boundary conditions applied to the unit cell				
	Side 1	Side 2	Side 3	Side 4	Load type
K_{11}, K_{21}	$\delta_2=0$	*LOADED*	$\delta_2=0$	$\delta_1=0$	Normal
K_{22}, K_{12}	*LOADED*	$\delta_1=0$	$\delta_2=0$	$\delta_1=0$	Normal
K_{33}	*LOADED*	*LOADED*	$\delta_1=0$	$\delta_2=0$	Pure shear

The stresses and strains are calculated with the following classical formulas, where L_1 and L_2 are the lengths of the sides of the unit cell (Figure II - 2), δ_1 and δ_2 are the displacements of the cell sides in the principal directions (in the case of shear loading δ_i represents the maximum displacement) and finally F_1 and F_2 are the forces acting in the principal directions.

$$\varepsilon_{11} = \frac{\delta_1}{L_1}, \quad \varepsilon_{22} = \frac{\delta_2}{L_2}, \quad \gamma_{12} = \frac{\delta_1}{L_2} + \frac{\delta_2}{L_1}$$
$$\sigma_{11} = \frac{F_1}{L_2}, \quad \sigma_{22} = \frac{F_2}{L_1}, \quad \tau_{12} = \frac{F_1}{L_1} = \frac{F_2}{L_2}$$

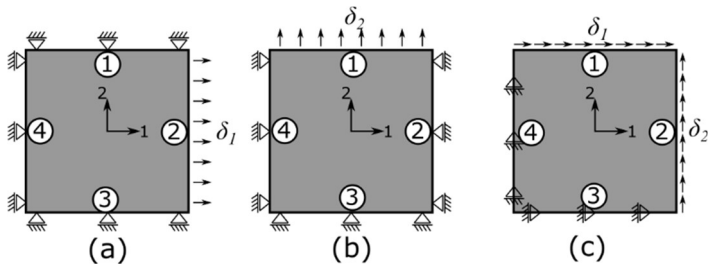

Figure II - 3. Boundary conditions defining the stiffness matrix method applied to the unit cell (in term of displacements).

Once all the components of ***K*** are determined, the elastic constants can be easily derived with few passages:

$E_{11} = \frac{K_{11}K_{22} - K_{12}K_{21}}{K_{22}}$, $E_{22} = \frac{K_{11}K_{22} - K_{12}K_{21}}{K_{11}}$, $\nu_{12} = \frac{K_{21}}{K_{11}}$, $\nu_{21} = \frac{K_{12}}{K_{22}}$, $G_{12} = K_{33}$

2.2.2.2 Compliance matrix method

This method is based on the stress-strain relationship expressed in terms of the compliance matrix ***C*** of Eq. (II – 8).

$$\begin{Bmatrix}\varepsilon_{11}\\ \varepsilon_{22}\\ \gamma_{12}\end{Bmatrix} = \begin{bmatrix}C_{11} & C_{12} & C_{13}\\ C_{21} & C_{22} & C_{23}\\ C_{31} & C_{32} & C_{33}\end{bmatrix}\begin{Bmatrix}\sigma_{11}\\ \sigma_{22}\\ \tau_{12}\end{Bmatrix} = \begin{bmatrix}\frac{1}{E_{11}} & -\frac{\nu_{21}}{E_{22}} & 0\\ -\frac{\nu_{12}}{E_{11}} & \frac{1}{E_{22}} & 0\\ 0 & 0 & \frac{1}{G_{12}}\end{bmatrix}\begin{Bmatrix}\sigma_{11}\\ \sigma_{22}\\ \tau_{12}\end{Bmatrix} \qquad \text{(II – 8)}$$

The procedure to calculate the principal strains and stresses is the same as for the stiffness matrix method, only the constraints and loads differ, as summarized in Table II - 2 and shown in Figure II - 4.

Table II - 2. Boundary conditions defining the compliance matrix method.

COMPLIANCE MATRIX METHOD					
C matrix components	Boundary conditions applied to the unit cell				
	Side 1	Side 2	Side 3	Side 4	Load type
C_{11}, C_{21}	FREE	*LOADED*	$\delta_2=0$	$\delta_1=0$	Normal
C_{22}, C_{12}	*LOADED*	FREE	$\delta_2=0$	$\delta_1=0$	Normal
C_{33}	*LOADED*	*LOADED*	$\delta_1=0$	$\delta_2=0$	Pure shear

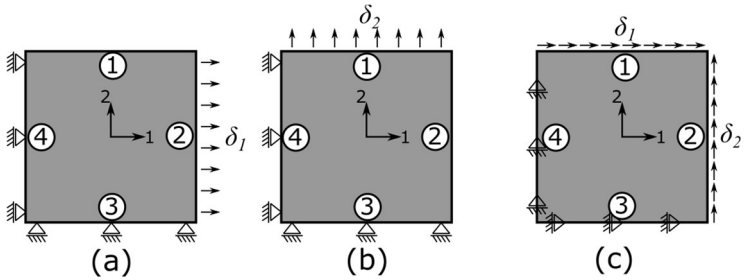

Figure II - 4. Boundary conditions of the compliance matrix method applied to the unit cell (in term of displacements).

Again, it is equivalent to apply the loads in terms of displacements or in terms of forces. Each elastic constant can be directly obtained from the relative component of $\boldsymbol{C}$, without the need to first determine all the components of the compliance matrix:

$$E_{11} = \frac{1}{C_{11}}, \quad E_{22} = \frac{1}{C_{22}}, \quad G_{12} = \frac{1}{C_{33}}, \quad \nu_{12} = -\frac{C_{21}}{C_{11}}, \quad \nu_{21} = -\frac{C_{12}}{C_{22}}$$

The two methods described above are perfectly equivalent in terms of the results, but both have advantages and disadvantages in terms of the calculation procedure. The stiffness matrix method has the advantage of constraining all the sides of the cell, thus making it more suitable to enforce the periodic conditions in the FE model. In fact, such lateral constraints make sure that the displacements of the nodes at the sides of the cell are compatible with periodicity. When applying the compliance matrix method to the FE model, it is always necessary to make sure that the displacements of the nodes at the free sides are compatible with the fact that the structure is periodic (done via node coupling). On the other hand, the compliance matrix method allows to directly compute the elastic constants, while the stiffness matrix method needs all the K_{ij} components to be determined before the elastic constants can be determined.

2.2.3 Analytical solution

In the analytical solution based on beam theory, the displacements δ of the sides of the unit cell are calculated by applying Castigliano's Second Theorem, assuming linear elasticity and small displacements:

$$\delta_k = \frac{\partial U(F_1,\dots,F_n)}{\partial F_k}, for\ k = 1,\dots,n \qquad \text{(II – 9)}$$

Where U is the complementary strain energy (equal to the strain energy in case of linear elasticity) expressed as a function of the generalized forces F_k applied to the structure.
The strain energy for 2D structures considering also the effect of shear is the following:

$$U = \frac{1}{2}\int_l \frac{N^2}{EA}ds + \frac{1}{2}\int_l k_t \frac{T^2}{GA}ds + \frac{1}{2}\int_l \frac{M^2}{EI}ds \qquad \text{(II – 10)}$$

Where A and I are respectively the area and the second moment of inertia of the section of the beam; N, T and M are the expressions of the normal, shear and

bending actions acting on the beam axis (which are functions of F_k), respectively, k_t is the shear coefficient and finally E and G are the elastic properties of the base material, assumed linear elastic. It is useful to remind that in the frame of linear elasticity $G = \frac{E}{2(1+\nu)}$ holds.

The analytical expressions of the elastic constants in the principal directions as a function of the geometrical parameters and the properties of the base material were obtained by applying the Euler-Bernoulli beam theory to the unit cell.

The radius R of the fillet between each cell wall was also considered in the analytical model by recognizing that the section t of the beam modeling the cell wall is not constant in the fillet zone (Figure II - 5), but it varies along the beam axis according to the following equations.

$$t(x_{AB}) = t_0 + 2\left[R - \sqrt{R^2 - (x_{AB} - R)^2}\right] \quad \text{(II – 11a)}$$

$$t(x_{BA}) = t_0 + 2\left(R - \sqrt{R^2 - {x_{BA}}^2}\right) \quad \text{(II – 11b)}$$

Where x_{AB} and x_{BA} are, respectively, the coordinate along the beam axis from the thickest section to the narrower and vice versa (see Figure II - 5). Eqs. II - 11 were used in place of the beam thickness in the expression of the area A and of the moment of inertia I of the section of the beams.

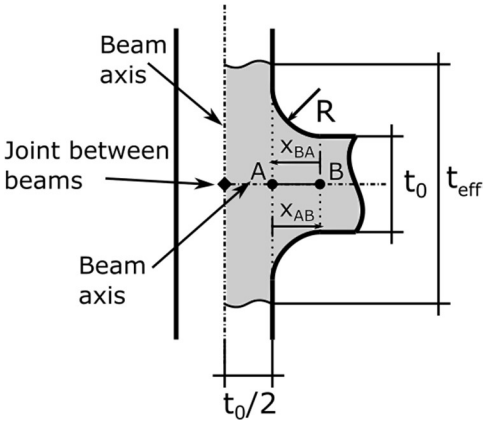

Figure II - 5. Fillet zone between cell walls with local coordinate systems. t_{eff} indicates the effective thickness of the (grey) beam in the joint between the cell walls.

Finite element analyses showed that the joints between the cell walls have a relevant effect on the mechanical behavior of the structure which is not captured by the simple beam model based on Euler-Bernoulli beams [8]. To account for the stiffening effect of joints, a fictitious section is introduced in the fraction of the cell wall (beam)

axis that goes from the intersection point of the beam axes itself to point A in Figure II - 5 (segment of length $t_0/2$). To this section an effective thickness t_{eff} is given, which is obviously not known a priori but has to be calculated by fitting the analytical model to the FE results. As will be shown and discussed later, this effective thickness depends on the geometry of the cell and on the loading mode

2.2.4 Numerical solution

Parametric models of the unit cells were built in ANSYS® and meshed with 2D 8-node structural elements with quadratic displacement behavior (PLANE183) and plane stress formulation. The boundary conditions were applied as displacements on the sides of the unit cells and the stresses were obtained from the reaction forces. The periodicity of the structure was enforced with constraint equations (CP command) that couple the displacement of corresponding nodes on the sides of the unit cell to guarantee the continuity of the strain field.

2.2.5 Fit strategies

The semi-analytical model was obtained by substituting to the unknown effective thickness t_{eff} an expression, function of the geometry of the unit cell, obtained by fitting the FE results. The analytical expressions of the elastic constants in the principal directions were equated to the results of the FE simulation to calculate t_{eff} by solving each equation. Once the values of t_{eff} became known for each combination of the geometrical parameters of the unit cell, the fit was accomplished by searching a function of several parameters that described with sufficient accuracy the dependence of t_{eff} on the geometrical parameters of the unit cell. For convenience, the geometrical parameters of the unit cell (the thickness of the cell walls t_0 and the fillet radius R) and t_{eff} have been normalized by the cell wall length L. Normalizing the unit cell parameters by the cell wall length is convenient because it removes a parameter without loosing the generality of the solution: indeed, scaling the lattice does not change its elastic properties. The normalized quantities are identified by an asterisk: $t_0^* = \frac{t_0}{L}$, $R^* = \frac{R}{L}$ and $t_{eff}^* = \frac{t_{eff}}{L}$.

Notably, for each t_0^* and R^* couple, the effect of the joint is different for each elastic constant because of the intrinsically different loading configurations applied to the structure to compute it. That is, the response of the same structure might be prevalently axial or flexural depending on how it is loaded. Therefore, t_{eff}^* also changes accordingly. In addition, considering that it is calculated from FE results, the t_{eff}^* parameter necessarily includes also the effect of factors other than the joint stiffening effect which are not considered by the beam model. For instance, the

strong approximation introduced by the modeling of the fillet radius as a beam of variable cross-section and the fact that in the FE model sections in bending do not stay parallel while the Euler beam theory assumes that they do. This latter effect is most probably very weak due to the small displacements involved.

2.2.6 Regular square structure

The regular square structure is composed of identical square cells periodically repeated in space, as shown in Figure II - 6a. Zooming on a single unit cell (Figure II - 6b) shows the geometrical details of the cell, which is made of struts of length L, with a rectangular section of thickness t_0 and depth b. The junctions between the cell walls are filleted with radius R. The structure is orthotropic because of its symmetry (the four symmetry planes are shown in Figure II - 6b), with material principal directions identified by the 1-2 reference system [21].

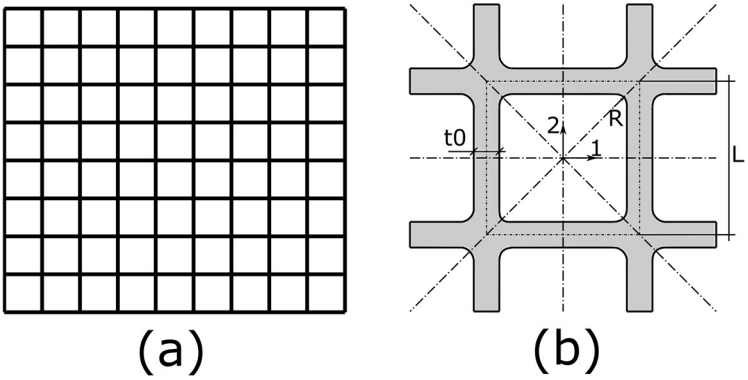

Figure II - 6. (a) Regular square structure; (b) Detail of the structure showing its fundamental geometric characteristics and the symmetry planes. 1-2 are the principal directions.

The regular cubic structure is peculiar because it shows a transition from a *stretching-dominated* behavior to a *bending-dominated* behavior as the angle between the material principal directions *1-2* and the loading direction increases. Consequently, deviating from the principal directions a remarkable drop in stiffness is expected, reaching a minimum along the bisecting direction of the *1-2* reference frame. In the same way, the stress-strain curve obtained by loading the cells along the principal directions shows post-yielding softening due to buckling failure of a layer while the stress-strain curve obtained by off-axis loading shows a smooth

transition from the elastic stage to the stress plateau, a behavior typical of bending-dominated lattices [22].

2.2.6.1 Analytical model of the regular square structure

The analytical model of the elastic constants of the lattice was developed by choosing the unit cell as a square cross with arms of length $L/2$, thickness t_0 and out-of-plane thickness b, as shown in Figure II - 7. The base material was assumed isotropic with elastic constant E_s and Poisson's coefficient v_s.

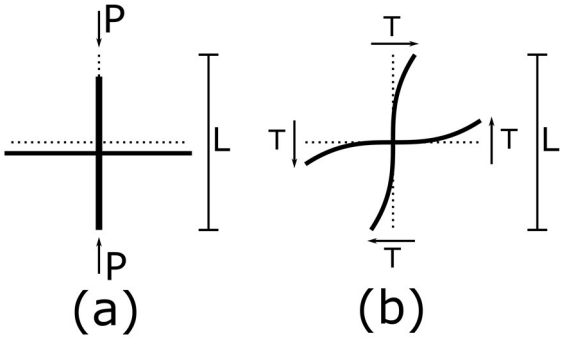

Figure II - 7. (a) Unit cell of the periodic square structure under uniaxial compressive loading (deformed and un-deformed structure); (b) Unit square cell loaded in pure shear (deformed and un-deformed structure).

The analytical expressions of the elastic constants in the principal directions were obtained by assuming the cell walls to behave as elastic Euler beams and by applying the constraints to the unit cells according to the compliance matrix method. The displacements induced by unitary loads applied in the principal directions were calculated with Castigliano's theorem. The unit cell loaded in compression parallel to either of the cell walls behaves like an elastic strut (Figure II - 7a) because the cell walls transversal to the load are unloaded, given that all the cells deform laterally of the same quantity. This consideration is true only if the assumption of an infinite domain holds. On the other hand, each arm of the unit cell loaded in shear behaves as a cantilever beam (Figure II - 7b). Consequently, the problem to solve becomes that shown in Figure II - 8, which is considerably simpler.

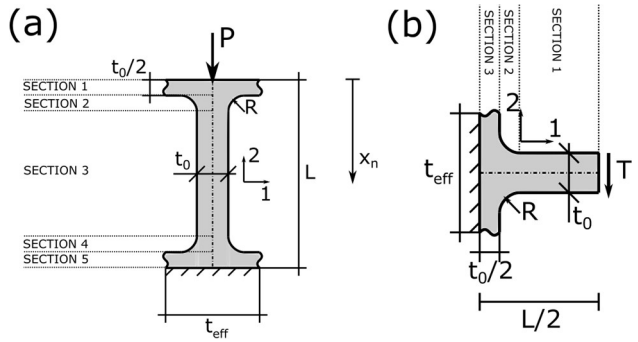

Figure II - 8. a) Cell wall model used to compute the elastic modulus and Poisson's coefficient; (b) cell wall model used to compute the shear modulus. Note the t_{eff} parameter that accounts for the joint stiffening effect.

2.2.6.1.1 Elastic modulus

Given the particular symmetry of the structure, the elastic modulus in the principal directions is the same, i.e. $E_{11} = E_{22}$. The in-plane thickness t of the sections is variable because of the fillet, and the strut has to be divided into five segments along its axis, defined by the coordinate x (Figure II - 8a):

- Section 1 ($0 \leq x_1 \leq \frac{t_0}{2}$): $t(x_1) = t_{eff}$
- Section 2 ($0 \leq x_2 \leq R$): $t(x_2) = t_0 + 2\left[R - \sqrt{R^2 - (x_2 - R)^2}\right]$
- Section 3 ($0 \leq x_3 \leq L - 2R - t_0$): $t(x_3) = t_0$
- Section 4 ($0 \leq x_4 \leq R$): $t(x_4) = t_0 + 2\left(R - \sqrt{R^2 - {x_4}^2}\right)$
- Section 5 ($0 \leq x_5 \leq \frac{t_0}{2}$): $t(x_5) = t_{eff}$

The total elastic energy U_T is given by the sum of the energies stored in each segment (Eq. (II – 10)). In this case, only axial actions are present:

$$U_T = \frac{1}{2}\sum_{n=1}^{5}\int_0^{x_{n,0}} \frac{N(x_n)^2}{E_s \cdot A_n(x_n)}\, dx_n$$

Where $x_{n,0}$ is the length of the interval in which section n is defined by a continuous function and x_n is the axial coordinate relative to the section n. Castigliano's theorem (Eq. (II – 9)) provides the vertical displacement δ by deriving the elastic energy by the vertical load:

$$\delta = \frac{\partial U_T}{\partial P}$$

The elastic modulus in direction 2 could be then computed by applying the compliance matrix method:

$$E_{22} = \frac{\sigma_{22}}{\varepsilon_{22}} = \frac{\frac{P}{bL}}{\frac{\delta}{L}} = \frac{P}{\delta}\frac{1}{b}$$

At this point, given that δ is known, Eq. (II -A1) is obtained (by normalizing t_0 and R).

2.2.6.1.2 Poisson's coefficient

The Poisson effect in the cellular lattice is manifested as the lateral displacement of the axially loaded strut and was calculated from the section of width t_{eff}. Doing so it allowed to easily fit the analytic expression to the FE data. Applying the definition of the Poisson coefficient the following expression is obtained:

$$\nu_{21} = \frac{\varepsilon_{11}}{\varepsilon_{22}} = \frac{\frac{\delta_1}{L}}{\frac{\delta_2}{L}} = \frac{\delta_1}{\delta_2}$$

Where δ_1 (the displacement of the cell side in direction 1) can be related to δ_2 (the displacement of the cell side in direction 2) by the Poisson's ratio of the base material:

$$\delta_1 = \nu_s t_{eff} \frac{\delta_2}{L} \qquad \text{(II - 12)}$$

By including Eq. (II - 12), the Poisson's ratio of the lattice structure is:

$$\nu_{21} = \nu_s \frac{t_{eff}}{L}$$

That is precisely Eq. (II – A2). Due to the symmetry of the structure, $\nu_{12} = \nu_{21}$.

2.2.6.1.3 Shear modulus

The expression for the shear modulus G_{12} is derived by a pure shear load applied to the unit cell, simplified to a cantilever beam of length $\frac{L}{2}$. In order to calculate the strain energy, the beam has to be divided into three segments because of the non-uniform section, as shown in Figure II - 8b. Defining an axial coordinate x going from

right to left, the following functions for the in-plane thickness of the beam (rectangular section of out-of-plane thickness *b*) hold:

- Section 1 ($0 \leq x_1 \leq \frac{L}{2} - R - \frac{t_0}{2}$): $t(x_1) = t_0$
- Section 2 ($0 \leq x_2 \leq R$): $t(x_2) = t_0 + 2\left(R - \sqrt{R^2 - {x_2}^2}\right)$
- Section 3 ($0 \leq x_3 \leq \frac{t_0}{2}$): $t(x_3) = t_{eff}$

Only shear and bending actions are present in the cantilever beam, thus the elastic energy U_T is (from Eq. (II – 10)):

$$U_T = \frac{1}{2}\sum_{n=1}^{3}\int_0^{x_{n,0}} k_t \frac{T(x_n)^2}{G_s \cdot A_n(x_n)} dx_n + \frac{1}{2}\sum_{n=1}^{3}\int_0^{x_{n,0}} \frac{M(x_n)^2}{E_s \cdot I_n(x_n)} dx_n$$

With the already defined quantities referred to section *n*. The vertical displacement can be calculated via Castigliano's theorem (Eq. (II – 9)):

$$\delta = \frac{\partial U_T}{\partial T}$$

The shear modulus of the unit cell was then calculated by applying the compliance matrix method:

$$G_{12} = \frac{\tau_{12}}{\gamma_{12}} = \frac{\frac{T}{bL}}{\frac{4\delta}{L}} = \frac{T}{4\delta}\frac{1}{b}$$

Dividing by 4 is necessary because, as shown in Figure II - 9, the shear deformation of the unit cell γ_{12} is four times the maximum displacement of each arm of the cross divided the unit cell size *L* (or, alternatively, considering that the elastic energy of the unit cell is $4U_T$). By replacing δ, Eq. (II – A3) is obtained.

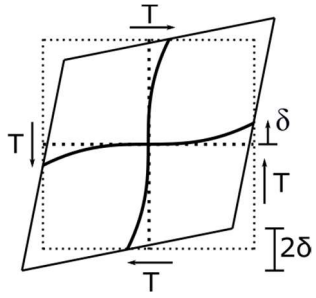

Figure II - 9. Deformation of the unit cell of the RR structure due to pure shear.

2.2.6.1.4 Observations

By neglecting the fillet radius, the effect of shear and the joint stiffening effect ($t_{eff} = t_0^*$), the previous procedure produces the well-known classical formulas for the elastic constants [23,24]:

$$\frac{E_1}{E_s} = \frac{E_2}{E_s} = \frac{t_0}{L}$$

$$\nu_{21} = \nu_{12} = \nu_s \frac{t_0}{L}$$

$$\frac{G_{12}}{E_s} = \frac{1}{2}\left(\frac{t_0}{L}\right)^3$$

The expressions for the elastic constants in the principal directions can be substituted into Eqs. (II – 6) to obtain a model able to predict the in-plane elastic behavior in any direction. Due to their length and the fact that their derivation is trivial, these expressions are not reported here; in fact, the best approach is to implement these models into a calculus software such as Mathematica ® or Matlab ®.

Given the symmetry planes of the regular square lattice (Figure II - 6), an equivalent alternative to the unit cell of Figure II - 6 is that indicated by the dotted square in Figure II - 10, where the structure is tilted of 45°. In this case, it is convenient to define a new set of material principal coordinates *1*2**, coinciding with the *x* and *y* directions of Figure II - 10.

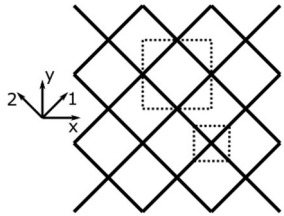

Figure II - 10. Square structure inclined of 45° to the principal axes 1-2. The dotted squares indicate possible unitary cells.

The symmetry of the structure made it possible to further simplify the unit cells, as shown in Figure II - 11. In the case of uniaxial compression along the *y* axis (along the *x* axis would be the same), the cell walls deform mainly by bending and the rotation at the nodes is zero (due to symmetry). The equivalent simplified structure loaded in compression is shown in Figure II - 11a. In the case of pure shear, the unit cell is loaded anti-symmetrically and it can be thus simplified to a bar in tension, as shown in Figure II - 11b.

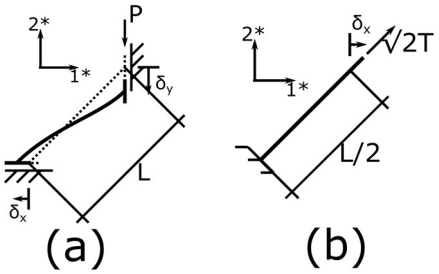

Figure II - 11. (a) Simplified unit cell of the 45° inclined square structure under uniaxial compressive loading (deformed and un-deformed structure); (b) Simplified unit square cell loaded in pure shear (deformed and un-deformed structure).

The analytical expression of the elastic constants in the *1*2** directions can be obtained with the same procedure that has been described in the previous paragraphs by solving the free body diagram in Figure II - 11. Clearly, the elastic constants in the *1*2** directions coincide with the values obtained by substituting those in the *12* directions into Eqs. (II – 6) with an angle of 45°. For brevity and because these results are not fundamental, the equations are omitted.

2.2.6.2 FE model of the regular square structure

A 2D Finite Elements model of the unit cell was developed to calculate the thickness t_{eff} of the fictitious section described with relation to Figure II - 5. Two parametric models were realized, one for loading in the principal directions *12* (Figure II - 12a) and one for loading in the direction 45° to the principal ones (Figure II - 12b). The periodic boundary conditions were implemented according to the *stiffness matrix* method, more convenient for FE models.

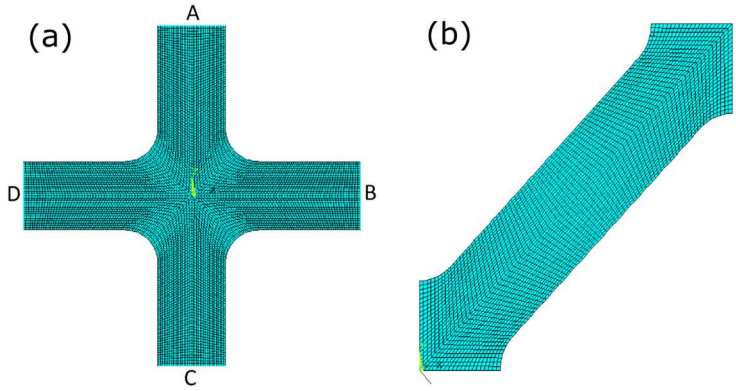

Figure II - 12. (a) FE model of the square unit cell loaded in the principal direction (along cell wall axis); (b) FE model of the square unit cell tilted of 45° to the principal directions.

A convergence analysis was carried out to verify the optimal mesh refinement for the various combinations of the geometrical parameters: the mesh was deemed acceptable when the error on each elastic constant with respect to the finest mesh was below 0.5% (in Figure II - 13, an example of a convergence analysis).

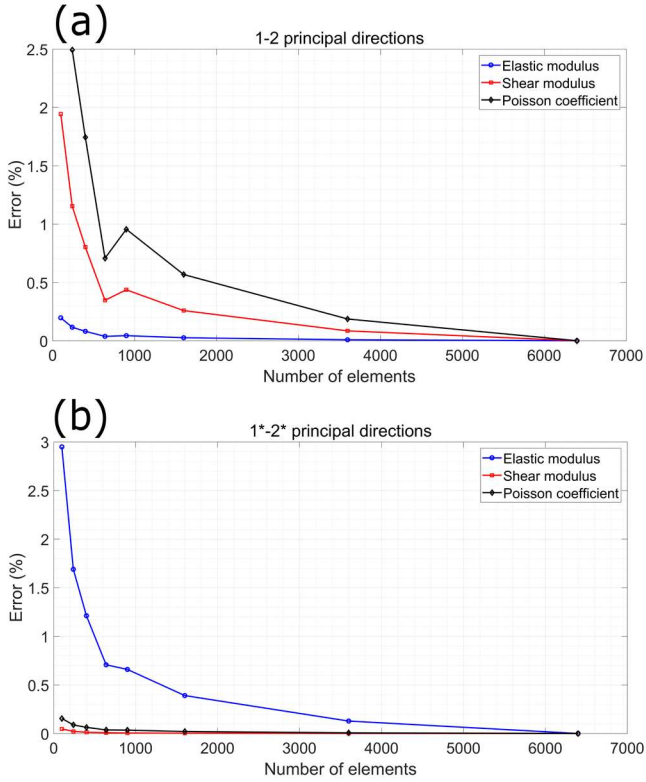

Figure II - 13. Example of a convergence analysis ($t_0^* = 0.17, R^* = 0$).

The results obtained from the FE model of the cell tilted of 45° (Figure II - 12b) and those calculated by substituting the FE results in the principal directions (Figure II - 12a) in Eqs. (II – 6) were compared for all the combinations of t_0^* and R^* and the agreement was excellent with an average error of 0.01%.

2.2.6.3 Fitting of the analytical model to the FE results: regular square structure

The fit was accomplished by searching a polynomial function of several parameters which could accurately predict the dependence of t_{eff}^* on t_0^* and R^*. This function was then substituted into the analytical expression of the elastic constants to obtain the complete model:

$$\frac{t_{eff_c}(t_0^*, R^*)}{L} = A_c + B_c\, t_0^* + C_c\, R^* + D_c\, t_0^*\, R^* + E_c\, t_0^{*2} + F_c\, R^{*2} + G_c\, t_0^{*2}\, R^{*2} \qquad \text{(II - 13)}$$

where the subscript *c* indicates the specific elastic constant (E_{11}, G_{12}, ν_{12}). Both the elastic modulus and the shear modulus were fitted using all the 7 parameters, while for Poisson's coefficient 6 were enough as the correlation between the squares of t_0^* and R^* is negligible. The parameters used to fit the effective thickness for each elastic constant are reported in Table II - 3.

Table II - 3. Fit parameters for the effective thickness t_{eff}^* for each elastic constant of the RR structure.

	A	B	C	D	E	F	G
E_{11}	-0.00080	1.21725	0.109427	1.47217	-0.26883	-0.88626	-8.31808
G_{12}	0.006607	0.926161	0.282039	2.96722	2.08427	-1.42098	95.0181
ν_{12}	-0.00362	1.33192	0.324018	3.06558	-0.44281	-1.57462	---

The fit was accomplished by considering five values for the thickness t_0^* (0.04, 0.08, 0.12, 0.16, 0.1) and eight values for the fillet radius R^* (0, 0.01, 0.02, 0.04, 0.06, 0.08, 0.1, 0.15) for a total of forty points (number of FE analyses) for each elastic constant. The fitting function uses a number of parameters that is much lower than the number of points, thus ensuring a low error also for values between the points considered. The values of t_{eff}^* and the percentage errors between the results of the fitted model and the FE model for t_{eff}^* are shown in contour plots as a function of t_0^* and R^* for E_{11}, G_{12} and ν_{12} in Figure II - 14, Figure II - 15 and Figure II - 16.

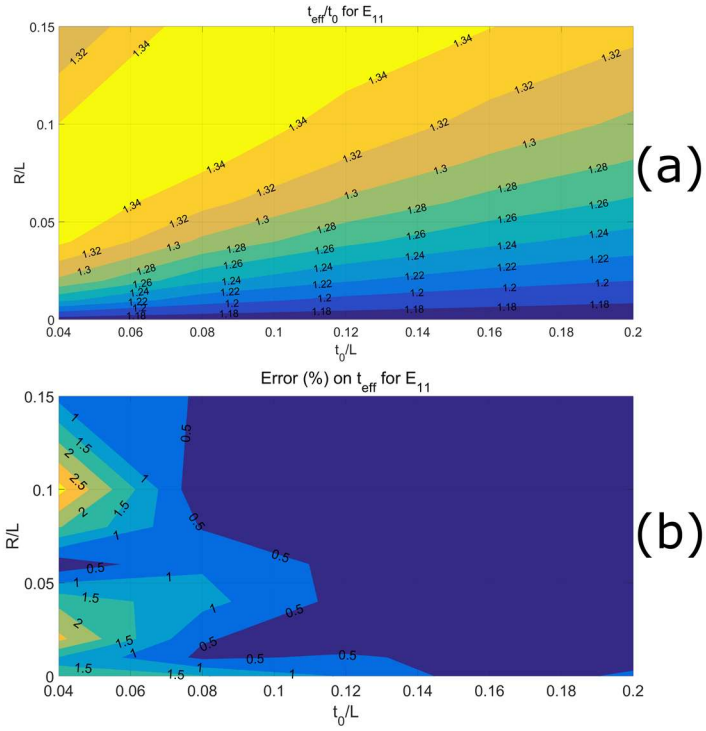

Figure II - 14. (a) Effective thickness calculated from the E_{11} data for the RR structure. (b) Percentage fitting error for E_{11} as a function of t_0^* and R^*.

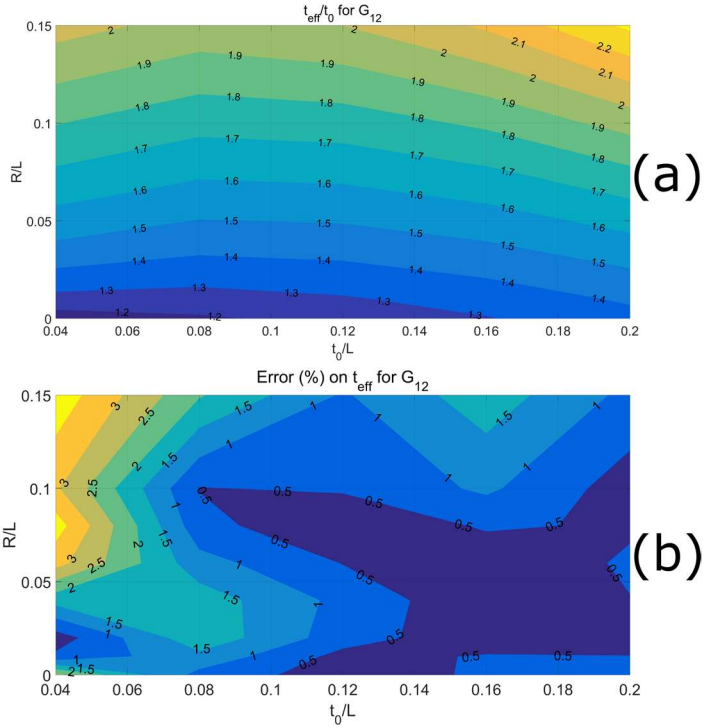

Figure II - 15. (a) Effective thickness calculated from the G_{12} data for the regular square structure. (b) Percentage fitting error for G_{12} as a function of t_0^* and R^*.

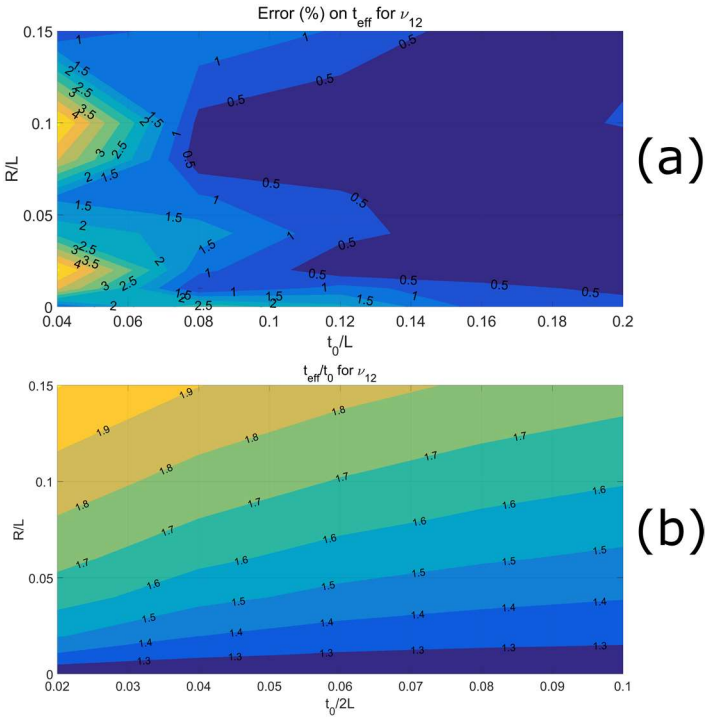

Figure II - 16. (a) Effective thickness calculated from the v_{12} data for the regular square structure. (b) Percentage fitting error for v_{12} as a function of t_0^* and R^*.

Table II - 4 reports the mean error, the standard deviation on the error and the maximum value of the error on the effective thickness.

Table II - 4. Statistical descriptors of the fitting errors on the effective thickness for the regular square structure.

	Mean error (%)	Standard deviation on error (%)	Maximum error (%)
t_{eff} for E11	0.64	0.75	3.16
t_{eff} for G12	1.05	1.01	3.82
t_{eff} for v12	1.11	1.34	5.11

The effective thickness calculated from the FE results is the highest for shear modulus (Figure II - 15) and the lowest for the elastic modulus (Figure II - 14). This can be understood by recalling the fact that under shear loading the structure is bending-dominated, which means that it relies on the rotational stiffness of the joints to avoid collapse. On the other hand, under loading in the principal directions, the

joints are less critical because the walls of the cell are loaded axially and no bending moment acts on the joints. A reasonable explanation for the intermediate values of t_{eff}^{*} calculated from the Poisson's coefficient (Figure II - 16) could be that the loading is axial so joint effect is lower than in the case of shear loading, but lateral expansion at the joint is strongly underestimated by the analytical model so a higher t_{eff}^{*} than that calculated for the elastic modulus is necessary to compensate. In general, the joint stiffening effect tends to be stronger with respect to the wall thickness t_0^{*} for thinner beams with greater fillet radius.

2.2.7 Staggered square structure

The staggered square structure is shown in Figure II - 17 and it is derived from the regular square structure by offsetting every other line of squares of half the length of the cell side. This structure can be also obtained from the hexagonal cell by decreasing the angle θ to zero, as shown in Figure II - 18. The structure is fully characterized by three parameters, the same as the regular square structure: the cell-wall length *L*, the cell-wall thickness t_0 and the fillet radius between the cell walls *R* (Figure II - 17b). The sections of the beams are rectangular of depth *b*, the same as the regular square lattice.

The material principal directions *1* and *2* are defined according to the two symmetry planes of the structure (Figure II - 17b). Recalling Maxwell's criterion, the staggered structure proves to be bending-dominated in all loading configurations apart from axial loading along principal direction *1*. Consequently, the stiffness in direction *1* is considerably higher than in all the other in-plane directions.

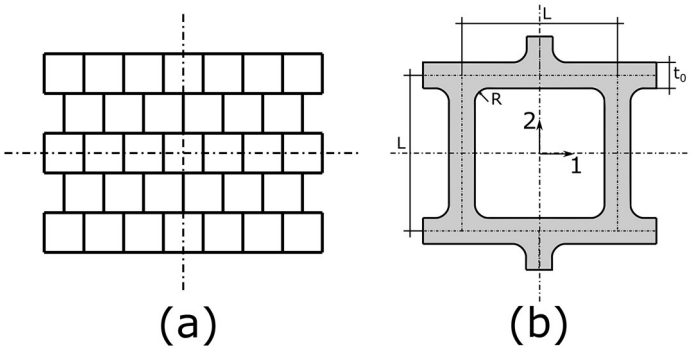

Figure II - 17. (a) Staggered square structure; (b) Detail of the structure showing its fundamental geometric characteristics and the symmetry planes. 1-2 are the principal directions.

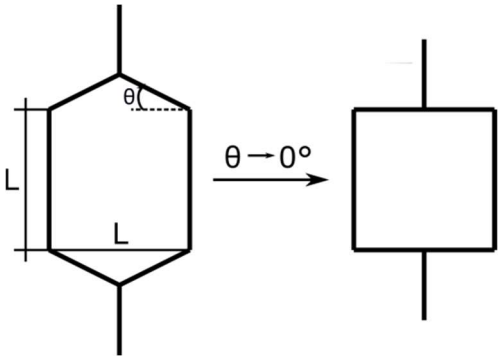

Figure II - 18. The staggered square structure is a particular case of the hexagonal structure.

2.2.7.1 Analytical model of the staggered square structure

The analytical expressions for the elastic constants are developed based on the unit cell of Figure II - 19. According to the compliance matrix method, three loading configurations need to be solved to calculate the four elastic constants (E_{11}, E_{22}, G_{12}, v_{21}): axial loads along directions *1* and *2* and in-plane pure shear. The loads applied to the infinite lattice (Figure II - 17a) are transferred to the unit cells as shown in Figure II - 19. In the following, the steps necessary to obtain the simple free body diagrams of Figure II - 19 will be briefly described.

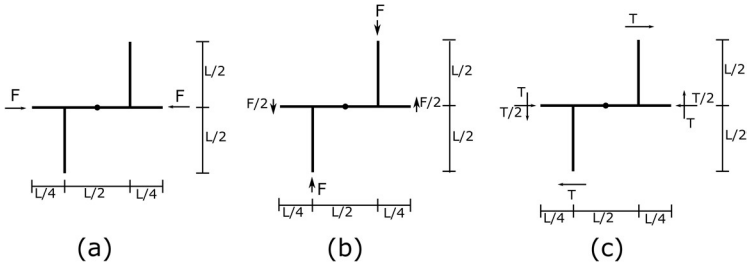

Figure II - 19. Load configurations on the unit cell of the S structure. (a) Axial loading in direction 1 to calculate E11; (b) Axial loading in direction 2 to calculate E22; (c) Shear loading in plane 12 to calculate G12.

The elastic modulus E_{11} in principal direction 1 is obtained by loading the structure axially in direction *1*, which translates to pure compression on the struts parallel to the loading direction. The struts parallel to direction *2* are unloaded because of symmetry with respect to principal direction *1* of the global structure (Figure II - 19a). The elastic modulus E_{22} in direction *2* and Poisson's coefficient v_{21} were obtained by applying a compressive load in direction *2*. The forces acting on the extremities of

the beams (Figure II - 19b) were determined from equilibrium (translation and rotation) and considerations based on symmetry and periodicity:

- Symmetry: the structure and the load are symmetric with respect to axis *2*, consequently the symmetry cannot be lost in the deformed lattice. For this reason, no point of the vertical beams is subjected to any rotation, bending moment or shear action and thus the vertical beams are loaded only axially.
- Periodicity: the structure being periodic, corresponding points of the unit cell should preserve the periodicity of the displacement field. Consequently, corresponding points have the same rotation and displacements and the internal actions must be equal and opposite.
- Polar symmetry: the lattice loaded uniformly in direction *2* has a polar symmetry to the midpoint between each couple of vertical struts (black dots in Figure II - 19). Similarly, the midpoints of the vertical struts also act as points of polar symmetry. Consequently, the bending moment must be zero in those points.

The expression for the shear modulus G_{12} was found by applying pure shear in the principal directions. This load case was solved with a similar reasoning as with the previous case, by combining equilibrium, periodicity and symmetry considerations (Figure II - 19c):

- Periodicity: corresponding points must have the same rotation and the same displacement, so the internal actions must be equal and opposite.
- Polar symmetry: the structure loaded in pure shear has a polar symmetry with respect to the midpoint between each couple of vertical struts (black dots in Figure II - 19) and, similarly, also the midpoints of the vertical struts act as points of polar symmetry. Consequently, the bending moment must cancel in those points.

Additionally, suppose that an alternative unit cell to the one shown in Figure II - 19c was considered, which is obtained by translating the "selection window" of *L/2* in direction *1*, so that the free extremity of the horizontal struts of the new cell becomes coincident with the midpoint between the vertical beams of the old one (black dot in Figure II - 19c). These two unit cells are perfectly equivalent because of the periodicity of the lattice, so they must have the same shear modulus and the same actions at corresponding points. Such consideration leads to the calculation of the shear forces on the horizontal beams and finally all the forces acting on the unit cell are determined (Figure II - 19c).

Once the loads acting on the unit cell are known, it is possible to calculate the displacements induced by modelling the cell walls as Euler beams and invoking

Castigliano's Second Theorem in order to get the elastic constants in the principal directions through the *compliance matrix method*. The geometrical details of the unit cell are shown in Figure II - 20. In the following, the derivation of the expression for each elastic constant will be discussed.

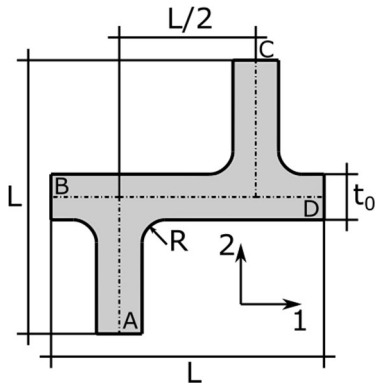

Figure II - 20. Detailed scheme of the unit cell solved analytically.

2.2.7.1.1 Elastic modulus in direction 1 (E_{11})

The behavior of the staggered structure in direction 1 is very similar to that of the regular square structure, with the only difference that it is not symmetric with respect to axis 1. On the other hand, due to the symmetry with respect to axis 2, only half of the structure was modeled, as shown in Figure II - 21. Obviously, when computing the elastic energy, the value obtained must be multiplied by 2.

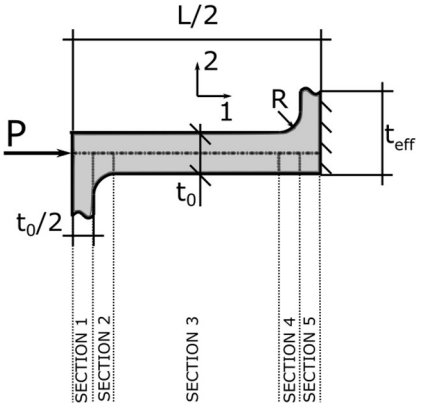

Figure II - 21. Beam structure used to calculate E_{11} for the staggered square structure.

The in-plane thickness *t* of the sections is variable along the axis of the strut (an axial coordinate *x* has to be defined, from left to right), and consequently the strut has to be divided into five segments along the same axis (Figure II - 21):

Section 1: $(0 \leq x_1 \leq \frac{t_0}{2})$: $t(x_1) = t_{eff}$

Section 2: $(0 \leq x_2 \leq R)$: $t(x_2) = t_0 + R - \sqrt{R^2 - (x_2 - R)^2}$

Section 3: $(0 \leq x_3 \leq \frac{L}{2} - 2R - t_0)$: $t(x_3) = t_0$

Section 4: $(0 \leq x_4 \leq R)$: $t(x_4) = t_0 + R - \sqrt{R^2 - {x_4}^2}$

Section 5: $(0 \leq x_5 \leq \frac{t_0}{2})$: $t(x_5) = t_{eff}$

The procedure to obtain the expression of E_{11} is the same as described for the calculation of the elastic modulus of the regular square structure and results in Eq. (II – A4)

2.2.7.1.2 Elastic modulus in direction 2 (E_{22})

The calculation of E_{22} could be simplified by exploiting the polar symmetry of the structure, so that only the part of the unit cell shown in Figure II - 22 had to be solved.

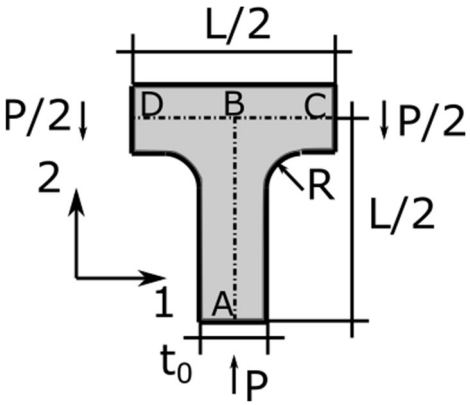

Figure II - 22. Beam structure used to calculate E_{22} for the staggered square structure.

The structure can be represented by three beams (AB, CB, and DB) that join in node B and that obviously have a variable cross-section, as already discussed. The in-plane thickness of the AB beam varies exactly as described for the shear modulus of the regular square structure (proceeding from A to B), while the other two are (moving from D to B and C to B):

$0 \le x_1 \le \frac{L}{4} - 2 - \frac{t_0}{2}: t(x_1) = t_0$

$0 \le x_2 \le R: t(x_2) = t_0 + R - \sqrt{R^2 - {x_2}^2}$

$0 \le x_3 \le \frac{t_0}{2}: t(x_3) = t_{eff}$

For each beam the elastic energy results from Eq. (II – 10):

$$U_{AB} = \frac{1}{2}\sum_{n=1}^{3}\int_0^{x_{n,0}} \frac{N(x_n)^2}{E_s \cdot A_n(x_n)} dx_n$$

$$U_{CB} = U_{DB} = \frac{1}{2}\sum_{n=1}^{3}\int_0^{x_{n,0}} k_t \frac{T(x_n)^2}{G_s \cdot A_n(x_n)} dx_n + \frac{1}{2}\sum_{n=1}^{3}\int_0^{x_{n,0}} \frac{M(x_n)^2}{E_s \cdot I_n(x_n)} dx_n$$

The total elastic energy calculated from this structure has to be multiplied by 2 in order to have the correct displacement of the unit cell.

$$U_T = 2(U_{AB} + U_{CB} + U_{DB})$$

At this point, the vertical (in direction 2) displacement of the unit cell δ can be calculated (using Castigliano's theorem, Eq. (II – 9)):

$$\delta = \frac{\partial U_T}{\partial P}$$

Finally, the elastic modulus in direction 2 can be obtained:

$$E_{22} = \frac{\sigma_{22}}{\varepsilon_{22}} = \frac{\frac{P}{bL}}{\frac{\delta}{L}} = \frac{P}{\delta}\frac{1}{b}$$

At this point, substituting δ leads to Eq. (II – A5) is obtained.

2.2.7.1.3 Poisson's coefficient

Poisson's coefficient is calculated exactly in the same way as for the regular square structure, considering the diagram of Figure II - 22.

$$\left.\begin{aligned} \nu_{21} = \frac{\varepsilon_{11}}{\varepsilon_{22}} = \frac{\frac{\delta_1}{L}}{\frac{\delta_2}{L}} = \frac{\delta_1}{\delta_2} \\ \delta_1 = \nu_s t_{eff}\frac{\delta_2}{L} \end{aligned}\right\} \Rightarrow \nu_{21} = \nu_s \frac{t_{eff}}{L}$$

The structure being orthotropic, from Eq. (II - 3) it results that v_{21} is:

$$\nu_{12} = \nu_{21}\frac{E_{11}}{E_{22}}$$

The previous two equations are reported in the Appendix as Eq. (II – A6) and Eq. (II – A7).

2.2.7.1.4 Shear modulus

The calculation of G_{12} could be simplified by exploiting the polar symmetry of the structure, so that only the part of the unit cell shown in Figure II - 23 had to be solved.

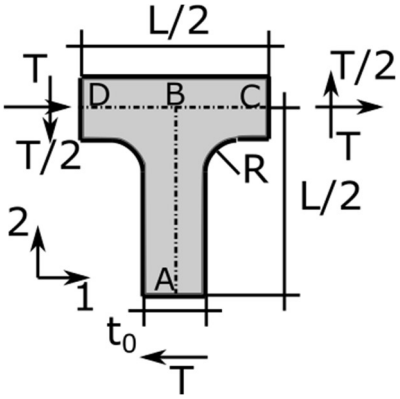

Figure II - 23. Beam structure used to calculate G_{12} for the staggered square structure.

The geometry of the structure is that already described for the elastic modulus in direction 2. For each beam the elastic energy results:

$$U_{AB} = \frac{1}{2}\sum_{n=1}^{3}\int_0^{x_{n,0}} k_t \frac{T(x_n)^2}{G_s \cdot A_n(x_n)}dx_n + \frac{1}{2}\sum_{n=1}^{3}\int_0^{x_{n,0}} \frac{M(x_n)^2}{E_s \cdot I_n(x_n)}dx_n$$

$$U_{CB} = U_{DB} = \frac{1}{2}\sum_{n=1}^{3}\int_0^{x_{n,0}} \frac{N(x_n)^2}{E_s \cdot A_n(x_n)}dx_n + \frac{1}{2}\sum_{n=1}^{3}\int_0^{x_{n,0}} k_t \frac{T(x_n)^2}{G_s \cdot A_n(x_n)}dx_n + \frac{1}{2}\sum_{n=1}^{3}\int_0^{x_{n,0}} \frac{M(x_n)^2}{E_s \cdot I_n(x_n)}dx_n$$

The elastic energy calculated from this structure has to be multiplied by 2 in order to have the total elastic energy of the unit cell.

$$U_T = 2(U_{AB} + U_{CB} + U_{DB})$$

At this point, the sum δ of the displacements of the extremities of the beams making up the unit cell of Figure II - 19c results (Castigliano's theorem):

$$\delta = \frac{\partial U_T}{\partial T}$$

The shear modulus can be then computed according to the following formula (compliance matrix method):

$$G_{12} = \frac{\tau_{12}}{\gamma_{12}} = \frac{\frac{T}{bL}}{\frac{\delta}{L}} = \frac{T}{\delta}\frac{1}{b}$$

Finally, substituting δ, Eq. (II – A8) is obtained.

2.2.7.2 FE model of the staggered square structure

Among the many different choices of unit cells, the FE model of the staggered structure was based on the geometry shown in Figure II - 24, because it is the easiest on which to apply the boundary conditions. The elastic constants were calculated by implementing the *stiffness matrix* method.

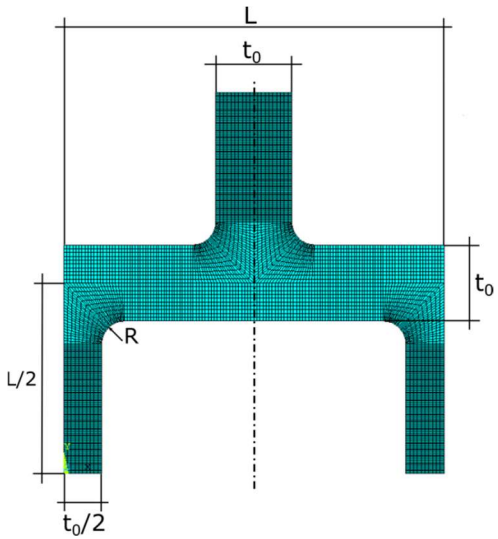

Figure II - 24. FE model of the unit cell of the staggered square structure.

A convergence analysis was carried out to verify the optimal mesh refinement for the various combinations of the geometrical parameters: the mesh was deemed acceptable when the error on each elastic constant with respect to the finest mesh was below 0.5% (in Figure II - 25, an example of a convergence analysis).

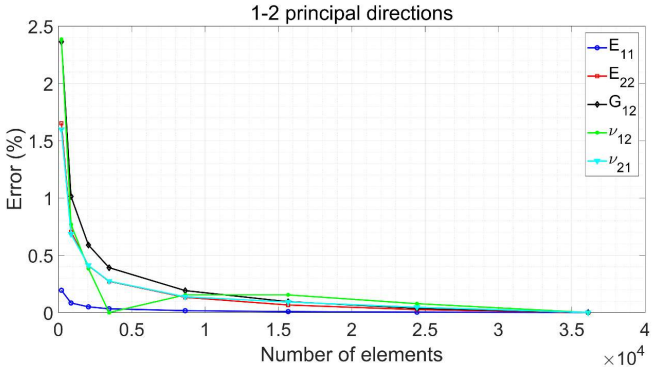

Figure II - 25. Example of a convergence analysis for the FE model of the staggered square unit cell ($t_0^* = 0.2$, $R^* = 0$).

2.2.7.3 *Fitting of the analytical model to the FE results: staggered square structure*

The fit was accomplished by searching a bivariate polynomial function of several parameters which could accurately predict the dependence of t_{eff}^* on t_0^* and R^*. This function was then substituted into the analytical expression of the elastic constants to obtain the complete model:

$$\frac{t_{eff_c}(t_0^*,R^*)}{L} = A_c + B_c\, t_0^* + C_c\, R^* + D_c\, t_0^*\, R^* + E_c\, t_0^{*2} + F_c\, R^{*2} + G_c t_0^{*2} R^* + H_c\, t_0^* R^{*2} + I_c\, t_0^{*2}\, R^{*2} + J_c t_0^{*3} + K_c R^{*3} + L_c t_0^{*3} R^* + M_c t_0^{*3} R^{*2} + N_c t_0^* R^{*3} + O_c t_0^{*2}\, R^{*3} + P_c t_0^{*3}\, R^{*3} \quad \text{(II - 14)}$$

Where the subscript *c* indicates the specific elastic constant E_{11}, E_{22}, G_{12}, ν_{21} (ν_{12} was calculated using Eq. (II - 3)). The parameters used to fit the effective thickness for each elastic constant are reported in Table II - 5.

The fit was accomplished by considering five values for the thickness t_0^* (0.04, 0.08, 0.12, 0.16, 0.1) and eight values for the fillet radius R^* (0, 0.01, 0.02, 0.04, 0.06, 0.08, 0.1, 0.15) for a total of forty points (number of FE analyses) for each elastic constant. The fitting function uses a number of parameters that is much lower than

the number of points, thus ensuring a low error also for values between the points considered. The values of t^*_{eff} and the percentage errors between the results of the fitted model and the FE model for t^*_{eff} are shown in contour plots as a function of t^*_0 and R^* for E_{11}, E_{22}, G_{12} and v_{21} in Figure II - 26, Figure II - 27, Figure II - 28 and Figure II - 29, respectively.

Table II - 5. Fit parameters for the effective thickness t^*_{eff} for each elastic constant of the S structure.

Parameter	E_{11}	E_{22}	G_{12}	v_{21}
A	0.000693372	-0.00029663	0.000505266	0.000726801
B	1.06838	1.14853	1.13508	-0.139817
C	-0.398212	0.0720867	0.0607638	0.156298
D	11.0735	5.658	15.1079	14.3162
E	-0.149596	-0.477329	0.557652	8.9652
F	4.7929	-0.732274	-0.350019	-4.7476
G	-73.8996	-32.8788	-142.681	-40.2354
H	-263.477	-13.5098	-149.039	236.1
I	2329.77	172.294	2427.87	-948.113
J	0.569601	10.6175	6.14161	-15.1424
K	-15.1999	3.55033	-2.06282	22.1804
L	157.463	129.187	576.972	45.9484
M	-5893.3	-48.1349	-10102.6	513.459
N	1005.96	32.8522	868.492	342.248
O	-9851.01	-323.785	-15023.4	-8753.23
P	26364	1173.33	71990.9	29340.7

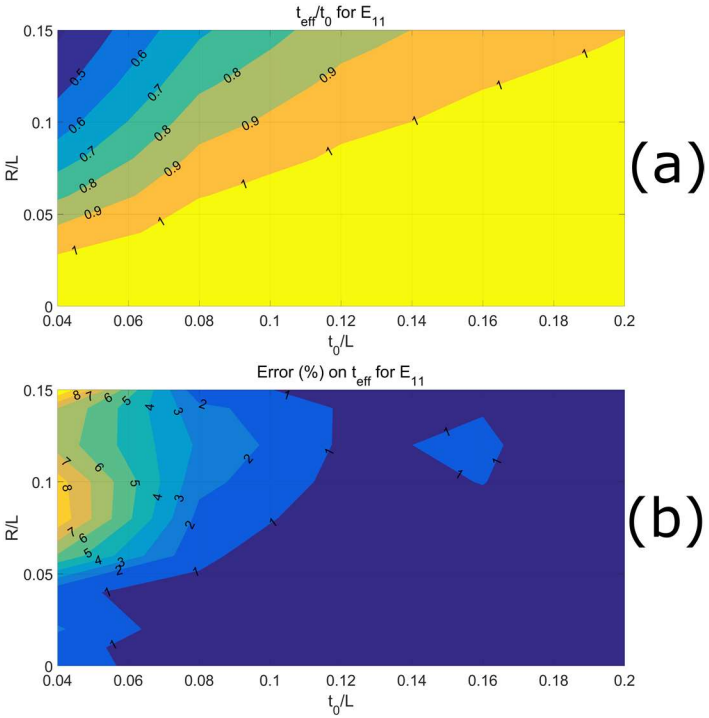

Figure II - 26. (a) Effective thickness calculated from the E_{11} data for the S structure. (b) Percentage fitting error for E_{11} as a function of t_0^* and R^*.

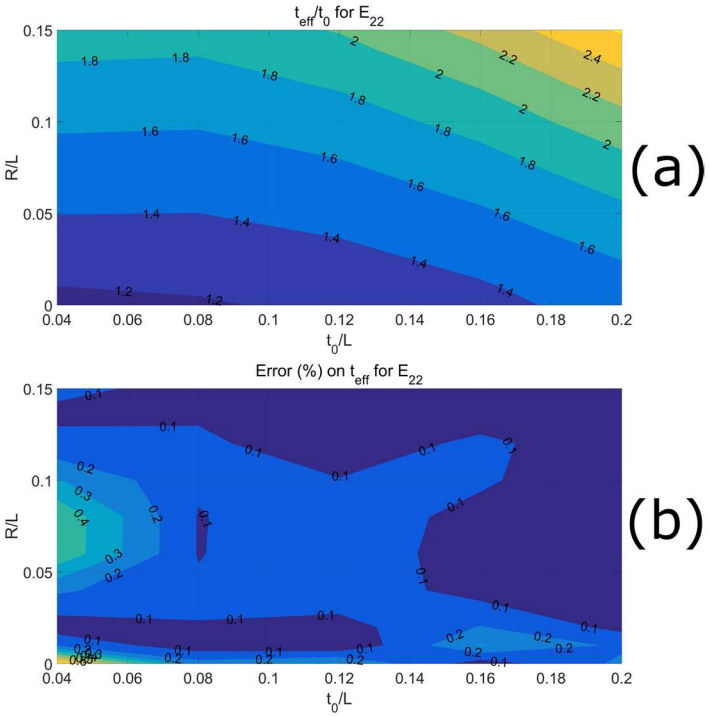

Figure II - 27. (a) Effective thickness calculated from the E_{22} data for the S structure. (b) Percentage fitting error for E_{22} as a function of t_0^* and R^*.

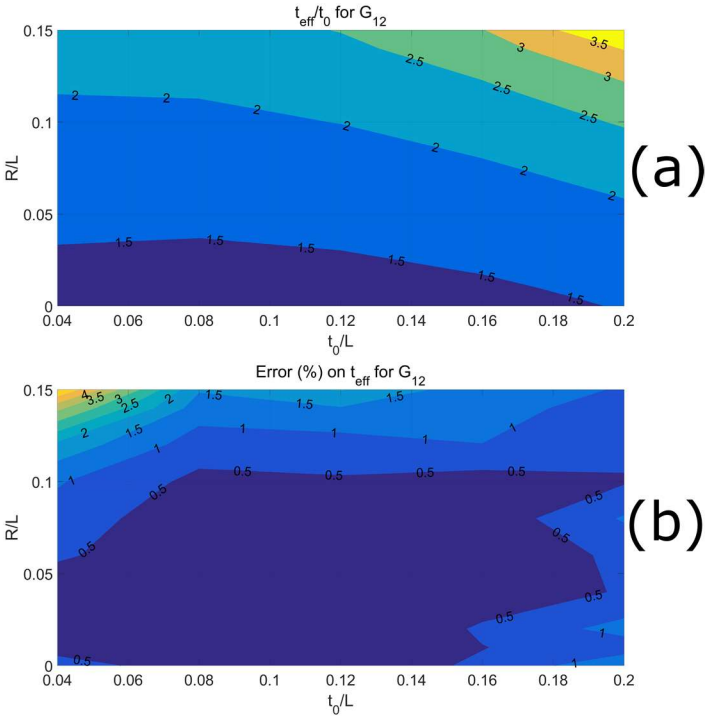

Figure II - 28. (a) Effective thickness calculated from the G_{12} data for the S structure. (b) Percentage fitting error for G_{12} as a function of t_0^* and R^*.

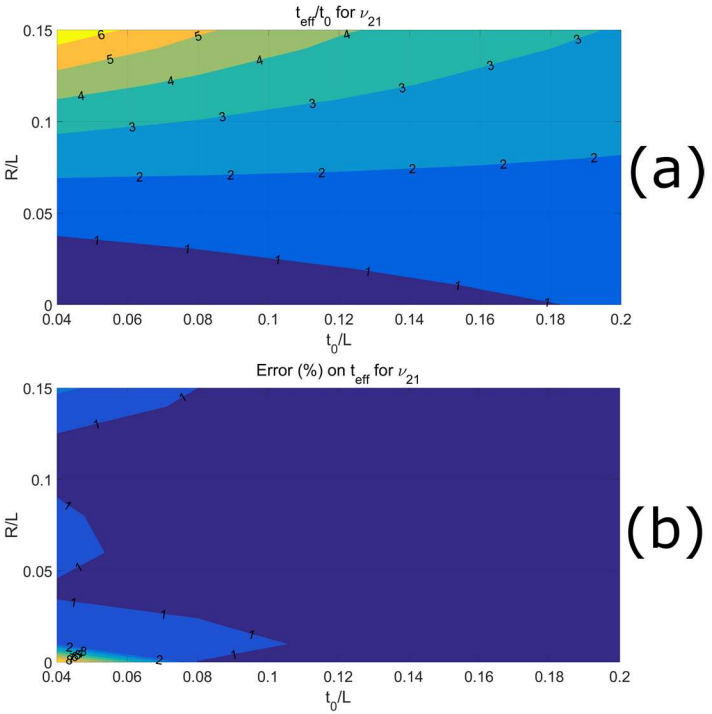

Figure II - 29. (a) Effective thickness calculated from the v_{21} data for the S structure. (b) Percentage fitting error for v_{21} as a function of t_0^* and R^*.

Table II - 6 reports the mean error, the standard deviation on the error and the maximum value of the error on the effective thickness.

Table II - 6. Statistical descriptors of the fitting errors on the effective thickness for the staggered square structure.

	Mean error (%)	Standard deviation on error (%)	Maximum error (%)
t_{eff} for E_{11}	1.32	2.19	9.91
t_{eff} for E_{22}	0.16	0.16	0.82
t_{eff} for G_{12}	0.49	0.41	0.5
t_{eff} for v_{21}	0.76	1.61	10.26

The joint effect is the weakest on E_{11} (Figure II - 26) because in that direction the structure is stretching-dominated, as expected from considerations on the nodal connectivity. The other elastic constants (Figure II - 27, Figure II - 28 and Figure II - 29), on the other hand, clearly show the bending-dominated character of the lattice with higher values of t_{eff}. Indeed, the effective thickness at the joints can be regarded as a parameter accounting for the rotational stiffness of the joints, which is the factor that avoids the collapse of bending-dominated structures: the higher t_{eff}, the stronger is the mechanical role of the joint rotational stiffness. In general, the joint stiffening effect tends to be stronger with respect to the wall thickness t_0^* for thinner beams with greater fillet radius.

2.3 Model development: Stress concentration factors

The semi-analytical model described in the following is aimed at predicting the equivalent stress concentration factor K_{eq} of 2D regular square cell cellular materials with filleted cell-wall junctions. K_{eq} is defined in Eq. (II – 15) as the ratio between the maximum equivalent stress $\overline{\sigma}$ in the fillet and the equivalent stress calculated by using the nominal stress components acting on the unit cell $\overline{\sigma_n}$.

$$K_{eq} = \frac{\overline{\sigma}}{\overline{\sigma_n}} \qquad \text{(II - 15)}$$

This definition can be justified with the fact that lattice structures are not “classical” structures, but rather structures that behave like materials, i.e. the scale of the structure is much smaller than that of the macroscopic component made of this material. Thus, it is possible to apply the stresses that exist at a specific point of the macroscopic component (as if it were a continuum) to the unit cell. Similarly, the equivalent stress $\overline{\sigma_n}$ can be calculated from the stresses on the sides of the unit cell.

The von Mises failure criterion has been chosen to calculate the equivalent stresses because it is the most used theory for ductile metals. The von Mises criterion in plane stress conditions is expressed by Eqs. (II – 16):

$$\overline{\sigma} = \sqrt{\sigma_1^2 + \sigma_2^2 - \sigma_1\sigma_2 + 3\tau_{12}^2} \qquad \text{(II – 16a)}$$

$$\overline{\sigma_n} = \sqrt{\sigma_{1,n}^2 + \sigma_{2,n}^2 - \sigma_{1,n}\sigma_{2,n} + 3\tau_{12,n}^2} \qquad \text{(II – 16b)}$$

The maximum local stresses on the fillet are related to the nominal stress components by a stress concentration factors matrix ***K***, as shown in Figure II - 30:

$$\begin{Bmatrix}\sigma_1\\ \sigma_2\\ \tau_{12}\end{Bmatrix} = \underline{K}\begin{Bmatrix}\sigma_{1,n}\\ \sigma_{2,n}\\ \tau_{12,n}\end{Bmatrix} = \begin{bmatrix}K_{1,1} & K_{1,2} & K_{1,12}\\ K_{2,1} & K_{2,2} & K_{2,12}\\ K_{12,1} & K_{12,2} & K_{12,12}\end{bmatrix}\begin{Bmatrix}\sigma_{1,n}\\ \sigma_{2,n}\\ \tau_{12,n}\end{Bmatrix} \qquad \text{(II - 17)}$$

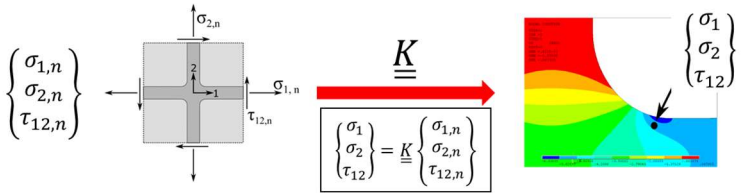

Figure II - 30. The stress concentration factors matrix *K* transforms the homogenous stresses into local stresses at the fillet.

By making explicit Eq. (II - 17), Eqs. (II -18) are obtained:

$$\sigma_1 = K_{1,1}\sigma_{1,n} + K_{1,2}\sigma_{2,n} + K_{1,12}\tau_{12,n} \qquad \text{(II – 18a)}$$
$$\sigma_2 = K_{2,1}\sigma_{1,n} + K_{2,2}\sigma_{2,n} + K_{2,12}\tau_{12,n} \qquad \text{(II – 18b)}$$
$$\tau_{12} = K_{12,1}\sigma_{1,n} + K_{12,2}\sigma_{2,n} + K_{1,12}\tau_{12,n} \qquad \text{(II – 18c)}$$

If the stresses are divided by the nominal equivalent stress $\bar{\sigma}_n$ and thus the $R_1 = \frac{\sigma_{1,n}}{\bar{\sigma}_n}$, $R_2 = \frac{\sigma_{2,n}}{\bar{\sigma}_n}$ and $R_{12} = \frac{\tau_{12,n}}{\bar{\sigma}_n}$ ratios are defined, Eqs. (II – 18) can be rewritten as a function of these non-dimensional ratios:

$$\sigma_1 = \left(K_{1,1}R_1 + K_{1,2}R_2 + K_{1,12}R_{12}\right)\bar{\sigma}_n = C_1\bar{\sigma}_n \qquad \text{(II – 19a)}$$
$$\sigma_2 = \left(K_{2,1}R_1 + K_{2,2}R_2 + K_{2,12}R_{12}\right)\bar{\sigma}_n = C_2\bar{\sigma}_n \qquad \text{(II – 19b)}$$
$$\tau_{12} = \left(K_{12,1}R_1 + K_{12,2}R_2 + K_{12,12}R_{12}\right)\bar{\sigma}_n = C_{12}\bar{\sigma}_n \qquad \text{(II – 19c)}$$

Substituting Eqs. (II – 19) into Eq. (II – 16a), the maximum equivalent stress can be written as

$$\bar{\sigma} = \sqrt{\bar{\sigma}_n^2C_1^2 + \bar{\sigma}_n^2C_2^2 - \bar{\sigma}_n^2C_1C_2 + 3\bar{\sigma}_n^2C_{12}^2} = \bar{\sigma}_n\sqrt{C_1^2 + C_2^2 - C_1C_2 + 3C_{12}^2} \qquad \text{(II – 20)}$$

And finally, the equivalent stress concentration factor K_{eq} can be expressed in a convenient way with the following equation:

$$K_{eq} = \sqrt{C_1^2 + C_2^2 - C_1C_2 + 3C_{12}^2} \qquad \text{(II – 21)}$$

Where

$$C_1 = K_{1,1}R_1 + K_{1,2}R_2 + K_{1,12}R_{12} \quad \text{(II – 22a)}$$
$$C_2 = K_{2,1}R_1 + K_{2,2}R_2 + K_{2,12}R_{12} \quad \text{(II – 22b)}$$
$$C_{12} = K_{12,1}R_1 + K_{12,2}R_2 + K_{12,12}R_{12} \quad \text{(II – 22c)}$$

That is, K_{eq} is a function of the components of the ***K*** matrix and the nominal stresses on the unit cell, as expressed by Eq. (II – 23).

$$K_{eq} = \frac{\overline{\sigma}}{\sigma_n} = f(K_1, K_{12}, \dots, \sigma_{1,n}, \sigma_{2,n}, \tau_{12,n}) \quad \text{(II – 23)}$$

The explicit expressions of the non-dimensional stress ratios R_1, R_2 and R_{12} are:

$$R_1(\sigma_{1,n}, \sigma_{2,n}, \tau_{12,n}) = \frac{\sigma_{1,n}}{\sqrt{\sigma_{1,n}^2 + \sigma_{2,n}^2 - \sigma_{1,n}\sigma_{2,n} + 3\tau_{12,n}^2}} \quad \text{(II – 24a)}$$
$$R_2(\sigma_{1,n}, \sigma_{2,n}, \tau_{12,n}) = \frac{\sigma_{2,n}}{\sqrt{\sigma_{1,n}^2 + \sigma_{2,n}^2 - \sigma_{1,n}\sigma_{2,n} + 3\tau_{12,n}^2}} \quad \text{(II – 24b)}$$
$$R_{12}(\sigma_{1,n}, \sigma_{2,n}, \tau_{12,n}) = \frac{\tau_{12,n}}{\sqrt{\sigma_{1,n}^2 + \sigma_{2,n}^2 - \sigma_{1,n}\sigma_{2,n} + 3\tau_{12,n}^2}} \quad \text{(II – 24c)}$$

It is easy to prove that these ratios are bounded, and they can assume values between a minimum and a maximum value:

$$-\frac{2}{\sqrt{3}} \leq R_1 \leq +\frac{2}{\sqrt{3}}$$
$$-\frac{2}{\sqrt{3}} \leq R_2 \leq +\frac{2}{\sqrt{3}}$$
$$-\frac{1}{\sqrt{3}} \leq R_{12} \leq +\frac{1}{\sqrt{3}}$$

These bounds can be found simply by calculating the minimum and the maximum of the previous functions.
It is important to highlight that R_{11}, R_{22} and R_{12} cannot freely assume any possible real number in the previously reported bounds because they are not completely independent one from the other (all three depend on the three stresses due to the normalization). For example, if $R_{11} = 0$ and $R_{22} = 0$ then R_{12} can be only $\frac{1}{\sqrt{3}}$. This is also the reason why Eqs. (II - 24) can be further simplified by rewriting them in cylindrical coordinates (Figure II - 31):

$$\sigma_{1,n} = R\, sin(\varphi)\, cos(\theta) \quad \text{(II – 25a)}$$
$$\sigma_{2,n} = R\, sin(\varphi)\, sin(\theta) \quad \text{(II – 25b)}$$
$$\tau_{12,n} = R\, cos(\varphi) \quad \text{(II – 25c)}$$

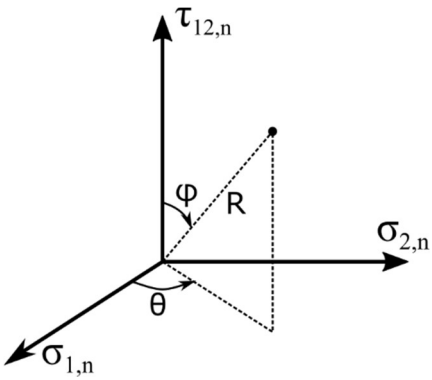

Figure II - 31. Cylindrical reference system with the homogenous material stresses as axes.

Substituting Eqs. (II – 25) into Eqs. (II – 24), the following equations are obtained:

$$R_1(\sigma_{1,n}, \sigma_{2,n}, \tau_{12,n})$$

$$= \frac{R\,sin(\varphi)\,cos(\theta)}{\sqrt{(R\,sin(\varphi)\,cos(\theta))^2 + (R\,sin(\varphi)\,sin(\theta))^2 - R\,sin(\varphi)\,cos(\theta) \cdot R\,sin(\varphi)\,sin(\theta) + 3(R\,cos(\varphi))^2}} \qquad \text{(II – 26a)}$$

$$= \frac{sin(\varphi)\,cos(\theta)}{\sqrt{sin^2(\varphi)\,cos^2(\theta) + sin^2(\varphi)\,sin^2(\theta) - sin^2(\varphi)\,cos(\theta)\,sin(\theta) + 3\,cos^2(\varphi)}}$$

$$R_2(\sigma_{1,n}, \sigma_{2,n}, \tau_{12,n})$$

$$= \frac{R\,sin(\varphi)\,sin(\theta)}{\sqrt{(R\,sin(\varphi)\,cos(\theta))^2 + (R\,sin(\varphi)\,sin(\theta))^2 - R\,sin(\varphi)\,cos(\theta) \cdot R\,sin(\varphi)\,sin(\theta) + 3(R\,cos(\varphi))^2}} \qquad \text{(II – 26b)}$$

$$= \frac{sin(\varphi)\,sin(\theta)}{\sqrt{sin^2(\varphi)\,cos^2(\theta) + sin^2(\varphi)\,sin^2(\theta) - sin^2(\varphi)\,cos(\theta)\,sin(\theta) + 3\,cos^2(\varphi)}}$$

$$R_{12}(\sigma_{1,n}, \sigma_{2,n}, \tau_{12,n})$$

$$= \frac{R\,cos(\varphi)}{\sqrt{(R\,sin(\varphi)\,cos(\theta))^2 + (R\,sin(\varphi)\,sin(\theta))^2 - R\,sin(\varphi)\,cos(\theta) \cdot R\,sin(\varphi)\,sin(\theta) + 3(R\,cos(\varphi))^2}} \qquad \text{(II – 26c)}$$

$$= \frac{cos(\varphi)}{\sqrt{sin^2(\varphi)\,cos^2(\theta) + sin^2(\varphi)\,sin^2(\theta) - sin^2(\varphi)\,cos(\theta)\,sin(\theta) + 3\,cos^2(\varphi)}}$$

Eqs. (II – 26) show that it is thus possible to express ratios R_{11}, R_{22} and R_{12} as a function of two parameters only, θ and φ, instead of the three stresses. The advantage of using Eqs. (II – 26) is that it is possible to obtain all the possible load cases (expressed through the R_{ij} ratios) by varying θ and φ between 0° and 360°.

$$\theta = tan^{-1}\left(\frac{\sigma_{2,n}}{\sigma_{1,n}}\right) \quad \text{(II - 27a)}$$

$$\varphi = cos^{-1}\left(\frac{\tau_{12,n}}{\sqrt{{\sigma_{1,n}}^2+{\sigma_{2,n}}^2}}\right) \quad \text{(II - 27b)}$$

2.3.1 Calculation of the components of the K matrix:

Eqs. (II – 18) show that the components of the stress concentration factors matrix ***K*** can be calculated by applying monoaxial nominal loads on the unit cell. The first column of ***K*** is calculated by applying a monoaxial load in direction *1* on the unit cell (Figure II - 32):

$$K_{1,1} = \frac{\sigma_1}{\sigma_{1,n}}$$

$$K_{2,1} = \frac{\sigma_2}{\sigma_{1,n}}$$

$$K_{12,1} = \frac{\tau_{12}}{\sigma_{1,n}}$$

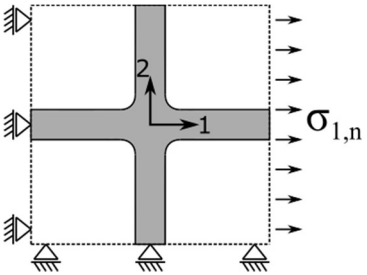

Figure II - 32. Monoaxial load in principal direction 1 applied to the unit cell to calculate the members of the first column of *K*.

The second column of ***K*** is calculated by applying a monoaxial load in direction *2* (Figure II - 33):

$$K_{1,2} = \frac{\sigma_1}{\sigma_{2,n}}$$

$$K_{2,2} = \frac{\sigma_2}{\sigma_{2,n}}$$

$$K_{12,2} = \frac{\tau_{12}}{\sigma_{2,n}}$$

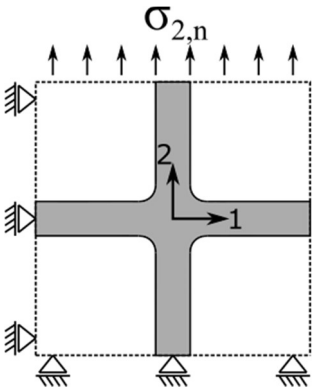

Figure II - 33. Monoaxial load in principal direction 2 applied to the unit cell to calculate the members of the second column of *K*.

The third column of ***K*** is calculated by applying pure shear in the *12* plane (Figure II - 34):

$$K_{1,12} = \frac{\sigma_1}{\tau_{12,n}}$$
$$K_{2,12} = \frac{\sigma_2}{\tau_{12,n}}$$
$$K_{12,12} = \frac{\tau_{12}}{\tau_{12,n}}$$

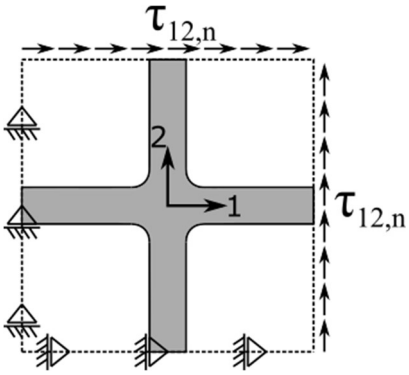

Figure II - 34. Pure shear applied to the unit cell to calculate the members of the third column of *K*.

2.3.2 Issues regarding the calculation of the components of K

The components of ***K*** can be calculated by building an FE model of the unit cell for each combination of the geometrical parameters t_0 and R and by applying the nominal loads. The greatest issue in this procedure is the choice of the point on the fillet where the local stresses σ_1, σ_2, τ_{12} should be extracted. Ideally, all the components of the ***K*** matrix should be calculated in the point in which the highest equivalent local stress is reached. This unfortunately is not trivial because the location where the maximum equivalent stress occurs depends on the ratio between the nominal stress components acting on the unit cell. In other words, given a specific combination of the nominal load, the point where the maximum local stresses occur is not known a priori. This issue is solved by extracting the values of the stresses from the FE model along the fillet radius as a function of angle α (Figure II - 35) and then calculating the components of ***K*** for each α, so that a ***K*** matrix is calculated for each point along the fillet. Note that since the components of ***K*** are calculated as in Subsection 2.3.1, they depend only on the geometry. The non-triviality is related to the fact that what is needed is the ***K*** matrix that causes the maximum K_{eq} (Eq. (II - 21)) and this value and the point on the fillet where it is reached both depend on the combination of the nominal stresses.

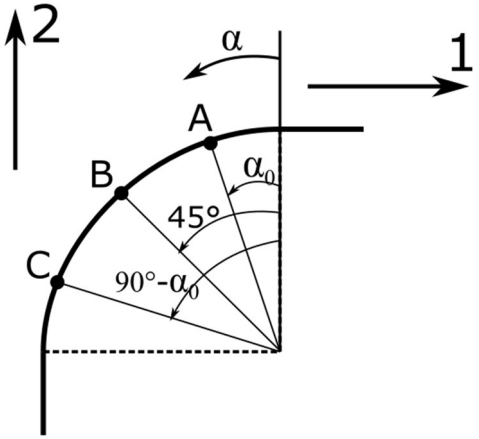

Figure II - 35. Points A, B and C are the locations where the components of the SCF matrix are calculated.

Referring to Figure II - 35, for each geometry, the maximum equivalent stress occurs in a point close to A (prevalently monoaxial load along direction 1, as in Figure II - 36) or C (prevalently monoaxial load along direction 1) or both, in the case of pure shear (Figure II - 37) or biaxial loading in wide fillet radii. On the other hand, point B is critical in the case of pure shear or biaxial loading for sharp fillets (Figure II - 38). It is thus clearly impossible to find a single point on the fillet to use as a reference to calculate ***K***. Therefore, the only viable strategy is to calculate the components of ***K*** at each of the three aforementioned points and then retain only those that correspond to the location of the highest K_{eq}. For practical reasons, locations A, B and C are kept

the same for all the load cases and geometries considered, despite the location of the maximum $\overline{\sigma}$ slightly fluctuates depending on the load ratios and the geometry. Nevertheless, as shown in the next Subsections, the maximum fitting error for each geometry considered (i.e. the maximum error among the fitting error for all the load cases) is reasonably low.

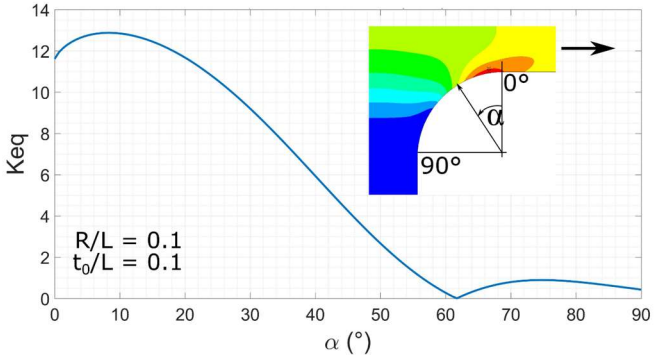

Figure II - 36. Equivalent stress concentration factor K_{eq} along the fillet in the lattice with $R/L = 0.1$ and t_0/L 0.1 under uniaxial load.

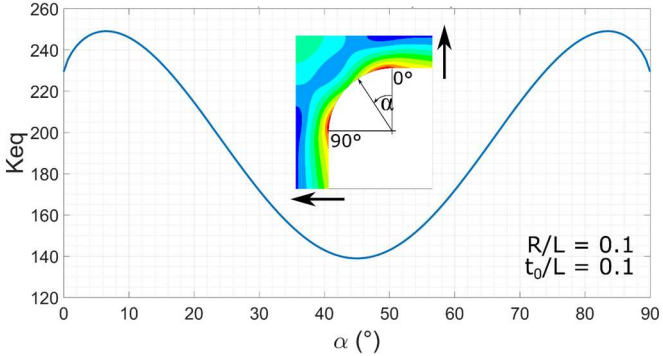

Figure II - 37. Equivalent stress concentration factor K_{eq} along the fillet in the lattice with $R/L = 0.1$ and t_0/L 0.1 under pure shear load.

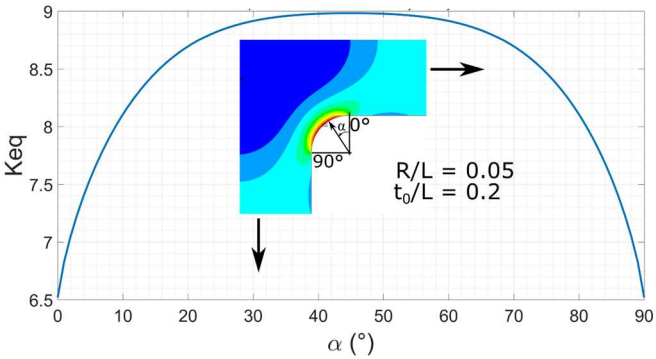

Figure II - 38. Equivalent stress concentration factor K_{eq} along the fillet in the lattice with $R/L = 0.05$ and t_0/L 0.2 under biaxial load.

The value of α_0 is calculated as to minimize the error between the equivalent stress concentration factor K_{eq} in the reference points and the actual maximum values, for all the geometries considered and the load ratios R_1, R_2 and R_{12}. The identification of a numerical quantity to use to find the optimal α_0 is not trivial given the wide range of geometries and load cases involved and the consequent necessity to obtain a parameter that accounts for all of them. Therefore, the maximum % error (defined by Eq. (II - 28)) between the real (from FEM) maximum value of the equivalent stress concentration factor ($K_{eq,FEM}$) and the closest value between the three estimates provided by using points A, B and C ($K_{eq,estimate}$) is calculated considering all the load cases corresponding to each geometry:

$$error(\%) = \frac{K_{eq,estimate} - K_{eq,FEM}}{K_{eq,FEM}} \times 100 \quad \text{(II - 28)}$$

Subsequently, from the maximum % errors corresponding to each point in the domain defined by the geometrical parameters, the Quadratic Mean (QM), the average and the maximum are calculated. The QM is defined according to Eq. (II - 29):

$$QM = \sqrt{\frac{1}{N}\sum_{i=1}^{N\Sigma}(error_{max}(i)^2)} \quad \text{(II - 29)}$$

Where N is the number of data points in the geometrical domain and $error_{max}$ is the maximum % error for each data point.
This procedure is repeated for several positions α of A (expressed as an angle α, defined in Figure II - 35) and the results are shown in Figure II - 39. The position of A is chosen to be $\alpha_0 = 6°$ and, consequently, C is located in $\alpha = 90° - \alpha_0 = 84°$.
Despite this procedure being quite time consuming and tedious, once completed it provides a database of data that can be fitted with functions that consequently

become fast and useful design tools. Indeed, such functions that can calculate the stress concentration factors at the fillet for a wide range of the geometrical parameters and loading ratios avoiding the use of time-consuming FE simulations.

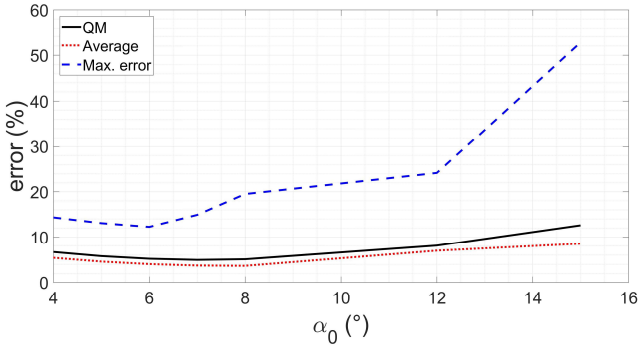

Figure II - 39. Quadratic mean (QM) on the maximum error, average of the maximum error and maximum error of all geometries and load cases as a function of the position α_0 of the critical point A on the fillet.

2.3.3 FE model

The values of the components of the K matrix as a function of the geometrical parameters t_0 and R were obtained with a parametric 2D FE model of the unit cell (Figure II - 40). The cell wall thickness-length ratio $^{t_0}/_{L}$ was varied in the [0.02-0.2] interval, while the fillet radius-cell wall length ratio $^{R}/_{L}$ was varied in the [0.01-0.15] interval. This model is in fact identical to the model used to calculate the elastic constants of the regular square structure, the only difference being a finer mesh at the fillet. The model was solved by applying the boundary conditions described in Subsection 2.3.1.

A convergence analysis was carried out to verify the optimal mesh refinement for the various combinations of the geometrical parameters: the mesh was deemed acceptable when the deviation of the von Mises equivalent stress with respect to the finest mesh was below 0.5%.

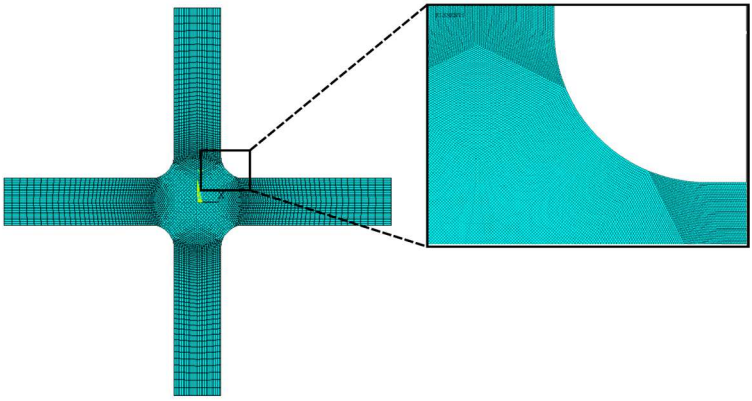

Figure II - 40. Parametric FE model used to calculate the components of the SCF matrix.

2.4 Results and Discussion: Elastic constants

In the following section, the results obtained from the FE analyses and the semi-analytical beam model regarding the dependence of the elastic constants on the geometry of the lattices will be discussed. The careful reader will object that the lattices examined in this work have already been thoroughly discussed in the literature (see, for instance, [7,8,23,24]), nevertheless not accounting for the presence of a fillet radius at the strut joints. Consequently, the discussion will focus on the results deemed more original, and more specifically on the effect of the fillet radius on the elastic constants and the error introduced by neglecting it.

The relative contribution of the fillet radius to the elastic constants of the lattices is quantified with and error-type quantity, defined as the error that would affect the value of the elastic constant if in the calculation the fillet radius was disregarded, that is, assumed zero. Such error is calculated by taking the difference between the elastic constant $C_{el}^{R^*=R_i^*}$ for the lattice with fillet R_i^* and the elastic constant of the corresponding lattice with zero fillet (sharp corners) $C_{el}^{R^*=0}$ and normalizing it by $C_{el}^{R^*=R_i^*}$:

$$error(\%) = \frac{C_{el}^{R^*=R_i^*} - C_{el}^{R^*=0}}{C_{el}^{R^*=R_i^*}} \cdot 100 \qquad \text{(II – 30)}$$

It is noteworthy that the error is not expressed in terms of an absolute value, so it can also be negative.

2.4.1 Regular square structure

2.4.1.1 Regular square structure: E_{xx} and E_{yy}

Consequence of the symmetry of the regular cubic cell is that $E_{xx} = E_{yy}$, so that the results and the discussion apply to both constants. The fillet radius and the cell wall thickness increase the stiffness of the structure, but the effect of the fillet radius is less marked (Figure II - 41). The elastic modulus is linear to the cell wall thickness (as expected, recognizing the stretching-dominated nature), independently on the fillet radius. Nevertheless, this linear behavior is lost as the angle α between the load direction and the principal directions increases (Figure II - 41b for $\alpha = 45°$): switching to a bending-dominated behavior, the effect of t_0^* on E_{xx} increases because the structure switches to a bending dominated behavior. Similarly, the stiffening effect of the fillet becomes more marked as the bending load on the joint increases.

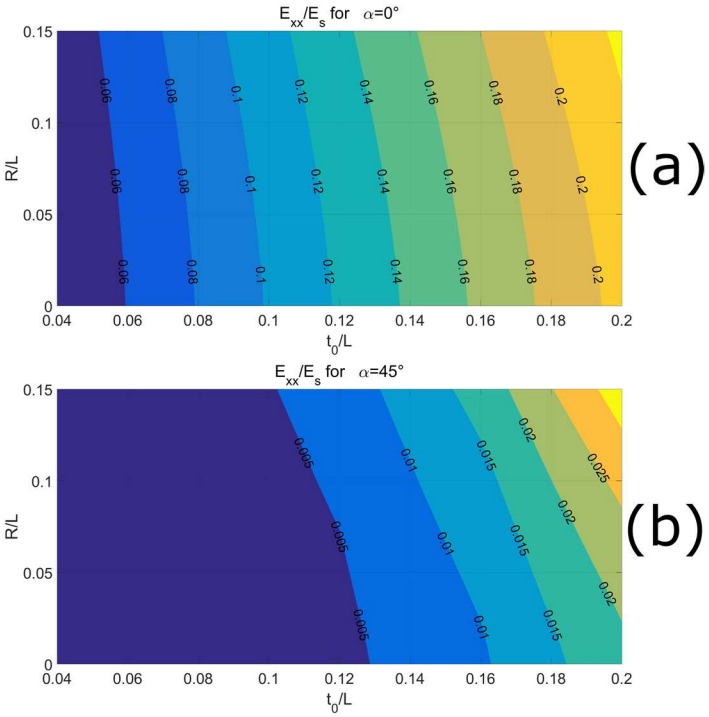

Figure II - 41. Contour plot of the normalized elastic modulus as a function of R^* and t_0^*. (a) $\alpha = 0°$; (b) $\alpha = 45°$.

The off-axis angle *α* has a very strong effect on the elastic properties of the square cell structure and this is clearly shown in Figure II - 42, where the normalized elastic modulus is plotted against *α* for various radii for two cell wall thicknesses $t_0^* = 0.04$ and $t_0^* = 0.2$. The thinner the cell wall, the faster the structure loses its stiffness with increasing *α* and the greater is the fraction of stiffness lost with respect to the value in the principal direction. The increase in the rotational stiffness of the joints caused by the fillet radius reduces the overall compliance of the lattice, but the effect is weaker than that of the cell wall thickness. Moreover, the joint stiffening effect is less marked in thin-walled cells (compare Figure II - 41and Figure II - 42) because of their high compliance. Similarly, it can be also observed that the stiffening effect of the fillet radius increases with the angle. Note that, recognizing that the structure has four axes of symmetry, one every 45°, it is enough to plot the properties as a function of *α* only between 0° and 45° because then the behavior is specular.

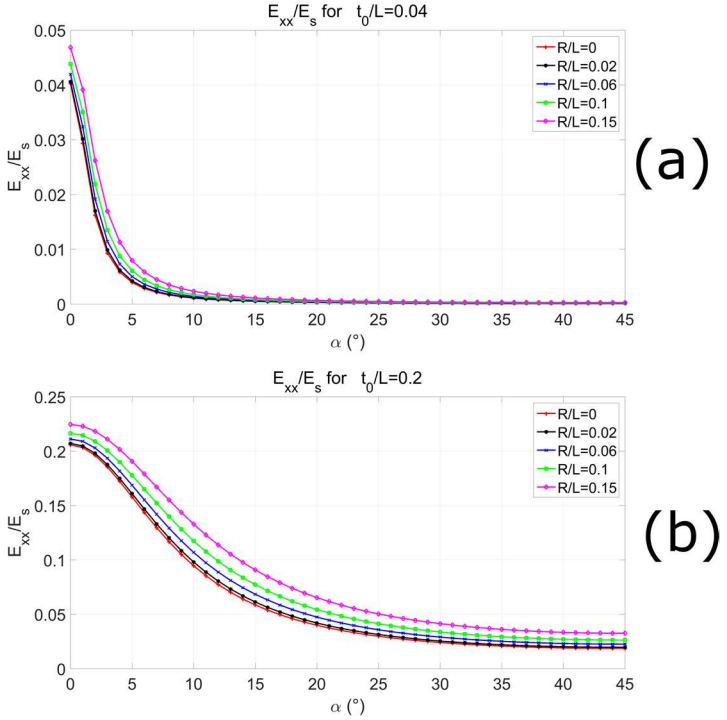

Figure II - 42. Elastic modulus vs α for different fillet radii: (a) at $t_0^* = 0.04$; (b) at $t_0^* = 0.2$.

Disregarding the fillet radius, the values of the elastic modulus calculated by a beam-based analytical model can be affected by a considerable error, up to 50% for the values of R^* and t_0^* considered in this article at $\alpha = 45°$ (Figure II - 43). In general, the error is higher for thinner cell walls because of the lower stiffness of these structures. The error is strongly affected by the off-axis angle because the effect of the fillet radius increases with α, as stated previously and shown in Figure II - 44: it is at a minimum at $\alpha = 0°$, then it rapidly increases until $\alpha = 10° - 20°$ (depending on R^* and t_0^*) and then it stays constant until 45°.

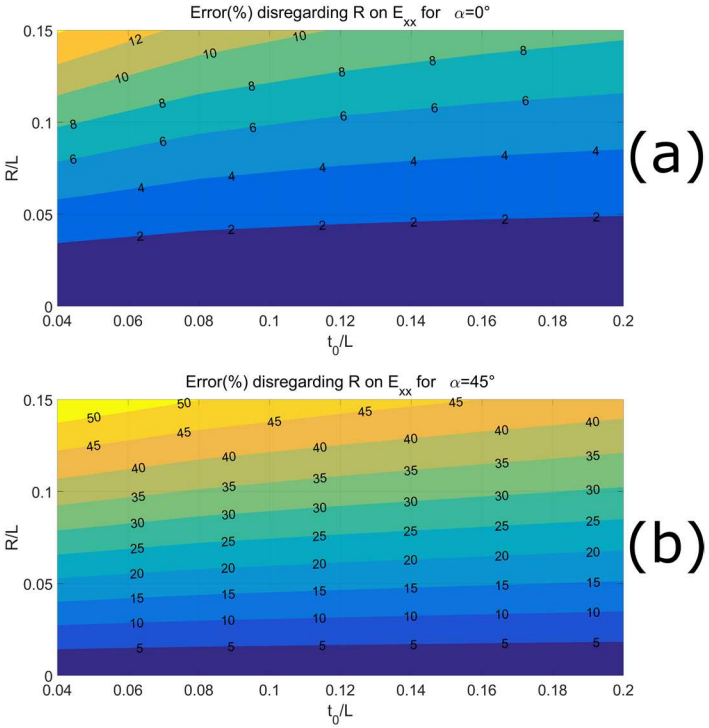

Figure II - 43. Contour plots of the error in % between the elastic modulus calculated taking into account the fillet radius and that calculated disregarding it. (a) $\alpha = 0°$; (b) $\alpha = 45°$.

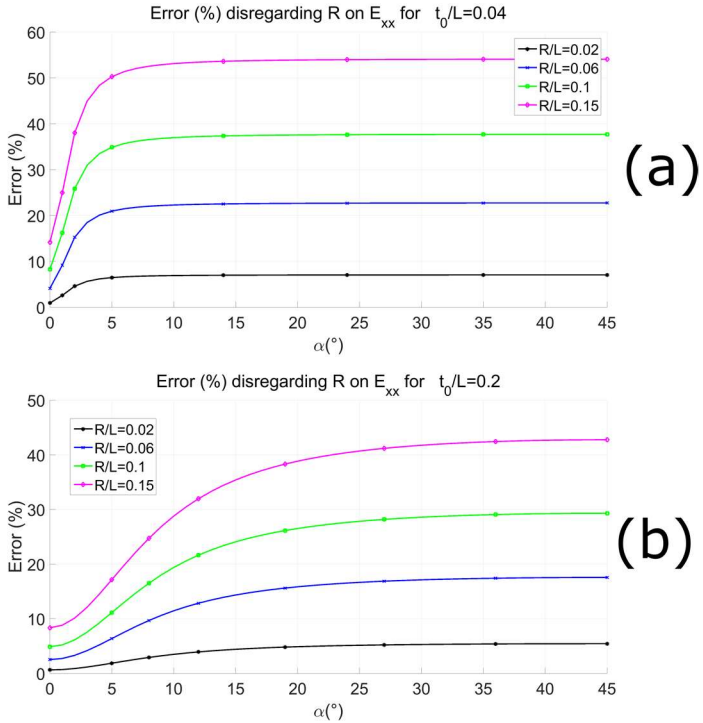

Figure II - 44. Error in % between the elastic modulus calculated taking into account the fillet radius and that calculated disregarding it as a function of the off-axis angle *α*. (a) at $t_0^* = 0.04$; (b) at $t_0^* = 0.2$.

The overall error on the elastic modulus is below 0.1% for all the values of R^* and t_0^* in the principal directions. The error has been evaluated also for other angles up to 45° and it has been observed that the error increases slightly to reach a maximum of 0.6% at 45°. This increase in error is mainly due to the lower accuracy achieved for the fit of Poisson's coefficient which has a greater effect on the bending-dominated configuration.

2.4.1.2 Regular square structure: G_{xy}

The behavior of the shear modulus with respect to the angle *α* is the inverse of the behavior of the elastic modulus, since pure shear loading at $\alpha = 0°$ translates as bending actions on the cell walls while at $\alpha = 45°$ as axial actions. Consequently, the effect of the cell wall thickness t_0^* on the shear modulus is highly non-linear at $\alpha = 0°$ while it becomes linear at 45° as shown in Figure II - 45a and Figure II - 45b, respectively.

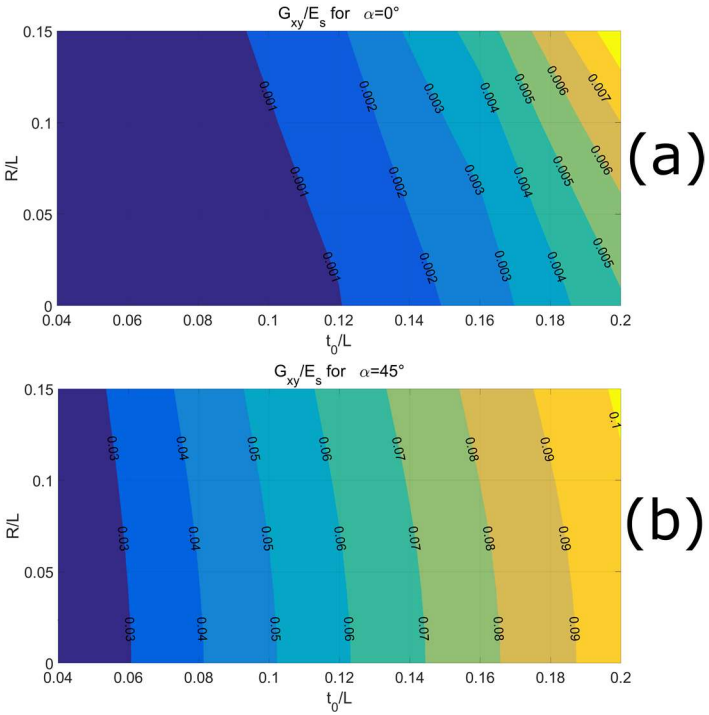

Figure II - 45. Contour plot of the normalized shear modulus as a function of R^* and t_0^*. (a) $\alpha = 0°$; (b) $\alpha = 45°$.

Indeed, the effect of the fillet radius on the shear modulus decreases with the angle, but it is more marked for cell walls with a higher thickness-to-length ratio as for the elastic modulus (Figure II - 46).

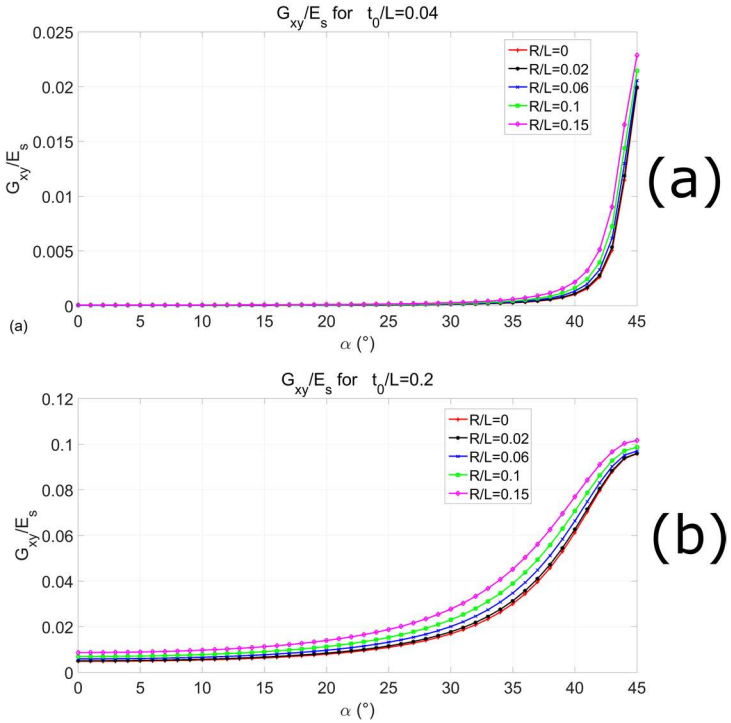

Figure II - 46. Shear modulus vs α for different fillet radii: (a) at $t_0^* = 0.04$; (b) at $t_0^* = 0.2$.

The same observations done for the elastic modulus apply to the error caused by disregarding the fillet radius (Figure II - 47 and Figure II - 48), only inverted with respect to the angle, as previously mentioned.

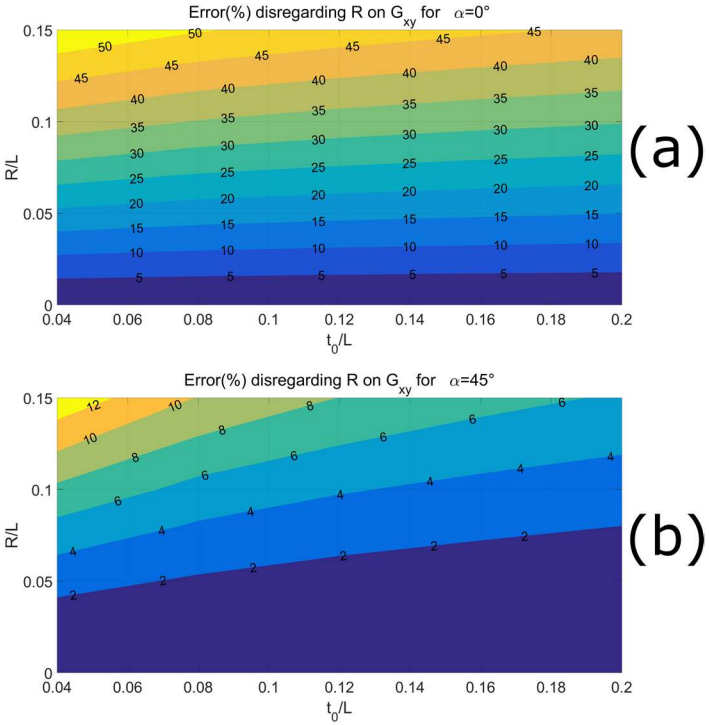

Figure II - 47. Contour plots of the difference in % between the shear modulus calculated considering the fillet radius and that calculated disregarding it. (a) $\alpha = 0°$; (b) $\alpha = 45°$.

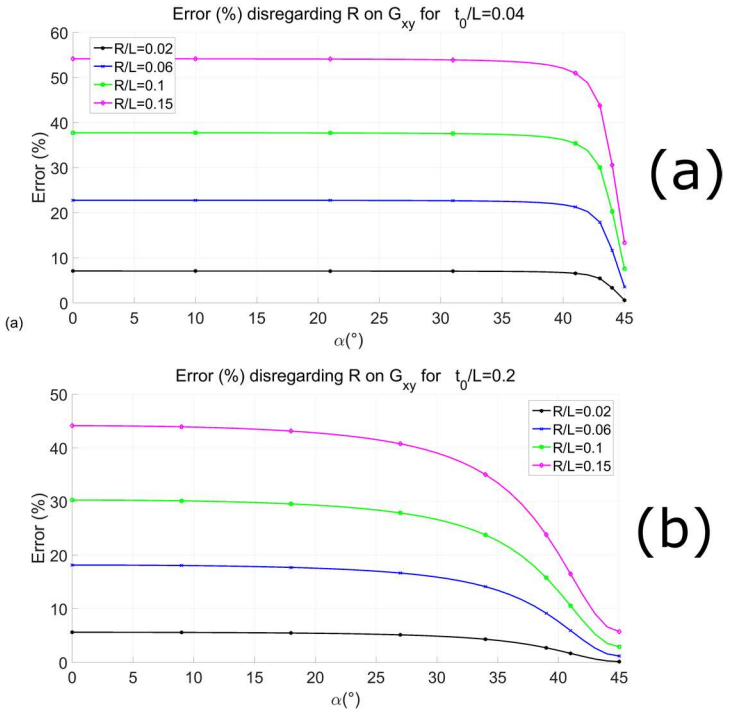

Figure II - 48. Error in % between the shear modulus calculated considering the fillet radius and that calculated disregarding it as a function of the off-axis angle *α*. (a) at $t_0^* = 0.04$; (b) at $t_0^* = 0.2$.

The percentage error between the analytic model obtained by substituting the fitted effective thickness and the FE results for the shear modulus has been evaluated also for all the angles up to 45° and it has been observed that the error decreases with the angle from a maximum of about 0.6% at 0° to a maximum of about 0.05% at 45°.

2.4.1.3 Regular square structure: v_{xy} and v_{yx}

Poisson's coefficient v_{xy} is linear with the wall thickness at $\alpha = 0°$, while linearity is lost at increasing *α*, similarly to the elastic modulus. The structure being more compliant when loaded off-axis, it displays a more intense lateral expansion at increasing angles and, consequently, a higher Poisson's coefficient (Figure II - 49). Nonetheless, the careful reader can notice that for very small values of *α* (at which axial actions dominate) Poisson's effect is more marked for higher fillet radii but this behavior is reversed at higher angles. In other words, the fillet radius increases

Poisson's effect synergistically with the cell wall thickness at low angles (Figure II - 49a and Figure II - 50a), while it decreases it as the lattice is tilted (Figure II - 49b and Figure II - 50). The explanation for this is straightforward: when axial actions prevail, a higher fillet radius (and thickness) favors lateral expansion but as soon as bending actions prevail, a bigger radius stiffens the structure, hindering Poisson's effect.

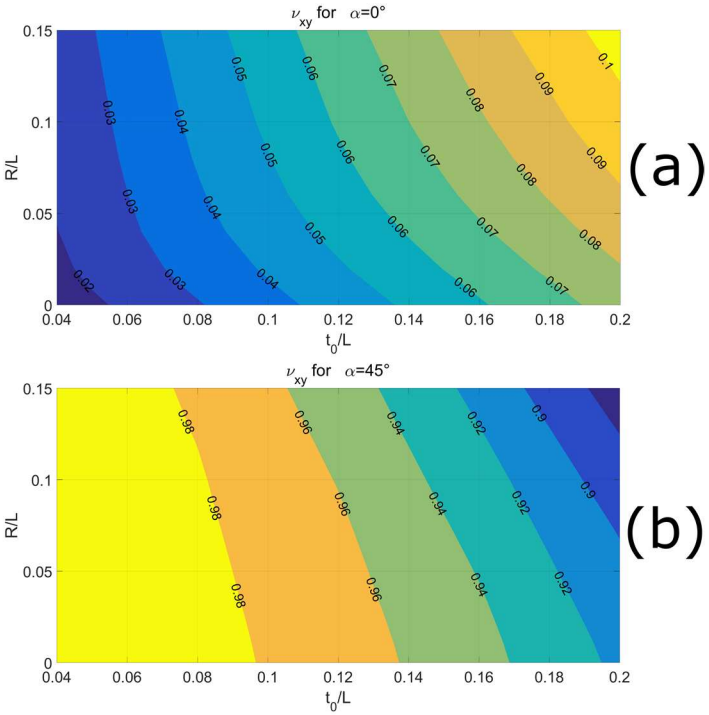

Figure II - 49. Contour plot of the normalized shear modulus in the principal directions as a function of R^* and t_0^*. (a) $\alpha = 0°$; (b) $\alpha = 45°$.

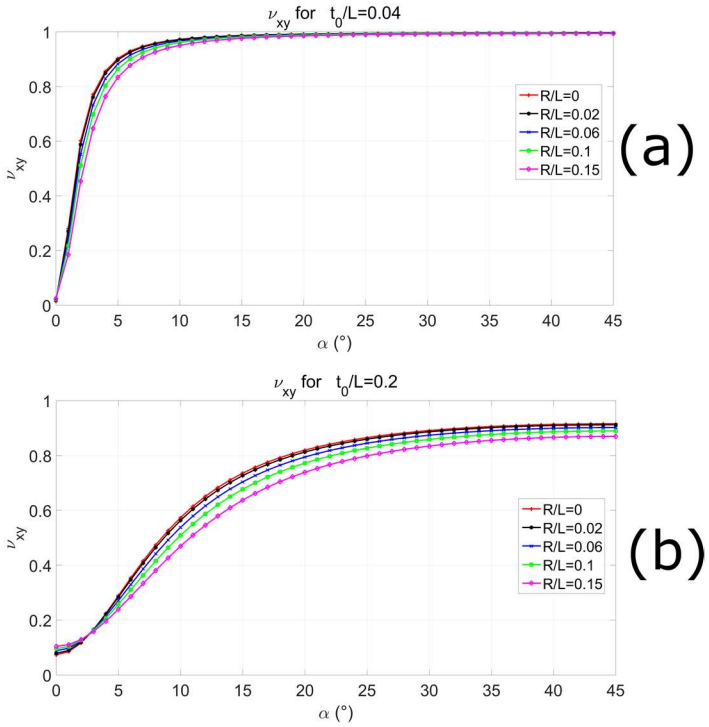

Figure II - 50. Poisson's coefficient vs α for different fillet radii: (a) at $t_0^* = 0.04$; (b) at $t_0^* = 0.2$.

The error caused by disregarding the fillet radius reflects the previous considerations. For very small angles the error is higher for more slender cell walls than as the angle increases, the highest values for the error are obtained for increasingly "stubbier" cell walls (Figure II - 51a and Figure II - 52). Moreover, due to the inversion of the behavior of Poisson's coefficient with respect to the fillet radius, the error becomes negative after few degrees of rotation (Figure II - 51a and Figure II - 52).

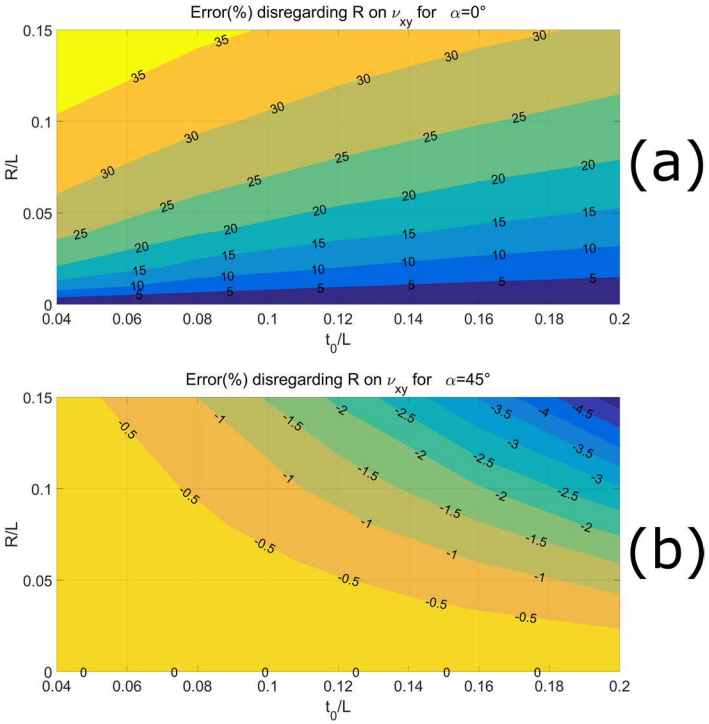

Figure II - 51. Contour plots of the difference in % between Poisson's coefficient calculated taking into account the fillet radius and that calculated disregarding it. (a) $\alpha = 0°$; (b) $\alpha = 45°$.

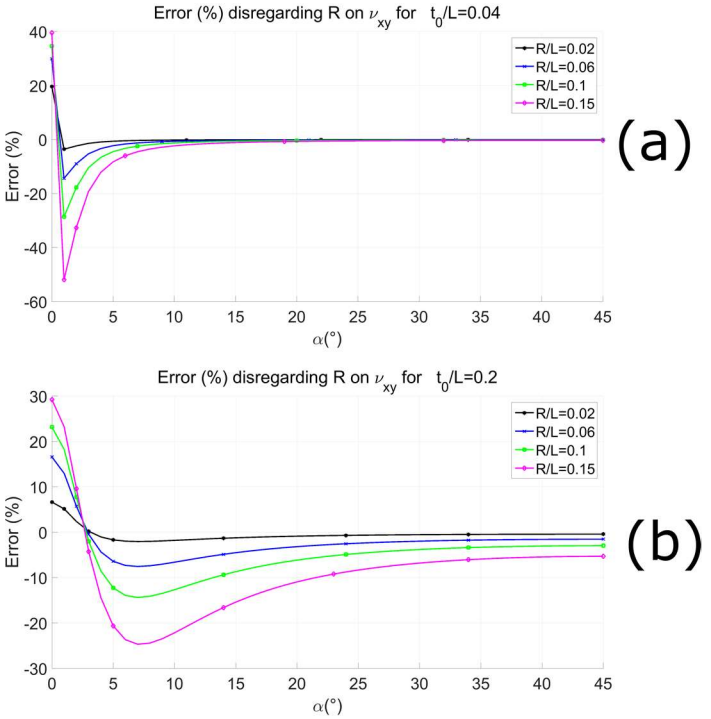

Figure II - 52. Error in % between Poisson's coefficient calculated taking into account the fillet radius and that calculated disregarding it as a function of the off-axis angle *α*. (a) at $t_0^* = 0.04$; (b) at $t_0^* = 0.2$.

The fitting error on Poisson's coefficient in the principal directions is considerably higher than that for the other elastic constants as it reaches a maximum of 5%. This is due to the fact that Poisson's coefficient displays a more complex behavior with respect to the fillet radius than that assumed by classical beam theory. The fitting error sharply decreases with the angle to reach about 0.06% at 45°, as the bending actions on the cell walls increase and the simple beam model is able to capture more accurately the displacements in the structure. In fact, at higher angles the highest error occurs for stubbier cell walls for which the displacements are less accurately predicted by Euler-Bernoulli beam theory.

2.4.2 Staggered square structure

2.4.2.1 Staggered square structure: E_{xx} and E_{yy}

The orthotropic nature of the lattice can be exploited to simplify the discussion of the results. Indeed, the in-plane elastic moduli E_{xx} and E_{yy} can be treated together because their behavior is perfectly reversed with respect to the off-axis angle α. Thus, to avoid confusion and to simplify the discussion, only E_{xx} will be described, but the reader should keep in mind that the following hold: $Exx(\alpha = 0°) = E_{11} = Eyy(\alpha = 90°)$ and $Exx(\alpha = 90°) = E_{22} = Eyy(\alpha = 0°)$. So now on, α will always indicate the off-axis angle with respect to principal direction *1*.

E_{11} depends on R^* and t_0^* very similarly to the regular square structure (compare Figure II - 53a with Figure II - 41a), because the analytical model of the staggered square structure loaded in direction *1* is that of an axially loaded strut. Nevertheless, this an approximation because, as shown in Figure II - 54, the symmetry axis of the structure in direction *1* does not pass for the axis of the cell walls. Thus, even if the cell walls appear to be subjected to purely axial loads, in truth, also bending actions are induced by the non-uniform distribution of loads in the cell walls. Indeed, the force lines in the struts are deviated from direction 1 by the presence of the asymmetric junctions. This behavior is captured only by the continuum elements of the FE model (Figure II - 54) and clearly not by a modelling approach based on beam elements. Indeed, a careful observation allows to notice that there are slight differences between the contour plots of Figure II - 53a and Figure II - 41a. Not surprisingly, this effect is more marked for thinner beams. As expected, the fillet radius has a stronger effect on the elastic modulus in *direction 2* (E_{22}) (Figure II - 53b) because the structure is bending dominated.

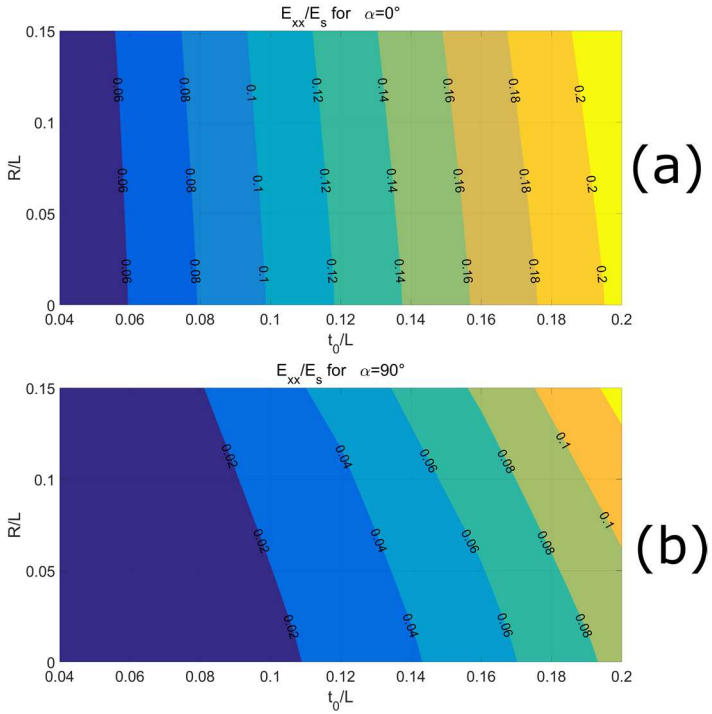

Figure II - 53. Contour plot of the normalized elastic modulus as a function of R^* and t_0^*. (a) $\alpha = 0°$; (b) $\alpha = 90°$.

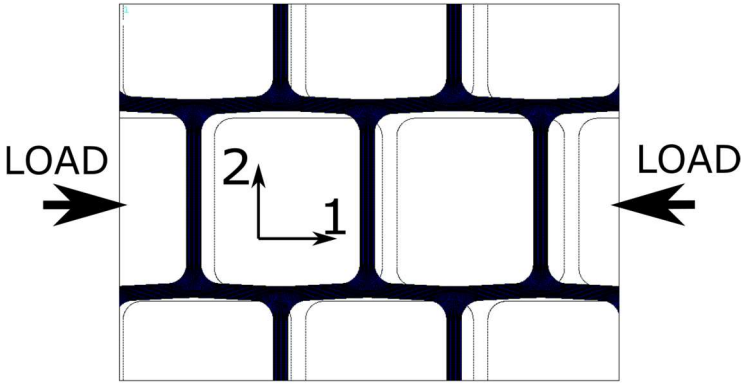

Figure II - 54. Asymmetric deformation due to pure axial load in direction *1* (FE model). The dashed lines indicate the undeformed model.

Considering the topological characteristics of the lattice, it is not surprising that E_{11} is considerably higher than E_{22}. Nevertheless, the minimum in elastic modulus is observed at 45°, similarly to the regular square lattice (Figure II - 55). The drop in elastic modulus with the angle is more intense for structures with thin cell walls. Moreover, the effect of the fillet radius increases form direction *1* to direction *2* (α increasing from 0° to 90° in Figure II - 55).

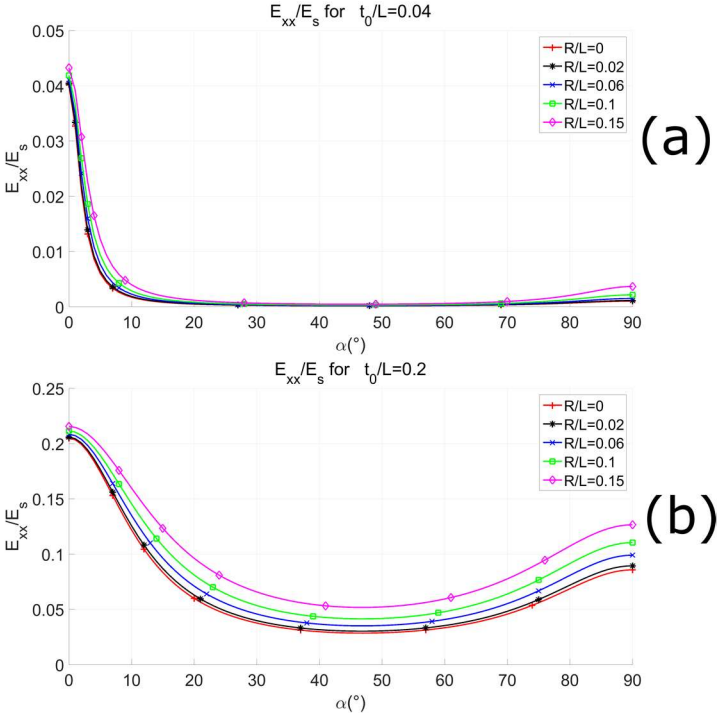

Figure II - 55. Elastic modulus vs α for different fillet radii: (a) at $t_0^* = 0.04$; (b) at $t_0^* = 0.2$.

The error made by disregarding the fillet radius in the calculation of the elastic modulus can be up to more than 60% for the values of R^* and t_0^* considered in this article, in direction *2* (Figure II - 56). On the other hand, as expected, the error on E_{11} is considerably lower (Figure II - 56a). The error is strongly affected by the off-axis angle because the effect of the fillet radius increases with α, as stated previously. Moreover, these plots confirm that the effect of the fillet radius is more marked for thinner cell walls.

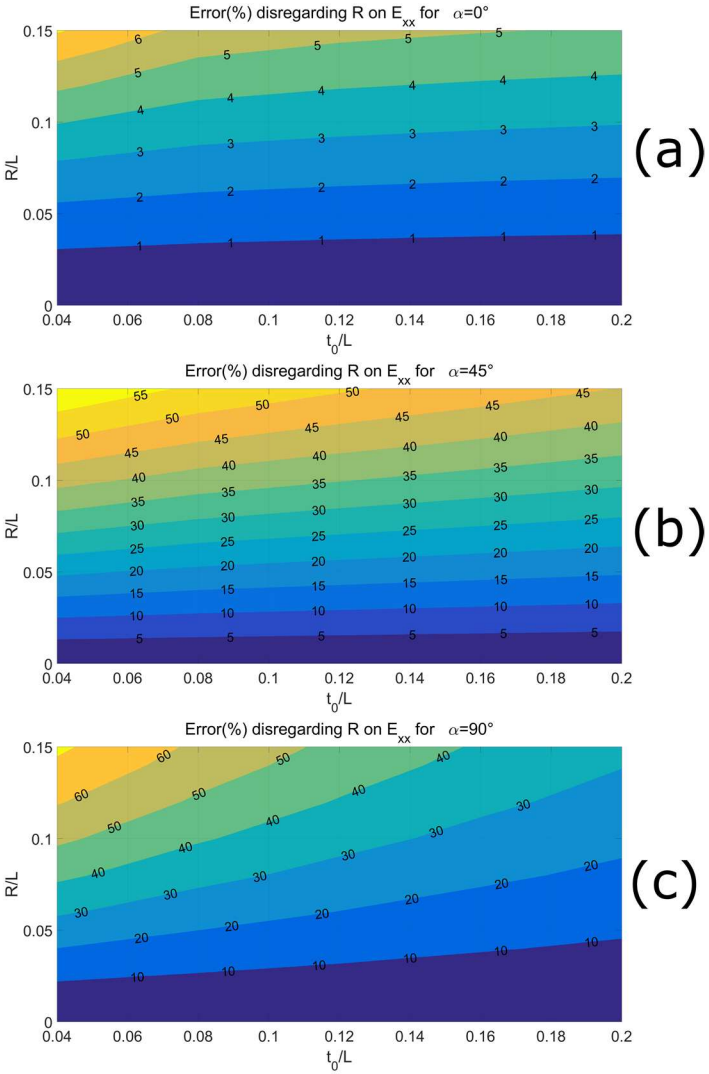

Figure II - 56. Contour plots of the difference in % between the elastic modulus calculated taking into account the fillet radius and that calculated disregarding it. (a) $\alpha = 0°$; (b) $\alpha = 90°$; (c) $\alpha = 45°$.

The general behavior of the error as a function of the angle is plotted in the graphs of Figure II - 57: as the off-axis angle from *direction 1* increases, the error grows very

rapidly in the first 10°-20° than it stays more or less constant until the last 20° to direction *2*, where it increases further for thin cell walls while it decreases for thick walls.

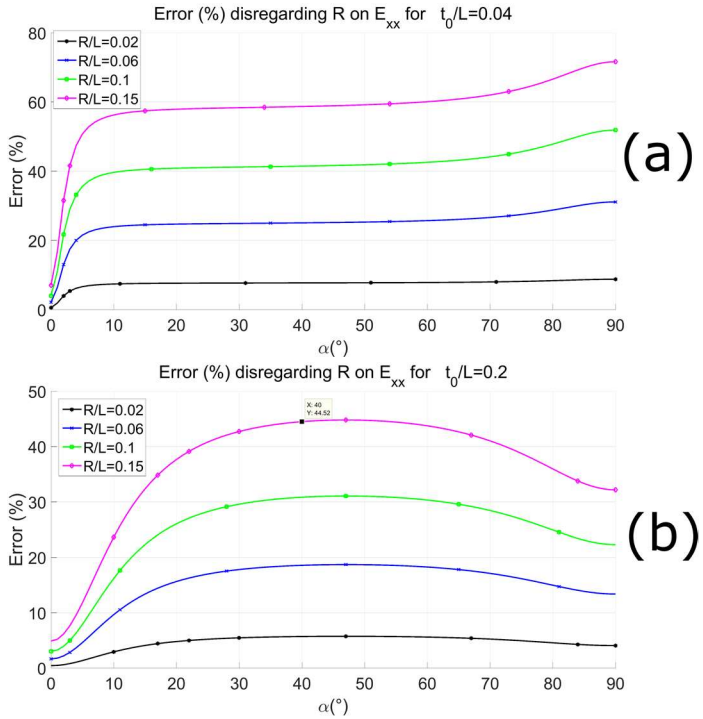

Figure II - 57. Error in % between the elastic modulus calculated taking into account the fillet radius and that calculated disregarding it as a function of the off-axis angle *α*. (a) at $t_0^* = 0.04$; (b) at $t_0^* = 0.2$.

The fitting error is low for the elastic modulus as it reaches a maximum of about 1.5% in principal direction *1* and it decreases to a maximum of about 0.3% in principal direction *2*.

2.4.2.2 Staggered square structure: Gxy

The effect of the unit cell parameters on the shear modulus of the staggered structure is qualitatively similar to that described for the regular lattice: slender cell walls appear to be more sensitive to the fillet radius than thicker cell walls (consider, for instance, the contour plots at 0° and 45° in Figure II - 58). Only the results related to the angles included in the 0°-45° interval are shown in this Paragraph because

G_{xy} has a symmetric behavior, the symmetry axes being at 0° and 45°. At $\alpha = 0°$ (principal direction *1*) the shear modulus is the lowest because the cell walls are loaded almost in pure bending, while it reaches a maximum at $\alpha = 45°$ (Figure II - 59). The sensitivity to the fillet radius tends to decrease with the angle, going from a highly non-linear behavior at 0° to an almost linear one at 45° (Figure II - 60). This is intuitive, as the actions on the cell walls change from pure bending to prevalently axial.

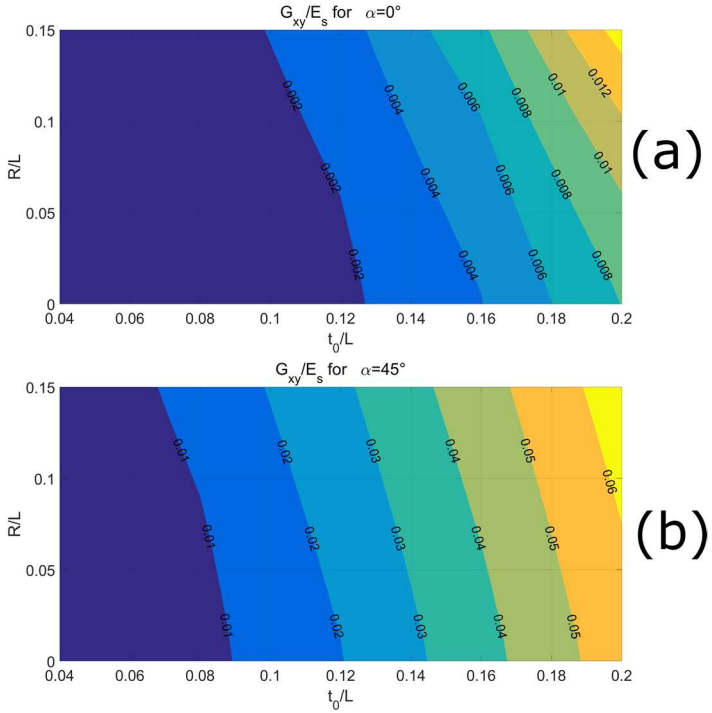

Figure II - 58. Contour plot of the normalized shear modulus as a function of R^* and t_0^*. (a) $\alpha = 0°$; (b) $\alpha = 45°$.

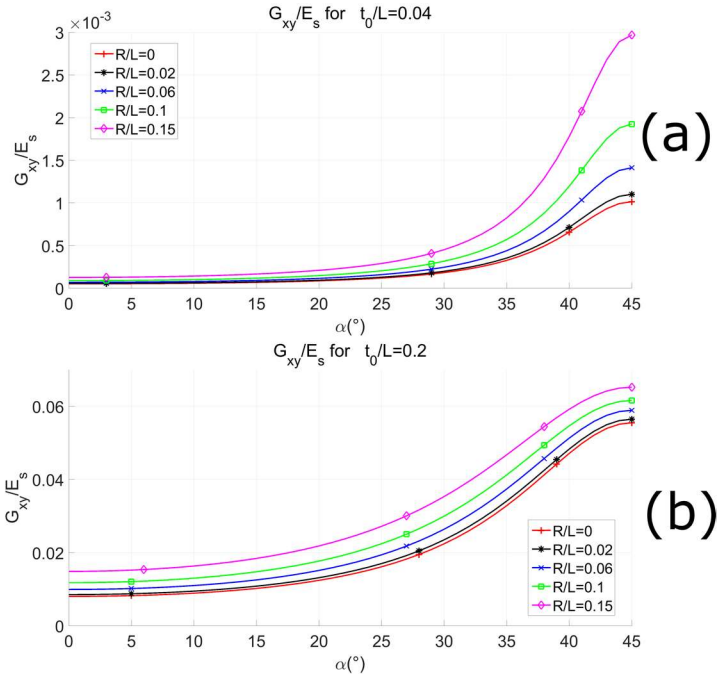

Figure II - 59. Shear modulus vs α for different fillet radii: (a) at $t_0^* = 0.04$; (b) at $t_0^* = 0.2$.

The error which can affect the calculations for the shear modulus if the fillet radius is disregarded reaches the 60% of the assumed correct value, for the intervals of R^* and t_0^* considered, as shown in the usual contour plots of Figure II - 60a for principal direction *1* and Figure II - 60b at $\alpha = 45°$. It is apparent that the shear modulus calculated for structures with thinner cell walls will be affected by a greater error if the fillet radius is disregarded.

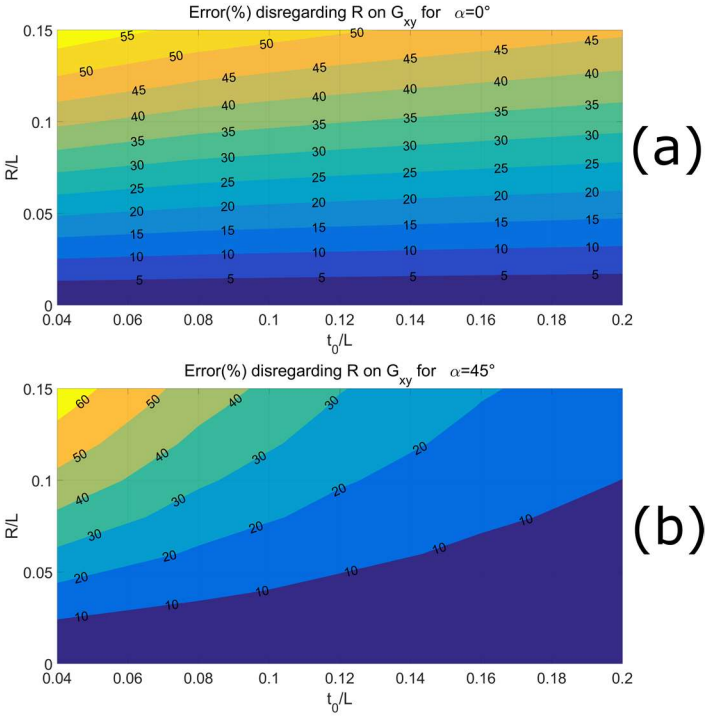

Figure II - 60. Contour plots of the difference in % between the shear modulus calculated taking into account the fillet radius and that calculated disregarding it. (a) $\alpha = 0°$; (b) $\alpha = 45°$.

Figure II - 61 shows two graphs in which the error is plotted as a function of the off-axis angle for different values of the fillet radius for two cell wall thicknesses $t_0^* = 0.04$ and $t_0^* = 0.2$.

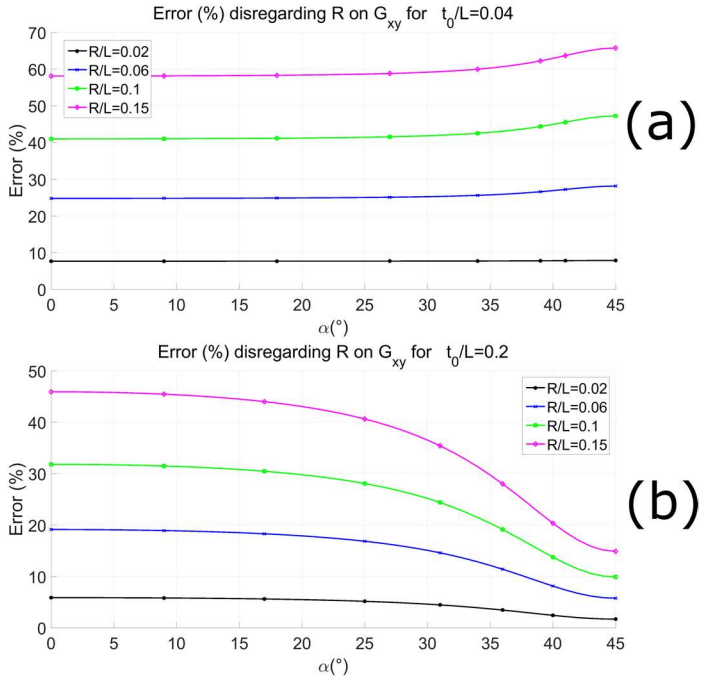

Figure II - 61. Error in % between the shear modulus calculated taking into account the fillet radius and that calculated disregarding it as a function of the off-axis angle *α*. (a) at $t_0^* = 0.04$; (b) at $t_0^* = 0.2$.

The maximum fitting error on the shear modulus was found to be slightly lower than that obtained for the elastic modulus, as it is about 0.8% in principal direction *1* and about 0.3% in principal direction *2*.

2.4.2.3 Staggered square structure: v_{xy} and v_{yx}

The orthotropic character of the lattice can be once more used to simplify the discussion on Poisson's ratio: it is sufficient to discuss the results only for v_{xy}, since the behavior of v_{yx} as a function of the off-axis angle *α* is simply its inverse. Poisson's ration of the staggered structure shows a somewhat surprising behavior, if compared with that of the regular square lattice. Indeed, for $\alpha = 0°$ (Figure II - 62a), it is higher at low cell wall thickness, contrary to what would be expected for an axially loaded strut. Moreover, v_{xy} at $\alpha = 0°$ is nowhere near the values obtained for the regular square structure in the principal direction. However, considering the asymmetry of the cell walls aligned with direction *1*, also bending actions are induced in the

apparently axially loaded walls and, consequently, lateral displacements. It is thus reasonable to think that thinner struts will have the tendency to generate a bigger displacement in direction 2 because of their lower bending stiffness. In addition, the higher the fillet radius, the more asymmetric is the structure and thus greater the lateral expansion and Poisson's effect. In principal direction 2, the cell wall axes act also as symmetry axes, so Poisson's effect is due only to the axial actions and it is thus considerably smaller (Figure II - 62b).

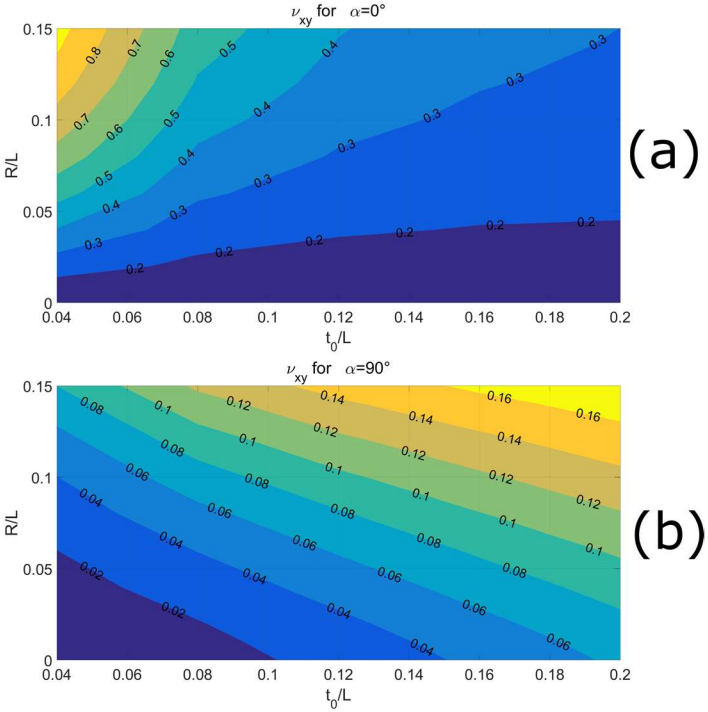

Figure II - 62. Contour plot of Poisson's coefficient as a function of R^* and t_0^*. (a) $\alpha = 0°$; (b) $\alpha = 90°$.

Figure II - 63 displays the plots of ν_{xy} as a function of α for different values of the fillet radius calculated for two values of the cell wall thickness t_0^*, supporting the previous comments. Lattices with thicker struts (Figure II - 63b) behave more similarly to the regular structure, as the curves are almost symmetric with respect to $\alpha = 45°$ and show the inversion of Poisson effect with respect to the fillet radius. The inversion does not occur for thin cell walls because of the effect of the asymmetry.

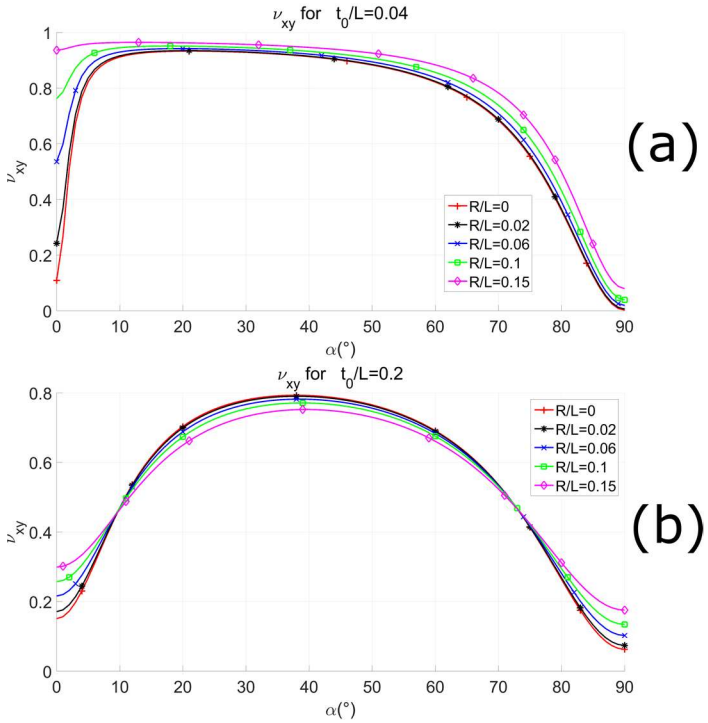

Figure II - 63. Poisson's coefficient vs α for different fillet radii: (a) at $t_0^* = 0.04$; (b) at $t_0^* = 0.2$.

The error which can affect the calculations for Poisson's coefficient if the fillet radius is disregarded reaches the 90% of the assumed value, for the intervals of R^* and t_0^* considered, as shown in the usual contour plots of Figure II - 64a and Figure II - 64c for the two principal directions. The high values for the error in principal direction *1* are due to the effect of the fillet radius on the asymmetry. The error in direction *2* is due to the axial loading of the cell walls aligned in *direction* 2, but it is considerably higher than that obtained for the regular square structure because of the offset of the cells. For intermediate directions (Figure II - 64b) the error is considerably lower, as expected, because the Poisson's effect is mainly caused by the bending of the cell walls. Note that since the error is not in absolute value, negative values are also obviously present.

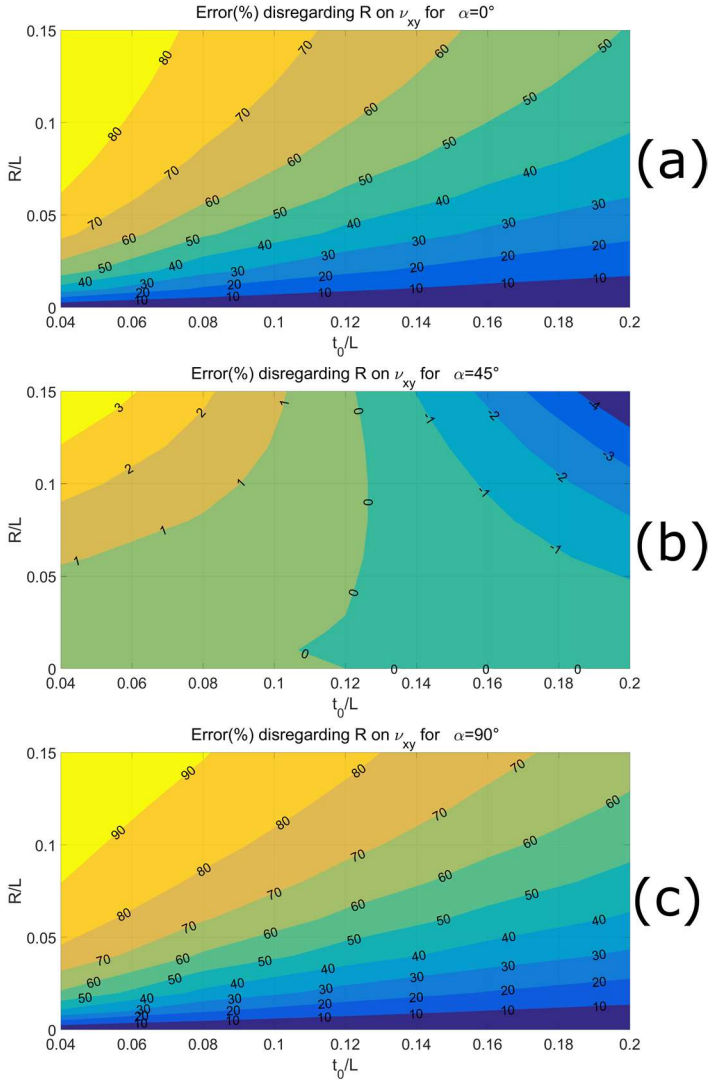

Figure II - 64. Contour plots of the difference in % between the Poisson's coefficient calculated taking into account the fillet radius and that calculated disregarding it. (a) $\alpha = 0°$; (b) $\alpha = 90°$; (c) $\alpha = 45°$.

Figure II - 65a and Figure II - 65b show the plots of the error as a function of the off-axis angle α for $t_0^* = 0.04$ and $t_0^* = 0.2$ respectively and for four different values of the fillet radius. These graphs, together with those of Figure II - 64a, Figure II -

64b and Figure II - 64c give the complete picture on the error which affects Poisson's ratio if the fillet radius is not taken into account. The error is very high only for directions nearly aligned with the principal directions.

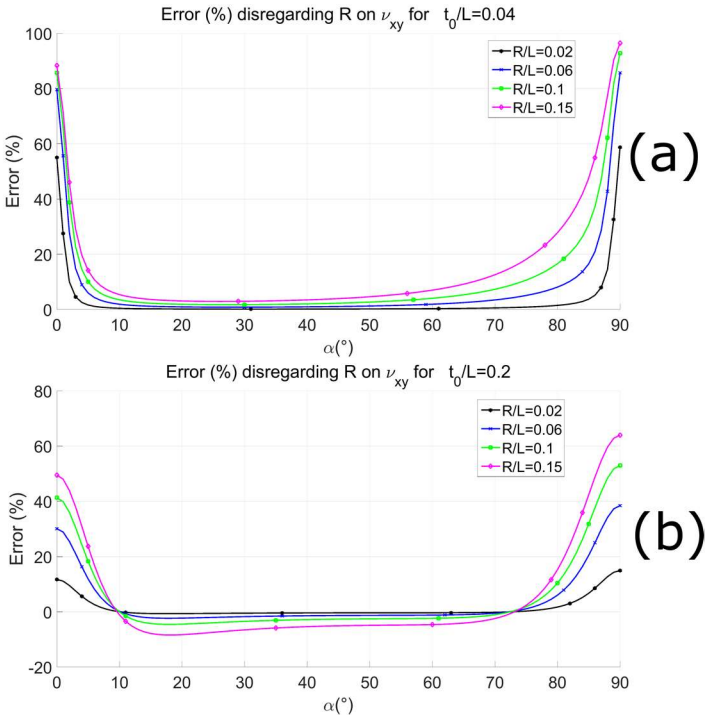

Figure II - 65. Error in % between the Poisson's modulus calculated taking into account the fillet radius and that calculated disregarding it as a function of the off-axis angle *α*. (a) at $t_0^* = 0.04$; (b) at $t_0^* = 0.2$.

The fitting error on Poisson's modulus reaches a maximum of 8% for v_{xy} at $\alpha = 0°$ (principal direction *1*) and at $\alpha = 90°$ (principal direction *2*). For intermediate directions it two orders of magnitude less.

2.4.3 An applicative example

To prove the effectiveness of the semi-analytical models of the elastic constants developed in this work, an illustrative structural problem will be solved by using these models. The aim is to show that such models can considerably ease and speed up the design of fully cellular structural parts. The problem chosen is shown in Figure II -

66: a simply supported beam of length *S* and thickness *W* stressed by a uniformly distributed load *q*. The beam was supposed fully cellular and the vertical displacement at the midspan v_{max} was calculated with a fully detailed FE analysis and compared with the results of a homogeneous FE model that implemented the elastic properties computed with the semi-analytical expressions.

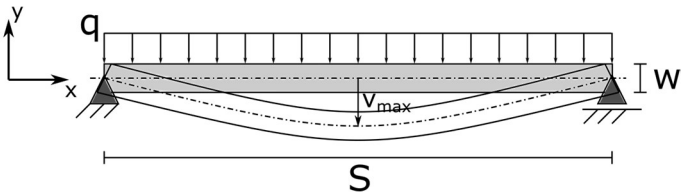

Figure II - 66. Simply supported 2D beam used as a benchmark to evaluate the performance of the model. Both the undeformed (grey) and the deformed beam is shown.

The beam was solved for three topologies of cellular lattice: regular square (Figure II - 67a), staggered oriented of 0° (Figure II - 67a) and staggered oriented of 45° (Figure II - 67a). Each beam is made of 13×130 cells, so that $S = 130 \cdot L$ and $W = 13 \cdot L$, where L is the unit cell size. Several combinations of the cell wall thickness and the fillet radius were considered for each case. Each structure was directly modeled in Ansys® with fully detailed geometry (Figure II - 67a-Figure II - 67c) and with a continuous orthotropic material with the properties calculated by implementing the semi-analytical expressions of the elastic properties. All the models were meshed with PLANE187 2D structural elements. The calculations were performed on a Dell workstation with 64GB of RAM and two Intel Xeon processors with a frequency of 3.40GHz.

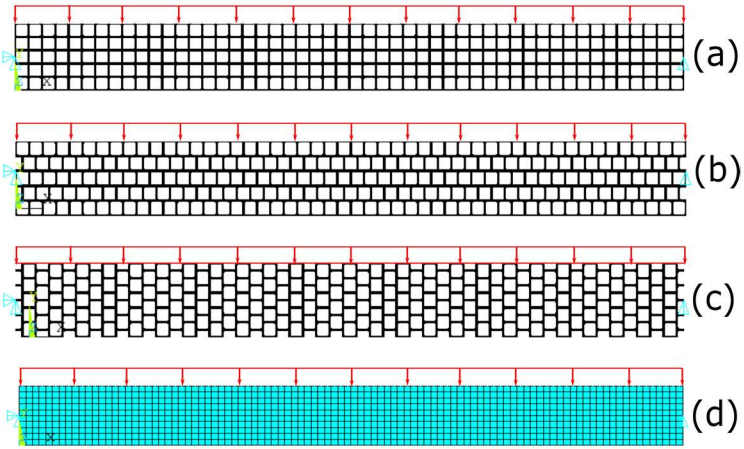

Figure II - 67. Direct modeling of the regular square cell structure (a), of the staggered square structure for $\alpha = 0°$ (b) and of the staggered square structure for $\alpha = 90°$. The cell density is lower than the one actually used for the calculation for representation purposes. (d) Beam made of a homogeneous orthotropic material with the properties calculated from the semi-analytic model. The red arrows indicate the distributed load.

The results of the simulations are reported in Table II - 7, Table II - 8 and Table II - 9 for the regular square, staggered 0° and staggered 90° structures, respectively. The relative error of the homogenous model, calculated using the result of the fully detailed model as a reference, is also reported. Moreover, the error which would affect the midspan displacement if the fillet radius was neglected is also shown. This error is defined according to Eq. (II – 30) and is calculated from the results of the beam directly modeled as a cellular material.

Table II - 7. Comparison of the cellular beam and the continuous orthotropic beam made of the regular square cellular material.

t_0/L	R/L	v_{max}/S cellular	v_{max}/S homogenous	Error (%)	Error (%) neglecting radius
0.12	0.04	0.2362	0.2397	1.48	6.31
0.12	0.10	0.2046	0.2069	0.83	22.74
0.12	0.15	0.1795	0.1803	0.40	39.85

Table II - 8. Comparison of the cellular beam and the continuous orthotropic beam made of the staggered square cellular material ($\alpha = 0°$).

t_0/L	R/L	v_{max}/S cellular	v_{max}/S homogenous	Error (%)	Error (%) neglecting

					radius
0.12	0.04	0.1966	0.1942	1.22	6.55
0.12	0.10	0.1744	0.1724	1.19	20.07
0.12	0.15	0.1576	0.1560	1.02	32.87

Table II - 9. Comparison of the cellular beam and the continuous orthotropic beam made of the staggered square cellular material ($\alpha = 90°$).

t_0/L	R/L	v_{max}/S cellular	v_{max}/S continuous	Error (%)	Error (%) neglecting radius
0.12	0.04	0.6852	0.5812	15.18	13.08
0.12	0.10	0.5293	0.4443	16.05	46.39
0.12	0.15	0.4170	0.3478	16.59	85.80

These results confirm the good accuracy of the model developed in this work, despite the relatively high errors for the staggered structure rotated of 90°. Indeed, additional analyses showed that by increasing the cell density the error strongly decreases (for a cell density of 35×350 it becomes about 7%). This configuration of the staggered structure is more sensitive to the cell density because of its intrinsic lower stiffness related to prevalence of bending actions. In fact, homogenization methods work on the assumption that the cell is small compared to the size of the component. Indeed, as the cell density per side increases, the midspan displacements of the cellular beam and the homogenous beam tend to converge to the same value. As expected, the presence of a fillet radius at the joints has a remarkable influence on the mechanical behavior of the structure, thus it should not be neglected. Finally, the true power of the model is revealed when the computation time is considered: in average, the computation speed is increased by at least 300 times.

2.5 Results and Discussion: Stress concentration factors

2.5.1 SCF matrix components

The originality (and the usefulness) of this work consists in the development of a model to estimate the stress concentration factors at the filleted junctions for wide range of the geometrical parameters of the unit cell. On the other hand, it is appropriate to provide the reader with some preliminary information concerning the results of the FE simulations of the stress behavior of a 2D fillet junction of regular square lattices.

The components of the ***K*** matrix are calculated with the FE model by applying the procedure described in Subsection 2.3.1 on wide intervals of the geometrical parameters:

- t_0/L : [0.02, 0.03, 0.04, …, 0.2];
- R/L: [0.01, 0.02, 0.03, 0.04, 0.05, 0.06, 0.07, 0.08, 0.09, 0.1, 0.12, 0.14, 0.15];

In the case of pure shear, opposite cell walls are bent in opposite direction, leading to fillets alternatively being loaded in prevalently tensile and prevalently compressive loads, (as shown in Figure II - 68). Consequently, the stress state is not equally severe on all the fillets as in the case of uniaxial tension (Figure II - 69), although the intensity of the von Mises equivalent stress is the same. In the development of the fitting model the stress concentration factors were calculated based on the most severe (tensile) stresses in the case of pure shear.

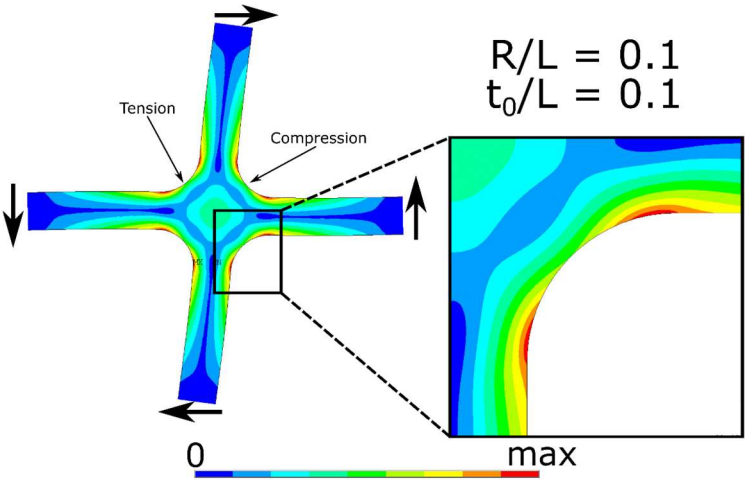

Figure II - 68. Von Mises equivalent stress contour plot in the case of pure shear for $t_0/L = 0.1$ and $R/L = 0.1$.

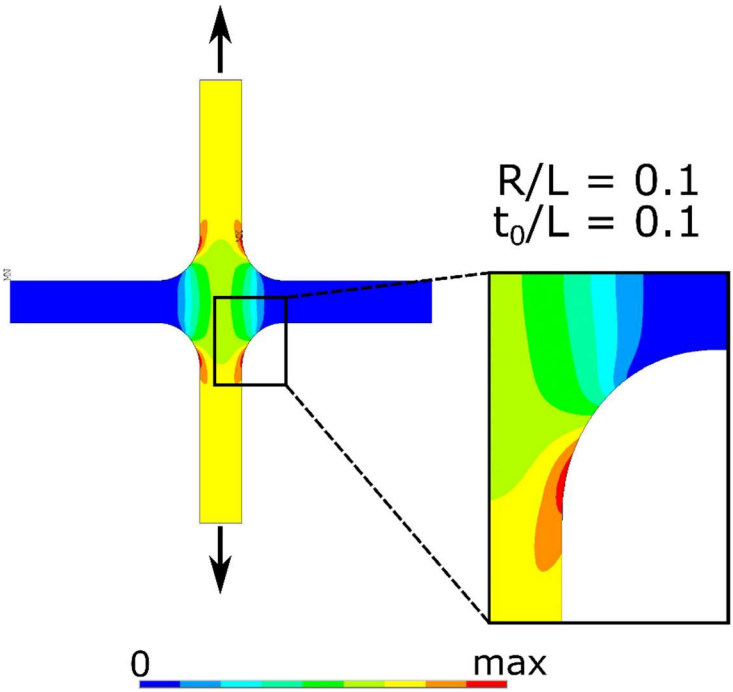

Figure II - 69. Von Mises equivalent stress contour plot in the case of uniaxial tension for $t_0/L = 0.1$ and $R/L = 0.1$.

The evolution of the components of ***K*** as a function of their position along the fillet depends only on the geometry and not on the load case, as already shown. Despite the strong influence of the geometry, some observations are valid throughout the entire span of the domain defined by the geometrical parameters. Given the symmetry of the unit cell, the first and second column of ***K*** are specular with respect to the position on the fillet (compare, for instance, subplots (a) and (b) of Figure II - 70, Figure II - 71 and Figure II - 72). Moreover, the components induced by pure shear (subplots (c) of Figure II - 70, Figure II - 71 and Figure II - 72) are specular to the bisecting line of the fillet. The values for pure shear refer to the fillet subjected to prevalently tensile stresses (as indicated in Figure II - 69). The maxima of $K_{1,ij}$ and $K_{2,ij}$ (the SCFs relating the nominal loads *ij* with σ_1 and σ_2) always occur in the proximity of the beginning of the fillet (points A and C), while the maxima of the shear stresses tend to move towards the center of the fillet (point B) as the fillet radius decreases with respect to the cell wall thickness. In the plots of Figure II - 70, Figure II - 71 and Figure II - 72 the value of each component in correspondence with locations A, B and C is also highlighted.

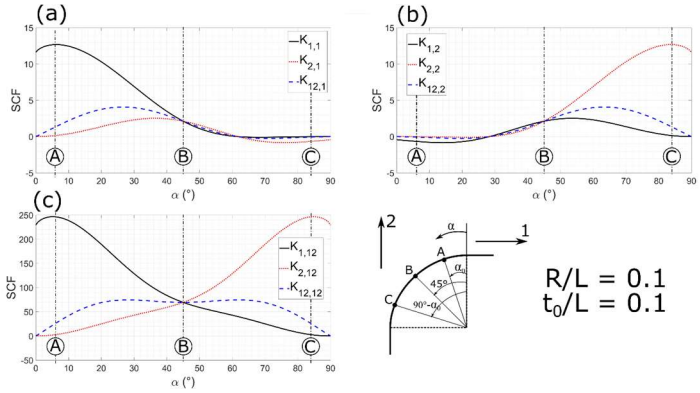

Figure II - 70. Components of the SCF matrix (FEM results) as a function of the position expressed by angle *α* along the fillet, for $t_0/L = 0.1$ and $R/L = 0.1$.

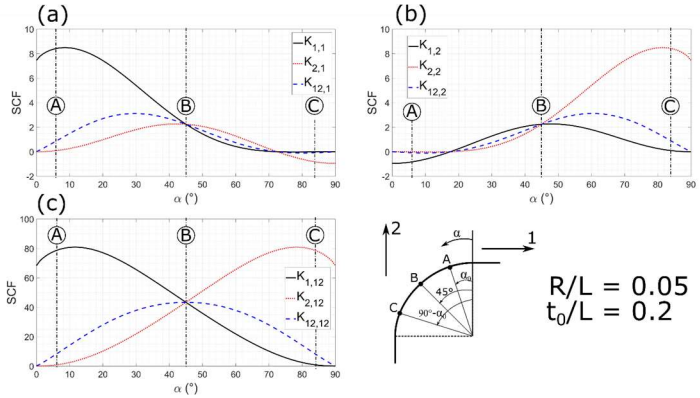

Figure II - 71. Components of the SCF matrix (FEM results) as a function of the position expressed by angle *α* along the fillet, for $t_0/L = 0.2$ and $R/L = 0.05$.

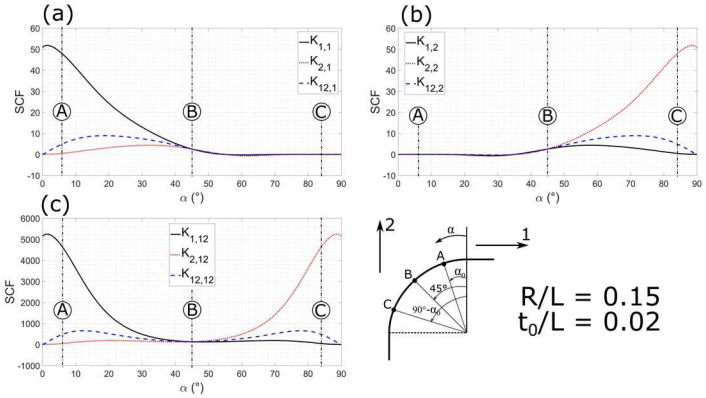

Figure II - 72. Components of the SCF matrix (FEM results) as a function of the position expressed by angle *α* along the fillet, for $^{t_0}/_{L} = 0.02$ and $^{R}/_{L} = 0.15$.

2.5.2 Fitting procedure

Each component of the SCF matrix was fitted with functions depending on $^{t_0}/_{L}$ and $^{R}/_{L}$ and several coefficients, of the following type:

$$K_{ij,ij} = A_1 + \mathrm{B}_1\left(\frac{R}{L}\right)^{C_1} + D_1\left(\frac{t_0}{L}\right)^{E_1} + \frac{F_1}{Q_1\left(\frac{R}{L}\right)^{G_1} + R_1\left(\frac{t_0}{L}\right)^{H_1}} + I_1\left(\frac{R}{L}\right)^{L_1}\left(\frac{t_0}{L}\right)^{M_1} + N_1 e^{\left(O_1\left(\frac{R}{L}\right) + P_1\left(\frac{t_0}{L}\right)\right)} \qquad \text{(II - 31)}$$

Once the expressions for the components of the ***K*** matrix are obtained, the equivalent stress concentration factor K_{eq} can be expressed with Eq. (II - 21). The coefficients of Eq. (II - 31) are listed in Table II - 10, Table II - 11 and Table II - 12 for location A ($\alpha = 6°$), location B ($\alpha = 45°$) and location C ($\alpha = 84°$), respectively.

Table II - 10. Coefficients of Eq. (II - 31) for $\theta = 6°$.

	A_1	B_1	C_1	D_1	E_1	F_1	G_1	H_1	I_1	L_1	M_1	N_1	O_1	P_1	Q_1	R_1
$K_{1,1}$	-0.1444	0.07579	-0.8865	0.80452	-1.0226	0.85602	0.87076	1.04083	0	0	0	0	0	0	0	0
$K_{2,1}$	0.00590	0.00009	-1.4316	0.00873	-1.0200	0.00715	0.97920	1.19472	0	0	0	0	0	0	0	0
$K_{12,1}$	-0.0152	0.00864	-0.8716	0.08661	-1.0159	0.08549	0.87789	1.05167	0	0	0	0	0	0	0	0
$K_{1,2}$	204.321	0	0	0	0	-0.1037	1.2119	1.72309	0.01549	-0.9169	-0.6629	-204.28	-0.0147	0.01588	0	0
$K_{2,2}$	6.31553	0	0	0	0	-0.0011	1.23912	1.76708	0.00022	-0.8786	-0.6389	-6.3173	-0.0064	0.00514	0	0
$K_{12,2}$	78.0063	0	0	0	0	-0.0109	1.2149	1.71803	0.00159	-0.9251	-0.6635	-78.000	-0.0041	0.00445	0	0
$K_{1,12}$ (*)	4.01565	0	0	-23.447	-1.9384	0	0	0	-1.5419 24.4906	-0.2139 -0.0633	-2.1126 -1.9633	0	0	0	0	0
$K_{2,12}$	-0.2112	3.41443* 10^-8	-3.6640	1.01533	-1.9569	-0.0031	2.64955	2.17095	-0.9985	0.01337	-1.9617	0	0	0	0	0
$K_{12,12}$	-0.7420	1.41087* 10^-8	-4.2453	1.36657	-1.8305	-0.1403	2.13057	1.69852	-1.4419	0.20659	-1.8335	0	0	0	0	0

(*) The terms with coefficients B1, C1, D1 and E1 appear two times in Eq. (II - 31).

Table II - 11. Coefficients of Eq. (II - 31) for $\theta = 45°$.

	A_1	B_1	C_1	D_1	E_1	F_1	G_1	H_1	I_1	L_1	M_1	N_1	O_1	P_1	Q_1	R_1
$K_{1,1}$	-0.21213	0.038764	-0.96343	0.000962	-1.65746	0.466843	0.850785	1.01039	0	0	0	0	0	0	0	0
$K_{2,1}$ (*)	-86.2013	19.8992 -3.97732	0.028009 1.00000	71.5695 -8.84358	0.021701 1.00000	0	0	0	0.327719	-0.47877	-0.47011	0	0	0	0	0
$K_{12,1}$	-0.22128	0.039791	-0.95661	0.000939	-1.65987	0.471551	0.848969	1.00493	0	0	0	0	0	0	0	0
$K_{1,2}$	-0.22976	0.039891	-0.95554	0.000926	-1.66035	0.47801	0.845103	0.999966	0	0	0	0	0	0	0	0
$K_{2,2}$	-0.21213	0.038764	-0.96343	0.000962	-1.65746	0.466843	0.850785	1.01039	0	0	0	0	0	0	0	0
$K_{12,2}$	-0.22128	0.039791	-0.95661	0.000939	-1.65987	0.471551	0.848969	1.00493	0	0	0	0	0	0	0	0
$K_{1,12}$	-16.9192	0.001650	-2.36115	4.36382	-2.78964	2.96856	1.5852	1.86625	-4.33791	0.001405	-2.79179	0	0	0	0	0
$K_{2,12}$	-16.9192	0.001650	-2.36115	4.36382	-2.78964	2.96856	1.5852	1.86625	-4.33791	0.001405	-2.79179	0	0	0	0	0
$K_{12,12}$	-16.9348	0.001687	-2.35605	4.40706	-2.79096	2.97028	1.58576	1.86553	-4.38129	0.001384	-2.79308	0	0	0	0	0

(*) The terms with coefficients B1, C1, D1 and E1 appear two times in Eq. (II - 31).

Table II - 12. Coefficients of Eq. (II - 31) for $\theta = 84°$.

	A_1	B_1	C_1	D_1	E_1	F_1	G_1	H_1	I_1	L_1	M_1	N_1	O_1	P_1	Q_1	R_1
$K_{1,1}$	6.3155	0	0	0	0	-0.0011	1.2391	1.7671	0.0002	-0.8786	-0.6389	-0.0002	-0.8786	-0.6389	0	0
$K_{2,1}$	195.87	0	0	0	0	-0.1037	1.2119	1.7231	0.0155	-0.9168	-0.6629	-195.8	-0.0153	0.0166	0	0
$K_{12,1}$	68.820	0	0	0	0	-0.0109	1.2149	1.7180	0.0016	-0.9251	-0.6635	-68.814	-0.0046	0.0050	0	0
$K_{1,2}$	0.0052	0	0	0	0	0.0116	4.6059	0.9096	0.0023	-0.5792	-0.6878	0	0	0	0	0
$K_{2,2}$	-0.1444	0.0758	-0.8865	0.8045	-1.0226	0.8560	0.8708	1.0408	0	0	0	0	0	0	0	0
$K_{12,2}$	-0.0152	0.0086	-0.8716	0.0866	-1.0159	0.0855	0.8779	1.0517	0	0	0	0	0	0	0	0
$K_{1,12}$	-0.9226	0	0	0.0067	-2.2903	0.0780	2.0298	1.6745	0	0	0	0	0	0	0	0
$K_{2,12}$	-1.9223	0	0	0	0	-50.338	27.078	1.7742	49.832	-0.0267	-1.7869	0	0	0	0	0
$K_{12,12}$	-1.4818	0	0	0	0	34628	61970	-10306	0.2258	-0.2285	-1.8709	0	0	0	34587	34611

The fitting errors for each component are reported as contour plots in Appendix 2.8.2. Here, the fitting error is in general defined as:

$$error_{fit}(\%) = \frac{K_{fit} - K_{FEM}}{K_{FEM}} \times 100 \qquad \text{(II - 32)}$$

Where K_{fit} is any of the components of $\boldsymbol{K}$ (or the equivalent SCF) obtained by the fit and K_{FEM} is the corresponding component (or the equivalent SCF) calculated from the FEM. The total maximum error on K_{eq} is shown in the contour plot of Figure II - 73. A similar plot is obtained when plotting the RMSD of the maximum error (Figure II - 74), although, clearly, the errors are lower. The errors are reasonably low in most of the domain, except in the case of sharp fillet radii and thick cell walls. In the use of such fitting model, the designer should be careful when working with ${}^{t_0}/_{L} > 0.15$ and ${}^{R}/_{L} < 0.02$. On the other hand, it must be considered that the maximum error (Figure II - 73) is positive, meaning that the model overestimates the severity of the fillet. In other words, the model is conservative.

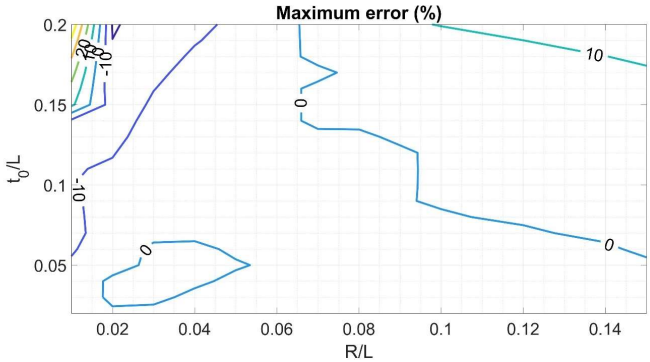

Figure II - 73. Contour plot of the maximum fitting error on K_{eq} (considering all the load cases) for each combination of the geometrical parameters.

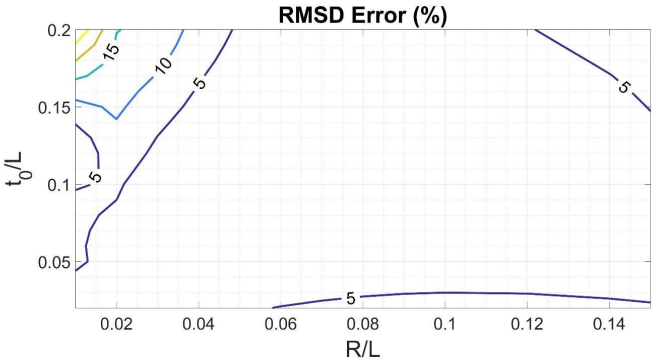

Figure II - 74. Contour plot of the RMSD of the maximum fitting error K_{eq} (considering all the load cases) for each combination of the geometrical parameters.

2.6 Conclusions

The in-plane elastic constants of planar regular square and staggered square lattice structures with filleted junctions were studied with analytical and numerical (FE) tools in large domains of the geometric parameters: wall thickness to edge length ratio t_0^* in the interval [0.04,0.20] and fillet radius to edge length ratio R^* in the interval [0,0.15]. Moreover, semi-analytical expressions based on Euler beam theory were developed to predict the elastic constants of such cellular structures in their material principal directions. To account for the complex effects of the filleted joints on the bending and stretching actions in the cell walls, the theoretical beam model is fitted to the results of the 2D FE analyses. Recognizing the fact that both structures are orthotropic, the semi-analytical model is also able to accurately predict the off-axis elastic constants.

The maximum errors that affect the semi-analytical model with respect to the FE results are of about 0.6% for the elastic modulus and the shear modulus and of about 5% for Poisson's coefficient for the regular square structure and of about 0.8% for the elastic modulus and the shear modulus and of about 8% for Poisson's coefficient for the staggered structure.

The following conclusions can be drawn:

- The effect of the fillet radius on the elastic constants is remarkable and in general should not be neglected. The error that would affect the calculation of the elastic constants of a cellular structure if the fillet radius were neglected was calculated and discussed. The elastic constants of structures with slender cell walls are particularly sensitive to the fillet radius.

- The staggered square structure is in general more influenced by the fillet radius with respect to the regular square structure, as the error affecting the elastic constants if the fillet radius was disregarded is greater for the former structure.

A similar approach was used to estimate the SCFs at the cell wall junctions of the 2D regular square cellular lattice. A model capable of calculating the values of the SCF as a function of the unit cell geometrical parameters was obtained, considering the wall thickness to edge length ratio t_0^* in the interval [0.02,0.20] and fillet radius to edge length ratio R^* in the interval [0. 01 ,0.15]. This was achieved by applying the FE method to the unit cell to calculate the components of the SCFs matrix for each couple of geometrical parameters. The values of the SCFs were then fitted with functions to identify a mathematical relationship with the normalized geometrical parameters. Moreover, using such fitted expressions, a mathematical relationship was found to define an equivalent stress concentration factor that appears to successfully relate the nominal homogenized loads acting in the cellular lattice to the local stresses at the filleted junctions, taking into account the geometrical features. Compared to the results of FE simulations, the quadratic mean of the errors of such fitting model are below 5 % for a wide range of the geometrical parameters, being only for $t_0/L > 0.15$ and $R/L < 0.02$ the errors above 10%.

The main contribution of this work to the field of cellular materials is an insight on the effect of fillets at the junctions on the elastic behavior of these structures. This aspect has been most often overlooked in the literature, although, as shown, it has a remarkable effect. For some applications, a fillet can be desirable, such as in the design of fatigue resistant lattices, as will be discussed in the next Chapter. Indeed, in fatigue resistant structures sharp edges have to be avoided at all costs. On the other hand, parasitic mass accumulation at the joints of AM lattices can introduce unwanted fillets that can unexpectedly influence the mechanical behavior if not accounted for. In this view, models that can accurately characterize the elastic stress behavior of filleted lattices with minimal computational effort are a powerful tool for the designer. Even more so if combined with structural optimization methods, for instance considerably facilitating the design of cellular lattices with assigned elastic properties and minimized stress concentration at the joints.

2.7 References

[1] Bagheri ZS, Melancon D, Liu L, Johnston RB, Pasini D. Compensation strategy to reduce geometry and mechanics mismatches in porous biomaterials built with Selective Laser Melting. J Mech Behav Biomed Mater 2017;70:17–27. doi:10.1016/j.jmbbm.2016.04.041.

[2] Liu L, Kamm P, García-Moreno F, Banhart J, Pasini D. Elastic and failure

response of imperfect three-dimensional metallic lattices: the role of geometric defects induced by Selective Laser Melting. J Mech Phys Solids 2017;107:160–84. doi:10.1016/j.jmps.2017.07.003.

[3] Latture RM, Rodriguez RX, Holmes LR, Zok FW. Effects of nodal fillets and external boundaries on compressive response of an octet truss. Acta Mater 2018;149:78–87. doi:10.1016/j.actamat.2017.12.060.

[4] Masoumi Khalil Abad E, Arabnejad Khanoki S, Pasini D. Fatigue design of lattice materials via computational mechanics: Application to lattices with smooth transitions in cell geometry. Int J Fatigue 2013;47:126–36. doi:10.1016/j.ijfatigue.2012.08.003.

[5] Simone AE, Gibson LJ. Effects of solid distribution on the stiffness and strength of metallic foams. Acta Mater 1998;46:2139–50. doi:10.1007/s11069-011-9918-1.

[6] Warren WE, Kraynik AM. Foam mechanics: the linear elastic response of two-dimensional spatiallly periodic cellular materials. Mech Mater 1987;6:27–37. doi:10.1016/0167-6636(87)90020-2.

[7] Kim HS, Al-hassani STS. A morphological elastic model of general hexagonal columnar structures. Int J Mech Sci 2001;43:1027–60.

[8] Kim HS, Al-hassani STS. Effective elastic constants of two-dimensional cellular materials with deep and thick cell walls. Int J Mech Sci 2003;45:1999–2016. doi:10.1016/j.ijmecsci.2004.02.002.

[9] Demiray S, Becker W, Hohe J. Investigation of the fatigue behavior of open cell foams by a micromechanical 3-D model. Mater Sci Eng A 2009;504:141–9. doi:10.1016/j.msea.2008.10.036.

[10] Huang JS, Lin JY. Fatigue of cellular materials. Acta Mater 1996;44:289–96. doi:10.1016/1359-6454(95)00170-4.

[11] Huang JS, Liu SY. Fatigue of isotropic open-cell foams under multiaxial loads. Int J Fatigue 2001;23:233–40. doi:10.1016/S0142-1123(00)00096-7.

[12] Fricke W. Fatigue analysis of welded joints: State of development. Mar Struct 2003;16:185–200. doi:10.1016/S0951-8339(02)00075-8.

[13] Hedayati R, Hosseini-Toudeshky H, Sadighi M, Mohammadi-Aghdam M, Zadpoor AA. Computational prediction of the fatigue behavior of additively manufactured porous metallic biomaterials. Int J Fatigue 2016;84:67–79. doi:10.1016/j.ijfatigue.2015.11.017.

[14] Hrabe NW, Heinl P, Flinn B, Körner C, Bordia RK. Compression-compression fatigue of selective electron beam melted cellular titanium (Ti-6Al-4V). J Biomed Mater Res - Part B Appl Biomater 2011;99 B:313–20. doi:10.1002/jbm.b.31901.

[15] Amin Yavari S, Wauthle R, Van Der Stok J, Riemslag AC, Janssen M, Mulier M, Kruth JP, Schrooten J, Weinans H, Zadpoor AA. Fatigue behavior of porous biomaterials manufactured using selective laser melting. Mater Sci Eng C 2013;33:4849–58. doi:10.1016/j.msec.2013.08.006.

[16] Lobontiu N, Paine JSN, Garcia E, Goldfarb M. Corner-Filleted Flexure Hinges. J Mech Des 2001;123:346. doi:10.1115/1.1372190.

[17] Lobontiu N, Paine JSN. Design of Circular Cross-Section Corner-Filleted Flexure Hinges for Three-Dimensional Compliant Mechanisms. J Mech Des 2002;124:479. doi:10.1007/s13213-015-1157-3.

[18] Lobontiu N, Garcia E, Hardau M, Bal N. Stiffness characterization of corner-filleted flexure hinges. Rev Sci Instrum 2004;75:4896–905. doi:10.1063/1.1806999.

[19] Yang L, Harrysson O, Cormier D, West H, Gong H, Stucker B. Additive Manufacturing of Metal Cellular Structures: Design and Fabrication. Jom 2015;67:608–15. doi:10.1007/s11837-015-1322-y.

[20] Webb DC, Kormi K, Al-Hassani STS. Use of FEM in performance assessment of perforated plates subject to general loading conditions. Int J Press Vessel Pip 1995;64:137–52. doi:10.1016/0308-0161(94)00078-W.

[21] Jones RM. Mechanics of composite materials. 2nd ed. Taylor & Francis; 1999.

[22] An Y, Wen C, Hodgson PD, Yang C. Investigation of cell shape effect on the mechanical behaviour of open-cell metal foams. Comput Mater Sci 2012;55:1–9. doi:10.1016/j.commatsci.2011.11.030.

[23] Wang A, Mcdowell DL. In-Plane Stiffness and Yield Strength of Periodic Metal. J Eng Mater Technol 2004;126:137–56. doi:10.1115/1.1646165.

[24] Gibson LJ, Ashby MF. Cellular Solids - Structure and Properties. Cambridge University Press; 2 edition; 1999.

2.8 Appendix II.A: Equations of the elastic constants

2.8.1 Regular square lattice

$$\frac{E_{11}}{E_s} = \frac{E_{22}}{E_s} = \frac{2t_0^*\sqrt{t_0^*(4R^* + t_0^*)}t_{eff,E}^*}{\pi t_0^*\left(2R^* + t_0^* - \sqrt{t_0^*(4R^* + t_0^*)}\right)t_{eff,E}^* + 2\left(\sqrt{t_0^{*5}(4R^* + t_0^*)} - (-1 + 2R^* + t_0^*)\sqrt{t_0^*(4R^* + t_0^*)}t_{eff,E}^*\right) + 2t_0^*(2R^* + t_0^*)t_{eff,E}^* \cdot arctan\left[\frac{2t_0^*}{\sqrt{t_0^*(4R^* + t_0^*)}}\right]} \quad \text{(II – A1)}$$

$$\nu_{12} = \nu_{21} = \nu_s t_{eff,\nu}^* \quad \text{(II – A2)}$$

$$\frac{G_{12}}{E_s}=\left(\frac{2\left(-1+2R^*+t_0^*\right)^3}{t_0^{*3}}+\frac{2t_0^*\left(3-3t_0^*+t_0^{*2}\right)}{t_{eff,G}^{*\ 3}}-\frac{4k_t\left(-1+2R^*+t_0^*\right)\left(1+\nu_s\right)}{t_0^*}+\frac{4k_t t_0^*\left(1+\nu_s\right)}{t_{eff,G}^*}-\frac{2k_t\left(1+\nu_s\right)\left(\pi\left(-2R^*-t_0^*+\sqrt{t_0^*\left(4R^*+t_0^*\right)}\right)-2\left(2R^*+t_0^*\right)\cdot\arctan\left[\frac{2R^*}{\sqrt{t_0^*\left(4R^*+t_0^*\right)}}\right]\right)}{\sqrt{t_0^*\left(4R^*+t_0^*\right)}}\right)^{-1}+$$

$$\frac{3}{\left(2R^*+t_0^*\right)\left(t_0^*\left(4R^*+t_0^*\right)\right)^{5/2}}\left(\begin{array}{l}4R^*\left(\begin{array}{l}-40R^{*4}\sqrt{t_0^*\left(4R^*+t_0^*\right)}+\sqrt{t_0^{*5}\left(4R^*+t_0^*\right)}-2\sqrt{t_0^{*7}\left(4R^*+t_0^*\right)}+2\sqrt{t_0^{*9}\left(4R^*+t_0^*\right)}-8R^{*3}\sqrt{t_0^*\left(4R^*+t_0^*\right)}\left(-1+2t_0^*\right)+\\6R^{*2}\left(\sqrt{t_0^*\left(4R^*+t_0^*\right)}-2\sqrt{t_0^{*3}\left(4R^*+t_0^*\right)}+4\sqrt{t_0^{*5}\left(4R^*+t_0^*\right)}\right)+2R^*\left(2\sqrt{t_0^{*3}\left(4R^*+t_0^*\right)}-5\sqrt{t_0^{*5}\left(4R^*+t_0^*\right)}+7\sqrt{t_0^{*7}\left(4R^*+t_0^*\right)}\right)\end{array}\right)+\\\pi\left(\begin{array}{l}96R^{*6}-t_0^{*6}+\sqrt{t_0^{*11}\left(4R^*+t_0^*\right)}+32R^{*5}\left(-3+7t_0^*\right)+24R^{*4}\left(1-6t_0^*+5t_0^{*2}\right)+8R^{*3}\left(3t_0^*-9t_0^{*2}-4t_0^{*3}+4\sqrt{t_0^{*5}\left(4R^*+t_0^*\right)}\right)+\\2R^{*2}\left(3t_0^{*2}-6t_0^{*3}-22t_0^{*4}+16\sqrt{t_0^{*7}\left(4R^*+t_0^*\right)}\right)+2R^*\left(-6t_0^{*5}+5\sqrt{t_0^{*9}\left(4R^*+t_0^*\right)}\right)\end{array}\right)+\\2\left(2R^*+t_0^*\right)^2\left(24R^{*4}-8R^*t_0^{*3}-t_0^{*4}+8R^{*3}\left(-3+4t_0^*\right)-2R^{*2}\left(-3+6t_0^*+4t_0^{*2}\right)\right)\cdot\arctan\left[\frac{2R^*}{\sqrt{t_0^*\left(4R^*+t_0^*\right)}}\right]\end{array}\right)$$

(II – A3)

2.8.2 Staggered square lattice

$$\frac{E_{11}}{E_s}=\frac{1}{2}\left(\frac{1-4R^*-2t_0^*}{2t_0^*}+\frac{t_0^*}{t_{eff,E}^*}+\frac{\pi\left(R^*+t_0^*-\sqrt{t_0^*\left(2R^*+t_0^*\right)}\right)+2\left(R^*+t_0^*\right)\cdot\arctan\left(\frac{R^*}{\sqrt{t_0^*\left(2R^*+t_0^*\right)}}\right)}{\sqrt{t_0^*\left(2R^*+t_0^*\right)}}\right)^{-1} \tag{II – A4}$$

$$\frac{E_{22}}{E_S}=16\left(\frac{3}{\left(R^*+t_0^*\right)\left(t_0^*\left(2R^*+t_0^*\right)\right)^{5/2}}\left(\begin{array}{l}-4R^*\left(2R^*+t_0^*\right)\left(3\pi R^*\left(R^*+t_0^*\right)^2+2\sqrt{t_0^*\left(2R^*+t_0^*\right)}\left(-R^{*2}+2R^*t_0^*+2t_0^{*2}\right)\right)+R^*\left(3\pi R^*\left(R^*+t_0^*\right)^2+2\sqrt{t_0^*\left(2R^*+t_0^*\right)}\left(3R^{*2}+4R^*t_0^*+2t_0^{*2}\right)\right)+\\ 4\left(2R^*+t_0^*\right)\left(2R^*\sqrt{t_0^*\left(2R^*+t_0^*\right)}\left(-10R^{*3}-R^{*2}t_0^*+20R^*t_0^{*2}+10t_0^{*3}\right)+\pi\left(R^*+t_0^*\right)\left(6R^{*4}+13R^{*3}t_0^*-9R^{*2}t_0^{*2}-8t_0^{*4}+8\sqrt{t_0^{*7}\left(2R^*+t_0^*\right)}+8R^*\left(-3t_0^{*3}+2\sqrt{t_0^{*5}\left(2R^*+t_0^*\right)}\right)\right)\right)+\\ 2\left(R^*+t_0^*\right)^2\left(48R^{*4}-128R^*t_0^{*3}-32t_0^{*4}+8R^{*3}\left(-3+10t_0^*\right)+R^{*2}\left(3-12t_0^*-100t_0^{*2}\right)\right)\arctan\left[\frac{R^*}{\sqrt{t_0^*\left(2R^*+t_0^*\right)}}\right]\end{array}\right)+\right.$$
$$\left.8\left(-\frac{2\left(-1+2R^*+t_0^*\right)}{t_0^*}+\frac{2t_0^*}{t_{eff,E_{22}}^*}+\frac{\pi\left(2R^*+t_0^*-\sqrt{t_0^*\left(4R^*+t_0^*\right)}\right)+2\left(2R^*+t_0^*\right)\cdot\arctan\left[\frac{2R^*}{\sqrt{t_0^*\left(4R^*+t_0^*\right)}}\right]}{\sqrt{t_0^*\left(4R^*+t_0^*\right)}}\right)\right)^{-1} \tag{II – A5}$$

$$\nu_{21} = \nu_s t^*_{eff,\nu_{21}} \qquad \text{(II – A6)}$$

$$\nu_{12} = \nu_{21}\frac{E_{11}}{E_{22}} \qquad \text{(II – A7)}$$

$$\frac{G_{12}}{E} = 4\left(\begin{array}{l}
\dfrac{1-4R^*-2t_0^*}{t_0^*} - \dfrac{\left(-1+4R^*+2t_0^*\right)^3}{t_0^{*3}} + \dfrac{2t_0^*\left(3-6t_0^*+4t_0^{*2}\right)}{t_{eff,G_{12}}^{*\ 3}} + \dfrac{2t_0^*}{t_{eff,G_{12}}^*} - \dfrac{8k_t(-1+4R^*+2t_0^*)(1+\nu_s)}{t_0^*} + \dfrac{16k_t t_0^*(1+\nu_s)}{t_{eff,G_{12}}^*} - \dfrac{16k_t(1+\nu_s)\left(\pi\left(-R^*-t_0^*+\sqrt{t_0^*\left(2R^*+t_0^*\right)}\right)-2\left(R^*+t_0^*\right)\cdot\arctan\left[\dfrac{R^*}{\sqrt{t_0^*\left(2R^*+t_0^*\right)}}\right]\right)}{\sqrt{t_0^*\left(2R^*+t_0^*\right)}} + \\
\dfrac{2\left(\pi\left(R^*+t_0^*-\sqrt{t_0^*\left(2R^*+t_0^*\right)}\right)+2\left(R^*+t_0^*\right)\cdot\arctan\left[\dfrac{R^*}{\sqrt{t_0^*\left(2R^*+t_0^*\right)}}\right]\right)}{\sqrt{t_0^*\left(2R^*+t_0^*\right)}} + \\
\dfrac{3}{\left(R^*+t_0^*\right)\left(t_0^*\left(2R^*+t_0^*\right)\right)^{5/2}}\left(\begin{array}{l}
-4R^*\left(2R^*+t_0^*\right)\left(3\pi R^*\left(R^*+t_0^*\right)^2+2\sqrt{t_0^*\left(2R^*+t_0^*\right)}\left(-R^{*2}+2R^*t_0^*+2t_0^{*2}\right)\right)+R^*\left(3\pi R^*\left(R^*+t_0^*\right)^2+2\sqrt{t_0^*\left(2R^*+t_0^*\right)}\left(3R^{*2}+4R^*t_0^*+2t_0^{*2}\right)\right)+ \\
4\left(2R^*+t_0^*\right)\left(2R^*\sqrt{t_0^*\left(2R^*+t_0^*\right)}\left(-10R^{*3}-R^{*2}t_0^*+20R^*t_0^{*2}+10t_0^{*3}\right)+\pi\left(R^*+t_0^*\right)\left(6R^{*4}+13R^{*3}t_0^*-9R^{*2}t_0^{*2}-8t_0^{*4}+8\sqrt{t_0^{*7}\left(2R^*+t_0^*\right)}+8R^*\left(-3t_0^{*3}+2\sqrt{t0n^5\left(2R^*+t_0^*\right)}\right)\right)\right)+ \\
2\left(R^*+t_0^*\right)^2\left(48R^{*4}-128R^*t_0^{*3}-32t_0^{*4}+8R^{*3}\left(-3+10t_0^*\right)+R^{*2}\left(3-12t_0^*-100t_0^{*2}\right)\right)\cdot\arctan\left[\dfrac{R^*}{\sqrt{t_0^*\left(2R^*+t_0^*\right)}}\right]
\end{array}\right) + \\
2\left(\begin{array}{l}
-\dfrac{2\left(-1+2R^*+t_0^*\right)^3}{t_0^{*3}} + \dfrac{2t_0^*\left(3-3t_0^*+t_0^{*2}\right)}{t_{eff,G_{12}}^{*\ 3}} - \dfrac{4k_t\left(-1+2R^*+t_0^*\right)(1+\nu_s)}{t0n} + \dfrac{4k_t t_0^*(1+\nu)}{t_{eff,G_{12}}^*} - \dfrac{2kt(1+\nu)\left(\pi\left(-2R^*-t_0^*+\sqrt{t0n\left(4R^*+t_0^*\right)}\right)-2\left(2R^*+t_0^*\right)\cdot\arctan\left[\dfrac{2R^*}{\sqrt{t_0^*\left(4R^*+t_0^*\right)}}\right]\right)}{\sqrt{t_0^*\left(4R^*+t_0^*\right)}} + \\
\dfrac{3}{\left(2R^*+t_0^*\right)\left(t_0^*\left(4R^*+t_0^*\right)\right)^{5/2}}\left(\begin{array}{l}
4R^*\left(\begin{array}{l}-40R^{*4}\sqrt{t_0^*\left(4R^*+t_0^*\right)}+\sqrt{t_0^{*5}\left(4R^*+t_0^*\right)}-2\sqrt{t_0^{*7}\left(4R^*+t_0^*\right)}+2\sqrt{t_0^{*9}\left(4R^*+t_0^*\right)}-8R^{*3}\sqrt{t_0^*\left(4R^*+t_0^*\right)}\left(-1+2t_0^*\right)+ \\ 6R^{*2}\left(\sqrt{t_0^*\left(4R^*+t_0^*\right)}-2\sqrt{t_0^{*3}\left(4R^*+t_0^*\right)}+4\sqrt{t_0^{*5}\left(4R^*+t_0^*\right)}\right)+2R^*\left(2\sqrt{t_0^{*3}\left(4R^*+t_0^*\right)}-5\sqrt{t_0^{*5}\left(4R^*+t_0^*\right)}+7\sqrt{t_0^{*7}\left(4R^*+t_0^*\right)}\right)\end{array}\right)+ \\
\pi\left(\begin{array}{l}96R^{*6}-t_0^{*6}+\sqrt{t_0^{*11}\left(4R^*+t_0^*\right)}+32R^{*5}\left(-3+7t_0^*\right)+24R^{*4}\left(1-6t_0^*+5t_0^{*2}\right)+8R^{*3}\left(3t_0^*-9t_0^{*2}-4t_0^{*3}+4\sqrt{t_0^{*5}\left(4R^*+t_0^*\right)}\right)+ \\ 2R^{*2}\left(3t_0^{*2}-6t_0^{*3}-22t_0^{*4}+16\sqrt{t_0^{*7}\left(4R^*+t_0^*\right)}\right)+2R^*\left(-6t_0^{*2}+5\sqrt{t_0^{*9}\left(4R^*+t_0^*\right)}\right)\end{array}\right)+ \\
2\left(2R^*+t_0^*\right)^2\left(24R^{*4}-8R^*t_0^{*3}-t_0^{*4}+8R^{*3}\left(-3+4t_0^*\right)-2R^{*2}\left(-3+6t_0^*+4t_0^{*2}\right)\right)\cdot\arctan\left[\dfrac{2R^*}{\sqrt{t_0^*\left(4R^*+t_0^*\right)}}\right]
\end{array}\right)
\end{array}\right) \qquad \text{(II – A8)}$$

2.9 *Appendix II.B: Fitting errors of the components of the SCF matrix*

2.9.1 Fitting errors for the values extracted at position A ($\alpha = 6°$).

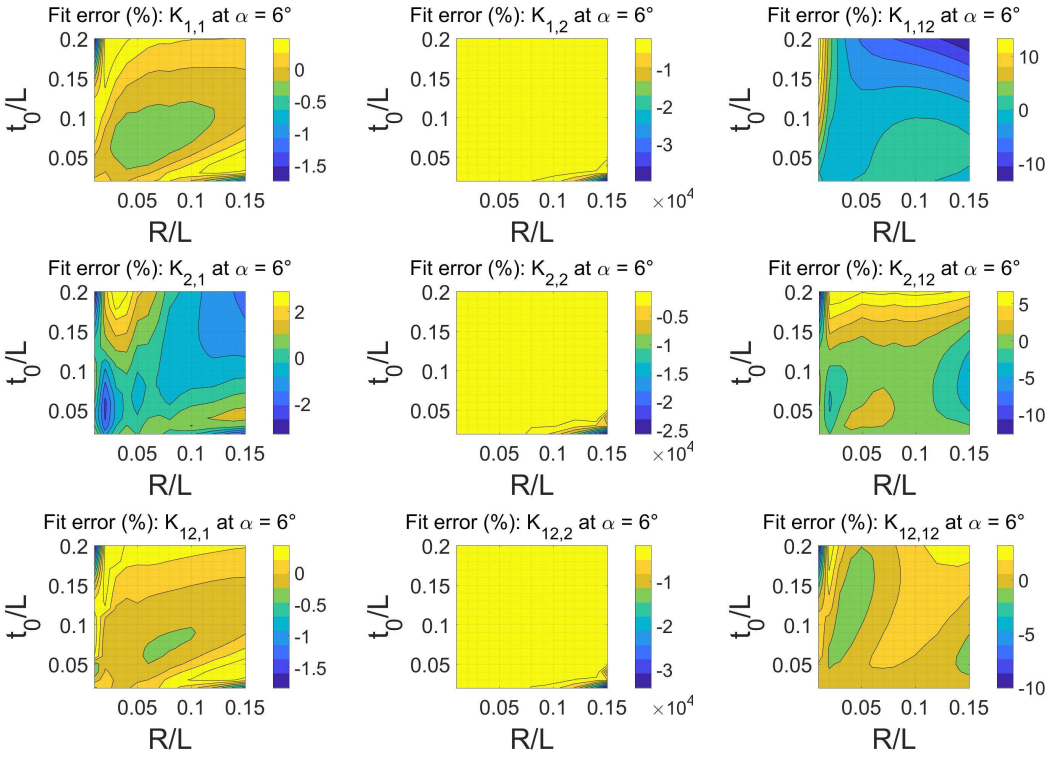

2.9.2 Fitting errors for the values extracted at position B ($\alpha = 45°$).

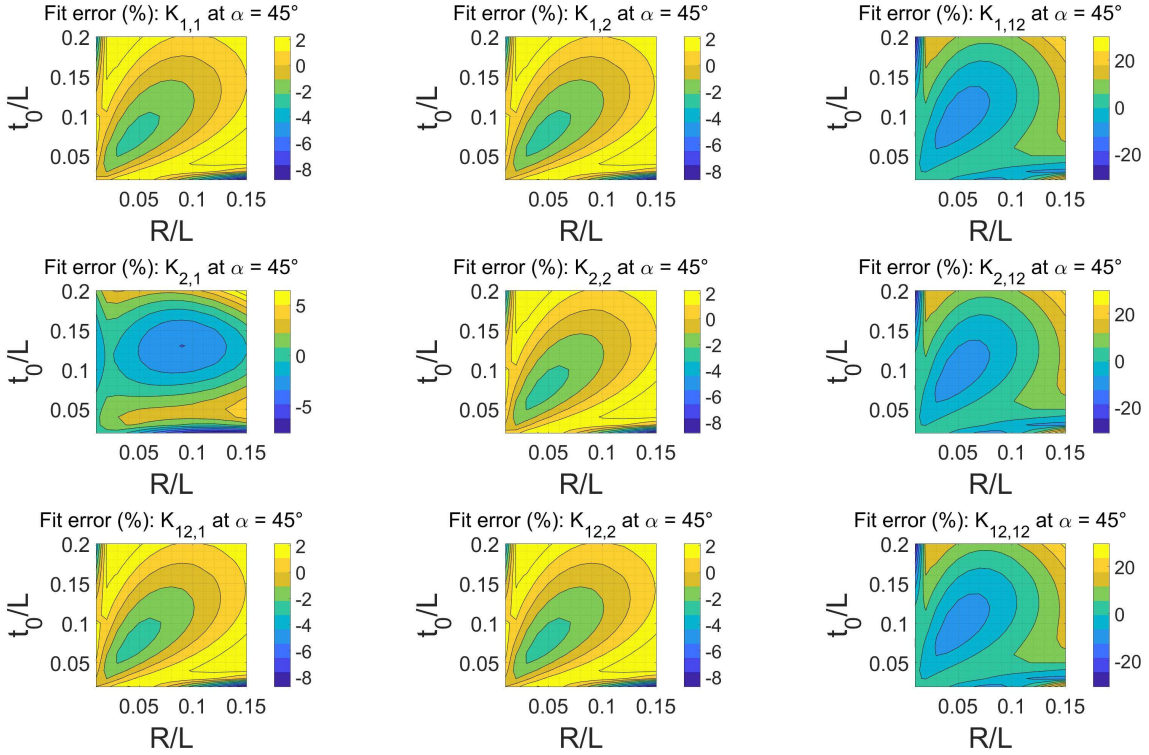

2.9.3 Fitting errors for the values extracted at position C ($\alpha = 84°$).

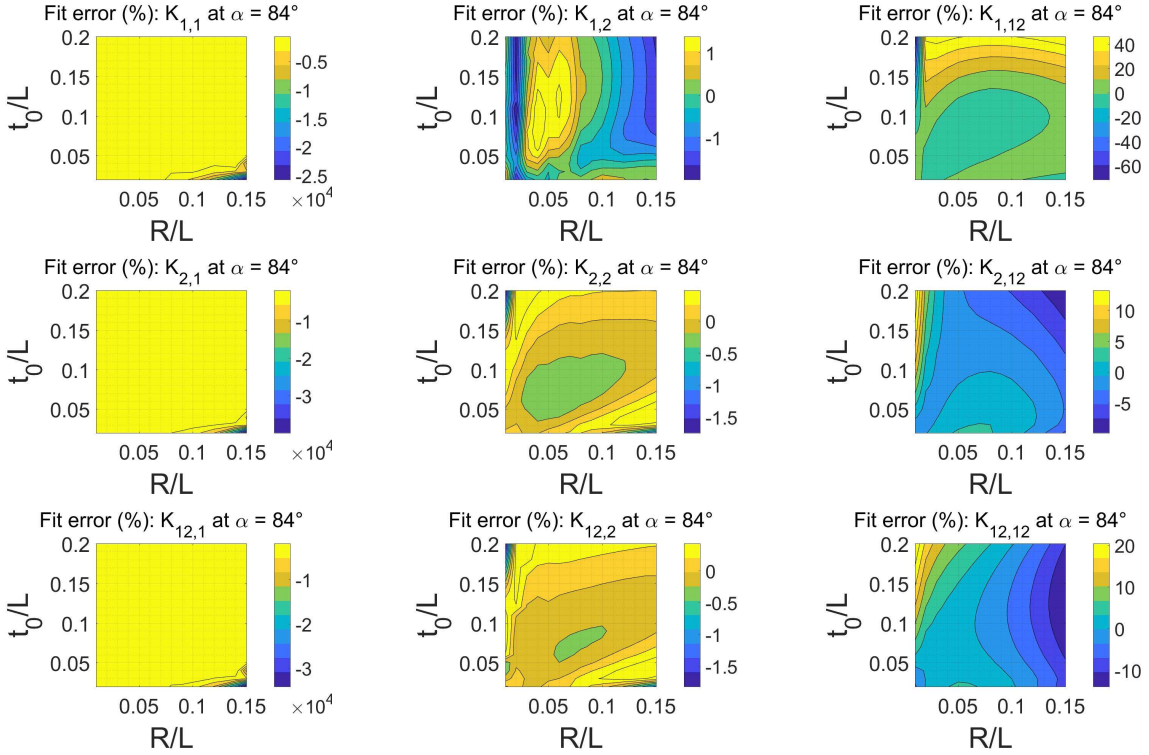

Chapter III

Morphological and mechanical characterization of variously arranged Ti-6Al-4V regular cubic lattices fabricated via Selective Laser Melting

Porous structures have great potential in the biomedical field because, compared to traditional fully dense implants, prostheses with a porous structure show reduced stress shielding and improved osseo-integration. The development of Selective Laser Melting (SLM) made possible to obtain metallic cellular materials with highly complex structures characterized by a wide range of cell morphologies that allow to finely tune the mechanical properties of the implant to the patient needs. Nevertheless, there are still several issues to address: among others, detrimental residual stresses and the discrepancy between the as-designed and the manufactured geometry. Micro X-ray computed tomography (μCT), being a high-resolution non-destructive measuring technique, combined with the Finite Elements (FE) method permits to carry out in-depth investigations on the effect of the number and severity of defects on the mechanical properties.

This Chapter presents the results of the mechanical and morphological characterization of different regular cubic open-cell cellular structures produced by SLM of Ti-6Al-4V alloy, all with the same nominal elastic modulus of 3GPa that matches that of human trabecular bone. The fully reversed fatigue strength at 10^6 cycles and the elastic modulus were measured and an attempt was made to link them to the manufacturing defects (porosity and geometrical inaccuracies). Half of the specimens was subjected to a stress relief thermal treatment while the other half to Hot Isostatic Pressing (HIP), and the effect of the treatments on porosity and on the mechanical properties was assessed. The results of fatigue and quasi-static tests on regular cubic lattices were compared with FE calculations based on the as-designed geometry and on the as-built geometry reconstructed from μCT scans. It was observed that the fatigue strength and, to a lesser extent, the elastic modulus are strongly correlated with the number and severity of defects and that predictions on the mechanical properties based on the as-designed geometry are not accurate. Fatigue strength seems to be highly dependent on the surface irregularities and notches introduced during the manufacturing process. In fully reversed fatigue tests, the high performances of stretching dominated structures compared to bending dominated structures are not found. In fact, with thicker struts, such structures proved to be more resistant, even if bending actions were present.

Part of this chapter has been published in:

M. Dallago, B. Winiarski, F. Zanini, S. Carmignato, M. Benedetti,

"On the effect of geometrical imperfections and defects on the fatigue strength of cellular lattice structures additively manufactured via Selective Laser Melting",
International Journal of Fatigue 124 (2019), pp. 348–360

M. Dallago, V. Fontanari, E. Torresani, M. Leoni, C. Pederzolli, C. Potrich, M. Benedetti,

"Fatigue and biological properties of Ti-6Al-4V ELI cellular structures with variously arranged cubic cells made by selective laser melting",
Journal of the Mechanical Behavior of Biomedical Materials 78 (2018), pp. 381–394

M. Dallago, F. Zanini, S. Carmignato, D. Pasini, M. Benedetti,

"Effect of the geometrical defectiveness on the mechanical properties of SLM biomedical Ti6Al4V lattices",
Procedia Structural Integrity 13 (2018), pp. 161-167

M. Dallago, V. Fontanari, B. Winiarski, P.J. Withers, F. Zanini, S. Carmignato, M. Benedetti,

"Fatigue properties of Ti6Al4V cellular specimens fabricated via SLM: CAD vs real geometry",
Procedia Structural Integrity 7 (2017), pp. 116-123

3.1 Introduction

Nowadays, metals are the best choice for load bearing biomedical implants [1] and the α+β Ti-6Al-4V alloy is one of the most popular because of a good combination of strength, ductility and corrosion resistance [2]. A promising strategy to reduce stress shielding, made possible by the advent of Additive Manufacturing (AM), is to fabricate orthopaedic implants with a highly porous cellular structure with mechanical properties that match that of human bone. Among the various AM techniques for metals, Selective Laser Melting (SLM) allows greater precision [3] and was employed to produce the specimens object of this study. Although SLM has been proven capable of producing structures of great complexity, there are still several issues to address. For instance, Ti-6Al-4V as-built SLM components are affected by detrimental residual stresses [4] and a brittle martensitic α' microstructure [5–7]. Hot Isostatic Pressing (HIP) is a thermomechanical treatment that consists in simultaneously applying a high temperature and pressure by submerging the component in a fluid with the effect of relieving residual stresses, increasing the ductility of the microstructure (α' martensite is decomposed into the more ductile α+β microstructure) and reducing closed porosity [4,6–8]. Geometrical defects are also an issue because they are inevitably introduced into the printed structures and these can affect the mechanical and biological properties. Discrepancy between the as-designed and the manufactured geometry is a well-known phenomenon in biomedical metallic lattices characterized by strut thicknesses of a few hundred microns, which is close to the manufacturing limits [9–12]. Micro X-ray computed tomography (μCT), being a high-resolution non-destructive measuring technique [13,14], combined with the FE method permits to carry out in-depth investigations on the effect of the number and severity of defects on the mechanical properties. For instance, Liu et al. [11] showed that FE models based on the as-built geometry of cellular lattices acquired via μCT scans can explain the mismatch between the mechanical properties measured experimentally and those predicted with simulations based on the as-designed geometry. The thickness of the as-built strut of the cellular lattice, and so the deviation from the as-designed thickness, is determined by the size of the melt pool which is the result of the complex interaction of the local thermal properties of the powder/solid system and the SLM process parameters such as the laser power, the scanning speed [15–17] and layer thickness [17]. To complicate the matter, not only the as-designed size of the strut is relevant, but also its inclination to the printing direction is a factor to consider. In fact, inclined struts are supported by loose powder which has lower thermal conductivity than the solid and thus a higher fraction of the powder is partially or completely melted compared to a vertical strut

[18,19]. The difficulty in predicting the as-built shape is further increased by the material shrinkage during solidification and cooling [20].

Fatigue resistance is a critical aspect in load-bearing biomedical implants [21]: consider, for example, the periodic nature of human gait in the case for hip implants [22]. Nevertheless, in comparison to the wide number of papers published on the static mechanical behavior of cellular materials, few studies on their fatigue resistance have been published until now. Ti-alloys in general have high notch sensitivity [23], so the fatigue resistance is strongly influenced by defects that act as stress raisers [4,24]. Fatigue is in fact caused by the accumulation of damage at spots where stress concentration occurs and thus, to be able to accurately predict the fatigue resistance of a structure, the focus must be shifted to the local details in geometry [25]. In other words, fatigue, more than anything else, is affected by the manufacturing process and the importance of defects is highlighted in many publications. For instance, the predominant role of surface notches and irregularities as crack initiators was already suggested in one of the first experimental works on Ti-6Al-4V lattice fatigue strength [26], and this observation was confirmed in subsequent investigations [27].

The focus in this Chapter is on the relationship between the results of fully reversed fatigue tests and the imperfections of SLM Ti-6Al-4V lattice structures. To the present, additively manufactured Ti-6Al-4V cellular specimens have only been almost exclusively tested by compression-compression fatigue tests. This is normally justified by the fact that human bones are loaded prevalently in compression. Nevertheless, it is worth to consider a worst-case scenario, regarding the mechanical behavior of biomedical cellular materials, in which the flexural load acting on the implant is significant. Moreover, completely reversed fatigue is the standard test for fatigue and thus more material data is available, specifically to compare the fatigue behavior of cellular and bulk specimens. Some of the structures studied in this research are stretching dominated while others are bending dominated, thus the struts are loaded differently. Consequently, in the case of compression-compression fatigue the stretching dominated structures work exclusively in compression while parts of the bending dominated structures still undergo tensile stresses. Thus, the two types will show a remarkably different behavior, to the advantage of the stretching dominated ones. In the case of completely reversed fatigue, the loading scenario is more equilibrated, as in both cases the struts are subjected to alternate normal stresses. Six different configurations of the cubic unit cell were chosen: in three the cubes are simply shifted to fill the 3D space, while in the other three the cubic cells are skewed to obtain structures with a cylindrical symmetry. The quality of the manufacturing process and the discrepancy between the actual measured cell parameters and the nominal CAD values were assessed through an extensive metrological analysis, that involved also the use of metrological micro X-ray

computed tomography. The fracture surfaces of the struts of the specimens broken by fatigue were observed by SEM and the fracture behavior of each structure is discussed based on these observations. The effect of HIPing on strut porosity and on the mechanical properties was investigated by applying this treatment to half of the specimens.

Among the several geometries, the regular cubic lattice was selected for a more in-depth analysis, in the form of a statistical analysis to measure and classify the geometrical defects in terms of as-designed/as-built deviations. The detailed information on the specimen geometry was then used to devise FE models to compare the elastic modulus and the stress distribution at the junctions of the as-designed lattice and the as-built lattice. Moreover, residuals stresses were measured in the regular cubic lattice using the Plasma FIB-SEM-DIC micro-hole drilling method in a region of interest located with a helical scanning trajectory µCT system.

3.2 Materials and methods

3.2.1 Specimen design and description

Six different open-cell cellular structures were considered in this work (Figure III - 1): regular cubic cells (CUB NS), single staggered cubic cells (CUB S), double staggered cubic cells (CUB 2S), regular cylindrical cells (CYL NS), single staggered cylindrical cells (CYL S) and double staggered cylindrical cells (CYL 2S). All the structures were designed with care in eliminating every sharp notch. The sections of the struts are thus circular, and all the junctions are filleted with the same nominal radius R. The structures with cylindrical symmetry were developed with the idea of skewing the cubic cell to perfectly fill a cylindrical volume without the necessity to cut unit cells and to keep low the boundary effects. In the cylindrical structures the size of the cubic cells changes along the radial direction, as shown in Figure III - 1a. From the biological point of view, leaving a channel centered on the axis of the structure, as in the cylindrical arrangement, should considerably enhance the transport properties parallel to the same axis. The geometrical parameters that characterize each cell are the strut length L, the strut thickness t_0 (the section of the struts is a circle, thus t_0 is in fact a diameter) and the fillet radius R.

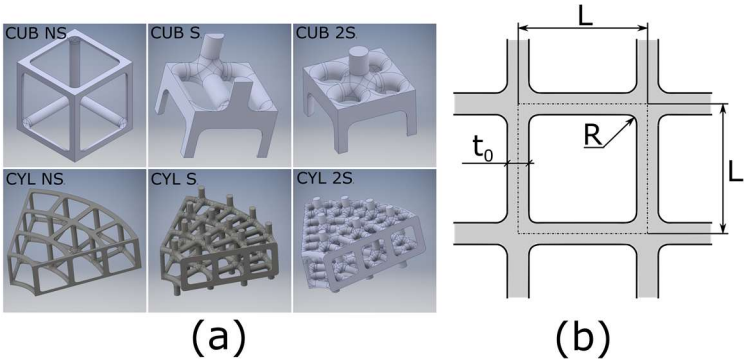

Figure III - 1. (a) CAD models of the unit cells of the six cellular structures studied in this work; (b) definition of unit cell parameters.

The simplest specimens (CUB NS and CUB S) were designed according to the procedure developed in Chapter II for 2D cellular structures and extended to the 3D case as illustrated in the following paragraph. The others were designed via a trial-and-error procedure based on the FE method. The design procedure consists in a simple optimization procedure according to which the unit cell parameters (strut length, strut thickness and junction fillet radius) are chosen based on the requirements listed in Table III - 1.

Table III - 1. Requirements for the unit cell parameters.

Quantity	Target value	Notes
Elastic modulus (E_{yy})	3 GPa	To match trabecular bone stiffness
Strut length (L)	1.500 mm	To ensure large pores for improved osseo-integration
Strut diameter (t_0)	≥ 0.200 mm	Should be the smallest possible (limited by 3D printer accuracy)
Fillet radius (R)	≈ $t_0/2$	(limited by 3D printer accuracy)

The cellular structures represented by the specimens are intended to be used in the production of fully porous orthopedic implants, thus the main requirement is to match the elastic modulus of trabecular bone to avoid the stress shielding effect. The stiffness target value was thus set to 3 GPa, which is a reasonable estimate of the elastic modulus of human trabecular bone. To ensure proper osseo-integration, i.e.

to permit the adherence and reproduction of osteoblasts on the structure of the implant and the proper flow of nutrients until full bonding is achieved, sufficiently large pores must be present (400-800 μm). After a benchmark analysis of the 3D printers available on the market, the smallest strut diameter allowed was set to 200 μm because this is the smallest achievable detail size. Given these considerations, the strut length was fixed to 1500 μm. The fillet radius between the junctions was imposed to be equal to the half of the strut diameter as a simplification.
There are some reasons behind the fact that such structures have been chosen. The cubic structures are in general the simplest to conceive, design and produce. The regular one has a very high stiffness to weight ratio because it is stretching dominated, while the other two are more compliant (given the same relative density) because they are bending dominated. Bending dominated structures present some advantages regarding their use in implants if we consider the failure process. In fact, although weaker (with respect to stretching dominated structures of the same density), under compression these structures fail more gradually, avoiding sharp decreases in loading capacity when buckling occurs and thus matching the behavior of the highly irregular structure of the human bone [28].

3.2.1.1 Design procedure

The design procedure of the specimens involves the following steps, in order:

1. Estimation of the unit cell parameters t_0 and R based on the conditions summarized in Table III - 1. This was done via analytical equations or FE modeling, depending on the structure. This will be further discussed in the following paragraphs.
2. Convergence analysis to establish the minimum number of unit cells that should be included in the specimen to reduce border effects.
3. Buckling analysis to verify that the structures don't fail by instability at the loads applied in the fatigue tests.
4. Design of the part connecting the thread to the cellular part of the specimen. This was done according to the UNI-5710 norm

The CUB-NS structure could be designed to meet the required stiffness by adapting the 2D semi-analytical model to the 3D case. The elastic modulus calculated for the 2D regular cubic cell structure can be used to obtain the stiffness of the corresponding 3D regular square cell structure with struts of square section simply by multiplying the 2D stiffness E_{2D} by the strut thickness t_0 normalized by the strut length L:

$$E_{3D}^{*}|_{SQ} = E_{2D}^{*}|_{SQ}\frac{t_0}{L} \quad \text{(III - 1)}$$

The real 3D structure has a circular section of diameter t_0, thus it is clearly less stiff than the corresponding structure with square sections of side t_0. On the other hand, if we correct the previous equation to take into account circular sections, the elastic modulus is:

$$E_{3D}^{*}|_{CIRC} = E_{2D}^{*}|_{SQ}\frac{t_0}{L}\frac{\pi}{4} \quad \text{(III - 2)}$$

Eq. (III – 2) is expected to underestimate the elastic modulus of the 3D structure because the stiffening effect of the fillet radii in the third dimension is neglected. It appears reasonable to assume the mean of the two previous expressions as the actual value:

$$E_{3D}^{*} = \frac{E_{3D}^{*}|_{SQ} + E_{3D}^{*}|_{CIRC}}{2} \quad \text{(III - 3)}$$

This consideration appears to be correct, as shown in Figure III - 2a, where the stiffness of the regular square structure calculated from a parametric FE models based on the unit cell of Figure III - 1 is compared with the values obtained from the above expressions (details on the FEM analyses will be given Subsection 3.2.9). The error (calculated with $error(\%) = \frac{E_{3D}^{*} - E_{3D,FEM}}{E_{3D,FEM}} \times 100$) introduced by such approximation is relatively low in the interval considered (Figure III - 2b). Thus, a reliable tool to predict the stiffness of 3D regular square cell structures considering also the fillet radius at the junctions has been obtained. Clearly, more accurate results could have been obtained by fitting the results of an extensive simulation campaign, as for the case of the 2D lattice described in Chapter II. On the other hand, relying on the results already obtained for the 2D lattice, is considerably simple, less time consuming, and reasonably accurate.

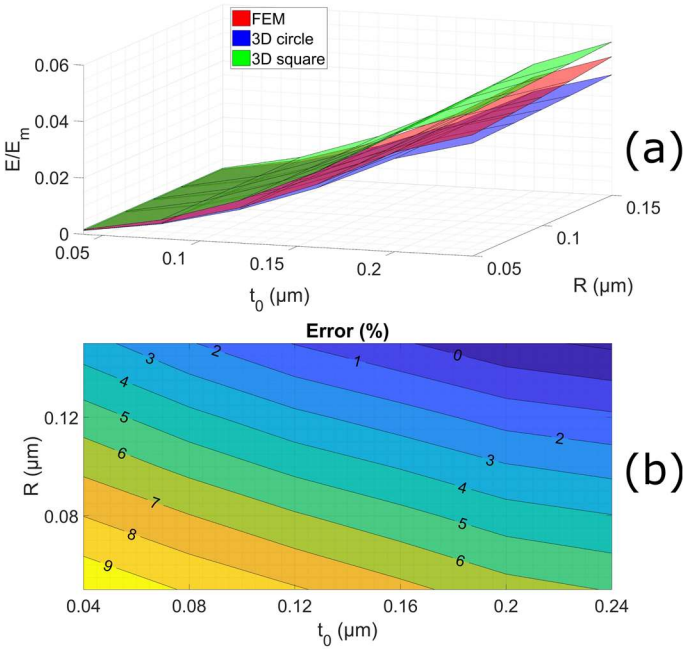

Figure III - 2. (a) Surface plot of the stiffness of the unit cell as a function of the unit cell geometrical parameters: comparison of the FE results and the estimates of Eqs. (III - 1) and (III - 2). (b) Contour plot of the error (%) affecting E^*_{3D} estimated with Eq. (III - 3).

Substituting the values of the parameters of Table III - 1 into Eq. (III - 3) directly gives the values of t_0 and R which represent a regular square cell structure of stiffness compatible with human bone. The same exact theoretical procedure can be applied also to the CUB-S structure to obtain the stiffness of the 3D structure from the 2D model. Such a simple design procedure cannot be applied to the other structures because no corresponding analytical expressions for the stiffness are available. Thus, the optimal unit cell is found with an iterative procedure that consists in solving several FE models of the unit cell until the criteria of Table III - 1 are met.

The size of the pores of each unit cell was calculated from the CAD model as the diameter of the largest sphere than can pass through neighboring cells [29]; in other words, is the smallest "hole" in the 3D lattice. This definition of pore size defines the interconnectivity of the cellular structure, which is a very significant parameter from the biological point of view. To avoid confusion with the internal porosity of the struts (which is due to the manufacturing process), we will refer to the lattice porosity as "unit cell pore size".

3.2.1.2 Specimen description

The unit cell parameters of the six types of unit cells are listed in Table III - 2. The smallest aperture in the CYL 2S lattice is smaller than the optimal pore size for osseo-integration, but due to the characteristics of the cylindric structures, the average pore size is considerably larger.

Table III - 2. As-designed (CAD) geometrical parameters of the cellular structures.

Structure	t_0 (mm)	R (mm)	Relative density (%)	Unit cell pore size (mm)
CUB NS	0.260	0.130	6.61	1.240
CUB S	0.340	0.170	15.32	0.410
CUB 2S	0.350	0.175	19.61	0.400
CYL NS	0.230	0.115	6.04	1.155
CYL S	0.300	0.150	12.39	0.425
CYL 2S	0.350	0.175	18.39	0.275

Each specimen is made up of a cylindrical cellular part connected to two threads, as shown in Figure III - 3. The threads are M10x1.5, as required by the testing machine.

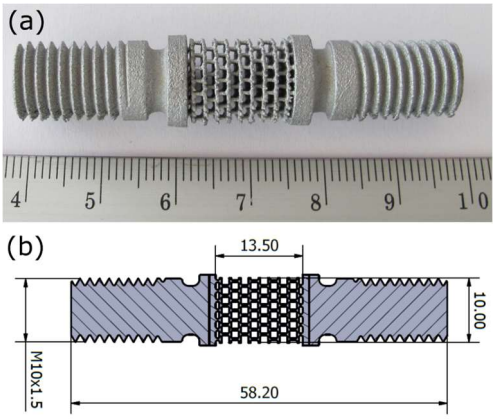

Figure III - 3. Example of specimen with the threaded heads for push-pull fatigue tests: (a) printed Ti alloy specimen; (b) longitudinal section of the CAD model (annotations in *mm*) The diameter of the cellular part is 10 mm for the cubic structures and 12 mm for the cylindrical ones.

A critical aspect is the connection of the cellular part to the base of the thread, which obviously is much stiffer. To avoid the failure of the specimen at that section, the struts have been made slightly thicker and are joined to the heads with a wide fillet. In addition, a relief groove has been added at the base of the thread according to the UNI EN 5710 norm to smooth off the flow of lines of force from the heads to the central cellular part.
The cellular part, regardless whether it has a cubic or a cylindrical symmetry, is cut in a circular shape, i.e. the nominal section of the specimen is a circle. The nominal diameter of the cellular part of the cubic structures is 10 mm while for the cylindrical structures is 12 mm. The height of the cellular part is 13.5 mm.
The number of unit cells that make up the specimen was chosen as the smallest possible that keeps border effects from substantially influencing the stiffness. Convergence analyses on the number of unit cells performed via the FE method indicate that the stiffness of the specimen matches reasonably well that of the unit cell when the size of the cellular specimen is 8 times *L* in height and 6 times *L* in width.

3.2.2 Specimen manufacturing

The fine details of the designed structures requested the use of a very fine powder. The specimens were additively manufactured via Selective Laser Melting (SLM) starting from biomedical grade Ti-6Al-4V ELI (Grade 23) in form of powder of mean diameter of 8.64 μm, shown in Figure III - 4. The results of a distribution analysis on the powder are shown in Figure III - 5.

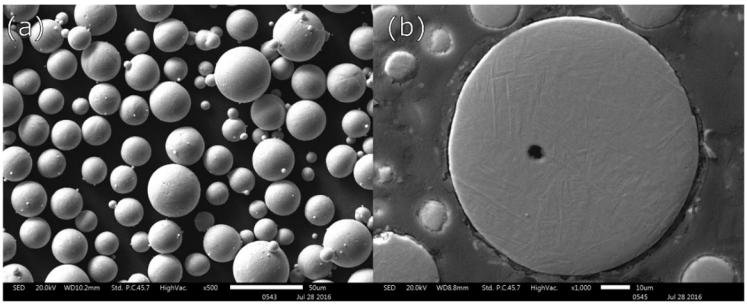

Figure III - 4. Ti-6Al-4V ELI powder used to produce the SLM cellular specimens. (a) Size distribution; (b) detail of a single particle.

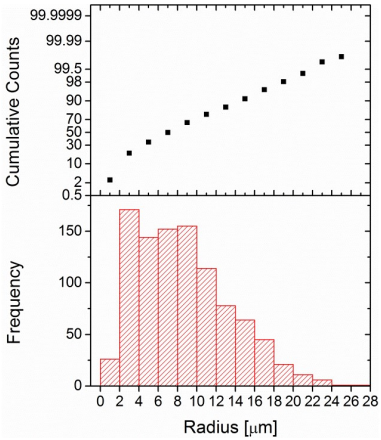

Mean	8.64 μm
Median	8.04 μm
St Dev	4.79 μm
Max	26.43 μm
Min	1.77 μm

Figure III - 5. Results of the size distribution analysis of the Ti-6Al-4V powder.

The specimens were manufactured using a 3D System ProX DMP 300 printer, inclined by 45° to the printing direction (Figure III - 6a), with one set of struts (identified by the *x* direction) laying in the printing plane and the other two sets inclined of 45° (Figure III - 6b).

The specimens were built inclined of 45° to the printing direction (Figure III - 6a), with one set of struts (identified by the *x* direction) laying in the printing plane and the other two sets inclined of 45° (Figure III - 6b).

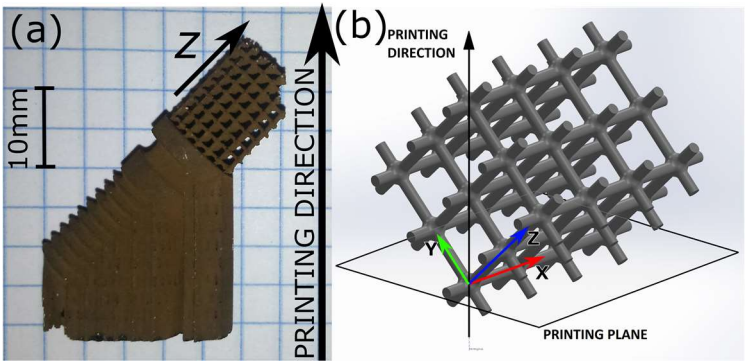

Figure III - 6. (a) As-built specimen with support structure; (b) details on the orientation of the struts to the printing direction and *xyz* reference system.

The specimens were divided into two batches. The first was heat treated at 670° C for 5 hours in Ar protective atmosphere to relieve residual stresses (referred to as

“stress relieved”), the second was treated by HIPing at 920° C and 1000 bar for 2 hours (referred to as “HIPed”) after sand blasting to remove the unmelted particles from the surface to prevent the HIP thermo-mechanical treatment from incorporating oxidized particles into the bulk, thus resulting in pores and lack-of-fusion defects.

3.2.3 Microstructure and porosity

Longitudinal and transversal sections were cut from two specimens for each type of lattice (one as-built and one HIPed), as shown in Figure III - 7. Thus, a total of 12 specimens were analyzed. The sectioned samples were then mounted, ground using SiC abrasive papers (with 120, 180, 320, 400, 600, 1000, 1500 grit sizes), and polished using a 3-micron diamond paste and a 0.04-micron alumina suspension. A Kroll's etching was applied to reveal the microstructures.

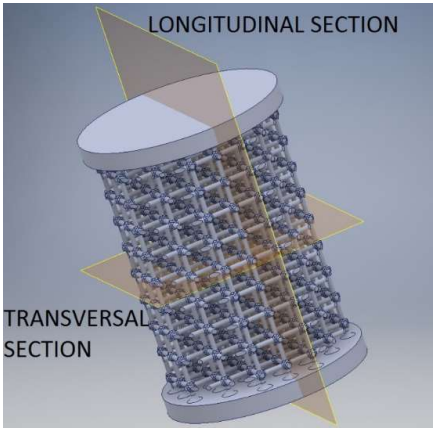

Figure III - 7. Definition of transversal and longitudinal sections of each cellular specimen.

Strut porosity was measured on three metallographic samples using image analysis software ImageJ® by counting the pores and calculating the area of each pore (Figure III - 8).

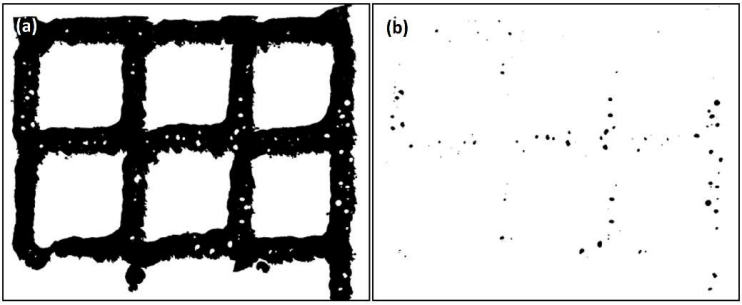

Figure III - 8. Metallographic section of a stress relieved CUB-NS specimen (a) and its pores (b).

Two different approaches were used to characterize strut porosity. The first and simplest method is to measure the sum of the area of the pores and express porosity as a percentage of the total area of the sectioned struts (area occupied by the struts):

$$\text{Porosity } [\%] = \frac{\sum \text{Area of pores}}{\text{Total area of section}} \times 100 \qquad \text{(III - 4)}$$

The second is a statistical approach based on the statistics of extreme values and it allows to estimate the maximum pore size in the whole specimen based on the distribution of pore sizes on the analyzed section. This approach permits to estimate the maximum defect size to estimate the fatigue strength of a component [30]. The authors followed the procedure described in [31], but here some aspects of the procedure are discussed for clarification:

1. Two specimens (one as-built and one HIPed) for each structure were sectioned and mirror polished, and the observable pores were counted and the area for each of them was measured.
2. The square root of the projected area of each pore on the section $\sqrt{area}$ was calculated. It is useful to clarify that we did not choose a control area S_0 to look for the maximum defect (as instructed in [31], but we calculated S_0 a-posteriori by dividing the area of the section by the number of the pores counted. S_0 is necessary to calculate the return period T defined as $T = \frac{S}{S_0}$, where S represents the area of prediction, which is the total area of the section our case. T in thus the number of the counted pores.
3. The expected maximum pore size on the section $\sqrt{area}_{max}$ was estimated using the least squares method.

4. As suggested in [31], the data with cumulative probability $F < 10\%$ and $F > 85\%$ was excluded if deviating from linearity when performing the linear regression.

The estimation of fatigue life is based only on the size of the defects projected on the section normal to the loading direction. In this work, this statistical approach was applied only to estimate the largest pore in each structure. The estimation of the fatigue strength is left for future work.

3.2.4 Micro-hardness

Microhardness profiles are measured to characterize the material's work hardening. A diamond Vickers indenter is used, applying a maximum force of 1 N. The load is applied at a constant 0.1 N/s rate with a dwell time of 10 s. Three measurements are performed at each depth (across the entire thickness of the strut) and averaged to account for material's heterogeneity and measurement errors.

3.2.5 Metrological characterization

The as-built geometrical parameters of the cellular structures were quantitatively analyzed to compare them with the CAD models using the metallographic specimens. The struts thickness and the fillet radius were both measured on the transversal and longitudinal sections for each type of structure (Figure III - 7). The definition of such sections is not related to the printing direction. This was done with a MATLAB routine that uses the standard image analysis functions embedded in the software. After binarizing the micrograph, the contours of the unit cells were extracted and, by appropriately selecting the data points, the fillet radii and the strut thicknesses were calculated. The fillet radius was estimated by trying to find the circle that fits best the curvature of the junction. A statistic of the measured values was carried out and the mean values and the standard deviations were calculated. This procedure is very simple and inexpensive, but its accuracy is limited by the preparation of the metallographic specimens. Indeed, the amount of strut thickness removed by polishing depends on a manual procedure, consequently it is affected by some degree of dispersion. On the other hand, the use of a µCT metrological system allows measuring an object with high dimensional accuracy [32]. The central cellular part of one specimen for each type was scanned using a metrological µCT system (Nikon Metrology MCT225) characterized by micro-focus X-ray tube, 16-bit detector with 2000×2000 pixels, high-precision linear guideways and controlled cabinet

temperature at 20 °C. The three-dimensional model of the specimen was reconstructed with a voxel size of 8.3 µm and then exported as high-density surface point cloud. The cell-wall diameter distribution of the cellular structures was evaluated using the evaluation software VGStudio MAX 3.0 (Volume Graphics GmbH, Germany) and was then compared with the nominal diameter. The information on the morphology of the lattices collected in such a direct way is unfortunately limited, because it does not provide data on the fillet radius and on the other morphological defects, such as the deviations in the strut cross-section. Moreover, the geometry cannot be related to the printing direction, which is known to have a considerable influence. For this reason, a HIPed regular cubic specimen was selected for a more in-depth metrological analysis.

The µCT point cloud was fed to an in-house Matlab (MathWorks, USA) routine to measure the geometrical features of the as-built lattice. A flowchart describing the basic characteristics of the routine is showed in Figure III - 9. As a first step, the centers of the junctions between the struts were estimated as the centroid of the data points of the 6 struts converging in the junction. This is the most important step because it influences all the other steps. The position of the center of the as-designed lattice was used as a first guess to find the six struts converging into the selected junction. The position of the centers was used to carry out a general comparison of the as-built geometry with the as-designed geometry by overlaying the two by minimizing the sum of the squares of the distances between corresponding junction centers. This operation made possible to capture also qualitatively the as-built/as-designed deviations strut by strut, junction by junction. Slices were sampled along the axis of each strut and the points were fitted with both circles and ellipses. The parameters registered in such way were analyzed statistically to characterize the as-built geometry and passed on to a FE code made of beam elements to study the effect of the as-built geometry on the mechanical behavior of the lattice.

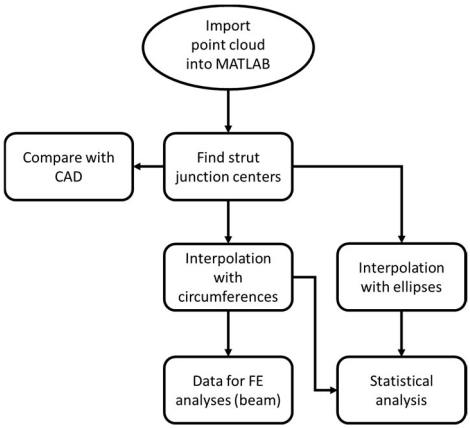

Figure III - 9 Flowchart of the Matlab routine used to analyze the point cloud generated by the µCT scanner.

3.2.6 Residual stresses

Residual stresses in a stress relieved specimen and a HIPed specimen were measured using the FIB-SEM-DIC micro-hole drilling method [33]. We have selected a suitable region of interest near a junction (A for the stress relieved specimen, in Figure III - 10 and B for the HIPed specimen, in Figure III - 11) to measure the residual stresses in the circumferential and axial directions of the strut. Later, we removed material near the junction (Figure III - 10b and Figure III - 10c) to create the flat and smooth surface needed for reliable measurements with the micro-hole drilling method. We have used Helios G3 Plasma Xe^+ FIB-SEM at 30 kV/1.3 µA for about 3 hours of continuous milling. Next, an array of submicron-holes (diameter ~400-800 nm) were milled with a PFIB using a bitmap file with predefined random pattern. The submicron-holes obtained after such procedure work in a similar way as Pt nano-dots, thus enhancing the topological contrast of FEGSEM imaging and improving the accuracy of DIC displacement/strain measurement [34]. Finally, two micro-holes 20 µm in diameter and 10 µm deep (1 and 2 in Figure III - 10d and Figure III - 11d) were milled with the PFIB (15 nA at 30 kV). The dimensions of the holes were selected so that the surface topography (roughness) after site preparation is much smaller than the micro-hole dimensions. In the stress mapping process, a sequence of three FEGSEM images (dwell time, Dt = 3 µs, 8 frames averaged, ETD detector) of the patterned areas were acquired at 0° stage tilt before milling and three images after milling.

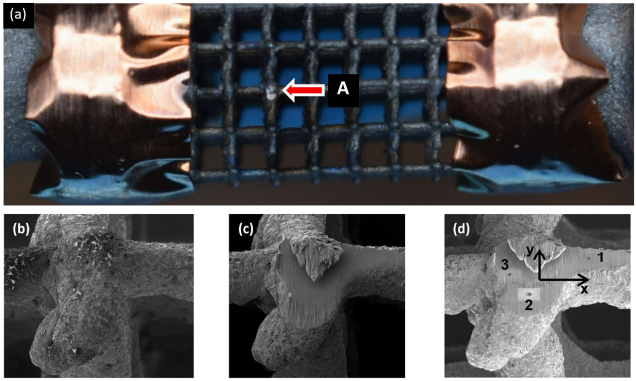

Figure III - 10. Position of residual stress measurements with the micro-hole drilling method on the stress relieved specimen: (a) optical image of the lattice, where A indicates the measurements location; SEM images if the junction before (b) and after (c) preparation for the measurements; locations of micro-holes 1 and 2, while micro-hole 3 is used for testing milling conditions before actual measurements (c).

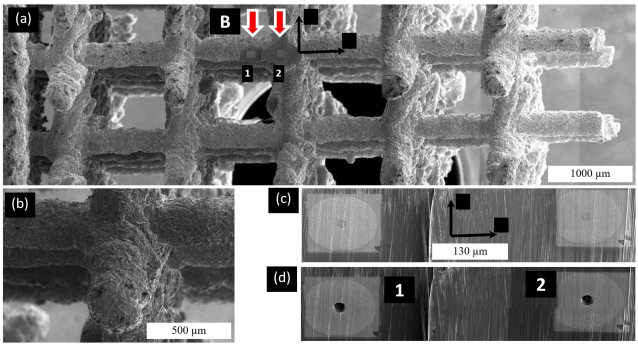

Figure III - 11. Position of residual stress measurements with the micro-hole drilling method on the HIPed specimen; (a) SEM image of the scaffold, where B indicates the measurements location, (b) junction before preparation for the measurements, (c) and (d) locations of micro-holes 1 and 2.

The radial displacements $\delta(r,\theta)$ of the surface around a circular hole of diameter a drilled in a uniformly stressed material with dimensions much greater than the hole size have a trigonometric from [33] (E is the Young's modulus):

$$\frac{\delta_r(r,\theta)}{a} = \frac{[P \cdot u_r(r) + Q \cdot v_r(r) \cdot cos(2\theta) + T \cdot v_r(r) \cdot sin(2\theta)]}{E} \qquad \text{(III - 5)}$$

where the stresses $P = \frac{(\sigma_x+\sigma_y)}{2}$, $Q = \frac{(\sigma_x-\sigma_y)}{2}$ and $T = \tau_{xy}$ respectively represent the isotropic stress, the 45° shear stress, and the axial shear stress. In Eq. (III - 5), $u_r(r,\theta)$ is the radial profile of the radial displacements caused by a unit isotropic stress *P*, and $v_r(r,\theta)$ is the radial profile of the radial displacements caused by unit shear stresses *Q* or *T*.

The corresponding circumferential displacements have the following form:

$$\frac{\delta_\theta(r,\theta)}{a} = \frac{[P \cdot u\theta(r) + Q \cdot v_\theta(r) \cdot cos(2\theta) + T \cdot v_\theta(r) \cdot sin(2\theta)]}{E} \quad \text{(III - 6)}$$

where $v_\theta(r,\theta)$ is the radial profile of the circumferential displacements caused by unit shear stresses *Q* or *T*.

The advantage of normalizing by the hole radius *a* and Young's modulus *E* (here 113 GPa) is that the radial displacement profiles $u_r(r)$ and $v_r(r)$ become non-dimensional. The resulting numerical values depend on hole depth and can be computed using finite element analysis [35].

After some mathematical rearrangements and correcting for SEM image stretch and shear artefacts, Eq. (III - 5) can be expressed in a compact 9 × 9 matrix form (see the derivation of formula in [33])

$$\overline{G}^T \overline{G} \overline{w} = \overline{G}^T \overline{\delta} \quad \text{(III - 7)}$$

Where $\overline{\boldsymbol{G}}$ is a matrix of the radial profile of the radial displacements caused by a unit stresses *P*, *Q* and *T;* $\overline{\boldsymbol{G}}$ has 2*N* rows and 9 columns, where *N* is the number of pixels of the image used for DIC calculations; $\overline{\boldsymbol{w}}$ includes the correction for SEM image stretch and shear artefacts; $\overline{\boldsymbol{G}}^T \overline{\boldsymbol{\delta}}$ (1 × 9 vector) are the products of the matrix coefficients and displacements at each pixel used for DIC calculations. Three images collected before the micro-hole milling and three after are used to average the measured stress components (σ_x, σ_y, τ_{xy}) from 9 data points. Indeed, cross-correlation of three SEM images collected before (Ib1, Ib2, Ib3) and three after (Ia1, Ia2, Ia3) micro-hole drilling permits to calculate 9 (Ib1 – Ia1, Ib1 – Ia2, Ib1 – Ia3, Ib2 – Ia1, Ib2 – Ia2, etc.) displacement field maps later used for the residual stress calculation. The uncertainty of the measurements of the three stress components is equal to the standard deviation of the 9 measured data points for each micro-hole.

3.2.7 Static testing

An Instron 4500 testing machine was used for both compressive and tensile quasi-static test equipped with a 10 kN load cell (nonlinearity ± 0.1% of R.O.) and an axial extensometer (10 mm gauge length, nonlinearity ± 0.15% of R.O.). The crosshead speed was 0.5 mm/min.
The elastic modulus was measured by calculating the slope of loading-unloading cycles according to ISO 13314. This is necessary because both in compression and tension the slope of the first portion (the elastic part) of the stress-strain curve is lower than that of the successive unloading-loading curves due to local plastic effects. The unloading-loading cycle was done between the 20% and the 70% of the compressive yield strength measured on identical specimens (the yield strength was determined as the 0.2% offset yield stress). For each structure, three stress relieved specimens were tested under quasi-static conditions: one in tension, one in compression and one to calculate the elastic modulus (unloading-loading curve). The homogenized stress-strain behavior of the lattices is obtained by considering the lattice specimen as if it was a bulk specimen, i.e. by dividing the load by the area of the specimen and the displacement by the distance between the forks of the extensometers.

3.2.8 Fatigue testing

Axial fatigue tests were carried out in laboratory environment using a RUMUL Mikrotron 20 kN resonant testing machine equipped with a 1 kN load cell operating at a nominal frequency of 120 Hz under load control. The specimens were subjected to constant amplitude fully reversed fatigue cycles (zero mean stress, $R = -1$).
The high cycle fatigue resistance of the different structures has been estimated according to a method developed by Maxwell et al. [36] for Ti alloys that considerably reduces the testing time and the amount of expensive experimental material with respect to standard methods. This method consists in a step loading procedure that starts from a load below the one expected to cause failure at a chosen number *N* of cycles, viz. 10^6 in the present work. If the specimen survives, the load is increased by a small amount (5%) and the procedure is repeated in blocks of *N* cycles on the same specimen until failure. The fatigue limit for *N* cycles can be calculated by the following interpolating formula:

$$\sigma_{N-H} = \sigma_{pr} + \frac{N_f}{N}\left(\sigma_f - \sigma_{pr}\right) \qquad \text{(III - 8)}$$

where σ_{N-H} is the estimated fatigue limit at *N* cycles, σ_{pr} is the stress level reached at the loading block prior the last one (at which failure occurred), N_f is the number of cycles in the last block that produced failure and σ_f is the stress level at the last loading block. Thus, if the specimen fails at the first loading block this approach cannot be used. A sample of three specimens was tested for each structure, for a total of 18 specimens (those failed prematurely were replaced to have an acceptable statistic). The fatigue test was interrupted when the resonant frequency of the specimen decreased of 1 Hz with respect to the beginning of the test. This avoided the complete failure of the specimen and allowed to identify the first struts to fail by heat tinting. After the fatigue test the specimen was put in tension and put in a furnace, so that only the struts failed by fatigue were oxidized.

The fracture surfaces and the external sample surfaces are investigated under a JEOL JSM-IT300LV Scanning electron microscope, pictures are taken in both secondary and back-scattered electron, the quantitative chemical analysis is performed by EDXS probe.

The fatigue notch factor K_f^* is a parameter that quantifies the actual sensitivity to notches of a material by comparing the fatigue resistance of notched and unnotched specimens. K_f^* is calculated as:

$$K_f^* = \frac{\text{fatigue resistance of bulk specimen}}{\text{fatigue resistance of the cellular specimen}} \qquad \text{(III - 9)}$$

The fatigue resistance of the cellular specimens was calculated by dividing the force applied to the cellular structure by its nominal cross section (i.e. the section measured as if the cellular material was a bulk material). The rationale behind the present definition of fatigue notch factor is that the cellular structure is intrinsically affected by notch effects and that the baseline fatigue resistance of the material can be estimated from fatigue tests carried out on bulk smooth samples.

3.2.9 FE modelling

FE models were built in ANSYS® to study and compare the mechanical behavior of the as-designed and the as-built geometry of the cellular lattices. Each CAD model was imported into ANSYS® and meshed with 10 node tetrahedral structural elements (SOLID187). Small-displacement linear elastic analyses were implemented to calculate the elastic modulus and the stress concentration factor K_t^* at the filleted joints of the as-designed structures. The stress concentration factor was calculated according to the following definition:

$$K_t^* = \frac{\text{maximum von Mises equivalent stress in the structure}}{\text{nominal homogeneous stress}} \qquad \text{(III - 10)}$$

Where the nominal homogeneous stress is the ratio between the load on the unit cell and the nominal area of the unit cell ($L \times L$ for the cubic cells and the projected area of the wedge for the cylindrical structures). This quantity is useful because it relates the homogenized stress in the lattice with the maximum stresses acting in the base material. The expected mechanical properties of the structures were calculated from the unit cells by applying the periodic boundary conditions, as described in Chapter II, by constraining the displacements of master nodes defined on the sections of the struts (Figure III - 12). In the case of the cylindrical structures, the unit cell is not a cube but a wedge of amplitude 60° (Figure III - 1): the applied boundary conditions consist in restraining the displacements normal to the bottom and lateral cuts and applying a vertical displacement to the top surface (Figure III - 12b). It is notable that in the cylindrical structures not all the junctions are loaded in the same way due to the cubes being skewed. For this reason, for the cylindrical structures, the highest SCF values have been considered. A convergence study was carried out for each FE model of the unit cell by refining the mesh and calculating the error on the SCF for each level of mesh refinement with respect to the finest one. The results were deemed to have converged satisfactorily when the error was 1% or less.

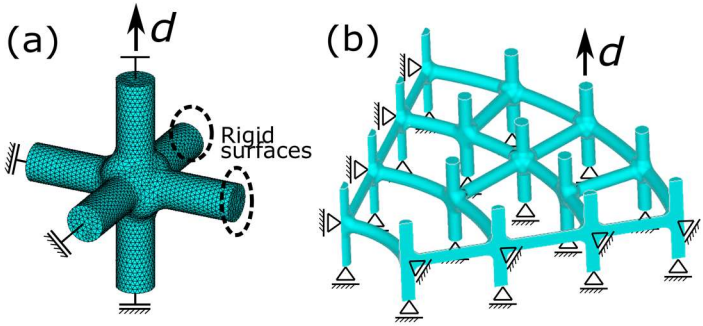

Figure III - 12. Periodic boundary conditions applied to the as-designed unit cells: (a) cubic unit cells; (b) cylindrical unit cells.

The FE software was also used to characterize the mechanical behavior of the as-built geometry of the regular cubic lattice acquired from the metrological μCT scans and to interpret the results of the mechanical tests. Models based on beam elements (3 node Timoshenko beam, BEAM189) of the entire specimen (Figure III - 13a) that

include the geometrical defects of the as-built lattice were devised. Such models are designed with different degrees of simplification of the real geometry to compare the effect of the different types of defects on the elastic modulus. Models of the unit cell obtained from the μCT scans based on solid elements (SOLID187) were also devised (Figure III - 13b) to calculate the elastic modulus of the lattice and the stress concentration factor at the joints using Eq. (III – 10). These models were obtained by meshing eight junctions extracted from the μCT scan. These set of BCs (**Errore. L'origine riferimento non è stata trovata.**b) were chosen because, in the author's opinion, PBCs are not appropriate in this case because the structure is not strictly periodic anymore (given the irregularities). On the other hand, it is reasonable to assume that the horizontal struts are unloaded while the vertical struts are constrained to deform along the vertical axis by the other vertical struts. Note that applying these set of BCs to the as-designed unit cell would give the same elastic modulus as with the PBCs given the perfect symmetry of the as-designed geometry. An accurate description of these models is provided in Section 3.3.7 and Section 3.3.9.

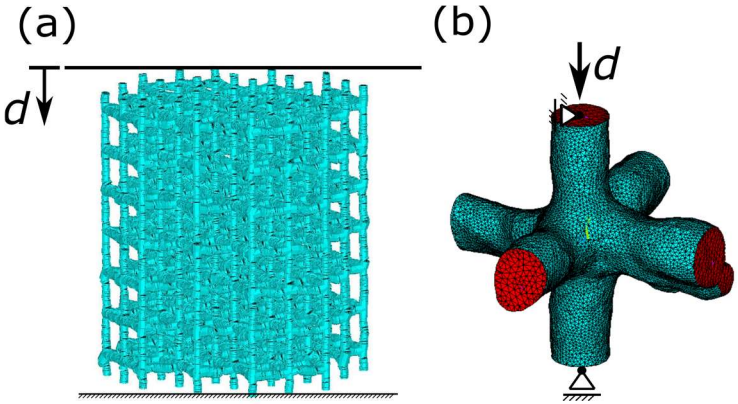

Figure III - 13. FE models devised to study the mechanical behaviour of the as-built regular cubic specimen (CUB NS) lattice and relative boundary conditions: (a) beam model; (b) solid model of a junction extracted form the μCT scans.

The elastic modulus of bulk Ti-6Al-4V specimens was measured in Benedetti et al. [6] to be 113 MPa for the stress relieved specimens and 110 MPa for the HIPed specimens (the elastic moduli were measured in specimens printed along their longitudinal direction). Quasi-static testing of cellular specimens was carried out only on stress relieved cellular specimens, thus the FE analyses were performed only with the elastic properties of the stress relieved Ti-64 ($E = 113\ GPa, \nu = 0.34$)

and assuming the material isotropic. The same material properties were implemented in the FE models aimed at estimating the SCFs.

Regarding the estimation of the stress concentration factor, a careful reader may object that the local maximum von Mises stress underpinning the K_t^* definition given by Eq. (III - 10) leads to an oversimplification of the fatigue behavior of such structures, as the fatigue damage is controlled by the stress-strain field reigning in a structural volume surrounding the critical notch. However, on the base of the analysis of the plain and notch fatigue behavior of the SLM base material conducted in [37] and [38], it can be noted that, owing to the low level of internal porosity displayed by the cellular samples, the expected size of such critical volume is on the order of few microns, a scale length still inaccessible to the resolution of the CT scans performed in the present study. Consequently, the analysis undertaken in the present paper must not be intended as a detailed notch fatigue prognosis, but a first simplified attempt to understanding the reasons of the discrepancy between the expected and the actual fatigue strength of such structures.

The creation of the FE solid models from the μCT point clouds was a challenging task. The data is exported from the μCT as a *stl* (STereoLitography) surface tessellation file of a junction. This file typically contains gaps, holes, and sharp edges so it cannot be directly converted to a solid file, but it needs to go through a correction procedure, consisting of the following steps:

- Rough correction of the tessellated surface in Autodesk NETFABB Standard 2018®. In this step the mesh is repaired, if necessary, by closing gaps and stitching the tessellation triangles. The complexity of the surface (protuberances, sharp edges) is retained. The file is exported as a binary *stl*.
- A more in-depth repair is carried out in Materialise MAGICS 21.1®. The mesh is smoothed to reduce its complexity and further repaired if necessary. Smoothing removes the micro-defects of the surface (gaps and sharp edges) which would make it impossible to obtain a closed surface necessary for the conversion to a solid model. The file is exported as a binary *stl*.
- The tessellated surface model is converted into a solid in Autodesk INVENTOR Professional 2018® with the *"Conversion to base feature"* plug-in. The struts of the solid model of the unit cell are then trimmed to obtain flat surfaces where to apply the boundary conditions. The file is exported in a *stp* format.
- The solid model is imported into Ansys WORKBENCH 18.0® for meshing.

3.3 Results and discussion

3.3.1 Microstructure

The stress relieved microstructure (Figure III - 14) is characterized by fine acicular martensite (α' phase). In the transversal section, some bigger plates are visible, which are most likely α phase. The effect of the HIP treatment on the microstructure is clearly shown in Figure III - 15. The microstructure is remarkably coarser, characterized by α lamellae in a β matrix (α+β structure). The micrographs shown here are taken from the regular cylindrical structures (CYL-NS), but these considerations apply to all the structures.

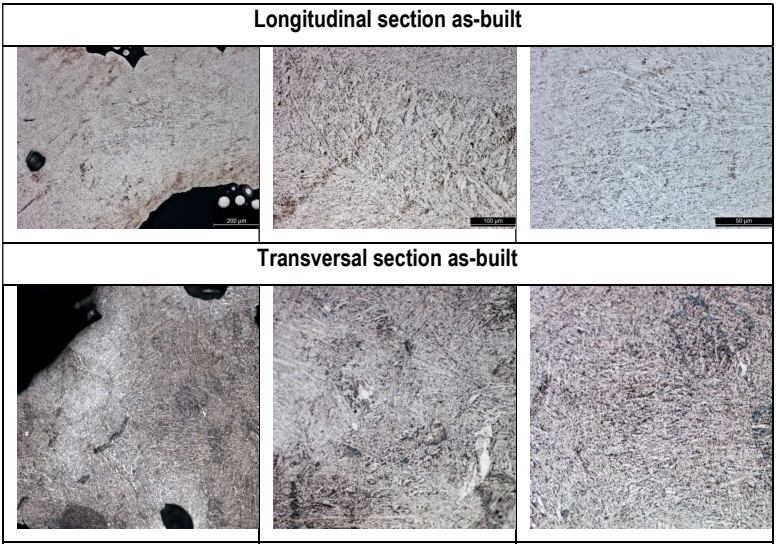

Figure III - 14. Light optical micrographs of the microstructure of the Ti-6Al-4V ELI SLM cellular samples in the stress-relieved condition. The microstructure is α' martensite.

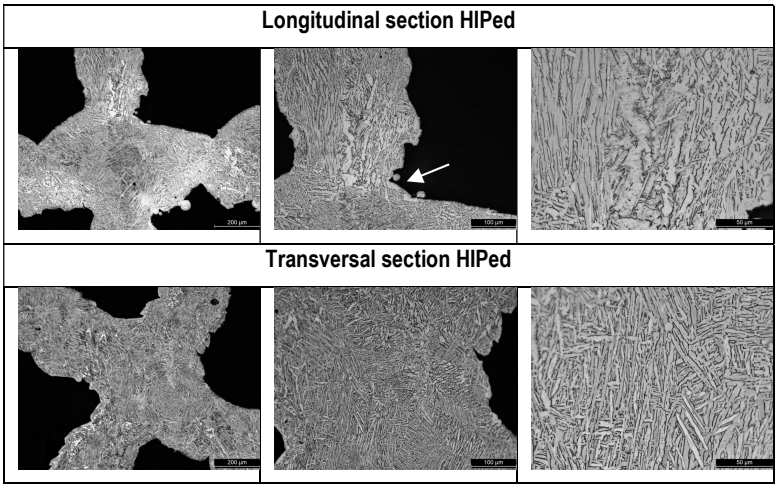

Figure III - 15. Light optical micrographs of the microstructure of the Ti-6Al-4V ELI SLM cellular samples after the HIP treatment. The microstructure is coarse α+β, with presence of alpha-case at some locations (indicated by the arrow).

3.3.2 Micro-hardness

The presence of a harder martensitic microstructure in the stress-relieved specimens is confirmed also by the indentation tests (Figure III - 16), being the stress relieved specimens significantly harder than the HIPed specimens. SLM Ti-6Al-4V bulk specimens (both stress relieved and HIPed with the same process parameters) have also been tested for micro-hardness [39]. The hardness of the lattices is slightly higher than the bulk material in the stress relieved condition, being the hardness roughly 400 HV and 380±10 HV, respectively, possibly due to the finer microstructure of the cell walls. On the other hand, the hardness of the material in the HIPed struts is about 380 HV, while in the bulk specimens this value is matched only in a 100 μm deep layer below the surface (subsequently, hardness decreases to 340 HV). Indeed, work-hardening induced by HIP is limited to the surface layer of a component, but, due to the small diameter of the lattice struts, this layer coincides with the entire thickness of the cross-section.
Micro-hardness does not show any clear dependence on the morphology of the structure, as expected.

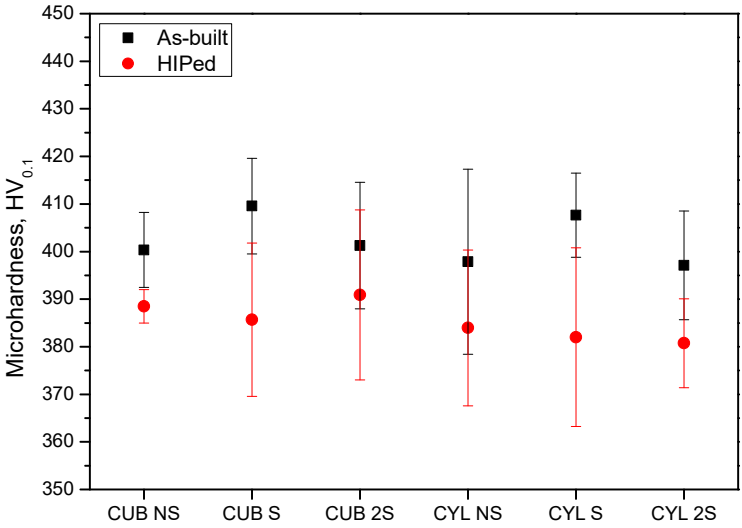

Figure III - 16. Results of the micro-hardness tests for each structure type in the as-built and the HIPed cases.

3.3.3 Strut porosity

Strut porosity is strongly reduced by HIPing (Figure III - 17 and Figure III - 18). It is possible to note how HIPing is particularly effective in reducing the size of the biggest pores. The cylindrical specimens are richer in pores than the cubic specimens and this is most likely because the cylindrical ones are characterized by a more intricate geometry that is complex to produce. It is also interesting to observe that both porosity and the size of the maximum pore tend to decrease with increasing staggering (NS → S → 2S). This could be explained by the fact that the strut thickness increases with staggering and thus a higher quality is obtained, as will be shown in the next Subsection.

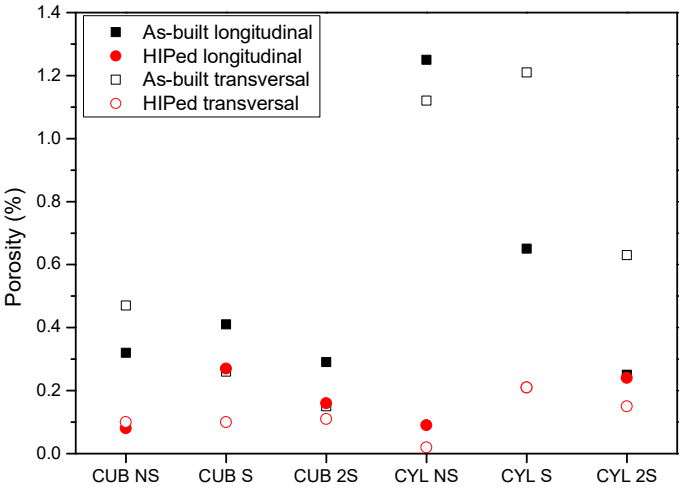

Figure III - 17. Porosity (%) calculated on the transversal (T) and longitudinal (L) sections with respect to the specimen axis.

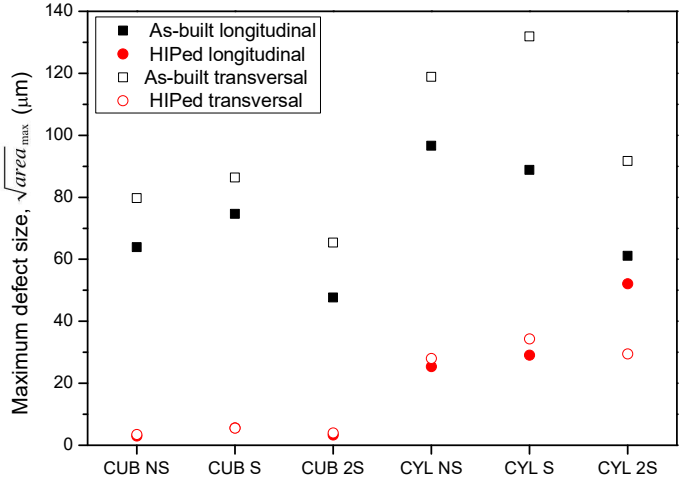

Figure III - 18. Maximum defect size expressed as $\sqrt{area}_{max}$. The pore sizes are shown for transversal (T) and longitudinal (L) sections with respect to the loading direction (specimen axis).

3.3.4 Metrological characterization

The surface of the stress relieved specimens is covered with loosely attached unmelt particles (as can be seen in Figure III - 19a) that increase the surface roughness. On the other hand, the sand blasting treatment considerably smoothed the surface of the HIPed specimens (Figure III - 19b). On the other hand, the notches and the irregularities of the geometry (thickness variation, strut waviness and strut misalignment) stay unchanged. Comparing Figure III - 19 with Figure III - 1 shows that the as-built junctions are sharper. Indeed, the fillets are considerably smaller than those in the CAD and, moreover, in some locations are not reproduced at all.

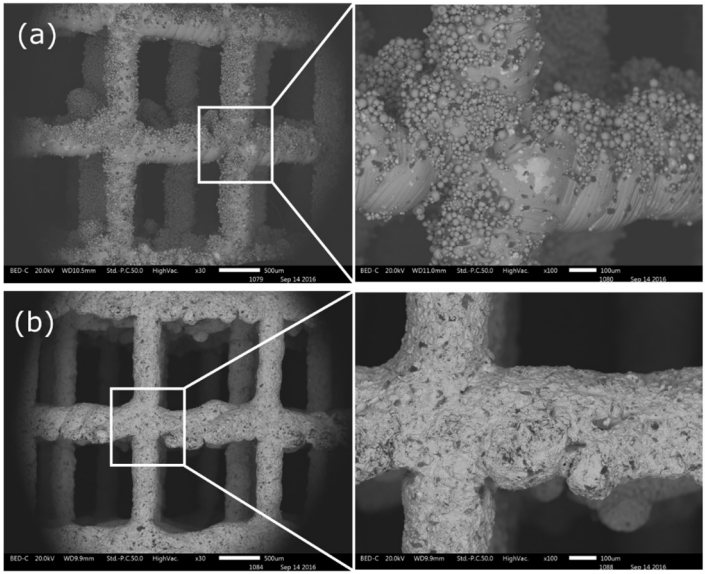

Figure III - 19. Surface appearance of the SLM Ti-6Al-4V specimens before (a) and after (b) HIP.

The metallographic sections (Figure III - 20a) provide a more quantitative assessment on the as-built morphology. The values of the fillet radius were difficult to measure since they were very badly reproduced by the printer and it was not always possible to identify a “true” fillet. Nevertheless, by interpolating with a circle the profiles corresponding to the location of the fillet in the as-designed junction (Figure III - 20b), the radius of each fillet could be estimated. Indeed, a very high dispersion on the measurements of the fillet radius was observed, making it hard to identify any correlation between the as-designed values and the as-built values.

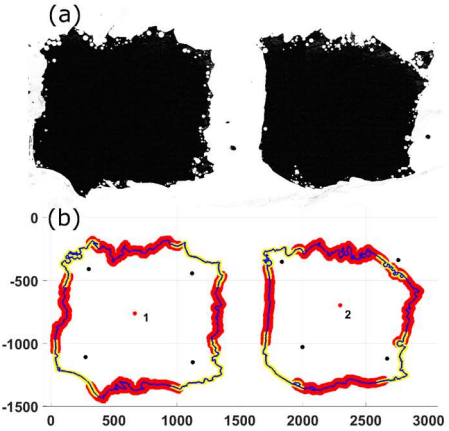

Figure III - 20. Detail of the procedure to estimate the fillet radius and the strut thickness from metallographic sections. This figure is purely demonstrative, the measurements are carried out on bigger images to have an appropriate statistic. (a) Micrograph to be analyzed (as built specimen, note the presence of pores); (b) MATLAB output: the yellow part of the contour are the data used to estimate the fillet radius, the red part of the contour are the data used to estimate the thickness of the horizontal and vertical struts, the red dot is the barycenter of the cell.

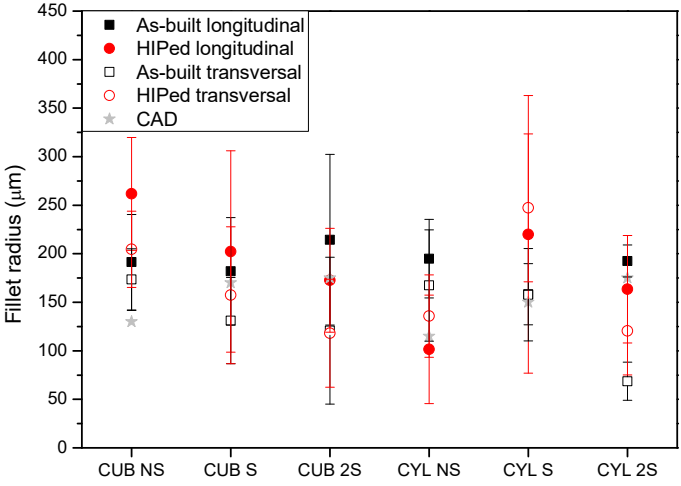

Figure III - 21. Mean value and standard deviation of the fillet radius calculated from the metallographic sections. The values are shown for the transversal (T) and longitudinal (L) sections with respect to the specimen axis.

The as-built strut diameters (Figure III - 22) are reasonably close to the respective nominal values, but in general the struts are oversized with respect to the CAD. There isn't a significative difference between the stress relieved and the HIPed (sand blasted) specimens, due to the wide dispersion of the data. The results of the μCT measurements (limited to the HIPed specimens) provide some interesting additional observations on the distribution of the strut thicknesses for each lattice (Figure III - 23). The staggered structures, which have thicker but shorter struts, show a wider distribution of the cell-wall diameters, but the modal value of the wall diameter is closer to the nominal CAD value. Most likely, on such a small scale the length of the struts has some influence on the accuracy of reproduction. On the other hand, the non-staggered lattices show a narrower distribution, but the deviation from the CAD geometry is more marked.

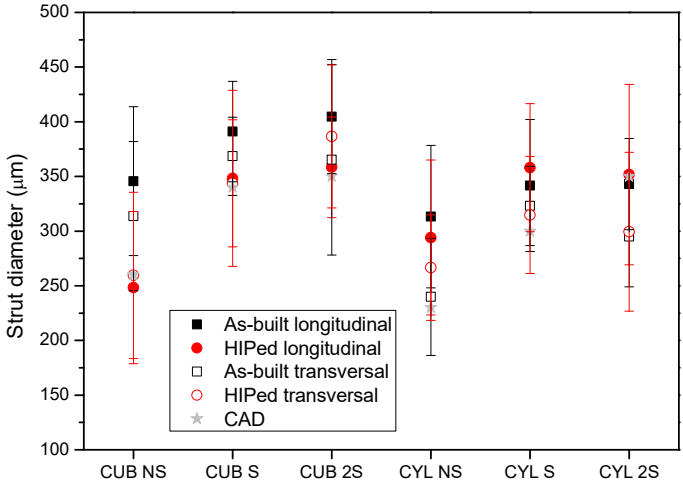

Figure III - 22. Mean value and standard deviation of the strut diameter calculated from the metallographic sections. The values are shown for the transversal (T) and longitudinal (L) sections with respect to the specimen axis.

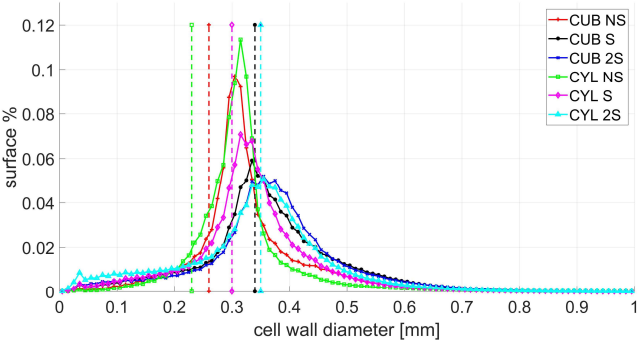

Figure III - 23. Cell-wall diameter distribution for the HIPed specimens (search angle 30°); the vertical lines represent the nominal CAD cell-wall diameters.

The previous results provide some interesting points to consider regarding the comparison between the geometry of a lattice expected from the CAD and that obtained after manufacturing, but a more in-depth analysis is necessary to increase the understanding of the consequences of manufacturing on the final component and possibly to provide adequate design tools to eventually overcome these issues. Unfortunately, being such an analysis quite complex and time consuming, it was limited only to one specimen. This granted, a regular cubic HIPed specimen was chosen for the more in-depth metrological analysis using the µCT point cloud (a detail is shown in Figure III - 24a, compared with the as-designed geometry), that was carried out with an in-house Matlab routine. An *xyz* reference system with the axes parallel to the struts is defined to identify the three set of struts (Figure III - 24b); the *z* axis is aligned with the loading direction of the specimen (Figure III - 6). The distance between the positions of the centers of the junctions of the as-built lattice (Figure III - 24c) and the corresponding centers of the as-designed lattice are measured to estimate the overall distortion of the lattice (Table III - 3). The average distance is low (35.5 µm) if we consider that the unit cell size is 1500 µm, and the maximum value confirms that the overall distortion of the lattice is not particularly severe. The junction centers were used to overlay the as-built lattice on the as-designed lattice (details of the outcome are shown in Figure III - 24a in 3D and in Figure III - 25 the *xy* plane in 2D) and this allows us to make some preliminary observations. The surface of the struts is highly irregular and specifically the struts laying in the printing plane (*x*-struts) show numerous protrusions.

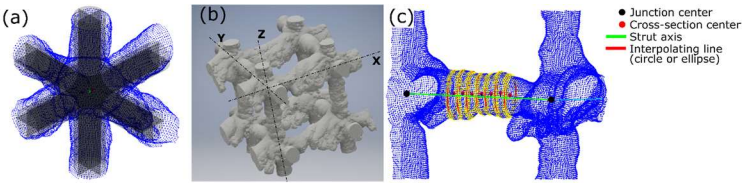

Figure III - 24. Details of the results of the µCT scan of the as-built lattice. (a) Overlay of an as-built unit cell (blue points) on the as-designed unit cell using the junction centers; (b) detail of the µCT scan with the *xyz* reference system; (c) µCT data cloud with sections, section centers and strut axis highlighted. Note the waviness of the strut (offset between the section centers and the strut axis).

Table III - 3. Statistical descriptors of the misalignment of the junction centers.

Statistical parameter	Value [µm]
Maximum deviation	95.0
Minimum deviation	2.8
Mean	35.5
Standard deviation	18.4
Median	32.2

Ten sections were sampled along each strut of the specimen and the following geometric parameters were measured (for clarity, only seven shown in Figure III - 24c):

- Cross-section equivalent radius (calculated as the radius of the circumference with the same area as the strut cross-section).
- Cross-section eccentricity $e = \frac{\sqrt{a^2-b^2}}{a}$, where *a* and *b* are the major and minor axis of the best fitting ellipse, respectively. $e = 0$ indicates a perfect circle, while $e = 1$ indicates a segment.
- Cross section orientation with respect to the *xyz* reference system.
- Offset of the cross-section center to the strut axis.

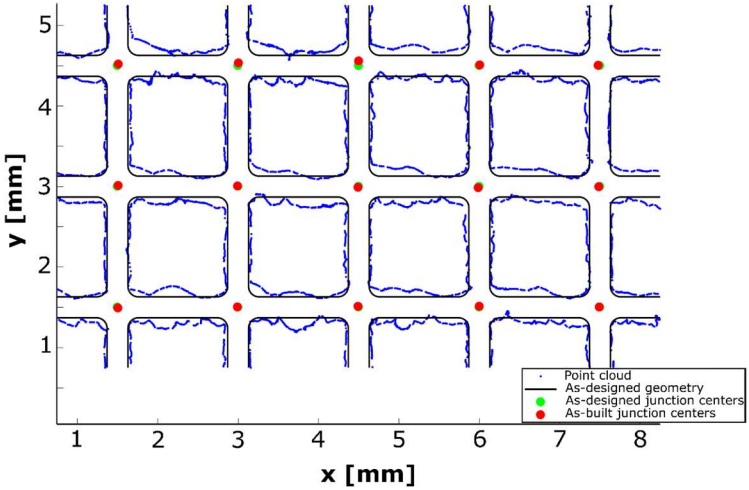

Figure III - 25. 2D view of the overlay of the as-built lattice (blue points) on the as-designed lattice (black lines) using the junction centers. Note the greater deviations of the horizontal struts (*x*-strut, parallel to the printing plane) compared to the vertical struts (*y*-struts, printed at 45° to the printing plane).

A first appreciation of the as-designed/as-built deviations is already possible from a visual comparison (Figure III - 24a and Figure III - 25). The statistical analysis carried out on the quantities previously listed gave a quantitative measure of the uneven distribution of material in the as-built lattice, which is ultimately determined by the local heat transfer properties of the powder-solid material system and it manifests as a series of defects that affect the lattice. According to this analysis, the following defects could be identified and classified:

- Variable strut cross-section equivalent radius.
  The equivalent radius has the statistical distribution shown in Figure III - 26a, characterized by the descriptors listed in Table III - 4. The most notable aspect is that the average cross-section equivalent radius is always higher than the as-designed value. The struts parallel to the printing plane (*x*-struts) show the greatest mean deviation from the design value (51.8%) and the widest distribution. The wider the distribution, the less predictable is the outcome of the printing process.
- Offset of the cross-section centers from the axis connecting two (as-built) junction centers.
  This offset is manifested as waviness in the struts and again the struts parallel to the printing plane (*x*-struts) show the highest average offset

(55.8%, 3) and the widest distribution (Figure III - 26b and Table III - 5). In fact, the struts laying in the printing plane are highly irregular with numerous protrusions (which are possible to appreciate also visually, see Figure III - 25 for example) that offset the barycenter of the section.

- Strut cross-section eccentricity.
  The cross-section of the as-built struts deviates somewhat from the circular shape and tends to become elliptical. The eccentricity measures the deviation from the circular shape. The best fitting ellipses of the cross-sections are shown in Figure III - 27 for each strut set. A statistical analysis of the eccentricity was also carried out and we observed that most of the struts deviate from a circular section (Figure III - 26c). The struts laying in the printing direction (*x*-struts) are the most elliptical ($e = 0.79$, Figure III - 27a) and show an inclination of 45° to the *y* and *z* directions, exactly aligned with the printing direction. The statistical distribution of the inclinations (Figure III - 26d) is very narrow around angles of -45°, +45° and 135°. The *y*- and *z*-struts show a more uniform distribution of inclinations, although there appears to be a prevalent orientation (16° and 20°, respectively, Figure III - 26d). The small inclination of the cross-sections of the other struts indicates that most likely the specimen was not printed perfectly at 45° as indicated in Figure III - 6b.
- Missing/interrupted struts.
  We observed a few struts with considerable thinning in the cross-section, as shown in Figure III - 28. An excessive thinning may lead to the interruption of the strut: in this specimen, of 910 struts, two vertical struts are interrupted due to an excessive thinning of the section.
- Junction center position.
- Observing Figure III - 24c and Figure III - 25, the uneven distribution of material in the proximity of the junction is immediately noticeable. Because of this, the junction centroids of the as-built lattice don not coincide with those of the as-designed lattice and there is a 35±18 μm offset on average, which is quite small compared to a 1500 μm unit cell size. Some statistical parameters of the as-built/as-designed junction center offset are reported in Table III - 3.

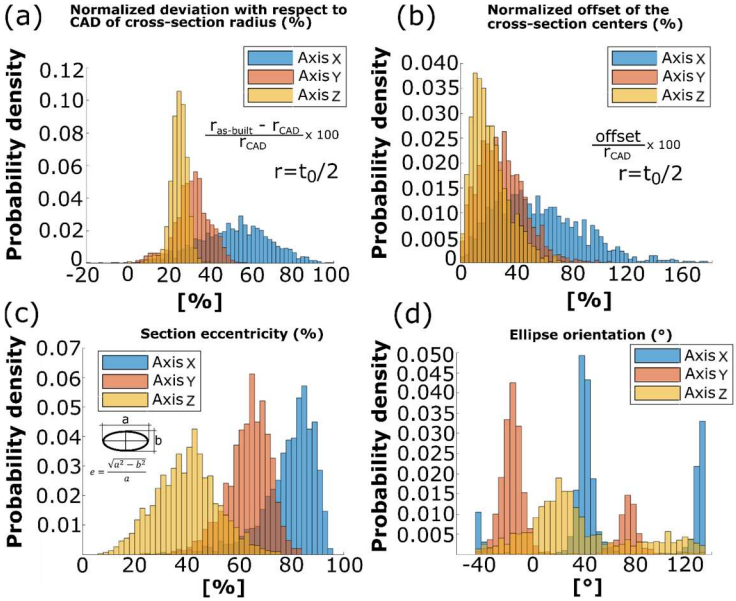

Figure III - 26. Results of the statistical analysis carried out on the µCT point cloud: (a) distribution of the normalized deviation between the as-built equivalent cross-section radius and the as-designed value (0.130 mm) in % ; (b) distribution of the normalized offset of the centers of the fitted circumferences from the strut axis; (c) distribution of the eccentricity values calculated form the ellipses fitted on the sampled cross-sections; (d) distribution of the orientations of the best fitting ellipses.

Table III - 4. Statistical descriptors of the cross-section radius variation (CAD: $t_0/2$ = 0.130 µm).

Statistical parameter	Cross-section radius variation					
	X [µm]	*Y* [µm]	*Z* [µm]	*X* [%]	*Y* [%]	*Z* [%]
Max. value	128.1	73.2	50.9	98.6	56.3	39.2
Min. value	-23.9	-0.18	-16.2	-18.4	-0.13	-12.5
Mean	67.3	40.8	32.2	51.8	31.4	24.8
Std. Dev.	22.3	11.0	5.90	17.20	8.50	4.50
Median	68.3	41.3	32.6	52.5	31.8	25.0

Table III - 5. Statistical descriptors of the cross-section center offset.

Statistical parameter	Cross-section center offset					
	X [µm]	*Y* [µm]	*Z* [µm]	*X* [%]	*Y* [%]	*Z* [%]
Max. value	226.2	139.4	96.1	174	107.3	73.9
Min. value	1.5	1.3	0.2	1.2	1.0	0.2
Mean	72.6	38.5	27.7	55.8	29.6	21.3
Std. Dev.	39.9	21.1	16.9	30.7	16.2	13.0
Median	67.3	36.5	23.8	51.8	28.1	18.3

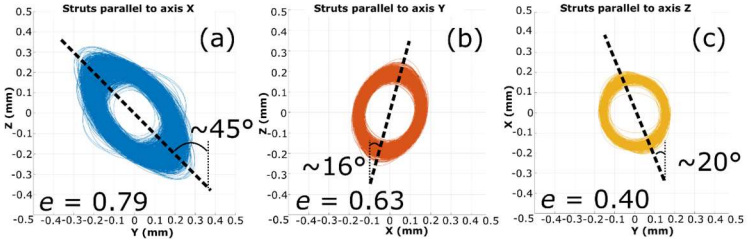

Figure III - 27. Plot of the best-fitting ellipses of the cross-section of each set of struts. The centers of the sections of each strut are translated to the (0,0) point with the correct inclination to the other two set of struts indicated by the *xyz* reference system. (a) x-struts; (b) y-struts; (c) z-struts.

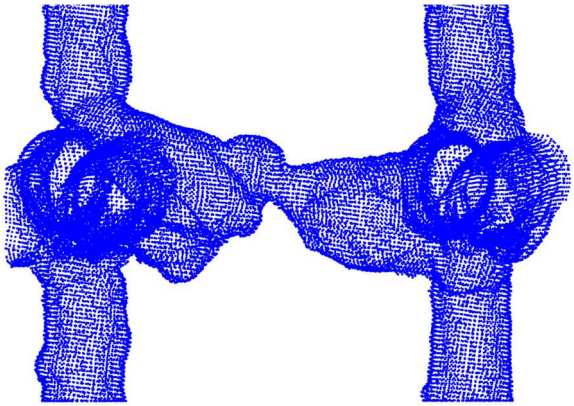

Figure III - 28. Example of a strut (*x*-strut) with considerable thinning in the cross-section.

3.3.5 Residual stresses

The residual stresses in a stress relieved specimen were measured using the Plasma FIB-SEM-DIC micro-hole drilling method. Detrimental tensile residual stresses were found in the surface regions of the junction in location 1 in the circumferential direction ($\sigma_y = +200 \pm 80MPa$) and in the axial direction ($\sigma_x = +100 \pm 70MPa$). While in location 2, both tensile and compressive residual stresses were present: $\sigma_x = +300 \pm 100MPa$ and $\sigma_y = -100 \pm 70MPa$ (see coordinates in Figure III - 10d). In the HIPed specimen, residual stresses were measurably lower, compared to the stress relieved case. In the surface regions of the junction, in location 1, stresses are reduced both in the circumferential direction (σ_y = + 50 ± 30 MPa) and in the axial direction (σ_x = + 70 ± 15 MPa). While in location 2, residual stresses are close to zero: σ_x = + 25 ± 10 MPa and σ_y = + 20 ± 15 MPa (see coordinates in Figure III - 11).

3.3.6 Static mechanical tests

The small number of specimens tested is a considerable limit to this discussion, nevertheless it can be observed that the deformation at fracture is higher in compression (Figure III - 29) than in tension (Figure III - 30) for all the lattices. The lower ductility in tension is most likely related to the effect of stress raisers (sharp joints and notches) that lead to a locally multiaxial stress state and subsequent low deformation at fracture. Moreover, it is notable that the non-staggered lattices are even less ductile compared to the staggered lattices, both in tension and in compression. Considered that the lattices have roughly the same elastic modulus, bending dominated structures, having thicker struts, allow for greater deformations and consequently, deformation energy absorption.

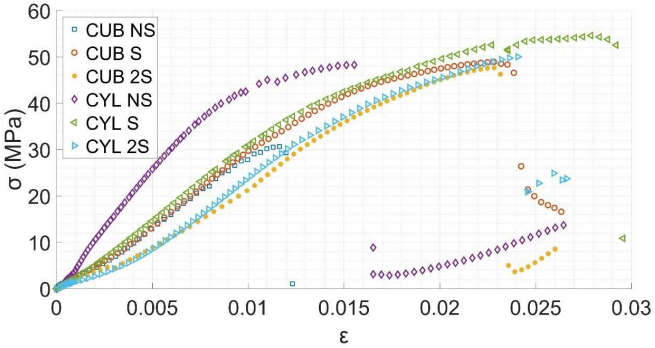

Figure III - 29. Compressive homogeneous stress-strain curves.

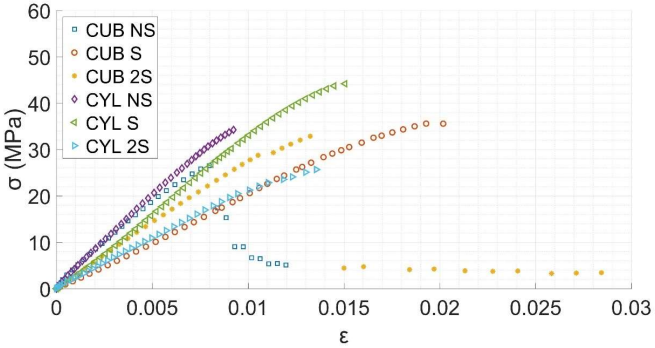

Figure III - 30. Tensile homogeneous stress-strain curves.

FE analyses based on the CAD models of the unit cells (Figure III - 31) were used to calculate the elastic modulus of each type of structure and to compare it with the experimental results (Table III - 6 and Figure III - 32). There is an overall good agreement, despite differences most likely caused by the geometrical defects of the specimens, namely strut oversizing due to the manufacturing process, strut cross-section variation along the strut-axis and strut misalignment. In order to identify more precisely the effects of such defects, a more in-depth analysis is required, which is discussed in the next Subsection.

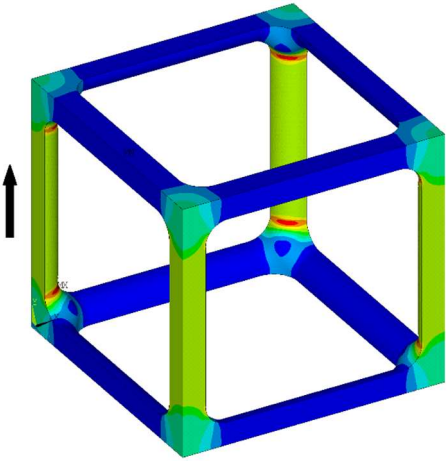

Figure III - 31. Example of FE model of a unit cell: contour plot of the von Mises equivalent stress in the CUB NS unit (axial load directed parallel to the arrow).

Table III - 6. As-designed and as-built (from loading-unloading curves) elastic moduli for each lattice.

Structure	t_0 (mm)	R (mm)	FE elastic modulus (MPa)	Experimental elastic modulus (MPa)
CUB NS	0.260	0.130	3021	3436
CUB S	0.340	0.170	3220	3188
CUB 2S	0.350	0.175	3208	3231
CYL NS	0.230	0.115	3000	2942
CYL S	0.300	0.150	2960	2504
CYL 2S	0.350	0.175	2480	2513

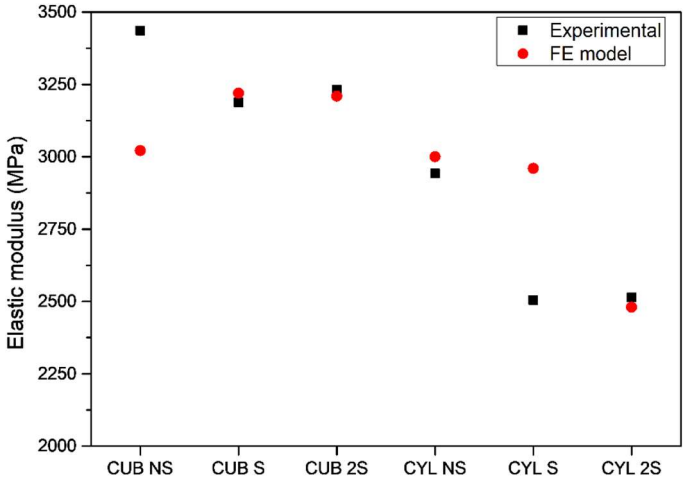

Figure III - 32. Comparison of the elastic modulus as calculated from the FE analyses based on the CAD model and the experimental values.

3.3.7 Elastic modulus and the effect of defects

The detailed information available on the morphology of the regular cubic lattice (CUB NS) made possible to carry out an in-depth investigation on the effect of manufacturing defects on the elastic modulus. FE models of the lattice including manufacturing defects have been solved and the results compared with the

experimental results. This analysis was limited to the regular cubic lattice due to the complex and time-consuming procedure to carry out a full metrological characterization necessary to obtain the data necessary to build the FE models. A solid FE model of the as-designed CUB NS unit cell was used to estimate the expected elastic modulus of the structure, by applying periodic boundary conditions. Solid models of the as-built structure were also devised by meshing the eight junctions extracted from the μCT scan.
Solid models are the most accurate, but also very computationally demanding. To overcome this limitation, the results of the μCT scan were used to build models made of beam elements of the entire specimen that include the geometrical defects of the as-built lattice. Four such models were created, of increasing complexity, to compare the effect of the different types of defects (in the first three models, the centers of the junctions are in the as-designed location):

- Beam model with variable cross-section diameter and zero center offset.
- Beam model with variable cross-section center offset and constant diameter, equal to the mean value calculated form the μCT data (the mean values are different for struts of different orientation).
- Beam model that combines the two previous defects.
- Beam model that includes all the defects: variable cross-section diameter and offset, missing struts and the junction centers location as calculated form the μCT data.

Although not useful to estimate the stresses, these models lead to some more insight into the effect of defects on the elastic modulus of the lattice. Each strut was meshed with beam elements with a circular cross-section and the section properties (diameter and center offset from the mean axis) assigned based on the statistics extracted from the μCT data (the beam model and its details are shown in Figure III - 33). The strut thickness (diameter) and the offset were assigned randomly from a normal distribution defined by the mean value and the standard deviation calculated from the μCT data analysis (Figure III - 26a and Figure III - 26b). The offset is defined by a vector of modulus extracted from the distribution of Figure III - 26b and direction an angle θ chosen randomly between 0° and 360° (Figure III - 33). It should be noted that the distributions of the offset in Figure III - 26b are not strictly normal, but for simplicity we assumed that they are. We simulated the compression tests by applying a small uniform displacement to the top side of the model and by fixing the bottom side, as shown in Figure III - 33. The simulations were repeated 15 times for each model type to achieve a suitable statistic.

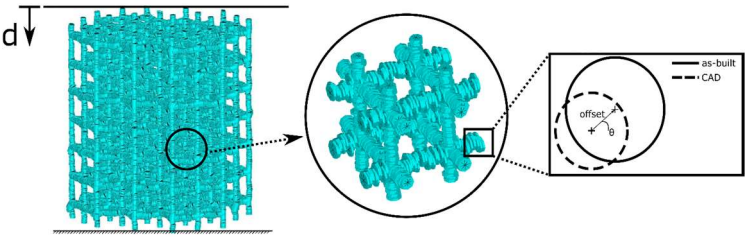

Figure III - 33. Beam model of the cellular part of the specimen, including geometrical defects. The struts are meshed with beam elements of circular cross-section and a random offset from the axis joining two junctions.

The comparison of the results of the various simulations provides some appreciation of the role of the geometrical defects on the elastic modulus (Figure III - 34). The as-designed model (E = 3111 MPa) with PBC considerably underestimates the elastic modulus of the as-built structure (3436 MPa). This mismatch is due to the combined effect of the defects in the as-built structure, predominantly due to the thicker struts of the as-built lattice. On the other hand, the elastic modulus of an ideal unit cell with the struts thickness equal to the as-built mean values is well over 4000 MPa, regardless of the fillet radius [7]. In fact, the analysis of the results of the beam models can resolve the contribution of the different types of defects:

- the offset of the cross-section centers (strut waviness) causes a remarkable drop in the elastic modulus (3870 MPa) compared to the model that accounts only for the cross-section diameter statistical distribution (4379 MPa);
- the cross-section diameter statistical distribution does not seem to have a significant effect on the elastic modulus;
- the misalignment of the junction centers further decreases the elastic modulus to 3659 MPa;
- Including also the missing struts, the elastic modulus becomes 3491 MPa, which is very close to the experimental value.

In conclusion, the increase in the mean cross section diameter has the obvious effect of increasing the elastic modulus, but it also appears that the width of the cross-section diameter distribution does not have a significant effect (very small standard deviation in the results of the beam models). The strut waviness and the misalignment of the junction centers significantly decrease the elastic modulus while the missing struts, even if parallel to the loading direction, do not have a major effect, if they are few compared to the total number of struts (two, in our specimen). This is

because the strut waviness and the misalignment of the junction centers introduce bending loads in the lattice. It is likely that a stretching dominated lattice such as the one considered in this work, is particularly sensitive to these types of defects. The results of the solid FEM model based on the CT scans are reasonably close to the experimental value, although slightly higher. This is most likely because only unit-cell sized models could be simulated, that cannot correctly reproduce the complex interaction between the various defect types.

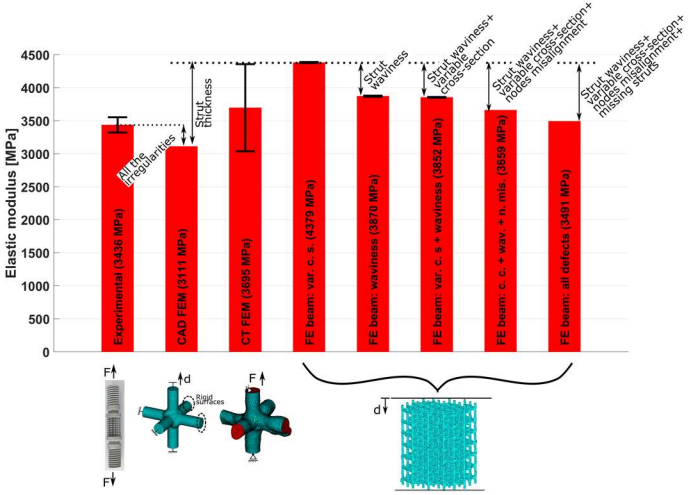

Figure III - 34. Bar chart comparing the elastic moduli calculated by the various FE models with the experimental measurement.

3.3.8 Fatigue strength

The results of the fully-reversed fatigue tests (Figure III - 35) indicate that HIPing does not have a clear effect on fatigue resistance. The most reasonable explanation for this is that fatigue resistance is controlled more by the manufacturing quality in terms of geometrical irregularities (especially notches) rather than by internal pores, which in turn are the main factor controlling the fatigue resistance of bulk materials fabricated via SLM. Indeed, the SEM images of the lattices previously shown indicate that HIPing does not reduce the severity of notches that are invariably present at the strut junctions. Moreover, the thermal treatment associated to HIPing reduces the material microhardness, negatively impacting on the fatigue resistance of SLM manufactured Ti-6Al-4V, as observed in (Benedetti, 2018).

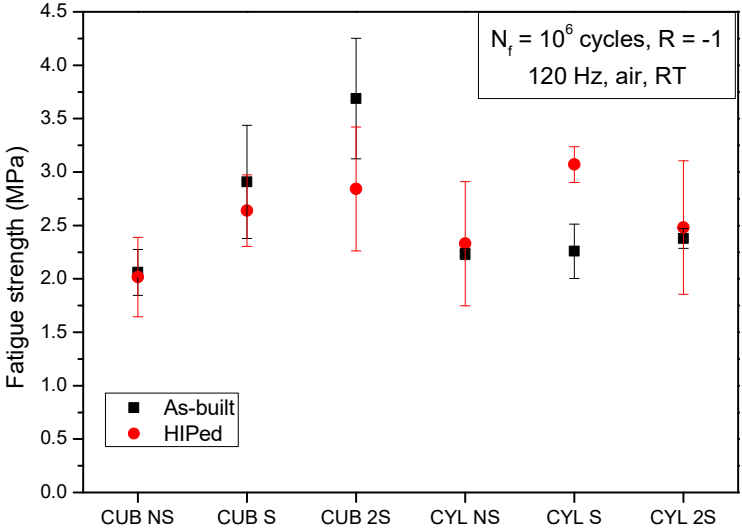

Figure III - 35. Fatigue resistance at 10^6 cycles for each structure type with error bars.

Staggering appears to have a positive effect on fatigue resistance and this effect is more marked in the cubic specimens. The most likely explanation is related to the highest SCFs (Table III - 7) measured at the strut junctions with FE simulations on the CAD models. Staggering the unit cells of the cubic lattices permits to reduce the stress concentration factor at the junctions, while preserving the stiffness, due to the increase of the struts thickness. The same does not apply to the cylindrical structures because of the more complex design that causes a non-uniform distribution of loads on the transversal section of the staggered structures. Thus, some struts carry more load than others and the tensions are higher at the corresponding junctions despite the higher values of t_0 and R.

In compressive-compressive fatigue tests, structures with small or absent bending actions (as the cubic structure) show very high fatigue resistance. Since this study is concerned with push-pull fatigue, all the structures are subjected to tensile stresses, included the cubic ones, and thus the fatigue strengths measured are not comparable with those reported in other works [40]. We observed that the fatigue resistance is in fact higher for structures with prevalently bending actions, but this is because those structures have thicker struts (given that the nominal elastic modulus is the same for all structures) and thus lower stresses. As observed also by Zargarian et al. [41], the effect of the strut cross section size appears to have the strongest influence on the fatigue strength, compared to the relative density (given the same base material).

The fully reversed fatigue strength at 10^6 cycles of unnotched bulk SLM specimens, printed with the same process parameters as their cellular counterpart, has been measured in [6]. The values are 238±24 MPa for stress relieved specimens and 379±21 MPa for HIPed specimens. Therefore, the fatigue stress concentration factors K_f^* of the cellular lattices could be computed with Eq. (III - 9) (Table III - 7). The fatigue notch factor K_f^* should be lower than or at most equal to K_t^* [42], but in this case, it is not. This indicates that the actual K_t^* is much higher than that predicted based on the ideal geometry and that the irregularities introduced during the manufacturing process have a strong effect on the fatigue properties. It is worth to stress that the notch factors are very high because of the way in which they are defined (see Eq. (III – 9)).

Table III - 7. Stress concentration factor and fatigue notch factors for each structure.

Structure	K_t^* (as-designed)	K_f^* (stress relieved)	K_f^* (HIPed)
CUB NS	65	115	188
CUB S	49	82	144
CUB 2S	37	65	133
CYL NS	58	107	163
CYL S	59	105	123
CYL 2S	68	100	153

The front of fatigue-failed struts propagates from the exterior to the interior of the specimen and this is a characteristic common to all the specimens. This is most likely related to the specimen not being perfectly aligned with the machine grips and the consequent bending load (this aspect is discussed more in-depth in the next Subsection). In Figure III - 36 a fractured section of a CUB S specimen after heat tinting is shown as an example.

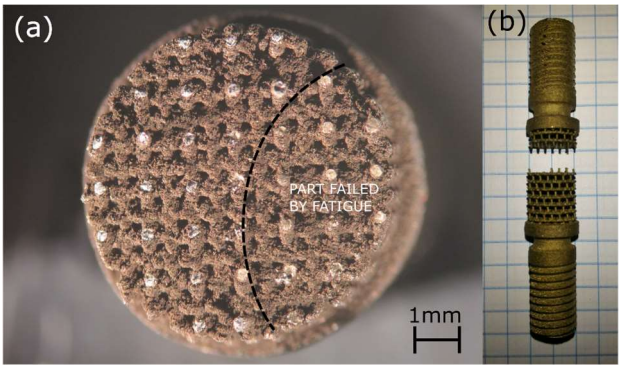

Figure III - 36. (a) Fractured section of a fatigue testes specimen (as built CUB S). The struts failed by fatigue (in the area indicated as "part failed by fatigue") are golden because of the heat tinting. (b) Fractured specimen after a fatigue test. The fracture is away from the bulk/cellular interface.

The fractured sections of the fatigue specimens were observed with the SEM to have a better understanding of the damage process and the following observations could be made, which apply to all the structures:

- the fatigue crack front propagates across the specimen section as one strut breaks after the other due to the cyclic loading until the stiffness of the structure decreases enough to stop the test.
- The fracture in almost every specimen propagates in a single plane, i.e. it rarely moves away from the transversal plane. The specimens generally break away from the bulk part, due to the thicker struts of the first plane of unit cells. This behavior is different from that observed in compressive-compressive fatigue tests, where the failed struts are located along a plane inclined of 45° at the load direction [8].
- The struts always break at the junctions where, according to the FE analyses, the stresses should be higher. The critical role of the junctions as stress raisers is observed also in compression-compression fatigue tests [8,24,43], although in that kind of fatigue test the unit cell geometry has a critical effect because it determines whether bending (and thus tensile stresses) or axial actions (and thus only compressive stresses) prevail. In push-pull tests, on the other hand, the geometry of the unit cell does not appear so crucial compared to the stress concentration factor, given that tensile stresses cannot be avoided.
- The fatigue crack in the strut section typically originates from surface irregularities and not from internal pores, as shown in Figure III - 37.

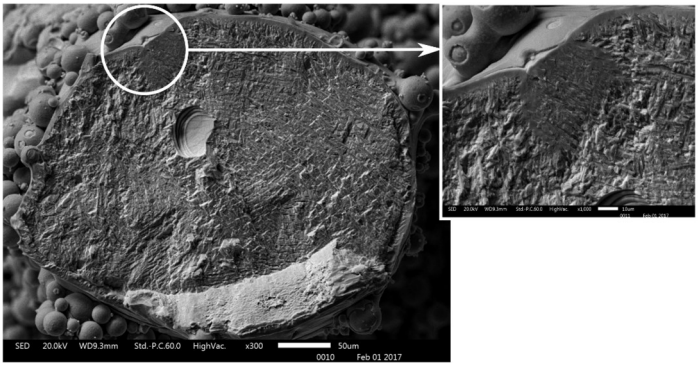

Figure III - 37. Fractured section of a strut of an as-built CYL-S specimen after termination of the fatigue test. Note that the fatigue crack nucleated on the surface (detail) and not at the pore.

3.3.9 Fatigue strength and the effect of defects

The effect of defects on the fatigue resistance of cellular lattices is discussed regarding the regular cubic lattice, being a full characterization of its morphology available. The mechanical properties of the base material and the as-designed geometrical parameters are used to calculate the expected mechanical properties of the as-built lattice. The stress concentration factor K_t^* of the as-designed unit cell was calculated with a linear elastic FE analysis to be 65 (the boundary conditions applied are those of Figure III - 12**Errore. L'origine riferimento non è stata trovata.**a). Assuming a conservative notch sensitivity q for SLM titanium equal to 1, the expected fatigue notch factor K_f^* is equal to the stress concentration factor [42]:

$$K_f^* = 1 + q(K_t^* - 1) = K_t^* \qquad \text{(III - 12)}$$

Therefore, according to Eq. (III - 6), $K_f^* = 65$. The theoretical (expected) fatigue strength of the cellular specimen is calculated with Eq. (III - 12) from the bulk fatigue resistance of the HIPed (379 MPa) and the stress relieved structures (238 MPa).

$$\sigma_a^{cell} = \frac{\sigma_a^{bulk}}{K_f^*}$$

The fatigue strength and the fatigue notch factor calculated based on the as-designed geometry are reported in Table III - 8.

Table III - 8. Fatigue properties calculated from the as-designed geometry.

	Stress relieved	HIPed
$\sigma_{a,10^6}$	3.4 MPa	5.4 MPa
K_f^*	65	65

The results of the fatigue tests are provided in Table III - 9 together with their standard deviation. The fatigue notch factor is calculated from the experimental data according to Eq. (III – 9). The effect of HIPing is not significant on the fatigue resistance because both values are within the bounds of the standard deviation. Arguably, the clear improvement induced by HIPing on the fatigue strength of the bulk specimens is not matched in the cellular lattices because, although the treatment is effective in closing the internal porosity in the struts [7], it does not reduce the severity of the surface irregularities. That put, it is possible to infer that the fatigue resistance of the cellular structures is controlled by the surface quality in terms of roughness and especially notches and not by the size of the internal pores. Moreover, the experimental fatigue notch factors are two to three times higher than the expected values and, in the author's opinion, this indicates that the notches introduced into these structures by the manufacturing process considerably increase the severity of the strut junctions compared to the as-designed geometry. The junctions between the struts are indeed the most critical part for fatigue in this kind of structures, given that the struts always broke at the junctions [7].

Table III - 9. Fatigue properties measured experimentally.

	Stress relieved	HIPed
$\sigma_{a,10^6}$	2.06±0.21 MPa	2.02±0.37 MPa
K_f^*	116	188

An estimation of the stresses acting at the strut junction in the as-built lattice could be carried out by selecting eight junctions (of the size of a unit cell) from the CT scan of the entire specimen and importing them into ANSYS. Due to limitations in computational power, the FE analysis was limited to a single junction at a time. These models were solved by applying the displacements on the extremities of the struts (on the "cuts"), obtained from the solution of the beam model that most accurately represents the specimen by including all the defects (Figure III - 33), at the corresponding locations. The accuracy of the FE results is restricted by the refinement of the mesh, chosen to be not far from that of the μCT spatial resolution: a convergence analysis was carried out on each junction by decreasing progressively the element size from 100 μm to 25÷30 μm. The effect of the high degree of irregularity of the as-built geometry on the stress distribution is qualitatively

shown in Figure III - 38, by comparing the von Mises equivalent stress distribution in the as-designed unit cell with that of two as-built junctions. The symmetry of the stress distribution is completely lost, and the maximum intensity is reached only in a specific location. Nevertheless, it is clearly shown that the most stressed part of the as-built lattice is close to the junction in all cases (red zones). The stress concentration factors calculated from the simulations are reported in Table III - 10 represented by the mean value and standard deviation of the values calculated from the models of the convergence analysis with element sizes between 25 and 50 μm. This choice is motivated by the high fluctuations of the stresses at the joints observed as the size of the mesh was decreased (more details on the convergence analysis are provided in the following paragraphs). Somewhat surprisingly, the stress concentration factors show an increase of only roughly 21% on average, compared to the as-designed geometry, although a wide variability is found. Notably, the junctions situated further away from the specimen axis (J6, J7 and J8), show higher stress concentrations. This is most likely due to the boundary conditions, as will be discussed further later. These results indicate that the as-built junctions are in fact more severe than the as-designed junctions, but not as much as expected from the fatigue tests. Clearly, there are several factors that influence the fatigue strength of the lattice, other than the junctions included in the simulations:

- only a limited number of junctions was analyzed (there may be more severe junctions that are responsible for the failure of the specimens);
- detrimental tensile residual stresses, which were in fact measured acting in the axial direction as described in Section 3.3.5;
- the unexpectedly high fatigue notch factor K_f^* displayed by the HIPed lattice, even higher than that of the as-built condition, can be imputed (at least in part) to the presence of brittle alpha case, shown in Figure III - 39, that increases the sensitivity of the structure to surface cracks [7]. The presence of alpha case on the surface of the lattice may be due to oxygen contamination of the Ar protective atmosphere in which the HIP treatment was conducted. This further supports the idea that the fatigue strength is dictated more by surface geometric defects rather than internal porosity, that was successfully eliminated by the HIP treatment.
- small distortion of the specimen that may introduce a bending load once the specimen is mounted in the fatigue testing machine that is added to the axial stresses;
- the smoothing procedure that was necessary to make it possible to mesh the μCT data has in fact decreased the severity of the notches to a certain degree. It is very difficult to quantify this effect because, on the

other hand, the discretization of the geometry with voxels produces an unrealistically rough surface.

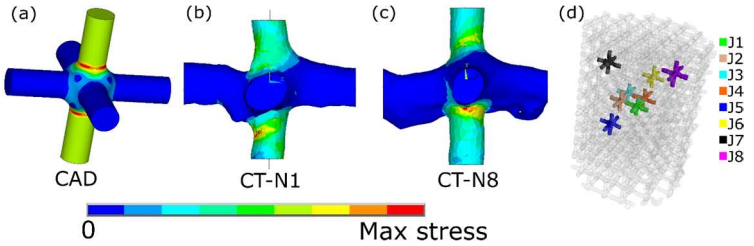

Figure III - 38. Von Mises contour plots obtained from the FE analyses. (a) As-designed geometry; (b) junction N. 1; (c) junction N. 8; (d) location of the junctions in the specimen.

Table III - 10. K_t^* calculated from the solid FE models based on the μCT unit cells: mean value (μ), standard deviation (σ) and % deviation on the K_t^* between the μCT and the CAD ($K_t^* = 65$) based FE models.

Junction	Average (K_t^* μCT)	Std. dev. (K_t^* μCT)	ΔK_t^* μCT vs CAD
J1	76.02	1.1	21.9%
J2	53.14	1.4	-14.7%
J3	76.75	4.5	23.1%
J4	68.54	0.9	9.9%
J5	76.80	1.0	23.2%
J6	85.00	1.3	36.3%
J7	88.90	1.0	42.7%
J8	80.34	3.8	28.9%
Average	75.67	10.9	21.4%

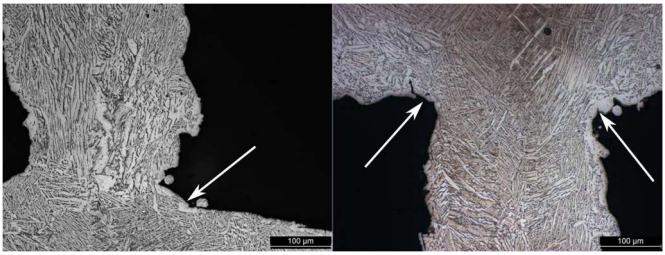

Figure III - 39. Microstructure of the HIPed specimens: α phase in a β matrix. The arrows indicate the α phase on the surface (α-case).

An interesting aspect to consider is the effect of the distortion and of the finite size of the specimen on the stress concentration at the junctions. We tried to give an estimate by comparing the stress distribution in the as-built junction when the periodic boundary conditions (PBC) are applied with that obtained with the boundary conditions applied as displacements corresponding to the position of each CT unit cell extracted from the beam model of the specimen that includes all the defects. The results of the convergence analysis for each of the eight junctions for both types of boundary conditions are shown in Figure III - 40, in terms of the stress concentration factor plotted against the element size. As observed previously, there is a strong variability of the results, but the stress concentration is always lower for the PBC. In Table III - 11, the differences between the stress concentration factor calculated with the PBC and the specimen BC are listed both in terms of absolute value and in percentage. The non-symmetrical loading found in the as-built structure further increases the severity of the junctions. Junctions further away from the mid-axis of the specimen (J6, J7 and J8) are more affected by the boundary conditions, as already observed. Figure III - 40 allows us to make some observations on the difficulties and on the limitations of this analysis. To achieve a sufficiently regular mesh, the point cloud representing each junction had to be smoothed at the expense of the finer surface details. In some cases (J1 for example), the convergence plateau for the smallest element size is not observed. This might be related to a difficulty in controlling the element size during meshing operations.

Table III - 11. Effect of the finite size of the specimen: variation of the stress concentration factors in the as-built junctions when switching from the BCs extracted from the beam model to the PBCs.

Junction	ΔK_t^*	ΔK_t^* (%)
J1	-6.11	-8.74%
J2	-	-
J3	-1.96	-2.62%
J4	-3.99	-6.19%
J5	-4.32	-5.96%
J6	-10.70	-14.40%
J7	-12.25	-15.98%
J8	- 26.10	-48.11%

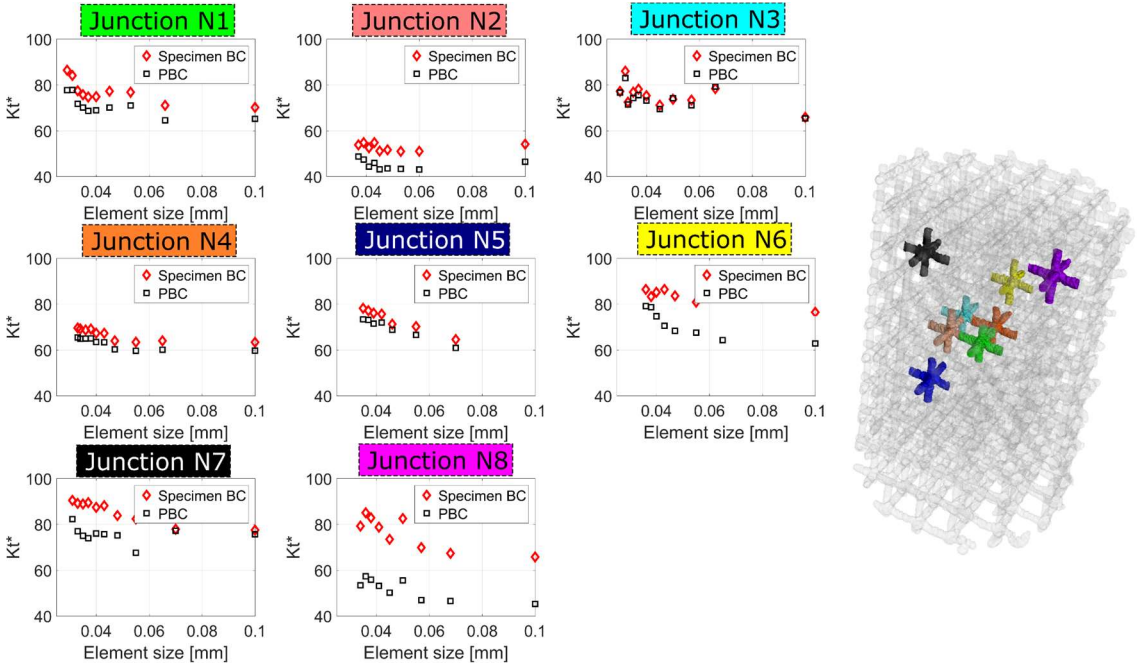

Figure III - 40. Convergence analysis of each as-built junction for the two types of BCs (displacements exported from the most realistic beam model and PBCs).

3.4 Conclusions

The results of a mechanical and dimensional characterization of variously arranged cubic cell open-cell cellular structures produced by SLM Ti-6Al-4V were presented. These structures are intended to be employed in the production of fully porous orthopedic implants. Six different configurations of the cubic cell were chosen: in three of them the cubes are simply shifted to fill the 3D space, while in the other three the cubic cells are skewed to obtain structures with cylindrical symmetry. Some of the structures being stretching dominated while others being bending dominated provided the chance to compare the behavior of struts loaded in different ways. Each cellular specimen was provided with threaded heads to carry out fully reversed fatigue tests and both compressive and tensile quasi-static tests. An extensive dimensional analysis was carried out using the pictures obtained with an optical microscope on metallographic specimens and the results μCT scan of a specimen for each type of structure. These measurements were used to assess the quality of the manufacturing process and the discrepancy between the actual measured cell parameters and the nominal CAD values. The effect of the manufacturing defects (porosity, surface roughness and geometrical inaccuracies) on the mechanical properties was investigated and discussed. The fracture surfaces of the struts of the specimens broken by fatigue were observed by SEM and the fracture behavior of each structure is discussed based on these observations. Half of the specimens was subjected to HIP and the effect of this treatment on porosity and the mechanical properties was investigated.
The following conclusions could be drawn:

- The HIPing treatment considerably reduces internal porosity, but it does not have a clear effect on fatigue resistance because fatigue resistance is not affected as much by internal porosity as by surface defects, especially sharp notches.
- Cellular structures designed with thicker struts (the staggered structures) appear to be less affected by internal porosity.
- The values of the elastic modulus compare well with those predicted by the finite element analyses based on the ideal geometry. This indicates that the elastic modulus is not particularly sensitive to the geometrical irregularities introduced by the manufacturing process.
- Staggering the unit cells introduces bending actions in the struts, therefore, to keep constant the elastic modulus, thicker struts and fillet radii are necessary, and, consequently, the stress concentrations are lower, and the fatigue resistance improves.

- The fact that K_t^* is much higher than the K_f^* predicted based on the ideal geometry suggests that the irregularities introduced during the manufacturing process have a strong effect on the fatigue properties. In general, the ideal geometry causes the overestimation of the fatigue properties because it does not obviously consider the fact that the additive manufacturing process is not always able to exactly replicate the geometry.
- The SLM technique has been pushed to its limits in printing the fine details of the designed specimens. Probably the current technology is unable to accurately reproduce the design at this level and thus to achieve the desired details (the fillet radius) it is advisable to use thicker struts.

The regular cubic structures were the object of more in-depth study on the effect of geometrical defects and residual stresses on the elastic modulus and on the fully reversed fatigue resistance at 10^6 cycles. The geometrical defects of the as-built lattice and the general as-built/as-designed morphological deviations were discussed on the basis of a statistical analysis of the results of the μCT scan of a specimen. FE simulations were completed by importing the as-designed geometry and the as-built geometry acquired with the μCT into ANSYS®. The results of the experimental measurements were then compared with the FE results and the effect of the as-built/as-designed morphological deviations on the mechanical behavior was discussed.
The more detailed analysis adds the following observations:

- There are remarkable morphological deviations between the as-built and the as-designed lattice structure. During printing, the distribution of the material does not depend only on the as-designed geometry fed to the machine but also on the parameters of the process and on the local variations of the thermal properties of the system. In other words, we observe that struts with a different orientation to the printing direction are reproduced with a different accuracy. More specifically, struts with a low angle to the printing plane are systematically affected by an overhang of accumulated molten material that increases the as-built thickness and offsets the barycenter of the cross-sections from the imaginary axis that connects the two junctions introducing a sort of "waviness". The uneven distribution of material affects also the strut junctions by slightly displacing their barycenter and by introducing sharp notches.

- The as-built/as-designed morphological deviations have a complex influence on the elastic modulus of the lattice. We could say that, in general, the higher thickness of the as-built struts increases the elastic modulus while the bending actions introduced by the strut waviness and the junction center displacement reduce the elastic modulus. Note that a stretching dominated structure such as the one of this study is particularly sensitive to these effects, definitely more than bending dominated structures.
- The fully reversed fatigue resistance appears to be more sensitive to the surface irregularities such as the sharp notches at the strut junctions than internal porosity. As a matter of fact, we observed that HIPing does not have a clear effect on fatigue resistance because, even if it considerably reduces the porosity of the struts [7], it does not change the surface notches. Fatigue resistance is most likely affected also by residual stresses, that were measured even after a stress relieving thermal treatment.
- FE analyses of the stress distribution at the strut junctions indicate that the as-built junctions induce a higher stress concentration, although not as high as expected from the experimental analyses. Most likely, fatigue strength is negatively influenced also by other factors such as tensile residual stresses, which have been measured even after stress relieving.

The comparison between the mechanical properties predicted considering the as-designed geometry and those measured experimentally highlights the fact that the mechanical behavior of SLM cellular is strongly influenced by the defects (notches, as-built/as-designed geometrical deviations) introduced by the manufacturing process. In other words, an in-depth knowledge of the characteristics of the manufacturing process is essential to design cellular structures.

3.5 Acknowledgments

The residual stress measurements have been performed by Dr Bartlomiej Winiarski (Thermo Fisher Scientific (FEI Czech Republic s.r.o) Vlastimila Pecha 12, Brno 627 00, Czech Republic).

3.6 References

[1] Ryan G, Pandit A, Apatsidis DP. Fabrication methods of porous metals for use in orthopaedic applications. Biomaterials 2006;27:2651–70.

doi:10.1016/j.biomaterials.2005.12.002.
[2] Rack HJ, Qazi JI. Titanium alloys for biomedical applications. Mater Sci Eng C 2006;26:1269–77. doi:10.1007/978-3-662-46836-4_8.
[3] Tan XP, Tan YJ, Chow CSL, Tor SB, Yeong WY. Metallic powder-bed based 3D printing of cellular scaffolds for orthopaedic implants: A state-of-the-art review on manufacturing, topological design, mechanical properties and biocompatibility. Mater Sci Eng C 2017;76:1328–43. doi:10.1016/j.msec.2017.02.094.
[4] Leuders S, Thöne M, Riemer A, Niendorf T, Tröster T, Richard HA, Maier HJ. On the mechanical behaviour of titanium alloy TiAl6V4 manufactured by selective laser melting: Fatigue resistance and crack growth performance. Int J Fatigue 2013;48:300–7. doi:10.1016/j.ijfatigue.2012.11.011.
[5] Wauthle R, Vrancken B, Beynaerts B, Jorissen K, Schrooten J, Kruth JP, Van Humbeeck J. Effects of build orientation and heat treatment on the microstructure and mechanical properties of selective laser melted Ti6Al4V lattice structures. Addit Manuf 2015;5:77–84. doi:10.1016/j.addma.2014.12.008.
[6] Benedetti M, Torresani E, Leoni M, Fontanari V, Bandini M, Pederzolli C, Potrich C. The effect of post-sintering treatments on the fatigue and biological behavior of Ti-6Al-4V ELI parts made by selective laser melting. J Mech Behav Biomed Mater 2017;71:295–306. doi:10.1016/j.jmbbm.2017.03.024.
[7] Dallago M, Fontanari V, Torresani E, Leoni M, Pederzolli C, Potrich C, Benedetti M. Fatigue and biological properties of Ti-6Al-4V ELI cellular structures with variously arranged cubic cells made by selective laser melting. J Mech Behav Biomed Mater 2018;78:381–94. doi:10.1016/j.jmbbm.2017.11.044.
[8] Van Hooreweder B, Apers Y, Lietaert K, Kruth JP. Improving the fatigue performance of porous metallic biomaterials produced by Selective Laser Melting. Acta Biomater 2017;47:193–202. doi:10.1016/j.actbio.2016.10.005.
[9] Parthasarathy J, Starly B, Raman S, Christensen A. Mechanical evaluation of porous titanium (Ti6Al4V) structures with electron beam melting (EBM). J Mech Behav Biomed Mater 2010;3:249–59. doi:10.1016/j.jmbbm.2009.10.006.
[10] Van Bael S, Kerckhofs G, Moesen M, Pyka G, Schrooten J, Kruth JP. Micro-CT-based improvement of geometrical and mechanical controllability of selective laser melted Ti6Al4V porous structures. Mater Sci Eng A 2011;528:7423–31. doi:10.1016/j.msea.2011.06.045.
[11] Liu L, Kamm P, García-Moreno F, Banhart J, Pasini D. Elastic and failure response of imperfect three-dimensional metallic lattices: the role of geometric defects induced by Selective Laser Melting. J Mech Phys Solids 2017;107:160–84. doi:10.1016/j.jmps.2017.07.003.
[12] Bagheri ZS, Melancon D, Liu L, Johnston RB, Pasini D. Compensation

strategy to reduce geometry and mechanics mismatches in porous biomaterials built with Selective Laser Melting. J Mech Behav Biomed Mater 2017;70:17–27. doi:10.1016/j.jmbbm.2016.04.041.

[13] Wits WW, Carmignato S, Zanini F, Vaneker THJ. Porosity testing methods for the quality assessment of selective laser melted parts. CIRP Ann - Manuf Technol 2016;65:201–4. doi:10.1016/j.cirp.2016.04.054.

[14] Khademzadeh S, Carmignato S, Parvin N, Zanini F, Bariani PF. Micro porosity analysis in additive manufactured NiTi parts using micro computed tomography and electron microscopy. Mater Des 2016;90:745–52. doi:10.1016/j.matdes.2015.10.161.

[15] Mullen L, Stamp RC, Fox P, Jones E, Ngo C, Sutcliffe CJ. Selective laser melting: A unit cell approach for the manufacture of porous, titanium, bone in-growth constructs, suitable for orthopedic applications. II. Randomized structures. J Biomed Mater Res - Part B Appl Biomater 2009;92:178–88. doi:10.1002/jbm.b.31504.

[16] Qiu C, Yue S, Adkins NJE, Ward M, Hassanin H, Lee PD, Withers PJ, Attallah MM. Influence of processing conditions on strut structure and compressive properties of cellular lattice structures fabricated by selective laser melting. Mater Sci Eng A 2015;628:188–97. doi:10.1016/j.msea.2015.01.031.

[17] Sing SL, Wiria FE, Yeong WY. Selective laser melting of lattice structures: A statistical approach to manufacturability and mechanical behavior. Robot Comput Integr Manuf 2018;49:170–80. doi:10.1016/j.rcim.2017.06.006.

[18] Pyka G, Kerckhofs G, Papantoniou I, Speirs M, Schrooten J, Wevers M. Surface roughness and morphology customization of additive manufactured open porous Ti6Al4V structures. Materials (Basel) 2013;6:4737–57. doi:10.3390/ma6104737.

[19] Kessler J, Balc N, Gebhardt A, Abbas K. Basic design rules of unit cells for additive manufactured lattice structures. MATEC Web Conf 2017;137. doi:10.1007/BF01171954.

[20] Zhu Z, Anwer N, Mathieu L. Deviation Modeling and Shape Transformation in Design for Additive Manufacturing. Procedia CIRP 2017;60:211–6. doi:10.1016/j.procir.2017.01.023.

[21] Zhao S, Li SJ, Hou WT, Hao YL, Yang R, Murr LE. Microstructure and mechanical properties of open cellular Ti–6Al–4V prototypes fabricated by electron beam melting for biomedical applications. Mater Technol 2016;7857:1–10. doi:10.1179/1753555715Y.0000000056.

[22] Bergmann G, Graichen F, Rohlmann A, Bender A, Heinlein B, Duda GN, Heller MO, Morlock MM. Realistic loads for testing hip implants. Biomed Mater Eng 2010;20:65–75. doi:10.3233/BME-2010-0616.

[23] Niinomi M. Mechanical biocompatibilities of titanium alloys for biomedical applications. J Mech Behav Biomed Mater 2008;1:30–42. doi:10.1016/j.jmbbm.2007.07.001.

[24] de Krijger J, Rans C, Van Hooreweder B, Lietaert K, Pouran B, Zadpoor AA. Effects of applied stress ratio on the fatigue behavior of additively

manufactured porous biomaterials under compressive loading. J Mech Behav Biomed Mater 2017;70:7–16. doi:10.1016/j.jmbbm.2016.11.022.
[25] Ren D, Li S, Wang H, Hou W, Hao Y, Jin W, Yang R. Fatigue behavior of Ti-6Al-4V cellular structures fabricated by additive manufacturing technique. J Mater Sci 2019;35:285–94.
[26] Hrabe NW, Heinl P, Flinn B, Körner C, Bordia RK. Compression-compression fatigue of selective electron beam melted cellular titanium (Ti-6Al-4V). J Biomed Mater Res - Part B Appl Biomater 2011;99 B:313–20. doi:10.1002/jbm.b.31901.
[27] Amin Yavari S, Wauthle R, Van Der Stok J, Riemslag AC, Janssen M, Mulier M, Kruth JP, Schrooten J, Weinans H, Zadpoor AA. Fatigue behavior of porous biomaterials manufactured using selective laser melting. Mater Sci Eng C 2013;33:4849–58. doi:10.1016/j.msec.2013.08.006.
[28] Luxner MH, Woesz A, Stampfl J, Fratzl P, Pettermann HE. A finite element study on the effects of disorder in cellular structures. Acta Biomater 2009;5:381–90. doi:10.1016/j.actbio.2008.07.025.
[29] Arabnejad S, Burnett Johnston R, Pura JA, Singh B, Tanzer M, Pasini D. High-strength porous biomaterials for bone replacement: A strategy to assess the interplay between cell morphology, mechanical properties, bone ingrowth and manufacturing constraints. Acta Biomater 2016;30:345–56. doi:10.1016/j.actbio.2015.10.048.
[30] Beretta S, Murakami. Statistical analysis of defects for fatigue strength prediction and quality control of materials. Fatigue Fract Eng Mater Struct 1998;21:1049–65.
[31] Petersen D, Murakami Y, Toriyama T, Coudert E. Instructions for a New Method of Inclusion Rating and Correlations with the Fatigue Limit. J Test Eval 1994;22:318. doi:10.1520/JTE11840J.
[32] Carmignato S, Dewulf W, Leach R. Industrial X-ray computed tomography. 2017. doi:10.1007/978-3-319-59573-3.
[33] Schajer GS, Winiarski B, Withers PJ. Hole-drilling Residual Stress Measurement with Artifact Correction Using Full-field DIC. Exp Mech 2013;53:255–65.
[34] Winiarski B, Schajer GS, Withers PJ. Surface decoration for improving the accuracy of displacement measurements by digital image correlation in SEM. Exp Mech 2012;52:793–804.
[35] Winiarski B, Withers PJ. Micron-Scale Residual Stress Measurement by Micro-Hole Drilling and Digital Image Correlation. Exp Mech 2012;52:417–28.
[36] Maxwell DC, Nicholas T. A Rapid Method for Generation of a Haigh Diagram for High Cycle Fatigue. In: Panotin TL, Sheppard SD, editors. Fatigue Fract. Mech. Twenty-Ninth Vol. ASTM STP 1332, West Conshohocken, PA: American Society for Testing and Materials; 1999, p. 626–41.
[37] Benedetti M, Fontanari V, Bandini M, Zanini F, Carmignato S. Low- and

high-cycle fatigue resistance of Ti-6Al-4V ELI additively manufactured via selective laser melting: Mean stress and defect sensitivity. Int J Fatigue 2018;107:96–109. doi:10.1016/j.ijfatigue.2017.10.021.

[38] Benedetti M, Santus C. Notch fatigue and crack growth resistance of Ti-6Al-4V ELI additively manufactured via selective laser melting: A critical distance approach to defect sensitivity. Int J Fatigue 2019;121:281–92. doi:10.1016/J.IJFATIGUE.2018.12.020.

[39] Benedetti M, Torresani E, Leoni M, Fontanari V, Bandini M, Pederzolli C, Potrich C. The effect of post-sintering treatments on the fatigue and biological behavior of Ti-6Al-4V ELI parts made by selective laser melting. vol. 71. 2017. doi:10.1016/j.jmbbm.2017.03.024.

[40] Amin Yavari S, Ahmadi SM, Wauthle R, Pouran B, Schrooten J, Weinans H, Zadpoor AA. Relationship between unit cell type and porosity and the fatigue behavior of selective laser melted meta-biomaterials. J Mech Behav Biomed Mater 2015;43:91–100. doi:10.1016/j.jmbbm.2014.12.015.

[41] Zargarian A, Esfahanian M, Kadkhodapour J, Ziaei-Rad S. Numerical simulation of the fatigue behavior of additive manufactured titanium porous lattice structures. Mater Sci Eng C 2016;60:339–47. doi:10.1016/j.msec.2015.11.054.

[42] Dowling NE. Mechanical Behavior of Materials. Fourth edi. Pearson Education; 2013.

[43] Zhao S, Li SJ, Hou WT, Hao YL, Yang R, Misra RDK. The influence of cell morphology on the compressive fatigue behavior of Ti-6Al-4V meshes fabricated by electron beam melting. J Mech Behav Biomed Mater 2016;59:251–64. doi:10.1016/j.jmbbm.2016.01.034.

Chapter IV

Geometrical assessment and compensation strategy of the morphological defects of selective laser melted Ti-6Al-4V cubic lattices

In the previous Chapter, an in-depth morphological analysis of SLM filleted square cell lattices was carried out. Several defects caused by the manufacturing process were recognized and their effect on the mechanical properties of the lattice were discussed and specifically the sensitivity of fatigue resistance to the joints' sharpness has been shown. Given the small size of such unit cells (the unit cell size is 1.5 mm and the strut thickness is 0.26 mm) and the limitations in accuracy of the printer, the fillet radii at the junctions were highly irregular and somewhat hard to recognize. In order to investigate the real benefit of filleted junctions on the stress concentration at the junctions and to assess the manufacturability of such minute geometrical detail, a new experimental campaign was set up. In this Chapter, a set of cubic lattice specimens with filleted junctions was designed and produced via SLM. The size of the unit cell is considerably larger than that of the previous specimens, being 8 mm, 6 mm and 4 mm with the rest of the geometrical parameters scaled accordingly. Thus, nine combinations of the geometrical parameters of the unit cell and three orientations with respect to the printing direction are considered. The aim is to investigate the relationship between the as-designed and the as-built geometry and to find the smallest radius which can be accurately reproduced by the printer. Moreover, a compensation strategy of the morphological defects is devised using the mathematical relationships obtained between the as-designed and the as-built strut thickness. This strategy consists in modifying the input CAD to compensate for the deviations introduced by the SLM process.

Part of this chapter has been published in:

M. Dallago, S. Raghavendra, V. Luchin, G. Zappini, D. Pasini, M. Benedetti,

"Geometric assessment of lattice materials built via Selective Laser Melting",
Materials Today: Proceedings 7 (2019), pp. 353-361

4.1 Introduction

The concept of manufacturing defects in SLM lattice structures and their effect on the mechanical behavior was, hopefully, thoroughly discussed in the previous Chapter and in the main Introduction.

Motivated by the desire to improve the fatigue resistance of SLM square cell cellular structures for biomedical implants, in the work described in the previous Chapter, we introduced filleted junctions to decrease the stress concentrations. The cellular specimens were scanned with a μCT system and differences with the nominal model were evaluated based on the thickness of the struts. It was also observed that the as-built fillets were highly irregular and sometimes even difficult to identify, and this showed the need for a deeper investigation of the correlation between the as-built and the as-designed geometry with the final aim of devising a model to compensate the geometrical mismatch.

The as-built/as-designed morphological mismatch is related to the SLM process parameters such as the laser power, the scanning speed [1–3] and layer thickness [3]. It is known that all these parameters affect the melt pool size which then determines the morphological accuracy of the part. Moreover, the difficulty in predicting the as-built shape is increased by the material shrinkage during solidification and cooling [4]. The inclination of the struts to the printing plane is also a factor to consider, as discussed in [5–7], because inclined struts are supported by loose powder which has lower thermal conductivity than the solid. Consequently, the heat of the laser tends to accumulate in a smaller volume, leading to a higher fraction of the powder is partially or completely melted compared to a vertical strut.

The as-built/as-designed mismatch in practice means that the mechanical properties deduced from the as-designed geometry are not accurate, leading to a somewhat unexpected mechanical performance of the part. However, it has been observed that there is a correlation between the geometrical parameters of the CAD and those of the AM lattice. In other words, the geometrical deviations are the sum of a systematical and a random component. For instance, van Bael et al. [8] observed that there is a linear correlation between the as-built and the as-designed pore size of SLM Ti-6Al-4V lattices which could be measured with CT scans in a first experimental batch to improve on the accuracy of a second batch (with same type of unit cell and printer settings) by appropriately modifying the CAD. Subsequently, Pyka et al. [5] fitted the as-built/as-designed strut thickness data points with linear functions and showed that such systematic offset could be reduced with well-controlled post-manufacturing chemical etching. This offset depends on the orientation of the strut to the printing direction [9], so different models should be defined, depending on the inclination of the struts. More recently, Bagheri et al. [10] proposed a strategy to compensate the as-built/as-designed deviation that consists in the definition of a geometrical compensation factor based on a statistical analysis

of the error between the as-designed strut thickness and the value obtained in the as-built structure. This factor, which depends on the as-designed strut thickness and its inclination to the build plane, was successfully used by the authors to improve the fidelity of the as-fabricated metallic lattices.
In this Chapter, the results of a metrological investigation of SLM regular square cell lattices with filleted junctions is presented. The size of the unit cell is considerably larger than that of the specimens discussed previously, being 8 mm, 6 mm and 4 mm with the rest of the geometrical parameters scaled accordingly (strut diameter and fillet radius). The junctions between the struts are filleted with a constant fillet radius. Nine combinations of the geometrical parameters of the unit cell and three orientations with respect to the printing direction were considered. A first set of specimens were used to assess the accuracy of the geometrical features of the SLM lattice. Based on the measurements and their statistical analysis, a set of mathematical relationships was obtained between the as-built and the as-designed geometric parameters. Such expressions were the base for the development of a compensation strategy of the geometrical mismatch of the as-built lattice, that consists in the modification of the input CAD model, using such expressions, to account for the geometrical deviations. Subsequently, a second set of specimens, designed implementing the compensation model, were printed and the effectiveness of the approach assessed. This work also aims at illustrating a procedure to analyze the geometry of lattice material by using only pictures taken with an optical microscope. This approach is less accurate than that based on CT scans, but it is much less expensive and somewhat faster. Moreover, the larger size of the lattices justifies of a less accurate metrological technique since less precise measurements can still provide the appropriate information. The metrological characterization of the specimens was carried out with an image segmentation routine developed in MATLAB, using pictures taken with a stereo microscope.

4.2 Materials and methods

4.2.1 Cellular specimens

The geometrical assessment described in this work has been carried out on regular cubic cell lattices with circular cross-section struts of uniform diameter t_0 and joints filleted with constant radius R; the size of the unit cell is L (Figure IV - 1). Nine combinations of the geometric parameters have been considered, as listed in Table IV - 1.

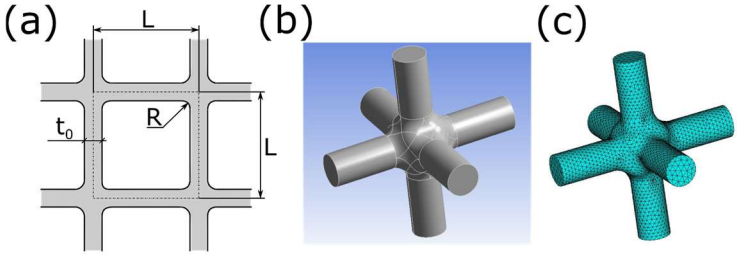

Figure IV - 1. Regular cubic unit cell with circular cross-section struts: (a) geometrical parameters; (b) 3D view; (c) tetrahedral FE mesh.

Table IV - 1. Geometric parameters of the unit cells.

# Specimen	L (μm)	t_0 (μm)	R (μm)	t_0/L	R/L	E_{FEM} (MPa)
1	4000	700	200	0.176	0.05	2944.3
2	4000	680	400	0.171	0.1	2952.6
3	4000	670	600	0.167	0.15	3097.3
4	6000	1060	300	0.176	0.05	3004.1
5	6000	1030	600	0.171	0.1	3017.6
6	6000	1000	900	0.167	0.15	3066.1
7	8000	1410	400	0.176	0.05	2989.4
8	8000	1370	800	0.171	0.1	3002.5
9	8000	1340	1200	0.167	0.15	3097.1

The structures have been chosen to have a nominal elastic modulus of 3 GPa, to preserve the continuity with the previous batch of specimens (Chapter III). The *R*/*L* ratios have been set to 0.05, 0.1 and 0.15 to span various sizes of the fillet radius, below and above the values of the previous batch. Approximate values of the t_0/L ratios have been calculated with the semi-analytical model developed in Chapter II adapted to the 3D topology with the procedure illustrated in Chapter III (Figure IV - 2). Subsequent FE simulations based on the CAD shown in Figure IV - 1a meshed with 3D 20 node structural continuum elements in Ansys® (Figure IV - 1c) provided the results reported in Table IV - 1. The expressions developed in Chapter II have been again proven to be useful in designing also 3D lattices. Although the results are not as accurate as for the 2D case, they can provide first guess values for subsequent iterative procedures applied to detailed FE analyses that are very close to the correct result.

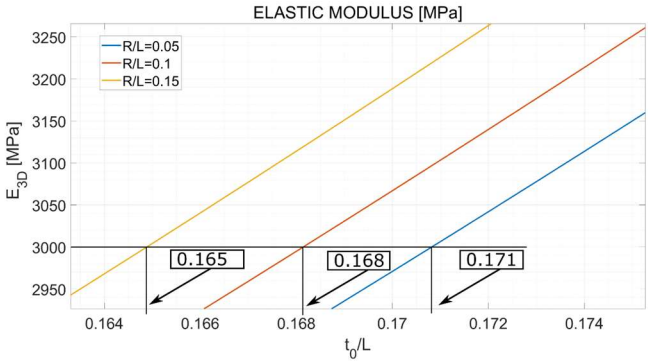

Figure IV - 2. Graphical implementation of the semi-analytical model for the elastic constants adapted to the 3D lattice: calculation of the unit cell parameters of the 3D regular cubic unit cell from the elastic modulus.

The effect of the printing direction on the as-built geometry was investigated by printing each of the nine geometries at three orientations, as illustrated in Figure IV - 3. In Figure IV - 3a and Figure IV - 3d, two series of struts (*X* and *Y*) are parallel to the printing plane while the third is perpendicular. In Figure IV - 3b and Figure IV - 3e, the specimen is oriented in such a way that one series of struts (*X*) is parallel to the printing plane while the other two are inclined of 45°. In Figure IV - 3c and Figure IV - 3f, the printing direction is the space diagonal of the unit cell and so all the struts are inclined of 35.26° to the printing plane. The specimens are named accordingly as "0°", "45°" and "45°-35.26°", respectively. Overall, 27 specimens were printed: nine combinations of the geometrical parameters per three printing directions.

The specimens were additively manufactured via SLM starting from biomedical grade Ti-6Al-4V alloy (O_2 < 0.2%) in form of powder of diameter < 45 µm. The thickness of the discretization slices is 60 µm. A stress-relief heat treatment was applied after printing, while no surface treatments were applied.

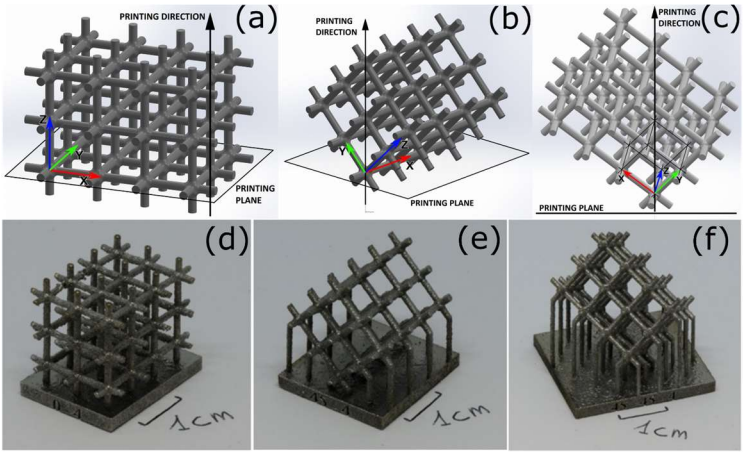

Figure IV - 3. Orientations of the specimens during printing. CAD models: (a) 0°, (b) 45°, (c) 45°-35.26°; and as-printed structures, with support structures (removed for the morphological assessment): (c) 0°, (d) 45°, (e) 45°-35.26°.

4.2.2 Metrological assessment

Pictures of each specimen were taken along the three directions identified by the *XYZ* axes with a stereo optical microscope (Nikon SMZ25) and two unit cells were randomly selected (Figure IV - 4), for a total of six images per specimen. That is, for each specimen, pictures of two unit cells per each *XY* – *XZ* – *YZ* plane were taken, for a total of six pictures.

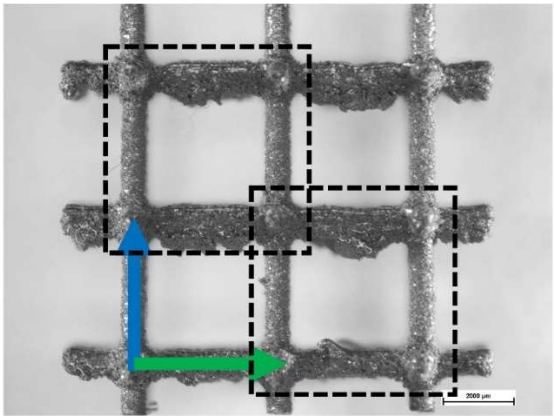

Figure IV - 4. Picture taken with the optical microscope of the side of a specimen (the blue arrow indicates the printing direction). The dotted squares indicate the unit cells selected for the metrological analysis.

An in-house MATLAB® routine was developed to recognize the boundaries of the unit cells from the pictures using the image segmentation functions embedded in MATLAB® (red line in Figure IV - 5a). The units of the acquired image are then transformed from pixels to the metric system (μm). It was not possible to obtain a picture of the whole face of a sample suitable for the segmentation procedure due to the difficulty of taking an image without shadows and with a perfect alignment of the struts to avoid including into the picture also the rows of struts below the top plane.
The boundaries of the acquired image are the inputs for the MATLAB routine to carry out the following measurements (Figure IV - 5b):

- Calculating the average thickness of the struts.
- Calculating the position of the center of each junction.
- Calculating the average fillet radius.
- Overlapping of the as-designed geometry to assess which parts of the unit cell are more affected by the manufacturing process.
- Calculating the distortion of the unit cell.

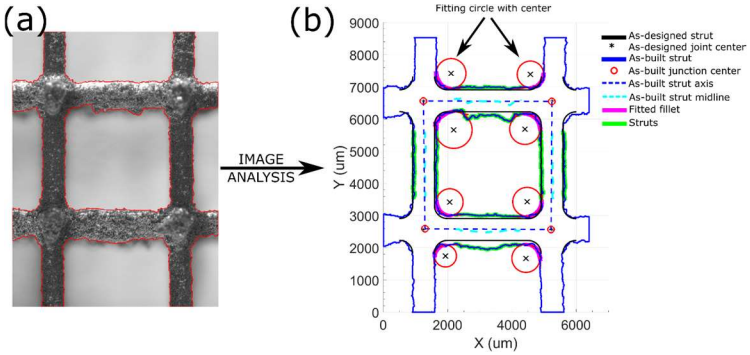

Figure IV - 5. Example of unit cell analysis (# specimen 2, 0° orientation): (a) Recognition of the unit cell boundaries through image segmentation techniques (the red line indicates the profile acquired by the code); (b) Output of the image analysis MATLAB code that identifies and measures the main features of each picture (strut thickness, fillet radii and unit cell distortion).

The calculation of the center of the junction is the most critical part as it is the input for all the other calculations and starting from the centers of the junctions, the code is completely autonomous in recognizing the features of each picture and in carrying out the requested measurements. The advantage of this approach is that a great number of images can be quickly analyzed with minimal human intervention. Given the irregularities of the struts and the possible distortions of the unit cell, the centers of the junctions are estimated by calculating the centroid of the junction with an iterative procedure (Figure IV - 6a). Given a first estimation of the center from the as-designed geometry (X0,Y0) in the global *xy* reference system, a selection square of suitable size (the smallest possible to include the whole junction) is defined around the junction (Figure IV - 6b). The corners of the square and the profile of the junction define four areas (A1, A2, A3, A4): if the areas are unbalanced it is reasonable to assume that the center of the square is offset to the center of the joint. A tolerance value (5%) is set on the maximum allowable difference between the smallest and the largest area to evaluate the unbalance of the areas. The difference between the extension of the areas at diagonally opposite corners is used to define two (*Vx'*, *Vy'*) vectors in the *x'y'* reference system of Figure IV - 6b. For ease in calculations these vectors are projected onto the global *xy* reference system. The *Vx* and *Vy* vectors are finally used to iteratively translate the square until the areas of the four corners are all equal inside the specified tolerance (5%). At that point, the center of the square and the center of the junction coincide.

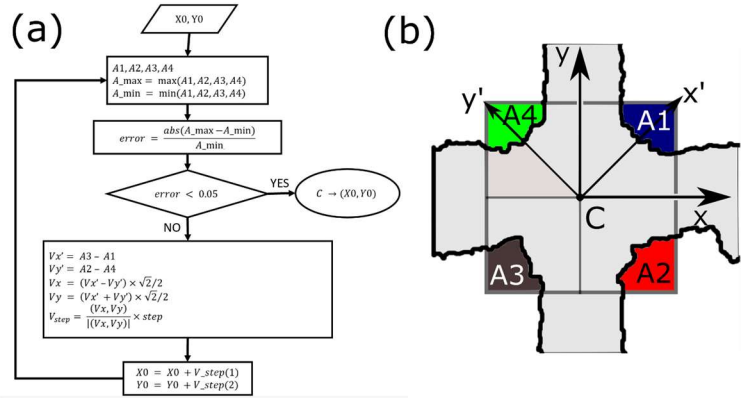

Figure IV - 6. Details of the estimation of the joint center: (a) algorithm implemented in Matlab® to find the joint center; (b) scheme of the joint and of the quantities defined to estimate the position of the joint center *C*.

The previous method works on the assumption that the four fillets of the junction are rather uniform, i.e. there is not a systematic deformation of one or more fillets, as in Figure IV - 6. If, on the other hand, due to a specific orientation of the lattice to the printing direction, there is a systematic accumulation of parasitic mass on one of the fillets (as on the fillet in the third quadrant of the *xy* reference system in Figure IV - 7), this method is not appropriate anymore. Indeed, considering that the aim is to use the junctions to overlay the as-designed lattice onto the as-built lattice to evaluate in which parts there is more accumulation of parasitic mass, it is expected that the relative position of the struts of the overlaid lattices reflect the physics of the problem. In other words, the bottom left fillet shown in Figure IV - 7 would cause an offset between the as-built and as-designed struts not related to the mechanisms leading to the accumulation of parasitic mass on the struts. To account for these cases, the algorithm of Figure IV - 6a can be slightly modified and, instead of using the areas defined in Figure IV - 6b, the areas defined in Figure IV - 7 should be used. This approach, although somewhat questionable, it is an attempt of the author to devise an automatic and objective procedure to relate the as-built lattice to the as-designed lattice. Nevertheless, in the discussion of the results it will be shown that the results are satisfactory and reasonable, allowing to get some additional insight into the deviation of the morphological features introduced by the manufacturing technique.

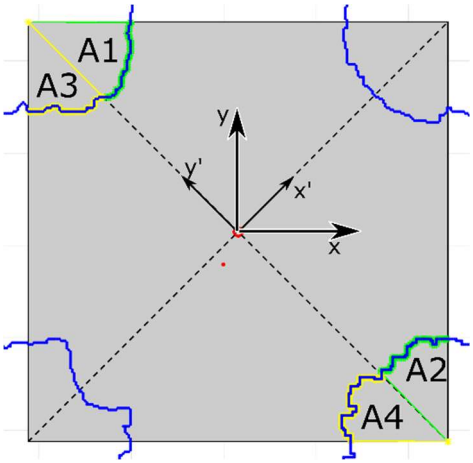

Figure IV - 7. Scheme of the joint and of the quantities defined to estimate the position of the joint center in the case of a systematic accumulation of parasitic mass on one of the fillets (in this case, the fillet in the third quadrant of the *xy* reference system).

The as-designed geometry is overlaid on the as-built geometry by using the centers of the junctions and the procedure is shown in Figure IV - 8a. Three cartesian reference systems are defined: the global reference system (*Oxy*, based on the rows and columns of pixels of the picture), the reference system integral to the as-built lattice ($O'x'y'$) and the reference system integral to the as-designed lattice ($O''x''y''$). The optimal overlap (position of *O''* and θ, in Figure IV - 8a) is found by minimizing the sum of the squares of the distances between the corresponding four centers of the as-designed (P_{CAD} in Figure IV - 8a) and four centers of the as-built geometries (P_{pr} in Figure IV - 8a):

$$P_{CAD,i}O = OO'' + P_{CAD,i}O'' = (x_{O''} \quad y_{O''}) + \left(x''_{P_{CAD,i}} \quad y''_{P_{CAD,i}}\right)\begin{bmatrix} +\cos\theta & +\sin\theta \\ -\sin\theta & +\cos\theta \end{bmatrix}$$

$$P_{pr,i}O = OO' + P_{pr,i}O' = (x_{O'} \quad y_{O'}) + \left(x'_{P_{pr,i}} \quad y'_{P_{pr,i}}\right)$$

$$d_i^2 = \left|P_{CAD,i}O - P_{pr,i}O\right|^2$$

$$min \sum_{i=1}^{4} d_i^2 \rightarrow (x_{O''}, y_{O''}, \theta)$$

The average thickness of the struts is calculated by sampling 100 points along the strut axis (sufficiently far from the junction to avoid the inclusion of the fillet) and by measuring the distance normal to the axis between the profile points of the struts (Figure IV - 8b). The precise overlay is useful to measure the distance between the

as-built and as-designed profiles. This is used to measure in which parts of the specimen the ideal geometry is reproduced the worst or the best. In Figure IV - 8c, a detail is shown of the quantitative comparison between the as-build (blue) and as-designed (black) profiles. The distances (normal to the strut axis) between the two profiles are sampled. The excess material (red) is defined positive while the lack of material (green) is defined negative.

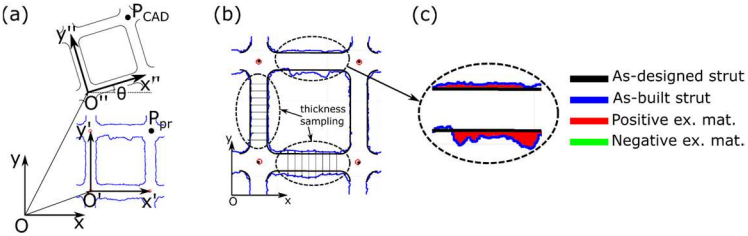

Figure IV - 8. (a) Superposition of the as-designed geometry on the as-built geometry; (b) Entire unit cell; (c) Detail regarding the calculation of the excess material.

The as-built fillet radius is measured by fitting the as-built profile with a circle. Estimating the fillet radius is a non-trivial task given the irregularity of the profile and often it is not clear where the fillet ends, and the strut starts. To ensure that the reasonably best fit is always found, an iterative procedure is applied (Figure IV - 9a). Starting from an initial guess (based on the as built lattice) of the position (XC_0, YC_0) of the center C_i of the fillet radius, the points of the profile are selected and fitted with a circle. The center of the new circle C_{i+1} is used to select the new set of points to fit (indicated by the black dashed lines in Figure IV - 9b) and this procedure is continued until the center of the circle is less than a given distance (5% in our case) from the previous center. The quality of the fit is ensured by the condition that the normalized root mean square deviation (NRMSD) of the residuals is below 5%. Moreover, to improve the performance of the iterative routine, the profile of the as-built radius is smoothed with MATLAB ® moving average lowpass filter (red dashed line in Figure IV - 9b).

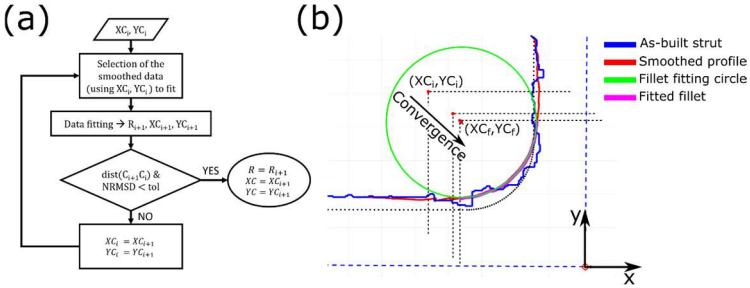

Figure IV - 9. Measurement of the fillet radius: (a) algorithm implemented in Matlab® to calculate *R;* (b) scheme of the fillet and of the quantities defined to estimate the radius. (XC_i; YC_i) is the first guess for the center of the fillet while (XC_f; YC_f) is the converged result.

The distortion of the as-built unit cell is evaluated by calculating the error on the length of the sides and on the diagonals of the square defined by the centers of the junctions, as in Eq. (IV – 1).

$$Error(\%) = \frac{AsBuilt - AsDesigned}{AsDesigned} \times 100 \qquad \text{(IV - 1)}$$

A statistical analysis was carried out on these measurements and the results are presented as mean values with the associated standard deviation. The struts of each sample type are named with respect to an *XYZ* reference system (Figure IV - 3).

4.3 Results and discussion: geometrical assessment

In this Section, the results of the morphological analysis of the cellular specimens will be presented and discussed. Moreover, the relationships between the as-built and the as-designed geometrical parameters of the unit cell (t_0 and R) are identified. These formulas will be used in Section 4.4 to devise the compensation model.

This work, given the high number of geometrical parameters and printing directions considered, produced a considerable amount of results which were at times challenging to interpret and to present in a compact and simple way. Consequently, also recognizing the many common aspects between this work and that presented in the previous Chapter, this discussion will refer to Chapter III whenever the concepts illustrated are not new, thus avoiding repetitions.

This Section is divided into 5 Subsections. Subsection 4.3.1 is aimed at giving the reader a general overview of the main morphological features of the printed lattices in order to, hopefully, make it easier to understand the following Subsections. Subsection 4.3.2, 4.3.3 and 4.3.4 present and discuss the relationship between the

as-built and as built strut thickness, excess material and fillet radius, respectively. The last Subsections briefly assesses the overall distortion of the lattice.

4.3.1 General observations on the morphology

A few but representative images taken with the optical microscope are shown in Figure IV - 10, with arrows indicating the printing direction. Despite these structures being considerably larger than those described in Chapter III, many similarities can be observed. A considerable amount of particles is attached on the surfaces: a higher amount is observed on the underside of the struts (Figure IV - 10e shows this feature the best) than on the upper side (indeed, the struts in Figure IV - 10a, showing only the top surfaces, are notably smoother and shinier). The underside of the struts (the part laying on powder during manufacturing) is noticeably more irregular, affected by varying quantities of parasitic mass (excess material), as shown very evidently in Figure IV - 10b and less evidently in Figure IV - 10b and e. Indeed, at a first glance the larger lattice (geometry #8) appears to be less affected by excess material relative to its size, although, as will be shown subsequently, the increase in thickness is roughly the same for both struts in absolute terms. Another aspect to be discussed is the effect of the strut inclination to the printing direction: as expected, as the inclination of the struts increases, so does their morphological quality. For instance, compare the horizontal struts in Figure IV - 10b with the vertical struts in the same picture or with the struts inclined at 45° in Figure IV - 10d or at 35.26 in Figure IV - 10f. Concerning the fillet radii, the most relevant aspect is that they appear to be successfully reproduced by the process, even in the smallest lattice (Figure IV - 10b). The printing direction does not have such an eye-striking effect as on the strut thickness, nevertheless a small accumulation of parasitic mass can be noticed on the fillets on the undersides, particularly in the lattices printed with an inclination (for instance, compare the fillets un the undersides with those on the upper side or in lateral position in Figure IV - 10d and f).

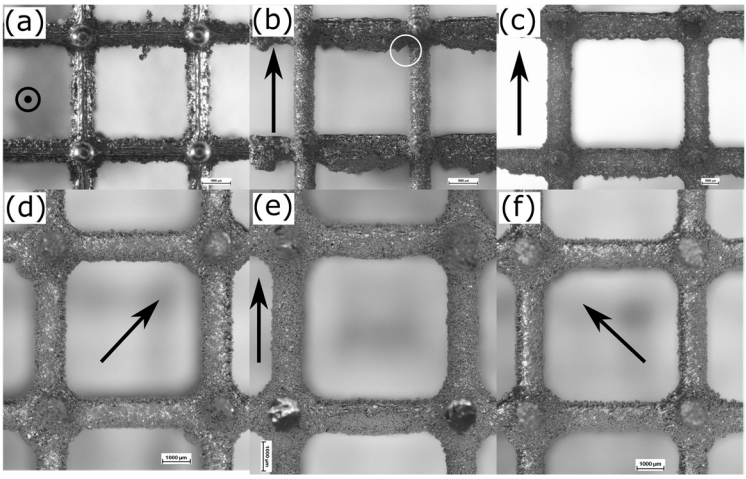

Figure IV - 10. Images taken with the optical microscope of various unit cells (the arrows indicate the printing direction): (a) specimen #1 printed at 0° (top view); (b) specimen #1 printed at 0° (lateral view), with sharp notch at junction (white circle); (c) specimen #8 printed at 0° (lateral view); (d) specimen #6 printed at 45°; (e) specimen #6 printed at 45°; (f) specimen #6 printed at 45°-35.26° (clearly, the printing direction is not in the picture plane, but points towards the reader, with an angle of 35.26° to the plane of the picture). The scale bars are always 1000 µm.

A more accurate comparison of the as-built and as-designed lattices is carried out by overlaying the 2D profiles using the joint centers. In Figure IV - 11, the result of this procedure is shown for two entire sides of geometry #3 printed at 0° (note the orientation of the printing direction relative to the struts). Unfortunately, due to the difficulty in obtaining high quality images suitable for image segmentation and because the lattices are too big for geometries from #4 to #9, pictures of the entire lattice could not be acquired. The lattice is reproduced quite accurately in the printing plane, despite the evident roughness (Figure IV - 11a) and the struts being slightly thicker than the CAD. On the other hand, the amount of parasitic mass on the horizontal struts is striking in Figure IV - 11b, producing an evidently elongated cross-section, reasonably approximable by an ellipse. Interestingly, there appears to be excess material also on the upper side of the struts, although considerably less. Considered that this added thickness on the top of the strut is not due to attached particles (the surface is smooth), it could be ascribed to the discrete nature of the slicing procedure. As observed previously, the fillets match satisfactorily the as-designed profile.

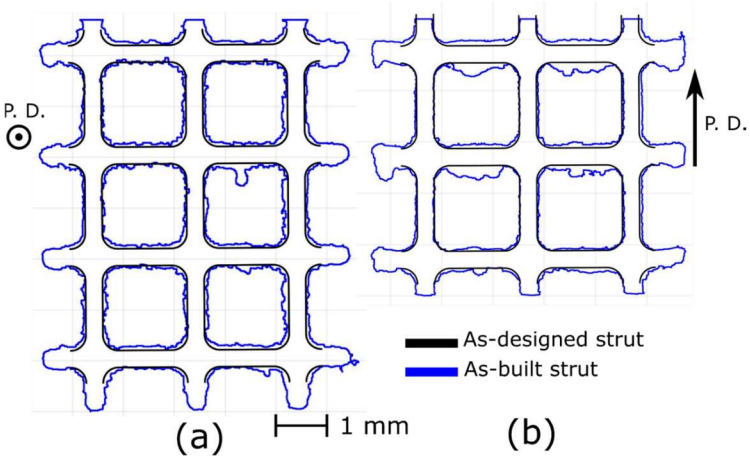

Figure IV - 11. Specimen # 3 printed at 0°, comparison between as-built and as-designed profile: (a) top view (plane perpendicular to the printing direction); (b) lateral view (plane parallel to the printing direction). Note the considerable amount of parasitic mass (excess material) in the lateral view.

An important aspect to clarify is the intrinsic difficulty of evaluating a 3D structure using only 2D images and this is the main limitation of this approach. Indeed, considering for instance the lattice printed at 45° (Figure IV - 3), it is logic to assume, based on what just discussed and on the observations of the previous Chapter, that the struts laying in the printing direction (set *X*) should show the same morphology as the horizontal struts of the lattices printed at 0° (Figure IV - 11b). Nevertheless, in the pictures of the 45° lattices (clearly always taken along the principal axes *XYZ*) the excess material is not as nearly evident as in those of the 0° lattice. The reason is that the elongated (elliptical) sections of the horizontal struts are seen "skewed" in these pictures. An attempt to illustrate the issue is shown in Figure IV - 12. The same is true for the struts of the 45°-35.26° lattice. Consequently, the thickness measured for the horizontal struts of the 45° lattice and for the struts of the 45°-35.26° lattice is an approximation of the true value. On the other hand, following the same logic, the struts inclined at 45° can be accurately characterized. The lattice printed at 0° is an exception in this sense because all the main features can be captured with the pictures taken along the principal axes *XYZ* (Figure IV - 3).

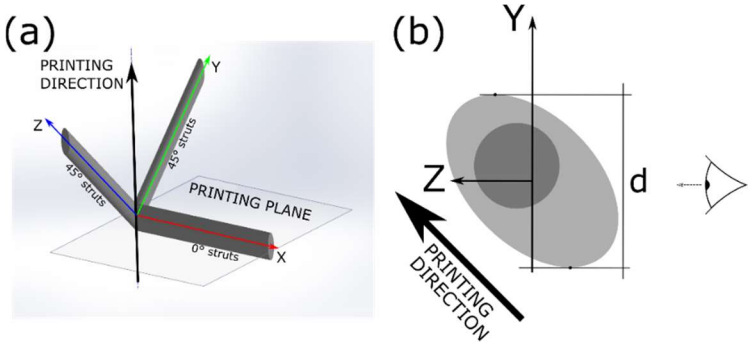

Figure IV - 12. Issue regarding the characterization of 3D objects with 2D pictures: (a) corner of a unit cell inclined of 45° to the printing plane (note that the cross-sections of the struts are elliptical, as in the as-built lattice); (b) the cross-section of the horizontal (*X*) struts is seen inclined in the pictures taken along the *Y* and *Z* axes.

4.3.2 Strut diameter t_0

The measurements carried out on the strut thickness are presented in two graphs for each printing direction. In the first, the as-built values are plotted against the as-designed values for each set of struts (*X*, *Y* and *Z*, as in Figure IV - 3) and for each plane of measurement (the plane of the picture, identified with the *XYZ* reference system). In the second, the data are grouped according to the orientation of the cross-section to the printing direction. In other words, the data are grouped considering the physical nature of the problem: for instance, there is no physical reason for which the vertical (*Z*) struts of the 0° (Figure IV - 13) should not have an axisymmetric section (their axis is parallel to the printing direction) and, consequently, the thickness measured from two different directions should belong to the same population. It is worth highlighting that, in this analysis, it was assumed that the as-built strut thickness is independent on both the fillet radius and the strut length. The negligible influence of the fillet radius seems quite logic, given that the measurements on the strut section were carried out sufficiently far from the influence of the joint. On the other hand, the strut length most likely is a relevant parameter, but reasonably only for struts considerably shorter than the ones considered here.
In the lattices printed at 0°, all geometries show a very similar behavior for each set of struts (Figure IV - 13). The struts printed parallel to the printing direction (*Z*) retain quite accurately the circular section (measurements taken using pictures of planes perpendicular to each other are statistically equivalent), while the struts laying in the printing plane are produced with an elongated section, with the major axis parallel to the printing direction and considerably larger than the as-designed thickness. The graphs in Figure IV - 13 confirm what expected from the observation of Figure IV - 10: due to a considerable amount of parasitic mass, the cross-section of the

horizontal struts (*X* and *Y*) deviates significantly form the as-designed geometry (circle), becoming roughly elliptical with a major axis parallel to the printing direction and a minor axis perpendicular to the printing direction.

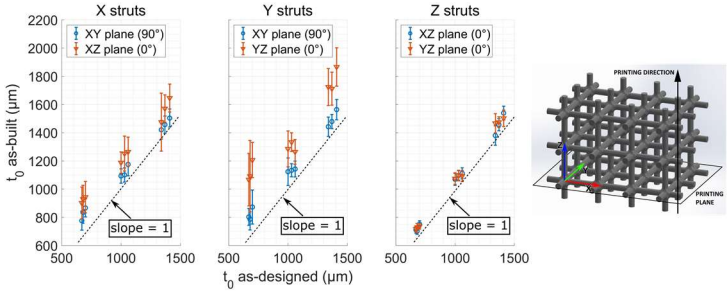

Figure IV - 13. As-built vs as-designed diameter of the struts of the specimens printed at 0° to the printing direction. The dashed line is the bisecting line, which indicates a perfect as-built/as-designed match. The classification of the struts is indicated by the reference system on the CAD.

Grouping the values measured for the *Z* struts and the corresponding values for the horizontal struts leads to the more compact plot of Figure IV - 14. The cross-section of struts printed vertically is well approximated by a circle and thus a parameter is enough to describe the as-built/as-designed relationship. Struts printed horizontally, being elliptical, need two parameters: a major axis ($t_{ab,vert}$) and a minor axis ($t_{ab,hor}$), as shown in Figure IV - 14.

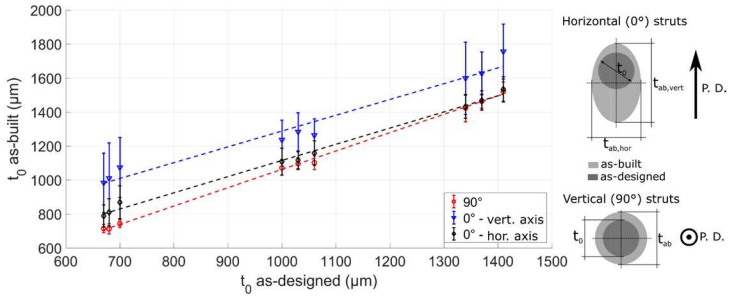

Figure IV - 14. Section parameters grouped according to the orientation of the struts to the printing plane in the 0° structure (t_{ab} is the as-built thickness). The dashed lines are the linear regression of the data points of corresponding color.

A prominent feature of these data is of being linear with the as-designed strut thickness. The result of the linear regression are the dashed lines in Figure IV - 14, that correspond to the following relations:

$$t_{90^\circ} = 1.08 t_{0,as-d.} - 17.29 \quad \text{(IV - 2a)}$$

$$t_{0^\circ,vert} = 0.93 t_{0,as-d.} - 358.58 \quad \text{(IV - 2b)}$$

$$t_{0^\circ,hor} = 0.95 t_{0,as-d.} - 163.31 \quad \text{(IV - 2c)}$$

Interestingly, the slope of the lines is close to unity, indicating that there is a roughly constant offset introduced by the manufacturing process between the as-designed and the as-built thickness. The data is also reported in Table IV - 1 with the standard deviation.

Table IV - 2. Section parameters grouped according to the orientation of the struts to the printing plane in the 0° structure (values in µm).

Specimen #	As designed	As-built		
	t_0	t_{90°	$t_{0^\circ,vert}$	$t_{0^\circ,hor}$
1	670	743±23	1074±177	869±97
2	680	713±30	1010±208	810±80
3	700	714±24	983±175	789±65
4	1000	1102±41	1264±96	1159±72
5	1030	1096±35	1284±112	1116±51
6	1060	1072±42	1236±115	1108±79
7	1340	1520±57	1756±162	1533±74
8	1370	1463±42	1627±126	1468±57
9	1410	1423±81	1599±213	1431±68

The struts inclined at 45° to the printing direction (*Y* and *Z* struts in the 45° specimens, as in Figure IV - 15) show a statistically significant difference between the size of the cross-section measured from different planes, indicating an elongated cross-section similarly to the struts printed at 0° to the printing plane. Nevertheless, the major and minor axes of the ellipse approximating the cross-section are not so different in values and closer to the as-designed thickness than the 0° struts. On the other hand, there is considerable deviation from the CAD among the *X* struts, as expected, considered that they lay perpendicular to the printing direction. It is important to remind that the values related to the horizontal struts are not sufficient to fully characterize the cross-section, as discussed at the beginning of this Section.

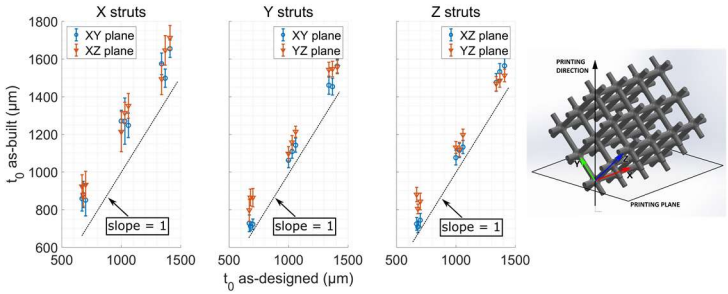

Figure IV - 15. As-built vs as-designed diameter of the struts of the specimens printed at 45° to the printing direction. The dashed line is the bisecting line, which indicates a perfect as-built/as-designed match. The classification of the struts is indicated by the reference system on the CAD.

The experimental data also in this case are linear to the as-designed thickness (Figure IV - 16) and the fitting functions are the following:

$$t_{0^\circ} = 1.03 t_{0,as-d.} - 192.98 \quad \text{(IV - 3a)}$$

$$t_{45^\circ,vert} = 0.98 t_{0,as-d.} - 162.81 \quad \text{(IV - 3b)}$$

$$t_{45^\circ,hor} = 1.14 t_{0,as-d.} - 58.32 \quad \text{(IV - 3c)}$$

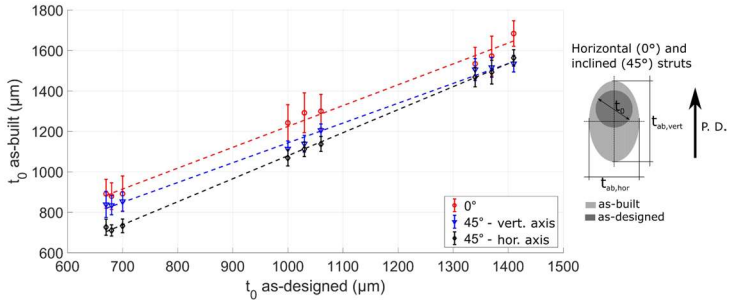

Figure IV - 16. Cross-section parameters grouped according to the orientation of the struts to the printing direction in the 45° structure. The dashed lines are the linear regression of the data points of corresponding color.

Again, the slope of the lines is close to unity, indicating that there is a roughly constant offset introduced by the manufacturing process between the as-designed and the as-built thickness. The data are also reported in Table IV - 3 with the standard deviation.

Table IV - 3. Cross-section parameters grouped according to the orientation of the struts to the printing plane in the 45° structure (values in µm).

Specimen #	As designed	As-built		
	t_0	$t_{0°}$	$t_{45°,vert}$	$t_{45°,hor}$
1	670	891±88	853±48	733±34
2	680	879±65	834±47	710±28
3	700	891±72	838±64	726±40
4	1000	1299±83	1205±31	1137±37
5	1030	1292±98	1138±41	1111±36
6	1060	1242±90	1114±39	1069±40
7	1340	1683±63	1535±41	1563±41
8	1370	1572±99	1516±49	1493±59
9	1410	1534±82	1506±54	1468±48

The struts of the 45°-35.26° lattice are all oriented of the same angle (35.26°) to the printing plane and the pictures represent the struts always from the same point of view, therefore the data collected from the measurements on the strut thickness should be very similar. This is indeed the case, as shown in Figure IV - 17. It is important to remind that these values are not sufficient to fully characterize the cross-section, as discussed at the beginning of this Section. It is indeed expected that the section are ellipticals similarly to those of the struts inclined of 45°, but from pictures taken along the *XYZ* directions it is impossible to accurately measure the major and minor axes (as the scheme in Figure IV - 18 illustrates).

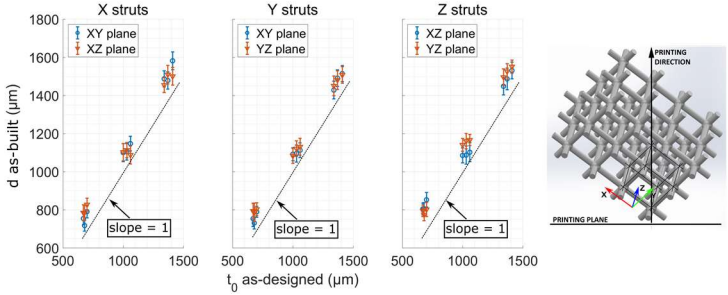

Figure IV - 17. As-built vs as-designed diameter of the struts of the specimens printed at 35.26° to the printing direction. The dashed line is the bisecting line, which indicates a perfect as-built/as-designed match. The classification of the struts is indicated by the reference system on the CAD.

The measurements can be grouped together and the average values with the respective standard deviation are plotted against the as-designed thickness in Figure IV - 18. The data lay on a line, as expected.

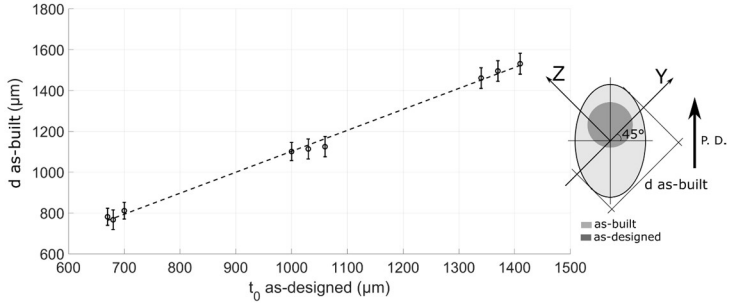

Figure IV - 18. Cross-section parameters grouped according to the orientation of the struts to the printing direction in the 45°-35.26° structure. The dashed line is the linear regression of the data points.

The data is also reported in Table IV - 4 with the standard deviation.

Table IV - 4. Cross-section parameters grouped according to the orientation of the struts to the printing direction in the 45°-35.26° structure (values in µm).

Specimen #	t_0	$d_{as\text{-}b.}$
1	670	811±41
2	680	766±48
3	700	781±42
4	1000	1124±50
5	1030	1114±49
6	1060	1101±45
7	1340	1531±51
8	1370	1495±50
9	1410	1461±51

To summarize, the thickness of the as-built strut strongly depends on both the as-designed thickness and on orientation of the strut to the printing direction. The results do not appear to indicate any influence of the orientation of the entire specimen, but it is the inclination of the individual strut that correlates with the as-built thickness. It also seems confirmed the assumption that the strut length does not measurably influence the as-built thickness, recognized the predominant effect of the as-designed thickness. The relationship between the as-built and the as-designed thickness is well represented by a linear function for all the orientations considered (0°, 45° and 90° to the printing plane). The average as-built thickness is always

higher than the as-designed thickness and the slope of the straight lines is near to one, indicating that the quantity of material in excess is roughly constant. In other words, the SLM process adds an offset to the struts cross-section that depends mainly on their orientation to the printing direction. The struts other than parallel to the printing direction have a section that can be approximated by an ellipse defined by a vertical axis that lies in a plane normal to the printing plane and a horizontal axis normal to the printing direction. The vertical axis is always larger than the horizontal axis. The horizontal struts reproduce the worst the as-designed geometry because they are considerably thicker along the vertical axis of the section. It is thus advisable to avoid as much as possible to print a cellular component with struts laying in the printing plane. The as-built vertical struts on the other hand retain the circular section with a diameter close to the as-designed value.

4.3.3 Excess material

The analysis discussed in the previous Subsection does not indicate where on the struts the material in excess accumulates: an accurate superposition of the as-designed profile on the as-built profile is the key to obtain this information. The results of the measurement of the excess material is presented here with a similar logic to the strut thickness: for each printing direction of the lattice, the excess material for each strut orientation is plotted against the as-designed thickness. To simplify the discussion, it was chosen to summarize the results in a single graph for each lattice orientation.

The material in excess has been measured on the upper side, on the underside and laterally in horizontal struts (as shown in Figure IV - 19), but most of the material is accumulated on the underside. Laterally, the excess material is distributed symmetrically to the strut axis. In the case of verticals struts, it was observed that the excess material is distributed uniformly around the section. Moreover, being the vertical struts reproduced the most accurately, they show the least amount of parasitic mass. The experimental data were fitted with linear functions (shown in Figure IV - 19 as dashed lines) of expression:

$$EM_{0^\circ}^{-} = -0.029 t_0^* + 207.70 \quad \text{(IV - 4a)}$$

$$EM_{0^\circ}^{+} = -0.041 t_0^* + 150.87 \quad \text{(IV - 4b)}$$

$$EM_{0^\circ}^{lat} = -0.024 t_0^* + 81.63 \quad \text{(IV - 4c)}$$

$$EM_{90^\circ} = +0.040 t_0^* - 8.64 \quad \text{(IV - 5)}$$

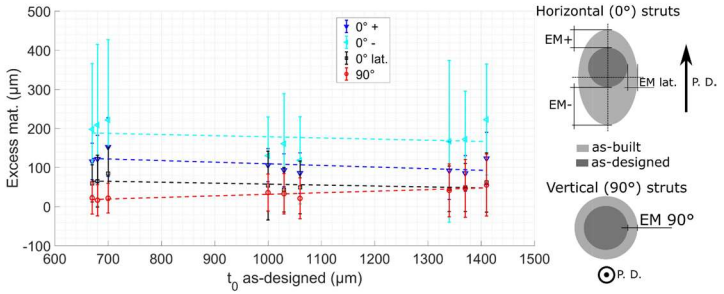

Figure IV - 19. Excess material distribution grouped according to the orientation of the struts to the printing plane in the 0° structure. The dashed lines are the linear regression of the data points of corresponding color.

The trend of the results measured in the structure printed at 45° is similar to those shown for the lattice printed at 0°. Most of the parasitic mass is accumulated on the underside of the struts, although the added thickness on the struts inclined of 45° is lower than that added to the horizontal struts. As discussed for the strut thickness, the excess material thickness measured for the 0° strut is not related to the major and minor axes of the elliptical cross-section. The experimental data were fitted with linear functions of expression:

$$EM^{-}_{45^\circ} = +0.017t_0^* + 48.66 \quad \text{(IV - 6a)}$$

$$EM^{+}_{45^\circ} = -0.037t_0^* + 114.13 \quad \text{(IV - 6b)}$$

$$EM^{lat}_{45^\circ} = +0.040t_0^* - 29.17 \quad \text{(IV - 6c)}$$

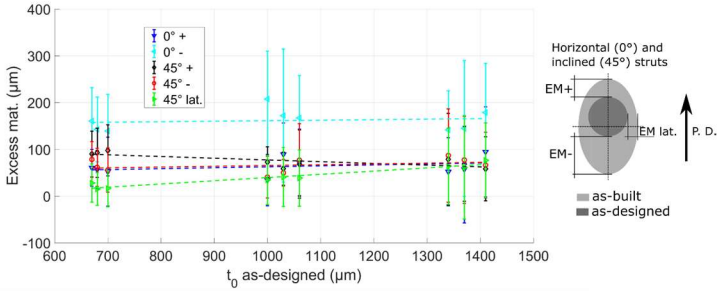

Figure IV - 20. Excess material distribution grouped according to the orientation of the struts to the printing plane in the 45° structure. The dashed lines are the linear regression of the data points of corresponding color.

The excess material for the 45°-35.26° lattice is plotted against the as-designed thickness in Figure IV - 21. As shown in the scheme, the excess material thickness

measured for the inclined struts does not allow to estimate the exact amount of parasitic mass on the upper side and on the underside of the struts.

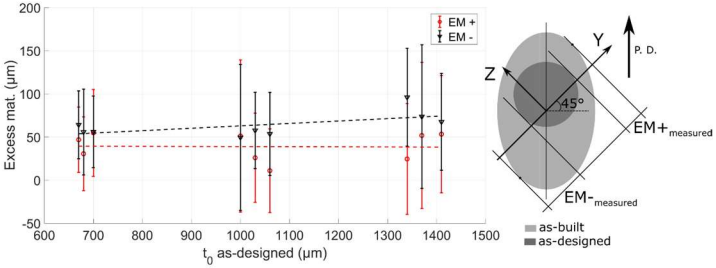

Figure IV - 21. Excess material distribution grouped according to the orientation of the struts to the printing plane in the 45°-35.26° structure. The dashed lines are the linear regression of the data points of corresponding color.

The material in excess is positive on average, that is, the as-built struts are on average thicker than the as-designed struts. The amount of excess material depends mainly on the orientation of the struts to the printing direction and only very weakly on the as-designed thickness. In other words, it appears that a nearly constant quantity of parasitic mass accumulates on the struts, which depends only on the process parameters and on the heat transfer properties of the powder. The weak dependence on the thickness can be due to the higher rate at which heat is carried away by thicker struts, thus reducing the amount of melted powder, although, given the very high scatter of the data, this aspect it is quite difficult to assess. The struts parallel to the printing plane (0°) show the greatest difference between the as-built and the as-designed geometries, with most of the material accumulated on the underside of the strut. This behavior is also observed in the inclined struts, although to a lesser extent. This is because horizontal and inclined struts are built on loose powder, which has lower thermal conductivity than the solid material. Indeed, the values of the excess material measure on the different locations are much closer for the inclined struts than for the horizontal struts. The vertical struts have the lowest distance between the as-designed and the as-built profiles, which is also uniformly distributed around the section.

4.3.4 Fillet radius *R*

The fillet radius shows the greatest complexity in behavior as it depends both on the as-designed fillet radius and on the as-designed strut thickness. In addition, the fillet radius is strongly influenced by its orientation to the printing direction. To have a meaningful representation of the data, the fillets have been classified into six

categories for statistical purposes, based on their location in the structure with respect to the printing direction, as shown in Figure IV - 22. In the case of the 0° sample, the author has distinguished between *positive fillets* (above the strut if we take the printing direction as a reference) and *negative fillets* (on the underside of the strut) for the vertical planes (as shown in Figure IV - 22a). This classification was applied also to the inclined planes of the 45° sample (planes XY and XZ in Figure IV - 3b). The radii laying in the horizontal plane of the 0° sample (XY in Figure IV - 3a) are called *lateral fillets* (Figure IV - 22b). The fillets of the vertical planes of the 45° sample (Figure IV - 22c) and of all the planes of the 45°-35.26° specimens are classified into three categories: *negative*, *positive* and *lateral*, depending on whether they lay on the underside, on the upper side or laterally to the joint, respectively.

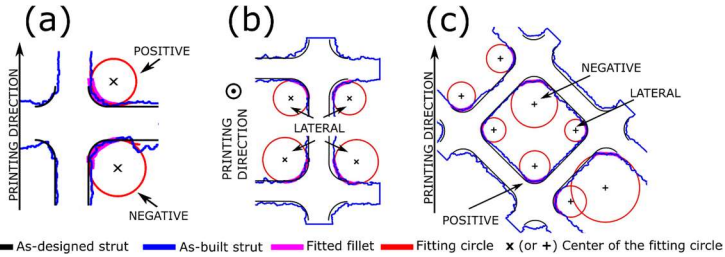

Figure IV - 22. Classification of fillets according to their orientation to the printing direction. (a) planes parallel (*XZ* and *YZ* planes of specimen 0°, in Figure IV - 3a) or inclined of 45° (*XY* and *XZ* planes of specimen 45°, in Figure IV - 3b) to the printing direction; (b) planes perpendicular to the printing direction (*XY* planes of specimen 0°, in Figure IV - 3b); (c) planes parallel to the printing direction but with inclined struts (*YZ* planes specimen 45°, in Figure IV - 3b) or with a small inclination (all the planes of the 45°-35.25° specimen, °, in Figure IV - 3c).

This Subsection is divided into three Paragraphs: in the first, the experimental measurements are shown and discussed, in the second the fitting of the data with bidimensional functions is illustrated and, finally, a brief analysis of the mechanical role of the fillets is presented.

4.3.4.1 Fillet radii measurements

In the specimens printed at 0° to the printing direction, the fillet radius on the underside of the struts ("negative" position) is systematically the smallest and, in some specimens, it is even slightly smaller than the as-designed value (Figure IV - 23). This may be because a considerably thicker layer of excess material accumulates on the underside of the struts, thus "closing" the fillet (observe, for instance, Figure IV - 10b). The fillets on the upper side of the horizontal struts ("positive") are of intermediate size, while the "lateral" fillets are the largest. The positive and lateral fillets are on average larger than the as designed value. As

visible in Figure IV - 23, the scatter of the data is quite high, meaning that it is not uncommon to observe fillets considerably sharper or considerably wider than what expected. In Table IV - 5, the average values of the fillet radii with the standard deviation are listed for each specimen.

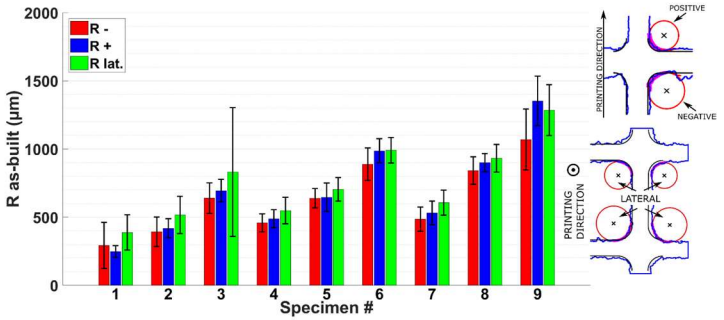

Figure IV - 23. Comparison between the as-built fillet radii at the locations defined for the lattice printed at 0° (the error bars indicate the standard deviation).

Table IV - 5. As-built fillet radii of the lattice printed at 0° with standard deviation (measures in µm).

Specimen	*As-designed*		*As-built*		
#	*R*	t_0	*R –*	*R +*	*R lateral*
1	200	700	292±169	247±43	388±129
2	400	680	392±108	418±70	516±137
3	600	670	639±112	694±83	831±473
4	300	1060	458±66	488±66	548±97
5	600	1030	638±71	645±104	703±87
6	900	1000	888±119	986±88	990±93
7	400	1410	485±89	530±86	607±92
8	800	1370	841±101	900±66	932±101
9	1200	1340	1069±224	1352±181	1285±187

The inclined planes of the 45° specimen show the same behavior for the negative and positive radii as the vertical planes for the 0° sample (Figure IV - 24): the average negative radius is systematically smaller. On the vertical planes, on the other hand, the struts are tilted of 45° to the printing direction. In this case, the negative fillets are considerably greater than the lateral and positive fillets, despite the statistical scatter (Figure IV - 24). The reason for this is that, most likely, the

parasitic mass tends to accumulate on the underside of the fillet, leading to a "flattening" of the same fillet. In Table IV - 6, the average values of the fillet radii with the standard deviation are listed for each specimen.

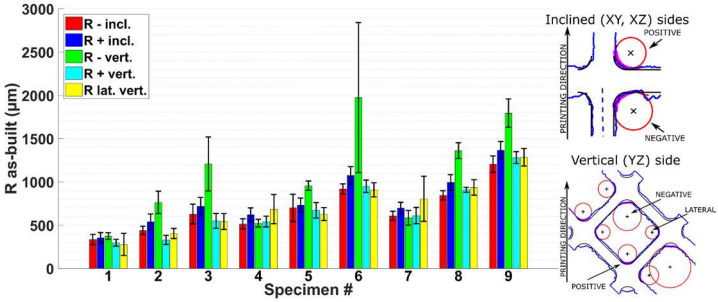

Figure IV - 24. Comparison between the as-built fillet radii at the locations defined for the lattice printed at 45° (the error bars indicate the standard deviation).

Table IV - 6. As-built fillet radii of the lattice printed at 45° with standard deviation (measures in μm).

Specimen #	*As-designed*		*As-built*				
	R	t_0	*R – incl.*	*R + incl.*	*R + vert.*	*R – vert.*	*R lat. vert.*
1	200	700	333±59	353±61	297±40	374±38	277± 128
2	400	680	439±48	538±91	329±53	762± 130	403±58
3	600	670	628± 115	718± 103	549±85	1207± 312	541±92
4	300	1060	514±59	621±78	541±63	523±44	685± 169
5	600	1030	700± 158	732±80	671±89	956±54	628±75
6	900	1000	919±58	1075± 101	949±71	1974± 868	908±82
7	400	1410	607±53	696±68	610±95	585±85	803± 260
8	800	1370	845±53	995±89	908±30	1361± 92	935±90
9	1200	1340	1205± 95	1366± 100	1280± 70	1794± 164	1284± 102

The planes of the specimens printed at 45°-35.26° are all inclined of a given angle to the printing direction and the faces of the unit cells are tilted, thus showing features very similar to the sides printed vertically of the 45° sample. Indeed, the negative fillets are consistently larger than all the other (Figure IV - 25). In Table IV - 7, the

average values of the fillet radii with the standard deviation are listed for each specimen.

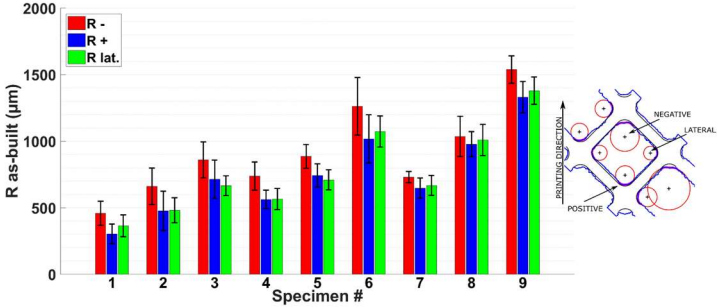

Figure IV - 25. Comparison between the as-built fillet radii at the locations defined for the lattice printed at 45°-35.26° (the error bars indicate the standard deviation).

Table IV - 7. As-built fillet radii of the lattice printed at 45°-35.26° with standard deviation (measures in μm).

Specimen #	*As-designed*		*As-built*		
	R	t_0	*R –*	*R +*	*R lateral*
1	200	700	458±91	303±73	363±82
2	400	680	660±137	476±148	480±94
3	600	670	859±135	713±145	665±74
4	300	1060	737±106	562±70	565±79
5	600	1030	885±89	742±88	709±76
6	900	1000	1262±216	1016±181	1073±117
7	400	1410	729±42	646±76	667±74
8	800	1370	1036±150	977±94	1009±117
9	1200	1340	1538±103	1330±118	1379±103

Common to all the fillet categories is that the as-built radius appears to be increased by both the as-designed fillet radius and strut thickness, although the former has a considerably stronger effect. Considering the average values of the fillet radii, relatively regular trends have been observed, indicating that it is reasonable to attempt to fit the experimental data onto the as-designed geometrical parameters to devise a predicting model. Moreover, the shape of the as-built fillets is rather regular (Figure IV - 10) indicating that this feature has been successfully reproduced by SLM. On the other hand, the scatter of the data is quite high, warning the designer on the fact that considerably sharp junctions can be found, due to local accumulations of parasitic mass or lack of melting (for instance, compare the sharp

radius at the junction indicated by the white circle in Figure IV - 10, caused by the parasitic mass on the underside of the cell wall, with the other fillets).

4.3.4.2 Fitting model

Based on the observations of the previous Paragraph, the behavior of the as-built fillet radius should be described by some function depending on both the as-designed fillet radius and thickness. In other words, it is not reasonable to assume that the only relevant parameter is the as-designed fillet radius. Moreover, recalling that the relationship between the as-designed and as-built thickness, it is likely for these relationships to be linear. Indeed, the as-built radius was fitted with functions linear to both as-designed geometrical parameters. The data is presented as 3D scatter plots, together with the interpolating plane and its contour plot. The accuracy of the fit is also shown with 3D scatter plots, reported in Appendix IV.A.

4.3.4.3 Specimens printed at 0°

The fillet radii of the specimen printed at 0° to the printing direction have been fitted with satisfactorily results by a plane (Figure IV - 26, Figure IV - 27 and Figure IV - 28), showing that the as-designed radius has a considerably stronger influence than the as-designed strut thickness. Nevertheless, neglecting the effect of the latter would lead to increased errors in predicting the outcome of the manufacturing process. The fitting errors are reasonably low, with errors around 10% (the error plot is shown in Appendix IV.A, Subsection 4.7.1.1). The expressions of the fitting formulas are:

$$R_{+} = -16.58 + 0.99R_{as-d.} + 0.12t_{0,as-d.} \quad \text{(IV - 7a)}$$

$$R_{-} = +97.86 + 0.75R_{as-d.} + 0.08t_{0,as-d.} \quad \text{(IV - 7b)}$$

$$R_{lat} = +210.19 + 0.85R_{as-d.} + 0.03t_{0,as-d.} \quad \text{(IV - 7c)}$$

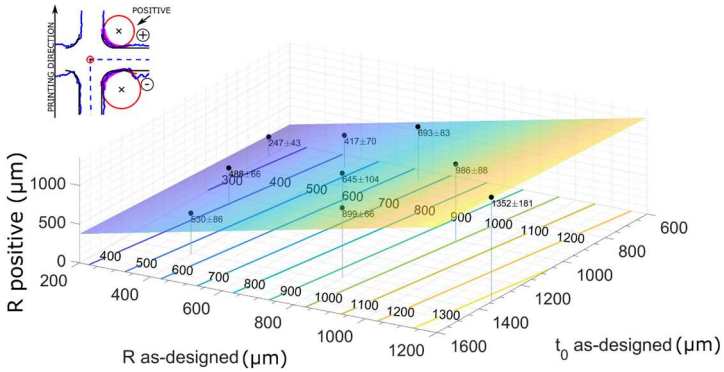

Figure IV - 26. Fillet radii of the specimen printed at 0°: positive position.

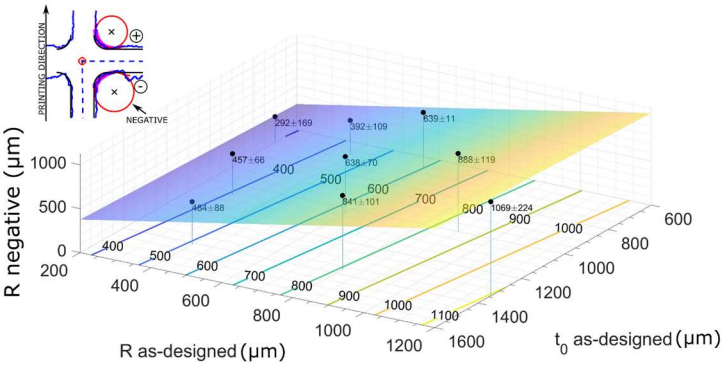

Figure IV - 27. Fillet radii of the specimen printed at 0°: negative position.

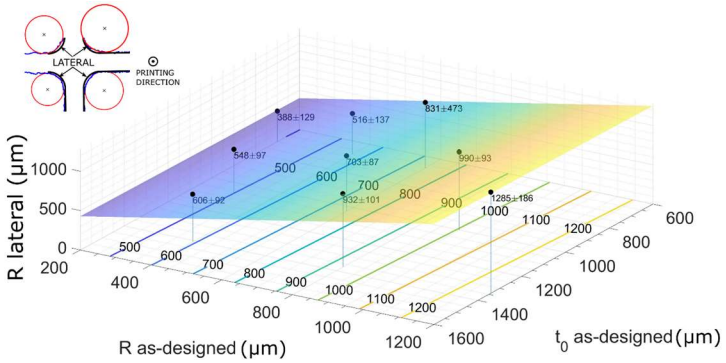

Figure IV - 28. Fillet radii of the specimen printed at 0°: lateral position.

4.3.4.4 Specimens printed at 45°

The fillet radii of the specimen printed at 45° to the printing direction have been also fitted with satisfactorily results by a plane (Figure IV - 29, Figure IV - 30, Figure IV - 31, Figure IV - 32 and Figure IV - 33). Considering the fillets measured on the plane of the lattice printed vertically (*XZ*), the as-designed radius has a stronger influence than the as-designed strut thickness, although not as marked as for horizontal and vertical struts (as measured in the lattice printed at 0°), as shown in Figure IV - 29, Figure IV - 30, Figure IV - 31. Indeed, in the case of the lateral radius the sensitivity of the as-built radius to to as-designed radius is comparable with the sensitivity to the as-designed strut thickness. The fitting errors are reasonably low, with errors around 15% (the error plot is shown in the Appendix IV.A, Subsection 4.7.1.2). The expressions of the fitting formulas for the fillets measured on the plane of the lattice printed vertically are:

$$R_{+,vert} = -129.20 + 0.79R_{as-d.} + 0.33t_{0,as-d.} \quad \text{(IV - 8a)}$$

$$R_{-,vert} = +360.08 + 1.84R_{as-d.} - 0.39t_{0,as-d.} \quad \text{(IV - 8b)}$$

$$R_{lat,vert} = -180.62 + 0.58R_{as-d.} + 0.53t_{0,as-d.} \quad \text{(IV - 8c)}$$

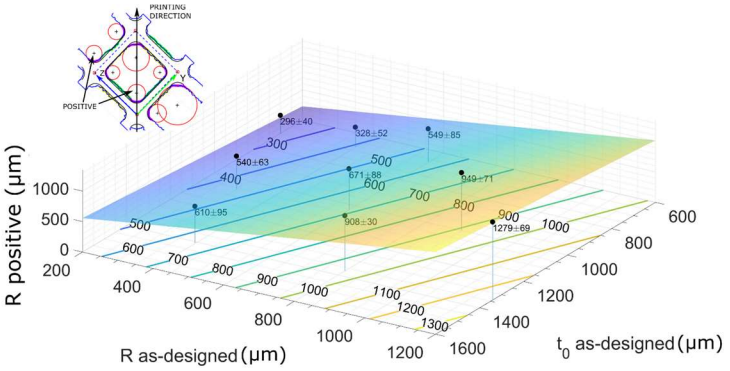

Figure IV - 29. Fillet radii of the specimen printed at 45°: positive position on vertical face.

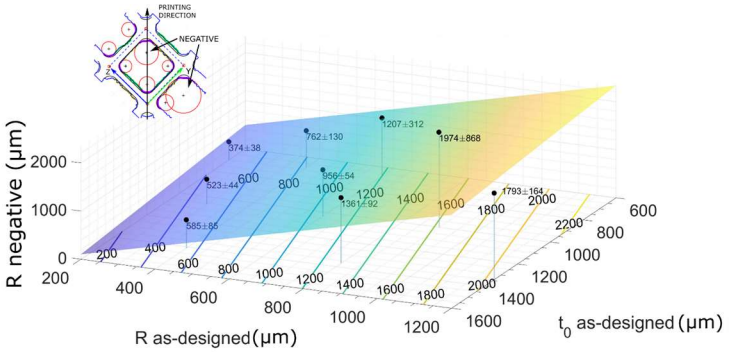

Figure IV - 30. Fillet radii of the specimen printed at 45°: negative position on vertical face.

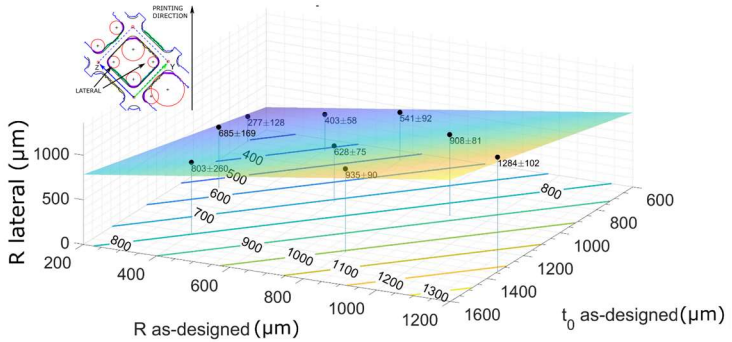

Figure IV - 31. Fillet radii of the specimen printed at 45°: lateral position on vertical face.

The measurements carried out on the fillets belonging to the inclined planes (Figure IV - 32 and Figure IV - 33) are similar to the results obtained for the positive and negative radii of the lattice printed at 0°. The fitting errors are reasonably low, with errors around 10% (the error plot is shown in the Appendix IV.A, Subsection 4.7.1.2). The expressions of the fitting formulas for the fillets measured on the inclined planes of the lattice:

$$R_{+,vert} = +64.70 + 0.84R_{as-d.} + 0.21t_{0,as-d.} \quad \text{(IV - 9a)}$$

$$R_{-,vert} = +59.81 + 0.74R_{as-d.} + 0.18t_{0,as-d.} \quad \text{(IV - 9b)}$$

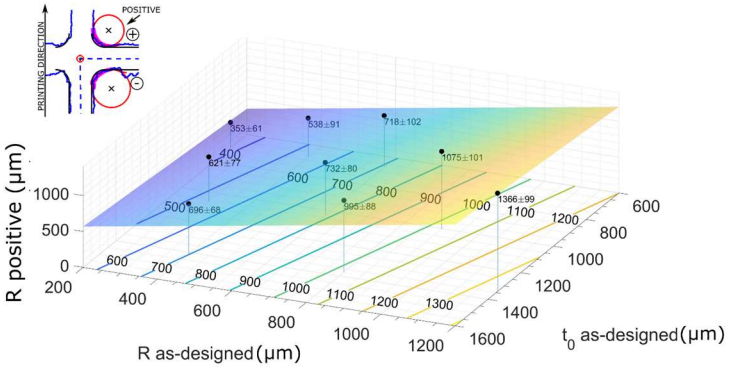

Figure IV - 32. Fillet radii of the specimen printed at 45°: positive position on inclined face.

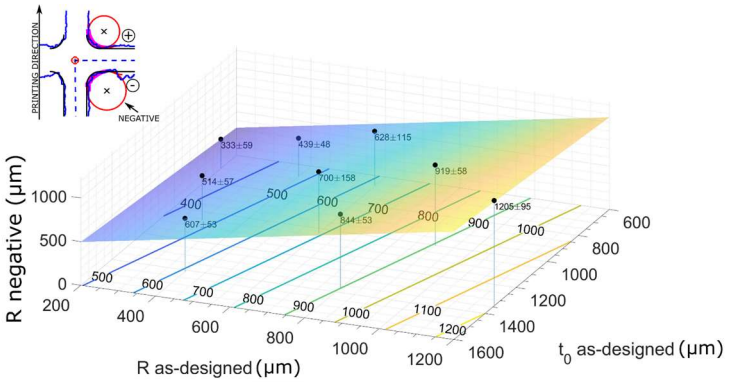

Figure IV - 33. Fillet radii of the specimen printed at 45°: negative position on inclined face.

4.3.4.5 Specimens printed at 45°-35.26°

The observations regarding the fitting of the fillets of the previous specimens essentially apply also to the specimens printed at 45°-35.26° (Figure IV - 34, Figure IV - 35 and Figure IV - 36). The dominant effect of the as-designed fillet is remarked. The fitting errors are reasonably low, with errors 10% or less (the error plot is shown in the Appendix IV.A, Subsection 4.7.1.3). The expressions of the fitting formulas for the fillets:

$$R_{+} = +21.45 + 0.87R_{as-d.} + 0.20t_{0,as-d.} \quad \text{(IV - 10a)}$$

$$R_{-} = +243.65 + 0.97R_{as-d.} + 0.077t_{0,as-d.} \quad \text{(IV - 10b)}$$

$$R_{lat} = -3.59 + 0.88R_{as-d.} + 0.24t_{0,as-d.} \quad \text{(IV - 10c)}$$

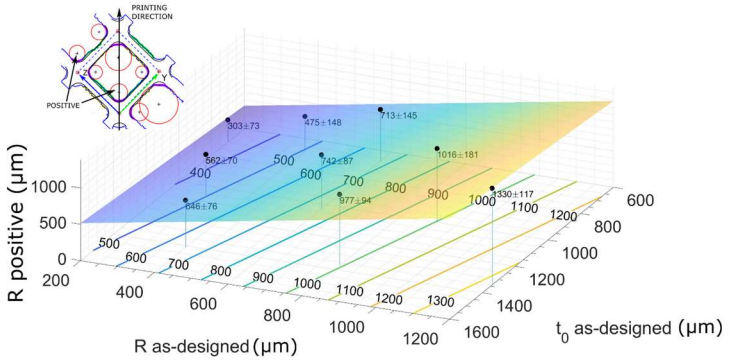

Figure IV - 34. Fillet radii of the specimen printed at 45°-35.26°: positive position on inclined face.

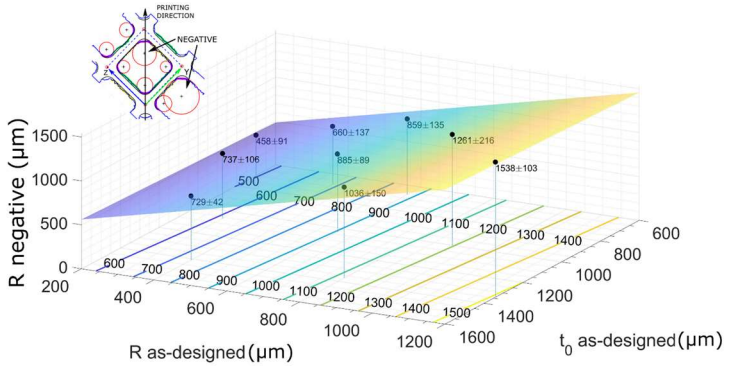

Figure IV - 35. Fillet radii of the specimen printed at 45°-35.26°: negative position on inclined face.

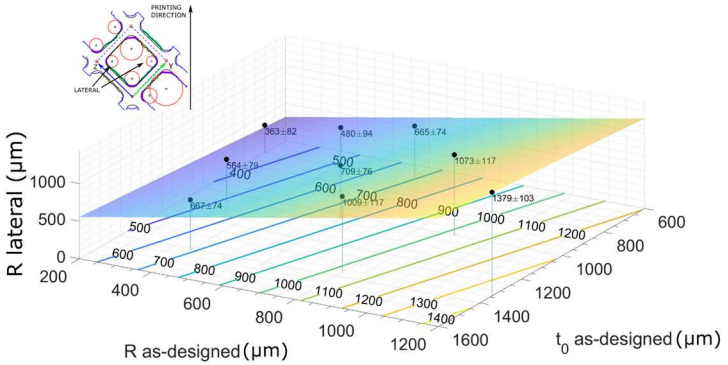

Figure IV - 36. Fillet radii of the specimen printed at 45°-35.26°: lateral position on inclined face.

4.3.4.6 Effect of the fillet radius on the stress concentration factor

The previous discussion highlighted the complexity of analyzing the results of the interactions of the as-designed geometry and of the printing direction on the manufacturing accuracy of the fillet radius at the junctions. It was observed that the fillets are on average larger than the as-designed value, suggesting that in practice the manufacturing deviation may be positive on the stress concentration at the junctions. Considering the wide scatter this may not always be the case, but on average certainly is. At this stage, the question may arise on how significative the effect of the fillet radius is on the stress concentration. In other words, can the statistical models previously described reliably predict whether the as-built lattice will be more vulnerable to stress concentration than the as-designed lattice? More precisely, if the fillets fitted at the junctions are larger than the CAD value, are the stress concentration factors correspondingly lower? To accurately answer to this question, 3D models of the as-built lattice should be available, for instance generated by µCT scans, but this is not the case. Nevertheless, it is possible to estimate the severity of the filleted junctions by comparing the SCF calculated from 2D images with the SCF of the corresponding 2D as-designed profile (as in Figure IV - 1a).

The same 2D profile of the as-built unit cell (Figure IV - 37a) used for the metrological analysis was filtered with a low pass filter to reduce the roughness due to the attached particles and then imported into Ansys® and meshed with 2D 8-node structural solid elements PLANE183 with plane stress formulation (Figure IV - 37b). A linear elastic analysis (E = 113GPa, v = 0.34) was carried out to estimate the stress concentration at the fillets, applying a uniform displacement on one side of the unit cell and constraining the other sides as shown in Figure IV - 37b. The mesh was refined via a convergence analysis until it was sufficiently fine (Figure IV - 37c).

The definition of stress concentration factor K_t^* in this context is the same as in the previous chapter, based on the homogenized axial stress of the unit cell and the local maximum von Mises equivalent stress:

$$K_t^* = \frac{\text{maximum von Mises equivalent stress at the fillet}}{\text{nominal homogeneous stress}} \qquad \text{(IV - 11)}$$

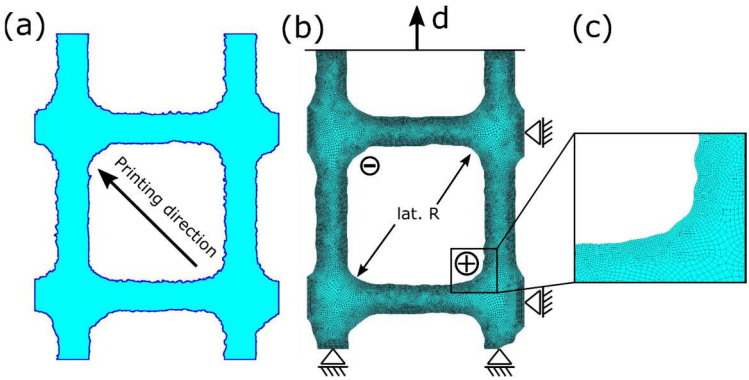

Figure IV - 37. Planar FE model (plane stress formulation) of specimen geometry #6 printed at 45°-35.26° (obvious symbols indicate the classification of the radii). The profile (a) acquired from the picture (blue line) has been filtered and then used to define an area then meshed (b) with 2D plane continuum elements and loaded axially. Effort has been put into guaranteeing a fine mesh (c) on the fillets.

As an example, the analysis of specimen #6 printed at 45°-35.26° is illustrated in detail (Figure IV - 37 and Figure IV - 38). To avoid border effects, only the joints inside the "square" were considered and the results are shown as contour plot of the von Mises stress in Figure IV - 38. For each fillet, the as-built radius, the SCF calculated from the FE analysis and the SCF calculated for the as-built radius are also listed. The SCF considering the as-designed geometry (in 2D) has been estimated as 7.9. The SCFs (other than those calculated with the FE analysis) have been estimated using the semi-analytical model described in Chapter II. Interestingly, the SCFs measured with the FE analysis are generally lower than expected from the as-designed geometry because of the wider fillets, with the exception of the positive fillet (bottom right) because of secondary stress concentrators (small notches due to surface irregularity). The SCFs estimated with the semi-analytical model from the as-built radii are reasonably close to the FE value, but the prediction is not very accurate. This work thus suggests that the approximation of the as-built fillets with a circular fillet is simple and yields reasonable results, but, not surprisingly, fails to capture local fluctuations of the profile that can measurably increase (bottom right fillet) or decrease (top right fillet) the SCF. Note that the 45°-35.26° unit cell is symmetric to the axis connecting the

negative and positive radii, so loading along the other direction yields very similar results.

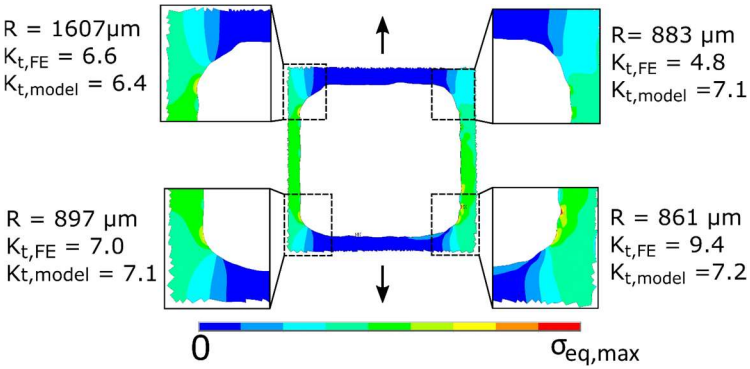

Figure IV - 38. Qualitative equivalent von Mises stress contour plot of the internal part of the unit cell with details of the fillets (the arrows indicate the load direction). As expected, the fillet with higher stress concentration is the *positive* (bottom right), also due to the more irregular surface. This example refers to geometry #6 printed at 45°-35.26, nominal radius 900 µm and theoretical K_t 7.9.

This analysis has been carried out for a selected set (specimens 3, 6, and 9 printed at 0° and specimens 6 and 9 printed at 45°-35.26°) of as-built lattices and the results are listed in Table IV - 8. The quantities are represented by an average value and standard deviation, calculated from two unit cells per side of the specimen, similarly to the metrological analysis. The SCFs based on the as-built radii have been also calculated with the semi-analytical model, listing in Table IV - 9 a minimum value (computed from the average value of the corresponding radius adding the standard deviation) and a maximum value (computed from the average value of the corresponding radius subtracting the standard deviation). Confirming the previous observations, the estimations based on the as-built circular radius slightly underestimate the SCF measured with the FE analysis, likely because of local irregularities. Nevertheless, it appears to be safe to assume that the SCFs in the as-built structure are only slightly higher than the estimate based on the as-designed geometry, if not lower.

Table IV - 8. K_t calculated from the 2D FE analyses of a selected set of as-built geometries. The K_t (in 2D) calculated form the as-designed geometry (R/L = 0.15, t0/L = 0.167) is 7.9.

Build angle	Specimen #	K^*_t		
		Positive R	Negative R	Lateral R
0°	3	10.9±1.2	10.7±1.1	---
	6	8.1±1.3	6.3±0.8	8.1±1.5

	9	8.8±3.5	7.4±1.2	8.3±1.5
45°-	6	7.0±1.2	6.2±1.2	6.3±1.1
35.26°	9	8.4±2.1	8.3±4.0	7.3±1.0

Table IV - 9. K_t calculated from the as-built geometry (see Table IV - 2 and Table IV - 4) with the semi-analytic model for the SCFs. The minimum and maximum SCFs are referred to the maximum (standard deviation added to the mean value) and minimum as-built radii (standard deviation subtracted from the mean value), respectively.

Build angle	Specimen #	K^*_t					
		Positive R		Negative R		Lateral R	
		Min	Max	Min	Max	Min	Max
	3	7.2	7.7	7.1	7.5	6.5	8.4
0°	6	7.3	7.7	7.2	7.5	7.2	7.5
	9	7.4	8.1	7.2	7.6	7.2	7.7
45°-	6	6.7	7.1	6.9	7.5	6.9	7.2
35.26°	9	6.9	7.1	7.1	7.4	7.1	7.3

Concluding, it appears reasonable to assume that, on average, the as-built fillets do not induce a more severe stress concentration than what expected from the as-designed geometry because, thanks to the accumulation of parasitic mass, the radius in most cases increases. On the other hand, it was observed that unpredictable irregularities of the fillet profile can be introduced by the manufacturing process that can considerably amplify the stress concentration. Nevertheless, considering the standard deviation related to the results listed in Table IV - 8, it is safe to say that the scattering of the SCFs is not high.

4.3.5 Distortion of the lattice

It has been shown how the printing process considerably affects the morphological accuracy of the minute details of the geometry such as the strut thickness and the fillet radius, but the same appears not to be true for the overall shape of the unit cell (Figure IV - 39, Figure IV - 40 and Figure IV - 41). Indeed, the distortion of the unit cells is very low (on average, between -0.5% and +2%) for all the geometries and all the printing directions. There appears to be no correlation between the unit cell distortion and the as-designed geometry or the printing direction, because the values seem to fluctuate randomly inside the mentioned interval.

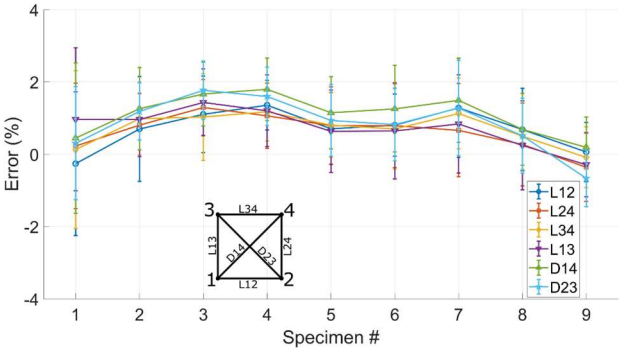

Figure IV - 39. Distortion of the lattice printed at 0°.

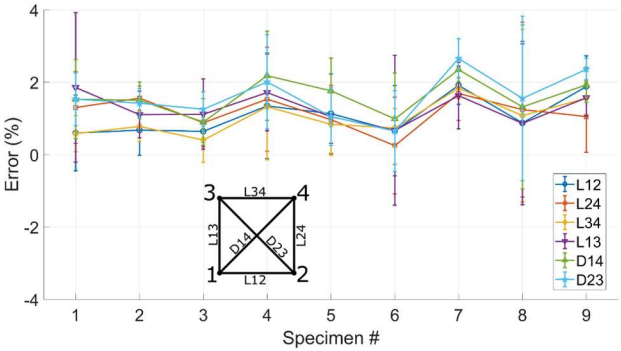

Figure IV - 40. Distortion of the lattice printed at 45°.

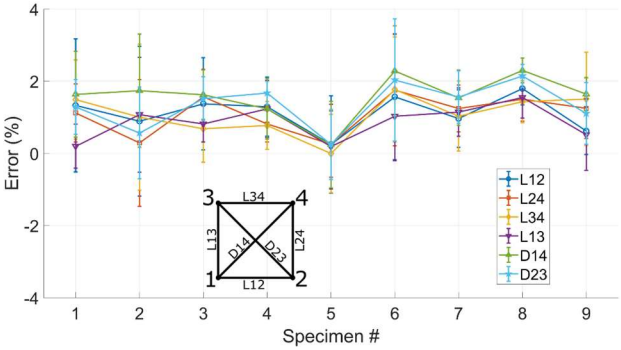

Figure IV - 41. Distortion of the lattice printed at 45°-35.26°.

4.4 Compensation strategy

The expressions tying the as-built geometrical parameters to their as-designed counterparts obtained by fitting the experimental measurements are useful in predicting the outcome of the SLM process of new lattices with different geometry, provided all the other parameters are unchanged. Moreover, by reversing the equations, it is possible to calculate the geometrical parameters of the CAD so that the as-built lattice will match the desired morphology. This procedure is known as a compensation.

4.4.1 Compensation procedure

Devising the compensation model is conceptually quite simple: a first experimental campaign is necessary to identify the mathematical relationships between the as-built and the as-designed geometrical parameters and then it is sufficient to reverse such formulas. In this way, expressions are obtained that express the CAD parameter as a function of the as-built parameter. In practice, the aim is to design a CAD with a geometry conveniently modified in order to obtain, after manufacturing, a lattice with the desired geometry (circular struts of diameter t_0), as in Figure IV - 42.

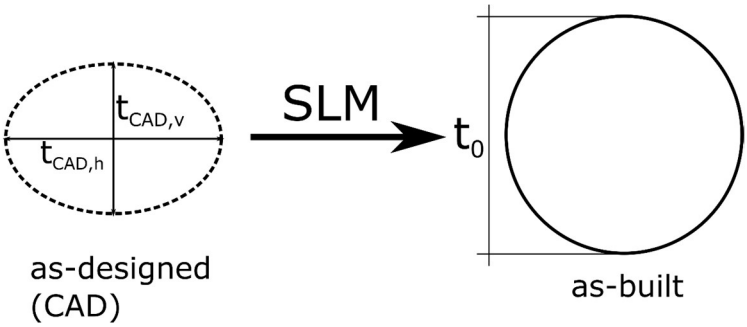

Figure IV - 42. The CAD strut cross-section is designed with the aid of the compensation mode to produce the desired (t_0) cross-section after manufacturing.

In the previous Section, three parameters were studied: the strut thickness, the excess material and the fillet radius. Consequently, compensation models can be devised for each tree of them.

The thickness of the struts, as discussed, has been accurately characterized for three inclinations to the printing plane: 0°, 45° and 90°. The section of the struts at 0° and 45° have been shown to have an elongated cross-section (reasonably assumed elliptical), defined by a major axis (or vertical axis because it is aligned with

the printing direction) and a minor axis (or horizontal axis, because it is perpendicular to the printing direction). On the other hand, the struts perpendicular to the printing plane have retained their circular cross section, thus the section is defined by its diameter. The appropriate dimensions of the compensated CAD can thus be calculated with the following equations (obtained by reversing Eqs. (IV – 2), (IV - 3b) and (IV - 3c)) from the diameter t_0 of the desired (nominal) cross-section:

- Compensated diameter $t_{90°}$ of the struts perpendicular to the printing plane:

$$t_{90°} = \frac{t_0 + 17.29}{1.08} \quad \text{(IV – 12)}$$

- Compensated vertical $t_{45°,v}$ and horizontal $t_{45°,h}$ axes of the struts inclined of 45° to the printing plane:

$$t_{45°,v} = \frac{t_0 + 162.81}{0.98} \quad \text{(IV – 13a)}$$

$$t_{45°,h} = \frac{t_0 + 58.32}{1.14} \quad \text{(IV – 13b)}$$

- Compensated vertical $t_{0°,v}$ and horizontal $t_{0°,h}$ axes of the struts parallel to the printing plane:

$$t_{0°,v} = \frac{t_0 + 358.58}{0.93} \quad \text{(IV – 14a)}$$

$$t_{0°,h} = \frac{t_0 + 163.31}{0.95} \quad \text{(IV – 14b)}$$

Following the same logic, the compensating equations for the excess material are devised. Essentially, the equations that compensate the cross-section thickness define the geometry of the cross-section while the equations that compensate the excess material define the position of the compensated cross-section with respect to the strut axis (Figure IV - 43).

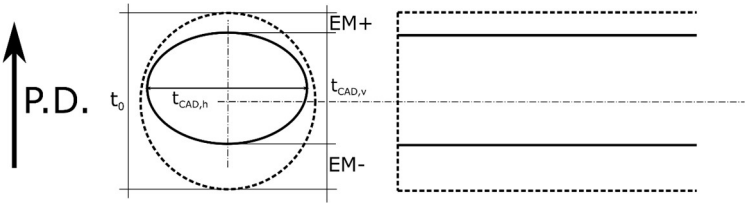

Figure IV - 43. Scheme of the principle of compensation.

Provided that the deviation between the as-built and the as-designed cross-section diameter is distributed uniformly along the circumference of the vertical struts, it is justified to let coincide the centers of both cross-sections. Moreover, assuming the cross-section symmetric with respect to the vertical axis, regarding the compensation of the excess material it is enough to calculate only one between the positive and the negative excess material to solve the problem. Considering, for instance, the negative excess material, the equations to calculate the appropriate thickness of the excess material for the compensated CAD are the following (corresponding to Eqs. (IV - 4a), (IV – 5), (IV - 6a)):

- Circumferential excess material in the struts perpendicular to the printing direction $EM_{90°}$:

$$EM_{90°} = +0.040t_0^* - 8.64 \quad \text{(IV – 15)}$$

- Negative excess material on the struts inclined of 45°:

$$EM_{45°}^- = -0.017t_0^* + 48.66 \quad \text{(IV – 16)}$$

- Negative excess material on the struts parallel to the printing plane:

$$EM_{0°}^- = -0.029t_0^* + 207.70 \quad \text{(IV – 17)}$$

Note that t^*_0 is the thickness of the cross-section of the CAD the excess material will be "added" to by the manufacturing process. In practice, on the compensated cross-section is determined, the excess material is calculated by substituting to t_0 the compensated thickness.
Similarly, the fillet radius can be compensated by appropriately applying the fitting functions identified in Section 3, which are of the generic $R_{as-built} = aR_{as-d.} + bt_{0,as-d.} + c$ type. By reversing such expression, the following is obtained:

$$R_{CAD} = \frac{R_{as-built} - bt_{0,CAD} - c}{a} \quad \text{(IV – 18)}$$

Where R_{CAD} is the compensated radius, $R_{as\text{-}built}$ is the desired radius in the manufactured lattice and $t_{0,CAD}$ is the compensated cross-section thickness. For brevity, the equations are not reported here.

4.4.2 Assessment of the compensation procedure

The effectiveness of the compensating procedure was assessed by designing and fabricating compensated lattices. To reduce the number of specimens, only geometries #3, #6 and #9 were repeated, printed at 0° and 45-35.26°. The CAD strut cross-section was compensated to obtain the as-designed geometry net of the manufacturing defects, using the appropriate compensating relations for the thickness and the excess material. Two variants of the compensation procedures were implemented, for comparison: the first, named “Standard” (S), is the approach described previously (Figure IV - 44a), the second, named “Alternative” (A), is a simplified approach that consists in placing all the excess material thickness on the underside of the strut (Figure IV - 44b). The resulting compensated unit cells (observed normal to the printing direction) are shown in Figure IV - 44c and Figure IV - 44d, respectively. The aim is to verify the sensitivity of the manufacturing process to the EM+, which is a quite small quantity. Moreover, the implementation of the *alternative* approach is operatively quite simpler. The fillet radius was not compensated in this batch and is left for future work. For a more accurate statistic, three specimens where manufactured for each geometry and printing direction, for a total of 36 specimens.

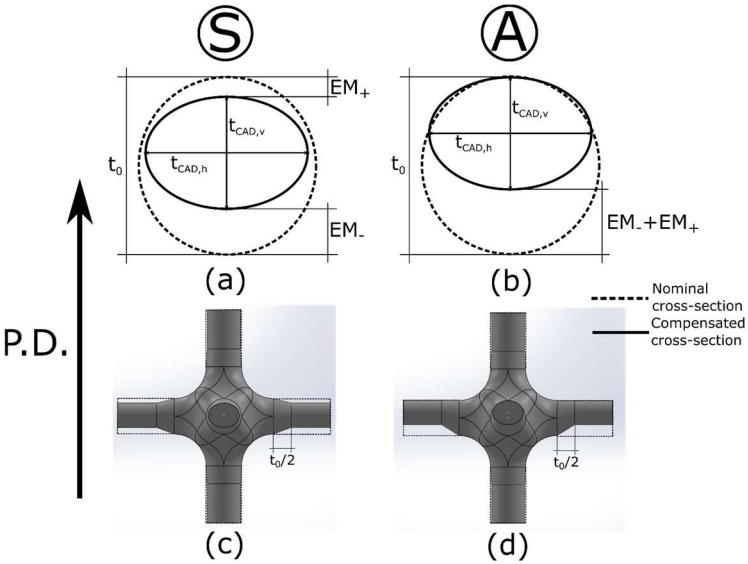

Figure IV - 44. Example of the implementation of the compensation procedures on the horizontal struts: (a) compensated and nominal (desired) cross-sections, *standard* approach; (b) compensated and nominal (desired) cross-sections, *alternative* approach; (c) compensated CAD of the unit cell, *standard* approach; (d) compensated CAD of the unit cell, *alternative* approach.

The parameters of the desired geometry and those of the corresponding compensated cross-section are listed in Table IV - 10 and Table IV - 11 for the 0° and the 45°-35.26° specimens, respectively.

Table IV - 10. Compensated batch printed at 0° to the printing plane.

Specimen #	Nominal geometry			Compensated CAD parameters				
	R (µm)	t_0 (µm)	L (µm)	$t_{90°}$ (µm)	$t_{0°,v}$ (µm)	$t_{0°,h}$ (µm)	$EM^-_{0°}$ (S)	$EM^-_{0°}$ (A)
3	600	670	4000	636	335	532	198	335
6	900	1000	6000	942	690	879	188	310
9	1200	1340	8000	1257	1056	1236	177	284

Table IV - 11. Compensated batch printed at 45°-35.26° to the printing plane.

Specimen #	Nominal geometry			Compensated CAD parameters			
	R (μm)	t_0 (μm)	L (μm)	$t_{45°,v}$ (μm)	$t_{45°,h}$ (μm)	$EM^{-}_{45°}$ (S)	$EM^{-}_{45°}$ (A)
3	600	670	4000	518	640	57	152
6	900	1000	6000	854	930	63	146
9	1200	1340	8000	1201	1229	69	130

An example of unit cell profile obtained by implementing the standard procedure and the alternative procedure is shown in Figure IV - 45, for geometry #6 printed at 0° to the printing direction. The results are satisfactory and very similar for both cases, although in specimens S a small step is observed in correspondence with the transition from the fillet to the strut (arrows in Figure IV - 45). This effect is increased in thinner struts (specimens #3).

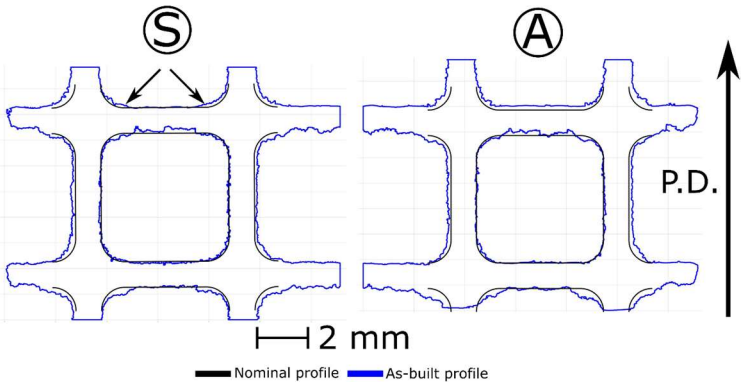

Figure IV - 45. Comparison between the standard (S) and the alternative (A) compensation procedures for geometry #6 printed at 0°. The arrows indicate the a "step" observed in specimens S caused by the transition from the fillet to the strut.

The same procedure devised to carry out the morphological characterization necessary to define the compensation equations was applied to the specimens of this batch to evaluate the effectiveness of the compensation procedure by comparing the compensated specimens with the non-compensated specimens of the first batch. The struts printed parallel to the printing plane were the most positively affected by compensation (Figure IV - 46 and Figure IV - 47), as expected. Moreover, being the strut thicknesses in the vertical and horizontal directions very similar, a circular cross-section was achieved. On the other hand, the cross-section thickness after compensation of the vertical struts (Figure IV - 48) are not significantly different from those of the uncompensated specimens. Most likely, since in the case of the vertical struts the excessive material was so little (~40μm), to be comparable with the mean

size of the powder (<45µm), the difference between the diameters of the compensated and uncompensated strut of the CAD is practically undistinguishable.

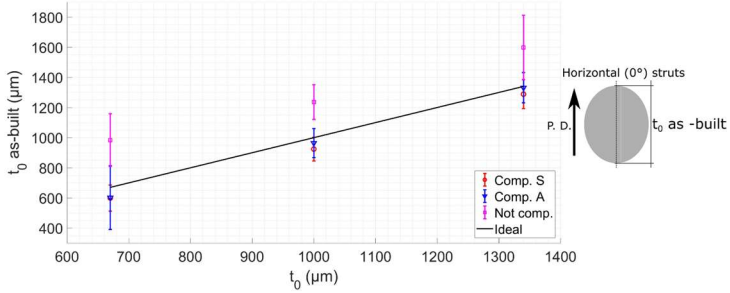

Figure IV - 46. As-built thickness of the struts printed parallel to the printing plane (0° struts) plotted against the nominal strut diameter. The specimens compensated with the standard (S) and the alternative (A) procedures are compared with the first experimental batch (non-compensated specimens). The continuous solid line is the bisecting line of the quadrant, referred to an ideal manufacturing process that reproduces perfectly the as-designed geometry.

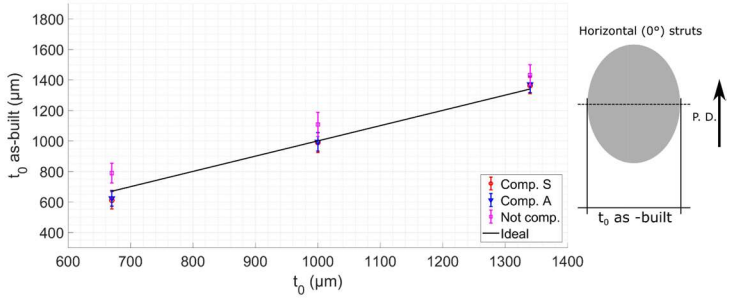

Figure IV - 47. As-built horizontal thickness of the struts printed parallel to the printing plane (0° struts) plotted against the nominal strut diameter. The specimens compensated with the standard (S) and the alternative (A) procedures are compared with the first experimental batch (non-compensated specimens). The continuous solid line is the bisecting line of the quadrant, referred to an ideal manufacturing process that reproduces perfectly the as-designed geometry.

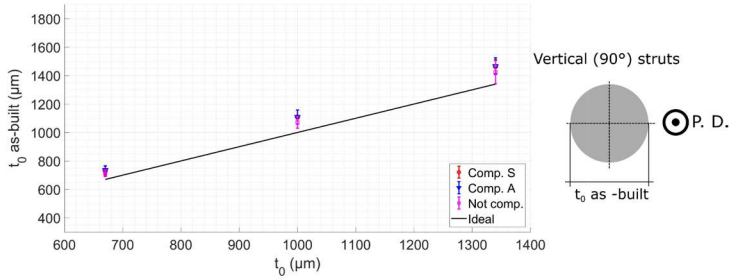

Figure IV - 48. As-built thickness of the struts printed perpendicular to the printing plane (90° struts) plotted against the nominal strut diameter. The specimens compensated with the standard (S) and the alternative (A) procedures are compared with the first experimental batch (non-compensated specimens). The continuous solid line is the bisecting line of the quadrant, referred to an ideal manufacturing process that reproduces perfectly the as-designed geometry.

The effectiveness of compensation was evaluated by calculating the error (%) on the as-built strut thickness relative to the nominal thickness t_0 with Eq. (IV – 19). In the calculation, given that the A and S compensation strategies have been proven to be equivalent, their results have been averaged.

$$error(\%) = \frac{\left|t_{0,as-built} - t_0\right|}{t_0} \times 100 \qquad \text{(IV - 19)}$$

Compensation remarkably reduced the error, in some instances up to 30 times, compared to the uncompensated lattice (Table IV - 12).

Table IV - 12. Comparison of the average errors of the batch printed at 0° to the printing plane for the compensated and not-compensated batches.

Specimen #	t_0 (μm)	Not compensated			Compensated		
		Error [$t_{90°}$] (%)	Error [$t_{0°,v}$] (%)	Error [$t_{0°,h}$] (%)	Error [$t_{90°}$] (%)	Error [$t_{0°,v}$] (%)	Error [$t_{0°,h}$] (%)
3	670	6.59	46.78	17.74	9.85	10.16	6.95
6	1000	7.16	23.62	10.79	10.89	3.62	0.63
9	1340	6.21	19.32	6.81	9.45	0.66	2.28

The struts of the specimen printed at 45°-35.26° are impossible to fully characterize with pictures taken perpendicular to the sides of the specimen, as already discussed. Nevertheless, it is still possible to evaluate the effectiveness of the compensation procedure by comparing the measurements of the compensated and uncompensated cross-sections, as shown in Figure IV - 49. Indeed, the values

measured on the compensated struts deviate less form the nominal thickness t_0, moreover indicating that the cross-section resembles more closely the circular shape. The error has been calculated with Eq. (IV – 19) and the results are reported in Table IV - 13, showing that the deviation between the as-built and the as-designed cross-section has been appreciably decreased.

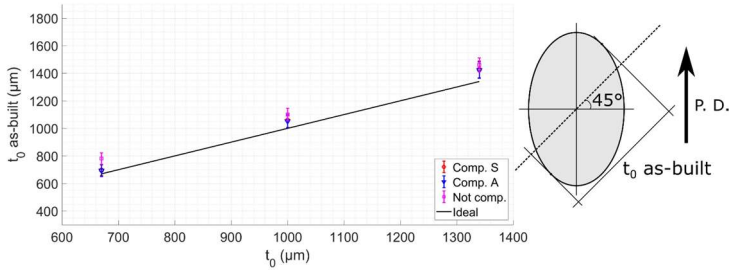

Figure IV - 49. As-built thickness of the struts printed parallel to the printing plane (0° struts) plotted against the nominal strut diameter. The specimens compensated with the standard (S) and the alternative (A) procedures are compared with the first experimental batch (non-compensated specimens). The continuous solid line is the bisecting line of the quadrant, referred to an ideal manufacturing process that reproduces perfectly the as-designed geometry.

Table IV - 13. Comparison of the average errors of the batch printed at 45°-35.26° to the printing plane for the compensated and not-compensated batches.

Specimen #	t_0 (μm)	Not compensated Error (%)	Compensated Error (%)
3	670	16.56	3.73
6	1000	10.05	5.51
9	1340	9.00	6.36

In practice, regarding the strut thickness, the performance of the S and A compensation strategies appears to be equivalent. On the other hand, strategy A has the advantage of being simpler to implement in CAD sofwares.

4.5 Conclusions

In this Chapter, regular cubic cellular lattices with filleted junctions and circular cross-section struts were designed with nine combinations of the fillet radius and strut diameter and printed along three orientations to the printing plane. The lattices are scaled up compared to the cellular structures studied in Chapter III, to assess the limits of the SLM system employed in reproducing minute details of the lattice, such

as the fillet radius, which was failed to obtain in the lattices of the previous chapter. After a morphological analysis carried out using images taken with a stereo optical microscope, a statistical analysis of the geometrical parameters (fillet radius, strut thickness and strut length) of the as-built lattices was carried out. The as-built and the as-designed geometrical features of the lattice were then compared, leading to the following observations:

- The distortion of the unit cell is minimal, even for the largest cells: it is on average between -0.5% and +2% of the strut length for all the geometries and all the printing directions. There appears to be no correlation between the unit cell distortion and the as-designed geometry or the printing direction, because the error seems to fluctuate randomly inside the mentioned interval.
- The as-built strut thickness strongly depends on both the as-designed thickness and on the orientation of the individual strut to the printing direction. There is a linear relationship between the as-designed and the as-built strut thickness for all the orientations of the strut to the printing direction considered, although the parameters of the relationship are a function of the angle. The struts other than parallel to the printing direction have a section that can be approximated by an ellipse defined by a vertical axis that lies in a plane normal to the printing plane and a horizontal axis normal to the printing direction. The vertical axis is always larger than the horizontal axis. Indeed, horizontal struts in a lattice are reproduced the least accurately by SLM. On the other hand, the as-built vertical struts retain the circular cross-section with a diameter close to the as-designed value.
- The deviation of the as-built cross-section from the nominal geometry is caused by excess material (or parasitic mass) added to the struts during the printing process due the excessive local melting and bonding of partially melted particles. The distribution of excess material highly depends on the inclination of the strut to the printing direction. In general, material tends to accumulate on the underside of struts (with respect to the printing direction). The most affected are the horizontal struts, the least affected are the vertical struts, which, moreover, show uniformly distributed excess material around the section. The dependence of the quantity of the excess material on the thickness of the struts is very weak, indicating that the quantity of material in excess is roughly constant. In other words, it appears that the nearly constant quantity of parasitic mass accumulated onto the struts depends only on the process parameters and on the heat transfer properties of the powder.

- The fillet radii have been rather accurately reproduced by SLM, and regular shape fillets have been obtained also for the smallest radius of 200 μm. Indeed, FE simulations showed that, on average, the as-built fillets do not induce a significantly more severe stress concentration than what expected from the as-designed geometry because, thanks to the accumulation of parasitic mass, the radius in most cases increases. On the other hand, the scatter of the data is quite high, warning the designer on the fact that considerably sharp junctions can be found, due to local irregularities in the accumulation of parasitic mass or lack of melting, despite the as-built radius being on average larger than the as-designed radius. In fact, FE simulations showed also that unpredictable irregularities of the fillet profile can amplify the stress concentrations locally. It was observed that the radii measured depend on both the as-designed fillet radius and as-designed strut thickness, although the former parameter has a considerably stronger effect. The dependence towards both variables is linear and was determined by a plane fit.

The functions that relate the as-built geometrical parameters with the as-designed parameters can be used to predict the outcome of a printing process given a specific design, provided that the process parameters are prescribed. Indeed, appropriately reversing and combining such functions, compensation models have been devised that provide the designer with a tool to generate a CAD geometry that, fed to the printer, accommodates for the parasitic mass and the geometrical errors leading to as-built lattices that very closely matche the desired geometry. An experimental campaign has been carried out to verify the accuracy of such compensation models and it was shown that the error affecting the geometrical parameters of the as-built lattice has been decreased from peaks of 20%-40% to less than 10% of the nominal geometry.

4.6 Acknowledgments

A considerable part of the work presented in this Chapter was carried out at McGill University (Montreal, Canada) under the supervision of Prof. Damiano Pasini.

4.7 References

[1] Mullen L, Stamp RC, Brooks WK, Jones E, Sutcliffe CJ. Selective laser melting: A Regular Unit Cell Approach for the Manufacture of Porous, Titanium, Bone In-Growth Constructs, Suitable for Orthopedic Applications. J Biomed Mater Res - Part B Appl Biomater 2009;89B:325–34.

doi:10.1002/jbm.b.31504.

[2] Qiu C, Yue S, Adkins NJE, Ward M, Hassanin H, Lee PD, Withers PJ, Attallah MM. Influence of processing conditions on strut structure and compressive properties of cellular lattice structures fabricated by selective laser melting. Mater Sci Eng A 2015;628:188–97. doi:10.1016/j.msea.2015.01.031.

[3] Sing SL, Wiria FE, Yeong WY. Selective laser melting of lattice structures: A statistical approach to manufacturability and mechanical behavior. Robot Comput Integr Manuf 2018;49:170–80. doi:10.1016/j.rcim.2017.06.006.

[4] Zhu Z, Anwer N, Mathieu L. Deviation Modeling and Shape Transformation in Design for Additive Manufacturing. Procedia CIRP 2017;60:211–6. doi:10.1016/j.procir.2017.01.023.

[5] Pyka G, Kerckhofs G, Papantoniou I, Speirs M, Schrooten J, Wevers M. Surface roughness and morphology customization of additive manufactured open porous Ti-6Al-4V structures. Materials (Basel) 2013;6:4737–57. doi:10.3390/ma6104737.

[6] Yan C, Hao L, Hussein A, Young P, Raymont D. Advanced lightweight 316L stainless steel cellular lattice structures fabricated via selective laser melting. Mater Des 2014;55:533–41. doi:10.1016/j.matdes.2013.10.027.

[7] Kessler J, Balc N, Gebhardt A, Abbas K. Basic design rules of unit cells for additive manufactured lattice structures. MATEC Web Conf 2017;137. doi:10.1007/BF01171954.

[8] Van Bael S, Kerckhofs G, Moesen M, Pyka G, Schrooten J, Kruth JP. Micro-CT-based improvement of geometrical and mechanical controllability of selective laser melted Ti6Al4V porous structures. Mater Sci Eng A 2011;528:7423–31. doi:10.1016/j.msea.2011.06.045.

[9] Weißmann V, Drescher P, Bader R, Seitz H, Hansmann H, Laufer N. Comparison of Single Ti6Al4V Struts Made Using Selective Laser Melting and Electron Beam Melting Subject to Part Orientation. Metals (Basel) 2017;7:91. doi:10.3390/met7030091.

[10] Bagheri ZS, Melancon D, Liu L, Johnston RB, Pasini D. Compensation strategy to reduce geometry and mechanics mismatches in porous biomaterials built with Selective Laser Melting. J Mech Behav Biomed Mater 2017;70:17–27. doi:10.1016/j.jmbbm.2016.04.041.

4.8 Appendix IV.A: Accuracy of the fillet radius interpolation functions

The residuals of the functions fitting the values of the as-built fillet radii are defined according to Eq. (IV – A1) and are plotted in the following graphs:

$$residual(\%) = \frac{R_{fit} - R_{as-built}}{R_{as-built}} \times 100 \qquad \text{(IV – A1)}$$

4.8.1 Specimens printed at 0°

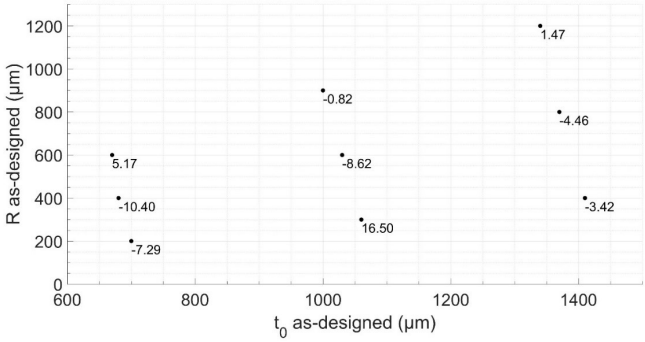

Figure 0.1. Residuals (%) on the fit of the fillet radii of the specimen printed at 0°: positive position.

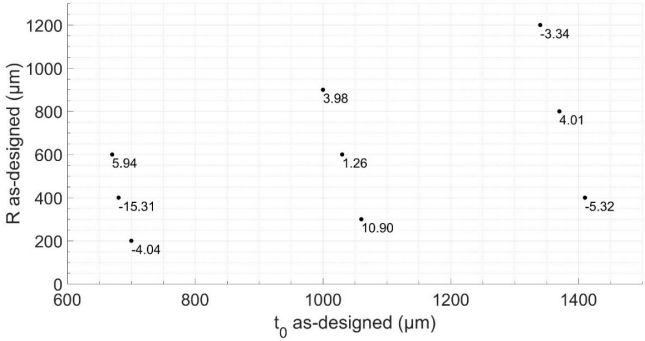

Figure 0.2. Residuals (%) on the fit of the fillet radii of the specimen printed at 0°: negative position.

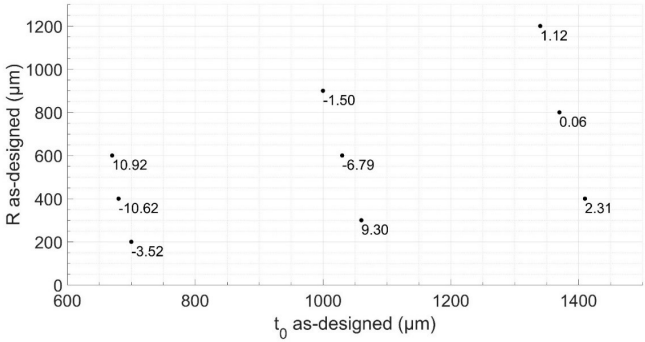

Figure 0.3. Residuals (%) on the fit of the fillet radii of the specimen printed at 0°: lateral position.

4.8.2 Specimens printed at 45°

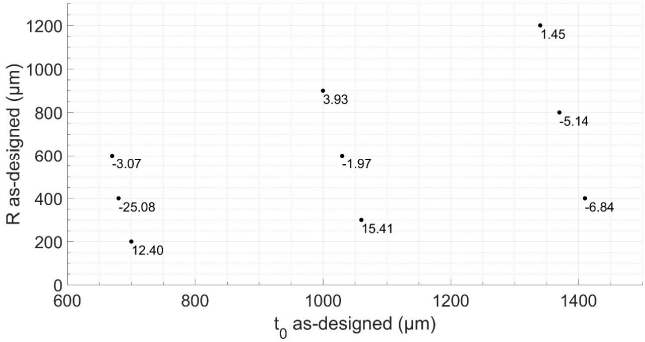

Figure 0.4. Residuals (%) on the fit of the fillet radii of the specimen printed at 45°: positive position on vertical face.

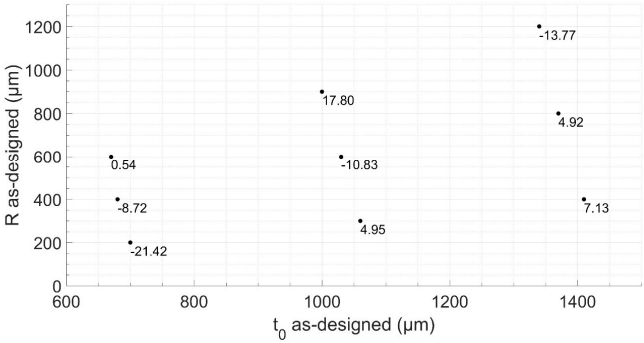

Figure 0.5. Residuals (%) on the fit of the fillet radii of the specimen printed at 45°: negative position on vertical face.

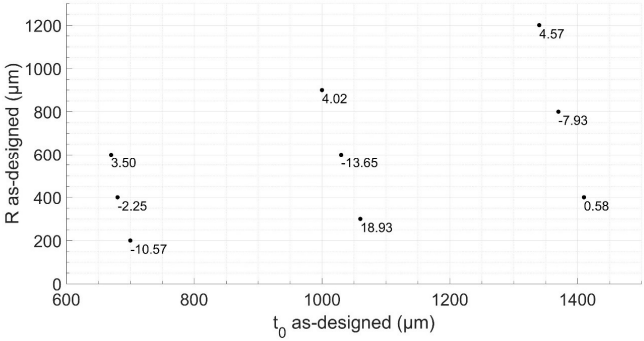

Figure 0.6. Residuals (%) on the fit of the fillet radii of the specimen printed at 45°: lateral position on vertical face.

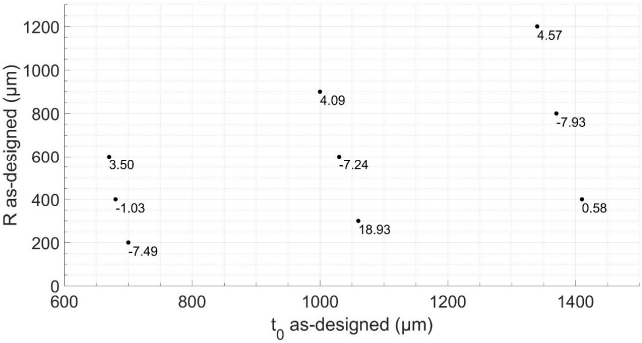

Figure 0.7. Residuals (%) on the fit of the fillet radii of the specimen printed at 45°: positive position on inclined face.

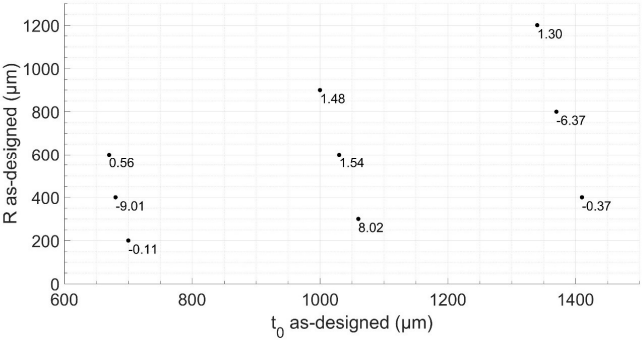

Figure 0.8. Residuals (%) on the fit of the fillet radii of the specimen printed at 45°: negative position on inclined face.

4.8.3 Specimens printed at 45°-35.26°

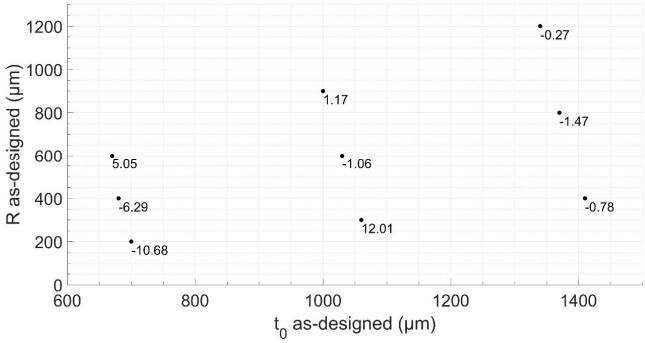

Figure 0.9. Residuals (%) on the fit of the fillet radii of the specimen printed at 45°-35.26°: positive position on inclined face.

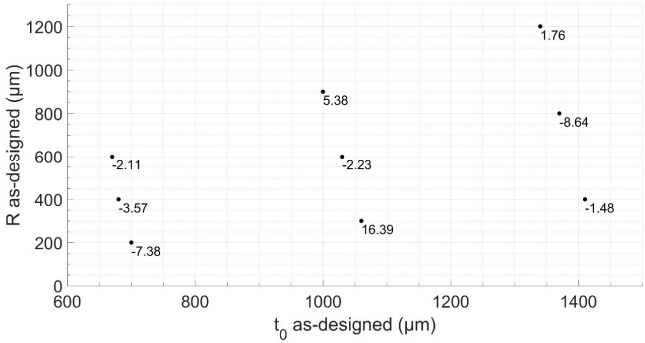

Figure 0.10. Residuals (%) on the fit of the fillet radii of the specimen printed at 45°-35.26°: negative position on inclined face.

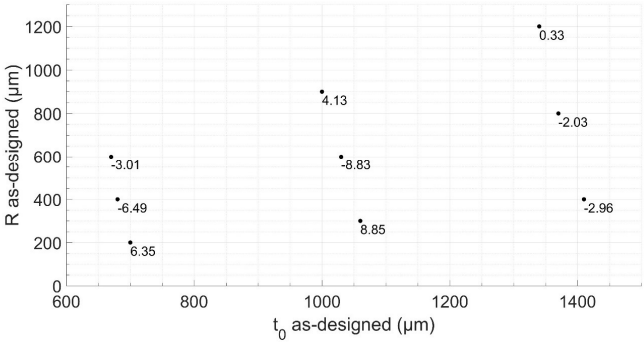

Figure 0.11. Residuals (%) on the fit of the fillet radii of the specimen printed at 45°-35.26°: lateral position on inclined face.

Chapter V

Conclusions and future perspectives

This work is an investigation into the relationship between the mechanical properties and the manufacturing geometrical accuracy of SLM Ti-6Al-4V biomedical lattice materials with filleted junctions for enhanced fatigue resistance. In the first part of the work, the effect of filleted junctions on the elastic constants and on the stresses at the junctions have been assessed in 2D square cell lattices and semi-analytical models have been devised to provide the designer with a tool to predict the elastic constants and the SCFs at the junctions. In the second part of the work, such design tools have been used as an aid in the design of a first batch of 3D cellular lattice specimens based on the cubic unit cell and with an elastic modulus of 3 GPa (matching that of human trabecular bone). These specimens have been used to carry out static and fatigue mechanical tests and have been also the object of an in-depth metrological study using a μCT system. The aim was to investigate the deviation between the as-designed and the as-built geometries caused by the manufacturing process and its effect on the mechanical properties. In the third part of the work, a second batch of SLM Ti-6Al-4V regular cubic cell specimens was designed and produced with the size of the unit cells scaled up to achieve a better reproduction of the junction fillets, which were not obtained in the first batch due to the minute size of the lattice. Moreover, the specimens, with nine combination of the geometrical parmeters (strut diameter and fillet radius), where printed along different printing directions to include also the effect of the inclination of the struts on the geometrical quality of the lattice. A metrological investigation was carried out with an optical system to establish mathematical relationships between the as-built and the as-designed geometrical parameters. Such relationships were used to compensate the manufacturing errors and to reduce the as-built/as-designed deviation.

5.1 Concluding remarks

Increasing the fillet radius at the junctions between the struts of lattice materials was shown to decrease the stress concentration factors, presumably leading to an improvement of the fatigue resistance. The fillet radius has a significant effect on the elastic properties of the lattice, and thus it shouldn't be neglected. Bending dominated structures, in which the joint stiffness has stronger effect on the properties of the lattice, are more sensitive to the fillet radius than stretching dominated structures.

There can be remarkable morphological deviations between the as-built and the as-designed lattice structure. During printing, the distribution of material does not depend only on the as-designed geometry fed to the machine but also on the parameters of the process and on the local variations of the thermal properties of the system. In other words, struts with a different orientation to the printing direction are reproduced with a different accuracy. More specifically, struts with a low angle to the printing plane are systematically affected by an overhang of accumulated molten material that increases the as-built thickness and offsets the barycenter of the cross-sections from the imaginary axis that connects the two junctions introducing a sort of "waviness". The uneven distribution of material affects also the strut junctions by slightly displacing their barycenter and by introducing sharp notches.

The fillet radii have been rather accurately reproduced by SLM and regular shape fillets have been obtained only for a radius above 200 μm. It was observed that the radii measured depend on both the as-designed fillet radius and as-designed strut thickness, although the former parameter has a considerably stronger effect. The scatter of the data is quite high, warning the designer on the fact that considerably sharp junctions can be found, due to local irregularities in the accumulation of parasitic mass or lack of melting. There is a linear relationship between the as-designed and the as-built strut thickness for all the orientations of the strut to the printing direction considered and the parameters of the relationship are a function of the angle.

The comparison between the mechanical properties predicted considering the as-designed geometry and those measured experimentally highlights the fact that the mechanical behavior of SLM cellular is strongly influenced by the defects (notches, as-built/as-designed geometrical deviations) introduced by the manufacturing process. In other words, an in-depth knowledge of the characteristics of the manufacturing process is essential to design cellular structures. The higher thickness of the as-built struts increases the elastic modulus while the bending actions introduced by the strut waviness and the junction center displacement reduce the elastic modulus. Stretching dominated structures are likely more sensitive to these effects, definitely more than bending dominated structures. The irregularities introduced during the manufacturing process have a significant effect on the fatigue properties. In general, the ideal geometry causes the overestimation of the fatigue properties because it does not obviously consider the fact that the additive manufacturing process is not always able to exactly replicate the geometry. Lattices with finer geometrical details are more sensitive to the manufacturing process.

It was shown that it is it is possible to devise compensation models that provide the designer with a tool to generate a CAD geometry that, fed to the printer, accommodates for the parasitic mass and the geometrical errors leading to as-built lattices that very closely matche the desired geometry.

5.2 Future work

Considering the results obtained, there is considerable room for improvement and, moreover, several directions of continuation of the reaserch are open. Among the many options, the following themes are natural prosecution of the work carried out until now:

- The semi-analytical models of the elastic constants and the SCFs of 2D lattices, despite having performed reasonably well in the design of the 3D SLM specimens, need an experimental verification campaign using 2D specimens. Furthermore, similar predictive models should be developed also for the staggered cubic lattices.
- The FE analyses carried out using the results of the μCT scans produced interesting results, but somewhat limited. On one hand, the solid FE models should be increased in size to include more unit cells in order to have more realistic boundary conditions and, consequently, a more accurate depiction of the stress state at the junctions. On the other, the data available from the μCT scans of the lattices other than the regular cubic should be used to carry out a similarly in-depth statistical analysis of the metrological data.

  These analyses would be particularly interesting regarding the staggered cubic lattices, since the presence of bending actions significantly change the mechanical behaviour of the lattice and consequently the effect of the geometrical imperfections.
- An attempt should be made to link the notches and the irregularities of the surface to the fatigue strength using Murakami's $\sqrt{area}$ concept.
- The work presented in Chapter IV is clearly partial and needs to be completed with mechanical testing of the structures described by designing appropriate specimens to verify the effectiveness of the fillet radius in increasing the fatigue strength, to assess the effectiveness of the compensation strategy in increasing the predictability of the mechanical properties and to evaluate the effect of printing direction on the mechanical properties. Such experimental campaign is currently underway. In order to reduce the number of specimens to manufacture, five types of specimens have been designed by varying each time a feature of a base specimen that includes all the lessons learned form the work presented in this thesis. Such base specimen (specimen A in Figure V – 1) has filleted junctions, is printed so that the load bearing struts are aligned with the printing direction and has compensated struts to reduce the as-built/as-designed deviation. Four other types of specimens are obtained by aligning the load bearing struts with the printing direction

(specimen B in Figure IV – 1) and by not compensating the struts (specimen C in Figure IV – 1). Furthermore, by removing the fillets from specimen A, specimen D is obtained and by decreasing the unit cell size, specimen E.

Ten specimens are to be manufacture for each type (Ti-6Al-4V via SLM), to carry out fatigue and static mechanical tests.

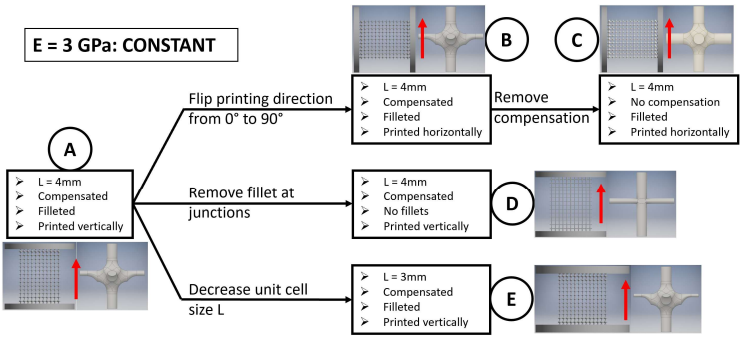

Specimen description:

A. Printed along the natural axis of the specimen, filleted junctions and compensated struts.
B. Printed normal to the natural axis of the specimen, filleted junctions and compensated struts.
C. Printed normal to the natural axis of the specimen, filleted junctions but without compensated struts.
D. Printed along the natural axis of the specimen, without filleted junctions and compensated struts.
E. Decrease unit cell size (and fillet radius and strut diameter to keep the modulus at 3 Gpa)

Figure V - 1. Scheme of the specimens to manufacture for static and fatigue testing to assess the effectiveness of the compensation strategy and of the addition of a fillet radius at the strut joints.

Scientific production

Journal articles

M. Dallago, M. Benedetti, V. Luchin and V. Fontanari, Orthotropic elastic constants of 2D cellular structures with variously arranged square cells: the effect of filleted wall junctions, International Journal of Mechanical Sciences 122 (2017), pp. 63–78

M. Dallago, V. Fontanari, E. Torresani, M. Leoni, C. Pederzolli, C. Potrich, M. Benedetti, Fatigue and biological properties of Ti-6Al-4V ELI cellular structures with variously arranged cubic cells made by selective laser melting, Journal of the Mechanical Behavior of Biomedical Materials 78 (2018), pp. 381–394

M. Dallago, B. Winiarski, F. Zanini, S. Carmignato, M. Benedetti, On the effect of geometrical imperfections and defects on the fatigue strength of cellular lattice structures additively manufactured via Selective Laser Melting, International Journal of Fatigue 124 (2019), pp. 348–360

Peer reviewed conference papers

M. Dallago, F. Zanini, S. Carmignato, D. Pasini, M. Benedetti, Effect of the geometrical defectiveness on the mechanical properties of SLM biomedical Ti6Al4V lattices, Procedia Structural Integrity 13 (2018), pp.161-167

M. Dallago, V. Fontanari, B. Winiarski, P.J. Withers, F. Zanini, S. Carmignato, M. Benedetti, Fatigue properties of Ti6Al4V cellular specimens fabricated via SLM: CAD vs real geometry, Procedia Structural Integrity 7 (2017), pp.116-123

M. Dallago, S. Raghavendra, V. Luchin, G. Zappini, D. Pasini, M. Benedetti, Geometric assessment of lattice materials built via Selective Laser Melting, Materials Today: Proceedings 7 (2019), pp. 353-361

Partecipation to *Congresses*, *Schools* and *Workshops*

Conferences

AIAS2018 - 47° Convegno Nazionale (annual conference of the Italian Scientific Society of Mechanical Design), Villa S. Giovanni (ITALY), September 5-7, 2018
Oral presentation: "Compensazione della geometria di strutture cellulari realizzate mediante manifattura additiva ed effetto sul modulo elastico"

ECF22 - 22nd European Conference on Fracture, Belgrade (SERBIA), August 26-31, 2018
Oral presentation: "Effect of the geometrical defectiveness on the mechanical properties of SLM biomedical Ti6Al4V lattices"

FDMD3 – Third International Symposium on Fatigue Design and Material Defects, Lecco (ITALY), September 19-22, 2107
Oral presentation: "Fatigue properties of Ti6Al4V cellular specimens fabricated via SLM: CAD vs real geometry"

AIAS2017 - 46° Convegno Nazionale (annual conference of the Italian Scientific Society of Mechanical Design), Pisa (ITALY), September 6-9, 2017
Oral presentation: "Computation of the stress concentration factors in 2D cellular structures"

AIAS2016 - 45° Convegno Nazionale (annual conference of the Italian Scientific Society of Mechanical Design), Trieste (ITALY), September 7-10, 2016
Oral presentation: "Stiffness of 2D cellular square cell structures"

Workshops

ProM Facility Open House – Rovereto, June 30, 2017
Oral presentation: "Fatigue and biological properties of parts manufactured by selective laser melting"

Summer Schools

PhD Summer School AIAS – Design of mechanical components using additive manufacturing, Ferrara (ITALY), June 12-15, 2017

PhD Summer School AIAS – Non-linear behaviour of materials – Theory and applications, Ferrara (ITALY), June 13-16, 2016

Acknowledgments

I would like to express my gratititude to my supervisors Prof. Matteo Benedetti and Prof. Vigilio Fontanari for their guidance, mentorship and for sharing their knowledge. Their support and encouragement were well beyond what a PhD student could expect form his supervisors. I owe Matteo a big thank you for his help, his faith in me and for having provided me with countless opportunities of professional growth.

A considerable part of this work would not have been possible without the contribution of Eurocoating Spa that provided most of the specimens used in this work. In particular, I wish to thank Gianluca Zappini, Valerio Luchin and Massimiliano Tommaselli who were very collaborative in sharing their considerable knowledge of the SLM process.

I am very to thankful to Prof. Damiano Pasini (McGill University, Montreal) who gave me the chance to join his research group for six months as a visiting researcher at McGill and allowed me to live a unique scientific and personal experience. I also wish to thank my friends and collegues at McGill for having made those months so enriching and for the many interesting technical discussions.

I was really lucky to have met Federico, Francesca, Marco and Michelangelo during my PhD because they made these years truly unforgettable. A special thank you goes to Michelangelo for having been such a great co-worker during our industrial projects and for all the help he gave me in my work. I am truly grateful to my friend and collegue Sunil Raghavendra for all the time he spent at the microscope taking pictures of the cellular specimens while I was in Montreal, for his suggestions and for all the proficuous discussions we had: his contribution to this work was really essential and I cannot thank him enough. I also whish to thank all my other collegues for creating the best possible working environment.

I wish to express my gratitude to my parents Agnes and Bruno, my sister Alice and all my friends for their continuos support.

Finally, I am very lucky and happy to have Giulia and I am very thankful for her love, understanding, support and motivation that guide me and give me strength to overcome all obstacles in my life.